



HAL
open science

Etude de la stabilité thermoélectronique des conducteurs supraconducteurs à basse température critique et contribution à l'étude de la stabilité thermoélectrique des supraconducteurs à haute température critique.

Frédéric Trillaud

► To cite this version:

Frédéric Trillaud. Etude de la stabilité thermoélectronique des conducteurs supraconducteurs à basse température critique et contribution à l'étude de la stabilité thermoélectrique des supraconducteurs à haute température critique.. Energie électrique. Institut National Polytechnique de Grenoble - INPG, 2005. Français. NNT: . tel-00181001

HAL Id: tel-00181001

<https://theses.hal.science/tel-00181001>

Submitted on 22 Oct 2007

HAL is a multi-disciplinary open access archive for the deposit and dissemination of scientific research documents, whether they are published or not. The documents may come from teaching and research institutions in France or abroad, or from public or private research centers.

L'archive ouverte pluridisciplinaire **HAL**, est destinée au dépôt et à la diffusion de documents scientifiques de niveau recherche, publiés ou non, émanant des établissements d'enseignement et de recherche français ou étrangers, des laboratoires publics ou privés.

INSTITUT NATIONAL POLYTECHNIQUE DE GRENOBLE

N°: |_|_|_|_|_|_|_|_|_|_|_|_|_|_|_|_|

THESE

pour obtenir le grade de

DOCTEUR DE L'INPG

Spécialité : Génie Electrique

préparée dans le Service des Accélérateurs, de Cryogénie et de Magnétisme du
Commissariat à l'Energie Atomique

dans le cadre de l'Ecole Doctorale "Electronique, Electrotechnique,
Automatique, Télécommunications, Signal"

présentée et soutenue publiquement

par

Frédéric Trillaud

le 28 Septembre 2005

Titre :

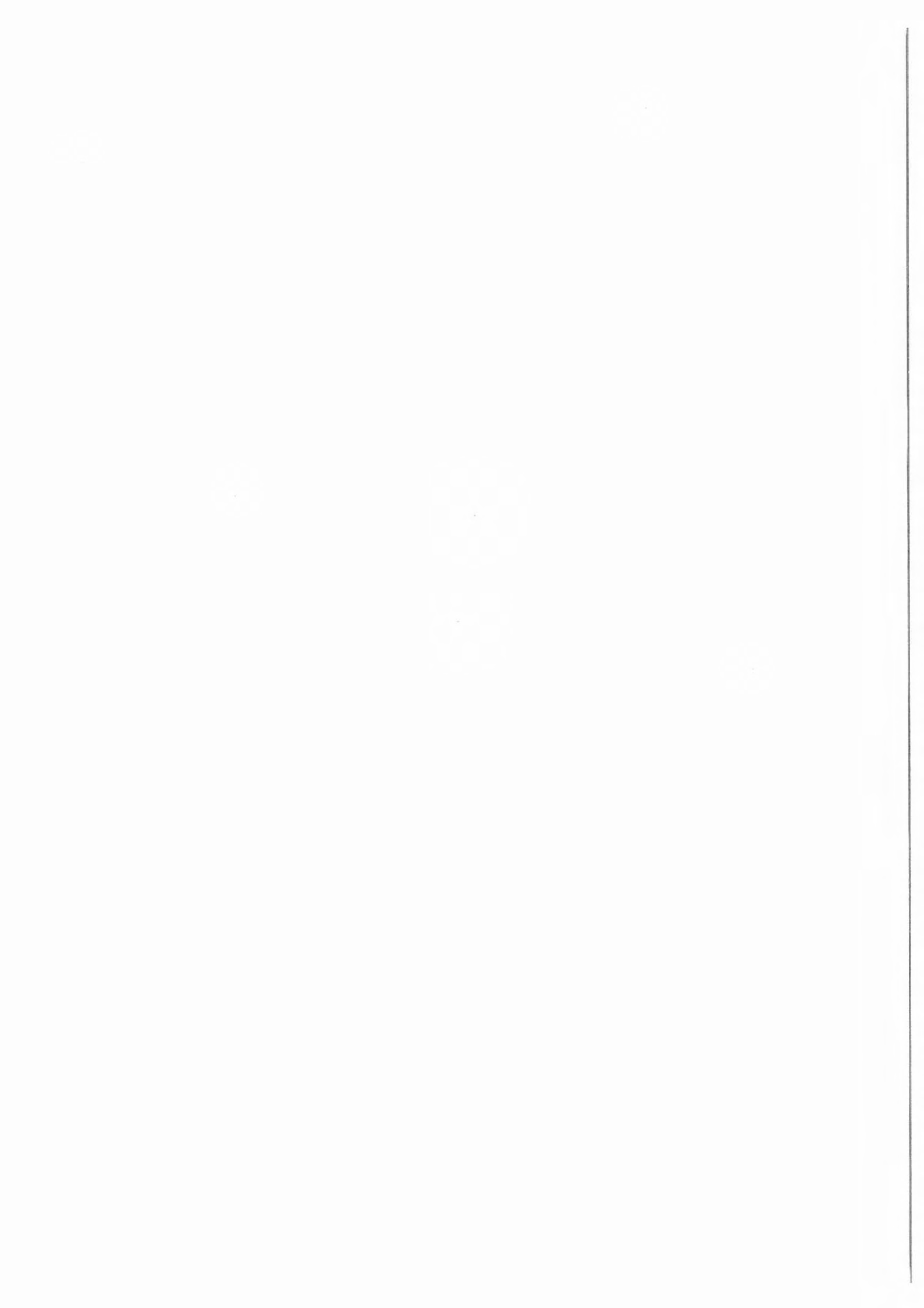
**Etude de la stabilité thermoélectronique des conducteurs
supraconducteurs à basse température critique et contribution à
l'étude de la stabilité thermoélectrique des supraconducteurs à
haute température critique**

*Développement de nouvelles techniques pour simuler les perturbations d'énergie de faibles
dimensions et de courtes durées dans les aimants supraconducteurs*

Directeur de Thèse : PASCAL TIXADOR

JURY

M. Jean-Luc Duchateau	, Président et Rapporteur
M. Lucio Rossi	, Rapporteur
M. Pascal Tixador	, Directeur de thèse
M. Arnaud Devred	, Co-encadrant
M. Justin Schwartz	, Co-encadrant
M. Gérard Grunblatt	, Examineur



Scholar years 2000-2001 and 2002-2005
Defended on September, 28th. 2005

Thesis

**Study of the thermo-electronic stability of LTS
conductors and contribution to the study of the
thermo-electric stability of HTS conductors**

*Novel techniques to simulate quench precursors in superconducting
electro-magnets*

Philosophiae Doctor

defended by **Frederic Trillaud**

Institut National Polytechnique de Grenoble

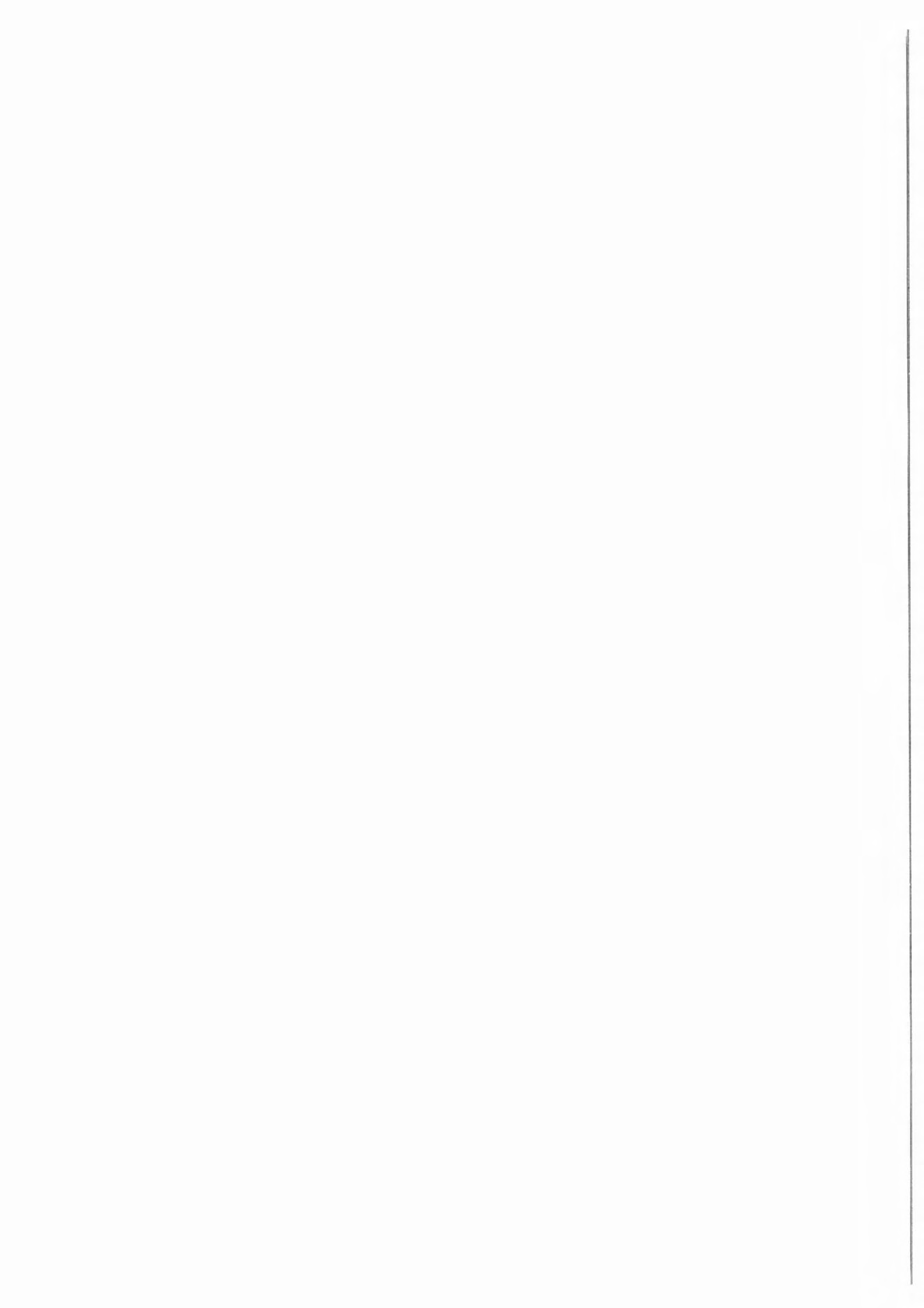
**EEATS (Electronique, Electrotechnique, Automatique,
Télécommunications, Signal”)**

Jury:

Dr. A. Devred	CEA advisor (CEA, France)
Dr. J.L. Duchateau	President/Reviewer (CEA, France)
Dr. G. Grunblatt	Industrial partner (Alstom/MSA, France)
Dr. L. Rossi	Reviewer (CERN, Switzerland)
Dr. J. Schwartz	NHMFL advisor (NHMFL/FSU, U.S.A.)
Dr. P. TIXADOR	PhD advisor (CNRS, France)



Work carried out at CEA/Saclay (France) and at the National High Magnetic field
Laboratory of Florida, NHMFL/FSU (US)



Acknowledgments

Je voudrais remercier mon partenaire industriel, Alstom/MSA (France), qui fournit, dans les meilleurs délais, les échantillons de brin supraconducteur nécessaires à mes travaux. Je voudrais également remercier l'ensemble des laboratoires qui m'ont chaleureusement accueilli au cours de ces années : le Service des Accélérateurs, de Cryogénie et de Magnétisme du Commissariat à l'Energie Atomique (SACM/CEA, France), le National High Magnetic Field Laboratory (NHMFL, Florida US) ainsi que le Centre de Recherche sur les Très basses Températures du Centre National pour la Recherche Scientifique (CRTBT/CNRS) de Grenoble (France). Je tiens à remercier tout particulièrement Messieurs A. Devred, J. Schwartz et P. Tixador pour leur soutien, et leur conseils scientifiques et techniques qui m'ont permis d'avancer dans mes recherches.

En m'excusant par avance envers tous ceux que j'aurais involontairement oubliés et qui m'ont également aidé, de nombreux mercis à :

A. Acker, F. Ayela, J. Barrow, B. Baudouy, P. Bauer, C. Berriaud, L. Bortura, M.P. Bourgeois, P. Brosse Maron, S. Calatroni, M. Carty, A. Caruso, M. Cazanou, P. Chesny, P. Contrepoids, M. Dalban-Canassy, P. Debu, T. Dechambre, J.L. Duchateau, M. Durante, M. Fratini, B. Gastineau, J.M. Gheller, G. Grunblatt, B. Hervieu, G.K. Hoang, Y. Iwasa, M. Jacquemet, F.P. Juster, F. Kirscher, L. Kulbicki, D. Leboeuf, P. Ledortz, M. Malabaila, S. Mzah, J.C. Paladji, H. Palanki, C. Perrier, J.M. Rey, J.M. Rifflet, J.P. Rodrigucz, F. Rondeaux, M. Segreti, S.H. Thompson, B. Trociewitz, U.P. Trociewitz, P. Vedrine, C. Verwaerde, H.W. Weijers.

Sans oublier mes parents, ma famille et mes amis, merci à tous!!

Frédéric Trillaud
le 28 Septembre 2005

"Hay que endurecerte pero sin perder la ternura, jamás!"
(Il faut s'endurcir sans jamais se départir de sa tendresse.)

"Soyez réalistes : demandez l'impossible."

Ernesto Che Guevara

Contents

I	Résumé de thèse	20
I.1	Chapitre II : introduction générale	22
I.2	Chapitre III : chaufferette résistive	29
I.3	Chapitre IV : diode laser et chaufferette inductive	33
I.4	Chapitre V : simulations numériques	40
I.5	Chapitre VI : supraconducteurs à haute température critique	44
I.6	Chapitre VII : conclusion générale	48
II	General Introduction	50
II.1	Collaborations and objectives of the thesis	51
II.2	Overview on stability	52
II.3	Notions of composite conductor stability	54
II.4	Review on the various means to simulate quench precursors	60
II.5	Our choice of heater technologies	71
III	Preliminary LTS experiment using a carbon point heater	77
III.1	LHC-type NbTi wire samples, batch NbTi-1	78
III.2	Experimental setup incorporating a point heater	80
III.3	A few results on contact resistance	86
III.4	Voltage trace recordings and phenomenology of the normal zone transition	92
III.5	Results on Quench Energies	97
III.6	Conclusions on carbon paste point heaters	101
IV	New LTS experiment using a diode laser	103
IV.1	LHC-type NbTi wire samples, batch NbTi-2	105
IV.2	New setup for inductive and laser heaters	106
IV.3	Determination of the optical energy produced by the diode laser	121
IV.4	Calibration of the optical energy absorbed by the oxidized sample	136
IV.5	Stability measurements	149
V	Numerical simulation of the thermal behavior of a Cu/NbTi multifilament composite wire	169
V.1	Introduction to the numerical analysis	171
V.2	Description of the numerical model	174
V.3	Heat generation in the multifilament composite wire	175
V.4	Initial heat perturbation	177
V.5	Heat transfer coefficient and adiabatic conditions	178

V.6	Results on the numerical simulation and comparison with experimental data	182
V.7	Conclusion on numerical simulations	194
VI	Preliminary HTS experiments using Ohmic heaters	196
VI.1	Description of the samples	198
VI.2	Heaters	199
VI.3	Helium gas cooling: preliminary study using strain gages	202
VI.4	Nitrogen gas cooling experiment	204
VI.5	Conduction cooling Experiment	216
VII	General Conclusions	227
VII.1	Superconducting magnet stability	227
VII.2	Further improvements of the actual experimental setup and numerical simulation	229
VII.3	Perspectives: Nb ₃ Sn	231
A	Residual resistivity of metals	234
B	Critical current parametrization	235
C	Interpolation of the optical power delivered by the diode laser	238
D	Description of the new probe for stability studies	241
D.1	G-10 tube and supports of the probe	241
D.2	Helium vapor cooled current leads	241
D.3	Main tube	244
D.4	Support of the vacuum chamber	244
D.5	Diode laser support and its fiber tube	245
E	Thermal and magnetic flux diffusion in a composite wire	246
F	Material properties	250
F.1	Heat capacity of the conductor	250
F.2	Resistivity of the wire	251
F.3	Thermal conductivity	253

List of Figures

I.1	Evolution du courant critique en fonction de la température.	24
I.2	Evolution typique de l'énergie de transition ("Quench Energy", QE) en fonction de la durée de la perturbation ou de la longueur de la zone chauffée.	25
I.3	Description de la chaufferette numéro 2.	30
I.4	Evolution de la résistance de contact de la chaufferette numéro 4 durant une campagne de tests de stabilité.	31
I.5	Energie de transition en fonction de la durée du pulse à 8 T, 4.2 K et 95% de I_c	31
I.6	Diode laser et sa fibre optique.	34
I.7	Deux photos montrant la partie inférieure du porte échantillon et une vue de côté de ce même support.	35
I.8	Caractéristique puissance optique/courant de diode pour une température de la diode laser de 293 K avec 2/3 de la fibre optique baignant dans l'azote liquide à 77 K.	36
I.9	Evolution du coefficient d'absorption en fonction de la puissance du laser.	37
I.10	Evolution de l'énergie de transition en fonction de la durée du pulse à différentes inductions magnétiques, à 4.2 K, et à 85% du courant critique.	39
I.11	Evolution de la vitesse de propagation en fonction du courant de transport du brin à différentes inductions magnétiques, à 4.2 K, et à 85% du courant critique.	39
I.12	Evolution de la tension V_1 , estimée numériquement, et des résultats expérimentaux en fonction du temps pour $\eta = 450 \text{ Js}^{-0.6}$ et $a_k = 300 \text{ W/m}^2/\text{K}^4$	41
I.13	Evolution de l'énergie minimale de transition numérique en fonction de la durée du pulse.	42
I.14	Description de la chaufferette en fil de NiCr.	45
I.15	Evolution de l'énergie minimale de transition en fonction du pourcentage de courant critique.	46
I.16	Evolution de la vitesse de propagation en fonction du pourcentage de courant critique.	46
II.1	Quench performances of LHC superconducting magnets.	53
II.2	Linearized critical current characteristic of a superconducting multifilament composite wire at a given background magnetic field	56
II.3	Comparison between HTS and LTS conductors.	56
II.4	Typical evolution of the quench energy as a function of pulse durations or heat disturbance lengths.	59
II.5	Induction coil wound around an alumina tube.	61
II.6	Ceramic resistor chip heater.	63

II.7	Ohmic wire.	64
II.8	Kapton [®] sandwich heater.	66
II.9	Comparison of carbon paste heater and tip-heater reproducibilities.	67
II.10	Tip-heater.	68
III.1	Cross-sectional view of a generic LHC-type Cu/NbTi multifilament composite wire used in accelerator magnet technology (courtesy Alstom/MSA).	79
III.2	Critical current versus background magnetic flux density of samples NbTi-1.	80
III.3	Description of charged point heater 2.	81
III.4	Pictures of the experimental setup (charged point heater).	83
III.5	Picture of the heater holder (Assembly 1).	84
III.6	Description of the tip of heater 2.	84
III.7	Pictures of the tip of heater 5 throughout its positioning.	85
III.8	Electrical sketch for contact resistance measurements.	87
III.9	Average contact resistance and contact pressure versus compression strain per washer for heater 2 and heater 5.	88
III.10	Evolution of the average contact resistance of heater 4 over a series of stability measurements.	89
III.11	Electrical sketch of the stability experimental setup.	91
III.12	Voltage traces at a quench (charged point heater).	92
III.13	Voltage traces showing the current redistribution (charged point heater).	94
III.14	Zoom on early normal zone creation (charged point heater).	96
III.15	Voltage traces at a recovery (charged point heater).	96
III.16	Quench energy versus pulse duration (heater 4).	98
III.17	Quench energy versus normalized current (heater 4).	98
III.18	Quench Energy versus pulse duration at 90% and 95% of I_c for different values of contact resistance obtained with heater 5.	100
IV.1	Micrographies of oxidized Cu/NbTi composite wire.	107
IV.2	Critical current versus background magnetic flux density.	108
IV.3	Schematic illustration of a laser chip making the diode laser.	109
IV.4	Diode laser and its pre-coupled optical fiber.	109
IV.5	Picture of the optical fiber extension.	111
IV.6	Schematic structure of an optical fiber.	112
IV.7	Tip of the optical fiber extension.	112
IV.8	Sketch of the thermal regulation system of the diode laser used at CEA/Saclay.	113
IV.9	two pictures and a 3D drawing showing the metallic assembly to maintain the tip of the optical fiber and a bottom view of the sample holder.	115
IV.10	Two pictures showing the metallic assembly to maintain the tip of the optical fiber and localization of the induction coils.	115
IV.11	3D view of the various assemblies to clamp the sample and the tip of the optical fiber.	116
IV.12	Electrical sketch of the acquisition system and the power circuitry.	117
IV.13	Localization of the pairs of voltage taps and of the heaters along the wire sample.	117
IV.14	V-I characteristic of NbTi sample at 7 T and 4.2 K.	120
IV.15	Sketch of the experiment to measure the optical power versus forward current characteristic of the diode laser.	122

IV.16	Optical power versus forward current characteristic of the diode laser measured at 293 K.	123
IV.17	Influence of the connector.	125
IV.18	Measurements at various temperature.	125
IV.19	Influence of the cryogenic fluid on the optical fiber transport properties. . .	127
IV.20	Influence of the cryogenic environment on the optical fiber.	128
IV.21	Examples of current pulses for two different pulse durations.	130
IV.22	Optical energy pulses.	130
IV.23	Definition of the different parameters to estimate the thickness of gaseous helium resulting in a total reflection of the outer rays of light flowing from the tip of the optical fiber.	132
IV.24	Estimation of the maximum half-angle of the cone of light for which the outer rays are totally reflected as a function of gaseous helium thickness. .	135
IV.25	Experimental setup used to perform calibration measurements.	136
IV.26	Optical power versus forward current characteristic of the diode laser used for calibration measurements at CRTBT/CNRS.	138
IV.27	The two different bolometers used to estimate the coefficient of absorption of the oxidized samples.	140
IV.28	Calibration of the thermal sensors used for the cylindrical and closed bolometer.	142
IV.29	Time evolution of the resistances of thermal sensors attached to the bolometers. .	143
IV.30	Temperature variation of the bolometers versus the optical power.	145
IV.31	Estimated RRR as a function of optical power.	147
IV.32	Absorptivity as a function of the optical power delivered by the diode laser. .	147
IV.33	Comparison of voltage data for a quench and a recovery at 4.2 K, 7 T and 85% of the critical current.	150
IV.34	Set of recordings of voltage V_1 at increasing forward current of the diode laser. .	151
IV.35	Voltage traces showing the plateau of residual resistivity of metals.	152
IV.36	Voltage traces showing the voltage increase after exceeding the plateau of residual resistivity.	153
IV.37	Determination of the Quench Decision Time.	154
IV.38	Example of the transformation of voltage traces into a plot of the time evolution of quenched zone.	155
IV.39	Evolution of the Quench Energy as a function of the pulse duration at 7 T, 85% of I_c and 4.2 K.	156
IV.40	Determination of the normal zone propagation velocity.	157
IV.41	Time evolution of the quenched zone for various pulse durations.	159
IV.42	Evolution of the Quench Decision Time as a function of pulse durations at various background magnetic flux densities.	160
IV.43	Evolution of the minimum absorbed energy and corresponding pulse energy triggering a quench as a function of the pulse duration.	161
IV.44	Evolution of the quenched zone for various background magnetic flux densities. .	161
IV.45	Evolution of the Quench decision time as a function of background magnetic flux density at various percentages of critical current.	162
IV.46	Evolution of the Minimum absorbed energy and the corresponding pulse energy triggering a quench as a function of background magnetic flux density. .	163
IV.47	Evolution of the Normal Zone Propagation Velocity as a function of background magnetic flux densities.	163

IV.48	Time evolution of the quenched zone at various percentages of critical current.	164
IV.49	Evolution of the Minimum Quench Energy and the corresponding Minimum Pulse Energy as a function of percentage of critical current at different background magnetic flux densities.	165
IV.50	Evolution of the Normal Zone Propagation Velocity as a function of the transport current.	165
V.1	Micrography of the cross-section of a LHC-type Cu/NbTi multifilament composite wire from batch NbTi-2.	172
V.2	Definition of the mesh based on an axi-symmetrical model.	173
V.3	Definition of the boundary conditions imposed on the model. Φ 's symbolize the fluxes exchanged through the surfaces S_i ($i \in \{1, 2, 3, 4\}$) [bold fonts representing vectors]. Here, T_0 is equal to 4.2 K.	174
V.4	Typical critical current versus temperature characteristic of a composite wire at a given background magnetic field.	176
V.5	Heat generation function for a multifilament composite wire.	176
V.6	Shape of the pulse power density implemented in CAST3M.	178
V.7	Transient heat transfer energy to form a film of gaseous helium as a function of time.	179
V.8	Fermi-Dirac-like function to smoothen the heat transfer coefficient h	181
V.9	Evolution of the Minimum Pulse Energy as a function of the parameters η and a_k	182
V.10	Time evolution of the maximum temperature along the sample for $\eta = 450 \text{ Js}^{-0.6}$	183
V.11	Evolution of the Minimum propagating Zone as a function of parameters η	184
V.12	Estimated Quench Decision times as a function of parameters η and a_k	185
V.13	Time evolution of the maximum temperature of the sample as a function of parameters η	186
V.14	Comparison between the heat flux exchanged between the sample and liquid helium and the Joule dissipation normalized to the wetted perimeter of the sample obtained at 4.2 K, 7 T, 85% of I_c and for a pulse duration of 50 μs	186
V.15	Time evolution of the voltage across the heated zone as a function of parameters η and a_k and comparison with experimental data.	188
V.16	Temperature profiles for a quench (a) and a recovery (b) for $a_k = 300 \text{ W/m}^2/\text{K}^4$ and $\eta = 450 \text{ Js}^{-0.6}$	190
V.17	Time evolution of film of gaseous helium extension and quenched zone for $a_k = 300 \text{ W/m}^2/\text{K}^4$ and $\eta = 450 \text{ Js}^{-0.6}$	192
V.18	Comparison of experimental and numerical Quench Energies versus pulse durations at 7 T, 4.2 K and 85% of I_c for $a_k = 300 \text{ W/m}^2/\text{K}^4$ and $\eta = 450 \text{ Js}^{-0.6}$	192
V.19	Temperature profiles for a quench (a) and a recovery (b) for $a_k = 300 \text{ W/m}^2/\text{K}^4$ and $\eta = 450 \text{ Js}^{-0.6}$	193
VI.1	Sketch of an YBCO tape (scale not respected).	199
VI.2	Micrography of Bi-2212 tapes on which is glued a strain gage.	200
VI.3	NiCr wire glued on an YBCO tape.	201
VI.4	Picture of a damaged strain gage.	203
VI.5	Local destruction of a Bi-2212 tape.	203
VI.6	Sample holder for stability study in Nitrogen gas cooling conditions.	204

VI.7	Localization of the pairs of voltage taps along the YBCO sample.	206
VI.8	Localization of the pairs of voltage taps along the YBCO sample.	206
VI.9	Electrical sketch of the quasi-adiabatic experiment conducted on HTS tapes.	207
VI.10	Typical pulse traces.	208
VI.11	Voltage traces and corresponding temperatures at 82.9 K and 0 T for $0.87I_c$	209
VI.12	Short sample critical current of Bi-2223 tapes versus temperature.	211
VI.13	Voltage traces V_3 and V_4 at 82.7 K in self-field for an energy pulse of 63 mJ.	211
VI.14	Voltage trace V_1 across the heater recorded at increasing energy pulse.	212
VI.15	Critical current measurements of an YBCO short sample at various temperatures. For these temperatures of measurements ("operating points"), the stability margin is given.	213
VI.16	Voltage traces V_1 , V_2 and V_3 versus time for different fractions of critical current at 80.6 K in self-field.	214
VI.17	Minimum Pulse Energy versus the fraction of critical current at 80.6 K in self-field.	214
VI.18	Normal Zone Propagation Velocity versus the fraction of critical current at 80.6 K in self-field.	215
VI.19	OFHC copper sample holder for quasi-adiabatic measurements, on which is mounted a Bi-2223 tape.	217
VI.20	Localization of the pairs of voltage taps along the YBCO sample for conduction cooling measurements.	217
VI.21	Verification of the hypothesis of critical current homogeneity along the sample.	218
VI.22	Voltage V_{10} recorded at increasing energy pulse.	219
VI.23	Quench Decision Time versus energy of the heat pulse at 65 K. The error bars are a measure of the accuracy with which the onset times can be determined from the $V(t)$ curves.	220
VI.24	Voltages V_{10} , V_{12} , and V_{13} recorded at ~ 79 K for 50% of critical current.	220
VI.25	Comparison of the normal zone propagation velocity versus the percentage of critical current of nitrogen gas cooling and conduction cooling.	222
VI.26	Minimum Pulse Energy versus the operating temperature.	223
VI.27	Comparison of Minimum Pulse Energy triggering a quench. The discrepancy is due to the influence of the coolant.	224
VII.1	Minimum Pulse Energy as a function of the pulse duration at 7 T and 4.2 K for various percentages of critical current.	231
VII.2	Normal Zone Propagation Velocity as a function of the transport current at 7 T and 4.2 K.	232
A.1	Schematic view of the temperature evolution of silver and copper.	234
B.1	Critical-current surface for commercial NbTi alloy.	236
C.1	Fit of the optical power versus forward current characteristic of the diode laser.	239
D.1	New probe for stability tests.	242
D.2	Cross-section of the vacuum chamber and sample holder.	243
D.3	Support of the diode laser and its fiber tube.	245
E.1	Sketch of the cross-section of a multifilament Cu/NbTi composite wire.	247

F.1	Heat capacity of the Copper and NbTi, and resulting average heat capacity of the wire as a function of temperature at 7 T.	252
F.2	Resistivity of the different coppers (pure copper Cu1 and degraded copper Cu2) and resulting average resistivity of the wire as a function of the temperature at 7 T.	253
F.3	Thermal conductivity of the different coppers (pure copper Cu1 and degraded copper Cu2) and the average thermal conductivity as a function of the temperature at 7 T.	254

List of Tables

I.1	Domaines d'application des différents systèmes de chaufferette existante et leur principale qualité.	26
I.2	Caractéristiques de la diode laser mono-mode et de la fibre optique additionnelle.	34
II.1	Disturbance spectrum.	54
II.2	A few generic physical properties of HTS and LTS conductors.	57
II.3	Domain of applications, advantages and drawbacks of the main heater technologies.	71
III.1	Salient parameters of NbTi-1 wires.	79
III.2	Contact resistances of charged point heaters at 4.2 K.	82
III.3	The different heaters used in the experiment and their corresponding assembly.	86
III.4	Voltage drops and the corresponding distance between their voltage taps.	91
III.5	Slope of the linear increasing part of voltage V_1 and V_2 and the corresponding Normal Zone Propagation Velocity.	95
IV.1	Salient parameters of NbTi-2 wires.	106
IV.2	Salient parameters of the single-mode diode laser at 293 K (used for stability measurements at CEA/Saclay).	110
IV.3	Distances between voltage taps.	118
IV.4	Voltage identification, localization, and acquiring devices.	119
IV.5	Description of the main electrical equipments.	119
IV.6	Summary of salient parameters of the diode laser.	126
IV.7	Minimum pulse durations achieved with the diode laser.	131
IV.8	Parameters of calculation.	134
IV.9	Salient parameters of the single-mode diode laser at 298 K used for calibration measurements at CRTBT/CNRS.	137
IV.10	Salient design parameters for the closed bolometer.	139
IV.11	Thermal properties of the thermal drain and the stainless steel support.	144
IV.12	Values of transport current as a function of percentage of critical current and background magnetic field.	149
V.1	Parameters to model the NbTi-2 wire.	172
V.2	Current sharing temperatures and critical temperatures.	177
VI.1	Salient features of YBCO tapes.	199
VI.2	Thermal properties of polyimides and Stycast [®] 2850FT at room and low temperatures.	200

VI.3	Salient parameters of silicone insulated 80%Ni20%Cr "Stablohm650" wire.	202
VI.4	Distances between voltage taps for Bi-2223 and YBCO tapes.	205
VI.5	Distances between voltage taps for the YBCO tapes (quasi-adiabatic measurements).	216
VI.6	Average critical current.	218
VI.7	Critical current measured in situ before the stability tests.	219
B.1	Intrinsic parameters of NbTi alloy.	236
B.2	Parameters of Luca Bottura's fit for NbTi-1 and NbTi-2 wires.	236
E.1	Homogeneous physical properties following the wire radius and estimation of the diffusion parameters at 4.2 K.	247
F.1	Numerical values to evaluate the heat capacity of NbTi.	251

Nomenclature

Latin letters

a	Thickness of gaseous helium	m
a_k	Kapitza coefficient	W/m^2K^4
A_{Cu1}	Cross-section of pure copper Cu1	m^2
A_{Cu2}	Cross-section of degraded copper Cu2	m^2
A_{SS}	Cross-section of stainless steel support	m^2
A_{TD}	Average cross-section of thermal drain	m^2
A_w	Cross-section of wire sample	m^2
B_{c2}	Upper critical magnetic flux density	T
c_B	Specific heat capacity of closed bolometer	J/kgK
C_i	Embedded Cernoxes [®]	
C_B	Heat capacity of closed bolometer	J/m^3K
C_w	Averaged heat capacity	J/m^3K
d	Distance between the apex of light cone and sample	m
D_{mag}	Magnetic diffusion	m^2/s
D_{th}	Thermal diffusion	m^2/s
E_{ab}	Absorbed optical energy by wire samples	J
E_p	Pulse energy	J
E_f	Energy to create film boiling	J
E_t	Heat transfer energy	J
G	Heat generation function	W/m^3
G_c	Maximum heat generation in conductor	W/m^3
G_{TD}	Thermal conductance of thermal drain	W/K
h	Heat transfer coefficient	W/m^2K
H	Volumetric heat transfer	W/m^3
h_{film}	Heat transfer coefficient of film boiling	W/m^2K
H_{c20}	Upper critical magnetic field at 0 K	T
I_b	Current supplied to the induction coils	A
I_c	Critical current	A
I_{CR}	DC current for contact resistance measurements	A
I_d	Monitored current of the diode laser driver	A
I_F	Forward current	A
I_m	Current flowing through metallic matrix	A
I_{mpc}	Minimum propagating current	A
I_p	Current pulse of charged point heaters	A
I_t	Transport current	A
I_{th}	Threshold current	A

J_c	Critical current density	A/m^{-2}
J_r	Radial current density	A/m^{-2}
J_w	Averaged current density	A/m^{-2}
l_{SS}	Length of stainless steel support	m
l_{TD}	Average length of thermal drain	m
l_1	Fraction of pure copper over the radius	
l_2	Fraction of degraded copper over the radius	
L_i	Distance between voltage taps V_i	m
L_{hz}	Length of heated zone in a 1D model	m
L_{mpz}	Length of Minimum Propagating Zone	m
L_{nz}	Length of normal zone and/or quenched zone	m
L_{tot}	Total length of simulated wire sample	m
L_w	Length of wire sample	m
L_0	Lorentz's constant: 2.45×10^{-8}	$\Omega W/K$
n	Parameter of the E_f	
n_i	Number of propagating fronts	
P_{ab}	Absorbed optical power	W
P_{offset}	Offset power dissipated in point heaters	W
P_{opw}	Optical power flowing out the optical fiber	W
P_p	Power pulse dissipated by charged point heaters	W
r	Copper-to-non-copper ratio of conductor	
r_{mz}	Copper-to-non-copper ratio of multifilament zone	
R_{CR}	Average contact resistance	Ω
R_m^{tot}	Matrix resistance of entire sample	Ω
R_1	Radius of copper core of wire sample	m^2
R_2	Outer radius of multifilament zone	m^2
R_w	Outer radius of wire sample	m
S_i	Boundaries of simulated wire $i \in 1, 2, 3, 4$	
t	Time	s
t_{dif}	Thermal diffusion time	s
t_f	Final time	s
t_i	Initial time	s
t_{idif}	Time of the onset of heat exchange with helium-I	s
T	Temperature	K
T_c	Critical temperature	K
T_{cs}	Current sharing temperature	K
T_{mpz}	Temperature profile of Minimum Propagating Zones	K
T_{op}	Operating temperature	K
T_q	Temperature at quench	K
T_0	Temperature of heat sink and/or initial temperature	K
\mathbf{u}	Cylindrical spatial coordinates	
V_{B1}	Voltage drop across induction coil 6 (reference)	V
V_{B2}	Voltage drop across induction coil 9 (heater)	V
V_{CR}	Voltage drop across contact resistances	V
V_i	Voltages ($i \in 1, 2, 3$)	V
V_p	Voltage pulse of charged point heaters	V
V_{1ref}	Voltage V_1 at full transition	V
V_{2max}	Voltage at full transition across V_2	V

x_{Cu1}	Fraction of pure copper	
x_{Cu2}	Fraction of degraded copper	
x_s	Fraction of non-copper	
X	Longitudinal coordinate	m
Y	Width	m
Z	Height	m
w	Half-width	m

Greek letters

β_{Debye}	Debye's parameter: 16.07	J/m^3K^2
ϵ	Coefficient of optical absorption	
ϵ_{opw}	slope efficiency	W/A
γ_{sum}	Summerfeld's parameter: 1011.8	J/m^3K^2
λ_m	Thermal conductivity of metallic matrix	$W.m^{-1}.K^{-1}$
λ_{mr}	Transverse thermal conductivity of metallic matrix	$W.m^{-1}.K^{-1}$
λ_{TD}	Thermal conductivity of thermal drain	$W.m^{-1}.K^{-1}$
ν	Normal Zone Propagation Velocity	m/s
ν_{ad}	Adiabatic Normal Zone Propagation Velocity	m/s
μ_0	Magnetic permeability in vacuum: $4\pi \times 10^{-7}$	H/m
ϕ_{max}	Maximum angle of incident ray of light	
$\Phi _{S_{1-4}}$	Heat fluxes	W/m^2
Φ_J	Flux of normalized Joule dissipation	W/m^2
ρ_m	Resistivity of metallic matrix	Ωm
ρ_{mr}	Transverse resistivity of metallic matrix	Ωm
τ_B	Time constant of bolometers	s
τ_{mag}	Magnetic diffusion time	s
τ_p	Pulse duration	s
τ_{th}	Thermal diffusion time	s
θ_{max}	Maximum half-angle for back reflection	
Θ	Maximum half-angle of light cone ($NA = \sin(\Theta)$)	
$\varphi _{S_{1-2}}$	Temperature gradient	K/m
ϑ_B	Volume of closed bolometer	m^3
ϑ_{mpz}	Volume of Minimum Propagating Zone	m^3
F	Parameter of the Fermi-Dirac distribution	
η	Parameter of E_f	Js^{-n}
χ	Cooling coefficient	

Indices

0	Initial
1 _{ref}	Voltage reference V_1
ad	Adiabatic
B	Bolometer
B ¹	Reference coil
B ²	Heater coil

c	Critical
CR	Contact resistance
Cu	Copper
cs	Current sharing
d	Diode
dif	Diffusion
f	Film
F	Forward
hz	Heated zone
i	Index $i \in \{1, 2, \dots\}$
nz	Normal zone or quenched zone
m	Matrix
mag	Magnetic
max	Maximum
mpz	Minimum Propagating Zone
mr	Matrix following radial axis
op	Operating
opw	Optical power
p	Pulse
s	Non-copper
SS	Stainless steel
sum	Summerfeld
TD	Thermal drain
tot	Total
th	Thermal
w	Averaged value over the cross-section of conductors
∞	Relative to infinity

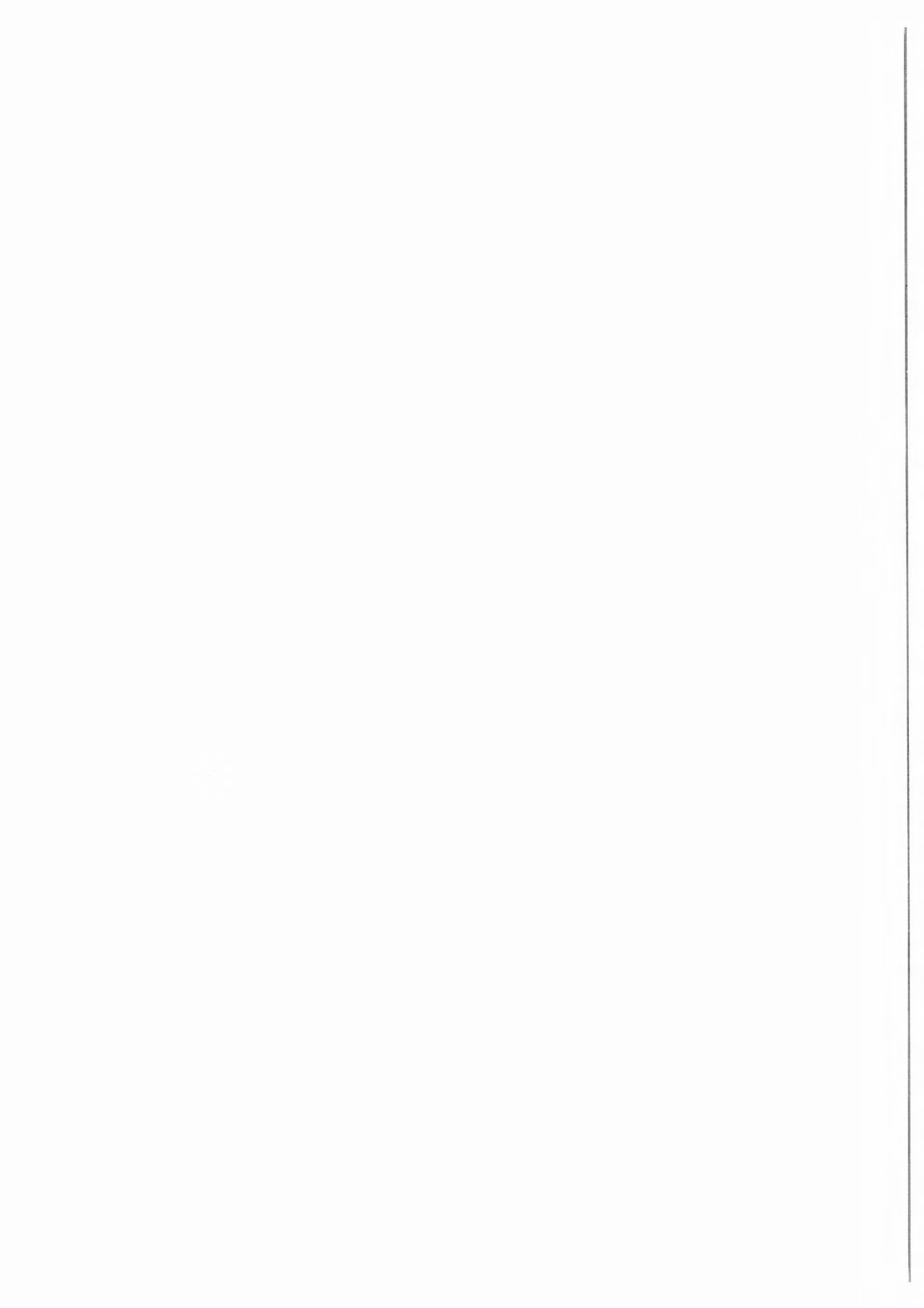
Mathematical operators

d	Derivation
Δ	Difference
FD	Fermi-Dirac distribution
\int	Single integration

Acronyms

CEA	<i>Commissariat à l'Énergie Atomique</i>
CERN	<i>Centre Européen pour la Recherche Nucléaire</i>
FRP	<i>Fiberglass Reinforced Plastic</i>
HTS	<i>High Temperature Superconductor</i>
LHC	<i>Large Hadron collider</i>
LTS	<i>Low Temperature Superconductor</i>
MIT	<i>Massachusetts Institute of Technology</i>
MQE	<i>Minimum Quench Energy</i>
MPE	<i>Minimum Pulse Energy</i>

MPZ	<i>Minimum Propagating Zone</i>
NA	<i>Numerical aperture</i>
NHMFL	<i>National High Magnetic Field Laboratory</i>
NZPV	<i>Normal Zone Propagation Velocity</i>
OFHC	<i>Oxygen Free High Conductivity</i>
QE	<i>Quench Energy</i>
QDT	<i>Quench Decision Time</i>
RRR	<i>Residual Resistivity Ratio</i>
SQUID	<i>Superconducting Quantum Interference Device</i>
VAMAS	<i>Versailles project on Advanced MAterials and Standards</i>
YAG	<i>Y₃Al₅O₁₂</i>



Chapter I

Résumé de thèse

Contents

I.1	Chapitre II : introduction générale	22
I.1.1	Introduction	22
I.1.1.1	Collaborations	22
I.1.1.2	Concepts relatifs à l'étude de stabilité	23
I.1.1.3	Quelques définitions	25
I.1.2	Revue sur les systèmes de chaufferette	27
I.1.3	Développement de nouvelles technologies	28
I.1.3.1	Supraconducteurs à basse température critique	28
I.1.3.2	Supraconducteurs à haute température critique	28
I.2	Chapitre III : chaufferette résistive	29
I.2.1	Description du dispositif expérimental	29
I.2.2	Contrôle de la résistance de contact	29
I.2.3	Mesures de stabilité	30
I.2.4	Discussion et conclusion	32
I.3	Chapitre IV : diode laser et chaufferette inductive	33
I.3.1	Echantillon oxydé de Cu/NbTi	33
I.3.2	Description de la chaufferette laser et de la fibre optique additionnelle	33
I.3.3	Description du support échantillon	34
I.3.4	Equipements électriques et système d'acquisition des tensions	35
I.3.5	Caractérisation de la diode laser équipée de sa fibre addi- tionnelle	36
I.3.6	Calibrage de l'énergie absorbée par le brin	37
I.3.7	Résultats expérimentaux	38
I.4	Chapitre V : simulations numériques	40
I.4.1	Géométrie modélisée, conditions initiales et limites	40
I.4.2	modélisation du coefficient d'échange avec l'hélium	40
I.4.3	Résultats de calculs et comparaison avec les données	41
I.5	Chapitre VI : supraconducteurs à haute température critique	44
I.5.1	Description de l'expérience	44

I.5.2	Comparaison entre les différentes mesures	44
I.6	Chapitre VII : conclusion générale	48

NOUS RÉSUMONS dans ce chapitre l'ensemble de la thèse. Nous portons une attention toute particulière à la partie la plus innovante de ce travail : une chaufferette laser. En effet, contrairement aux autres systèmes technologiques, les tests réalisés avec la chaufferette laser ont montré la bonne répétabilité des mesures. En outre, nous avons prouvé, à travers une pré-étude, que l'énergie absorbée par l'échantillon pouvait être calibrée (le calibrage de chaufferette de petites dimensions n'ayant jamais été, jusqu'à présent, répertorié dans la littérature).

Ce résumé, agrémenté de quelques figures, est présenté par chapitre.

I.1 Chapitre II : introduction générale

I.1.1 Introduction

Dans ce chapitre, nous introduisons les deux collaborations auxquelles nous avons participées. Par la suite, Nous présentons les concepts théoriques relatifs à la stabilité thermoélectrique de composites supraconducteurs. Nous effleurons la stabilité des électro-aimants supraconducteurs dont le lien avec le comportement d'un simple constituant tel qu'un conducteur reste une tâche très ardue. Nous focalisons notre propos sur les grandeurs qui permettent de caractériser cette stabilité : énergie minimale de transition et vitesse de propagation. Enfin, une revue de l'ensemble des systèmes de chaufferette existants et passés est présentée.

I.1.1.1 Collaborations

Nous avons développé des systèmes expérimentaux permettant l'étude de la stabilité thermoélectrique de supraconducteurs commerciaux. Ainsi, nous avons réalisé différents systèmes de chaufferette pour simuler les perturbations énergétiques de faibles dimensions et de courtes durées pouvant apparaître dans les aimants supraconducteurs à fort champ.

CEA/Saclay-Alstom/MSA : au Commissariat à l'Energie Atomique (France), nous avons travaillé au sein d'une collaboration liant contractuellement notre laboratoire à un partenaire industriel, Alstom/MSA (France). Cette collaboration vise à développer des brins Nb_3Sn performants. Ces brins pourront être utilisés en vue de réaliser un prototype d'aimant supraconducteur quadripolaire pour une nouvelle génération d'accélérateurs de particules.

Notre travail a consisté à élaborer une expérience innovante pour étudier la stabilité thermoélectrique de brins Nb_3Sn . Dans ce cadre, nous avons mis en oeuvre une nouvelle technologie pour simuler les perturbations locales dénergie pouvant apparaître dans les aimants supraconducteurs. Cette technologie devait être facile d'emploi, bon marché, fournir les résultats les plus reproductibles possibles et, en particulier, pouvoir être étalonnée. Cette dernière condition étant la plus difficile à remplir, à ma connaissance, seuls des chaufferettes inductives ont été calibrées à ce jour. Toutefois, celles-ci ne permettent pas d'étudier l'énergie minimale de transition (Minimum Quench Energie, MQE) et la zone minimale de propagation (Minimum Propagating Zone, MPZ) en raison de leur trop grande longueur.

NHMFL-MIT-Los Alamos : au laboratoire national des champs magnétiques intenses de Floride, aux U.S.A., nous avons réalisé une expérience pour étudier le

comportement de rubans d'YBaCuO soumis à des perturbations locales d'énergie. Cette expérience a été menée en milieu gazeux (azote ou hélium) pour se poursuivre en vide (cryogénération). A cette occasion, un nouveau système de chaufferette résistive a été développé et testé.

I.1.1.2 Concepts relatifs à l'étude de stabilité

Dans cette partie, nous présentons l'origine des perturbations de chaleur pouvant se produire dans les électro-aimants supraconducteurs. En utilisant le concept de spectre de perturbations, nous avons borné notre étude aux perturbations de faibles dimensions spatiales (inférieures à quelques millimètres) et de courtes durées (inférieures à la milliseconde). Par la suite, nous avons introduit la phénoménologie gouvernant la transition d'un conducteur composite de l'état supraconducteur vers l'état normal résistif. Pour cela, nous avons décrit le comportement du conducteur lorsque ce dernier entre dans un régime de partage de courant. Ce régime apparaît lors de la transition du supraconducteur vers son état résistif. Le courant de transport se partage alors entre la matrice métallique et les filaments supraconducteurs jusqu'à la transition complète de l'ensemble des filaments. Nous avons ensuite présenté les concepts d'énergie minimale de transition, de zone minimale de propagation et de vitesse longitudinale de propagation (Normal Zone Propagation Velocity, NZPV). Les principales différences entre supraconducteurs à basse et haute température critique en termes de stabilité sont alors évoquées.

Origines des perturbations dans un électro-aimant supraconducteur : un électro-aimant supraconducteur est sensible à toutes perturbations énergétiques susceptibles d'élever la température d'une portion du bobinage, que ce soit un conducteur, un câble ou un ensemble de câbles. Il peut alors perdre sa capacité à transporter le courant. Ce phénomène de changement de phase de l'état supraconducteur à l'état normal résistif est communément appelé "Quench" (avalanche). Nous utilisons ici la terminologie de "transition". Cette perte soudaine de supraconductivité peut être dommageable pour son bon fonctionnement ultérieur. Aussi, leurs concepteurs prennent en compte ce phénomène pour dimensionner l'ensemble des sécurités qui permettront de préserver l'intégrité de l'aimant.

Nous pouvons citer parmi les différentes causes entraînant une transition :

- le mouvement relatif des conducteurs [1],
- les fissures se produisant dans l'époxy d'imprégnation [2],
- les déformations plastiques des conducteurs,
- les pertes par courants induits,
- les sauts de flux,
- Les fuites cryogéniques, etc....

Dans notre étude, nous simulons les perturbations de faibles dimensions (au plus, quelques millimètres) et de faibles durées (au plus, quelques millisecondes).

Zone de partage du courant : cette notion est essentielle pour comprendre la transition de l'état supraconducteur à l'état normal résistif d'un conducteur composite. La figure I.1 (page 24) montre l'évolution du courant critique en fonction de la

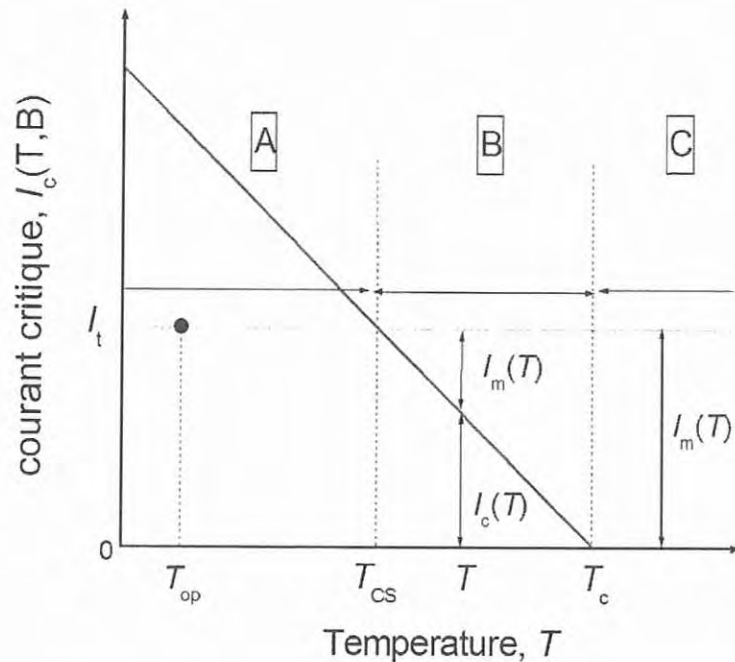


Figure I.1: Caractéristique du courant critique en fonction de la température pour un composite supraconducteur à un champ magnétique donné: [A], le courant circule entièrement dans le supraconducteur ; [B], le courant se partage entre la matrice métallique et les filaments supraconducteurs. [C], tout le courant circule dans la matrice métallique.

température du supraconducteur. En augmentant progressivement la température du conducteur de sa température initiale, T_{op} , jusqu'à une température supérieure à la température critique, T_c , différents régimes sont traversés. Nous distinguons ces régimes, en scindant la courbe en plusieurs domaines: A, B et C. Dans le domaine A, la température croît jusqu'à la température de partage du courant, T_{cs} , aucune dissipation ne se produit au sein du conducteur car les filaments supraconducteurs restent dans leur phase supraconductrice. A partir de T_{cs} , le courant se partage entre la matrice métallique et les filaments (domaine B). La fraction de courant circulant dans la matrice entraîne une dissipation de chaleur par effet Joule qui accroît la température du conducteur formant un processus s'auto-alimentant jusqu'à la perte totale de supraconductivité. Enfin, à partir de la température critique (domaine C), tout le courant de transport circule dans la matrice.

Différences entre supraconducteurs à haute température critique et à basse température critique : il existe une différence fondamentale entre ces deux familles de supraconducteurs. La température critique d'un supraconducteur à haute température critique se situe entre 80 K et 120 K alors que celle d'un supraconducteur à basse température est de l'ordre de 10 à 20 K. Cette différence influence fortement le comportement des conducteurs en terme de stabilité. Les

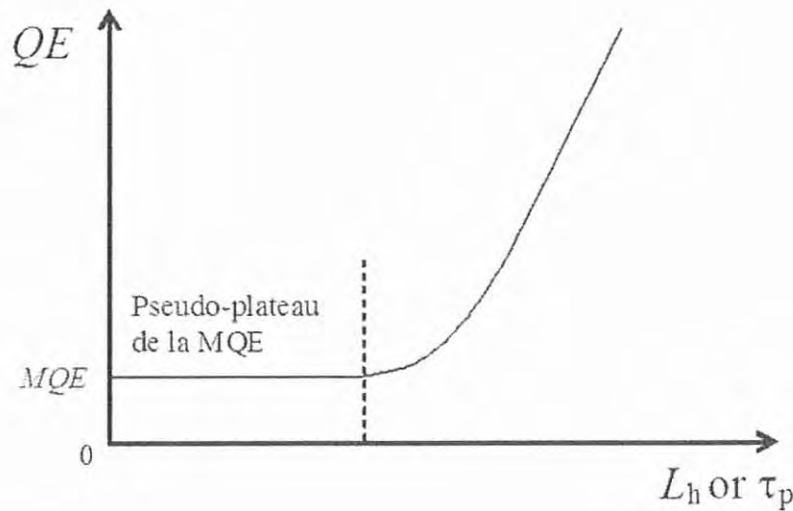


Figure I.2: Evolution typique de l'énergie de transition ("Quench Energy", QE) en fonction de la durée de la perturbation, τ_p , ou de la longueur de la zone chauffée, L_h .

supraconducteurs à haute température critique peuvent fonctionner autour de la température de l'azote liquide 77 K à laquelle, en outre, la capacité calorifique des matériaux est plus importante. Par conséquent, ils deviennent insensibles à des perturbations de faible niveau d'énergie pour lesquelles les supraconducteurs à basse température critique peuvent transiter. Toutefois, ils sont beaucoup plus sensibles à la création de points chauds. En effet, la zone normale qui se crée au sein du conducteur reste localisée avant de se propager ou de diffuser dans le composite supraconducteur ce qui peut entraîner sa destruction locale. Du moment que les énergies minimales de transition soient importantes (de l'ordre de quelques centaines de milli-Joule), il est peu probable qu'une transition survienne dans le bobinage. Cette affirmation n'est strictement valable que si le supraconducteur ne présente pas de défaut de fabrication. Ce défaut définira alors la marge en stabilité.

I.1.1.3 Quelques définitions

Zone Minimale de propagation (Minimum Propagating Zone, MPZ) : la zone minimale de propagation est définie comme la longueur du profil métastable de température du brin. Ce profil particulier de température apparaît en régime établi et correspond à un pseudo-équilibre entre l'énergie dissipée par effet Joule et le refroidissement. Pratiquement, c'est la longueur minimale de la zone normale à partir de laquelle il y a propagation de la transition.

Energie minimale de transition (Minimum Quench Energy, MQE) : c'est la plus petite énergie cédée au supraconducteur qui entraîne sa perte de supraconductivité. Usuellement, elle est définie comme l'énergie permettant la formation du profil métastable de température. Dans le cas adiabatique, cette énergie peut être

Table I.1: Domaines d'application des différents systèmes de chaufferette existante et leur principale qualité.

Systèmes de chaufferette	Utilisations	Avantages	désavantages
Bobines inductives	brin, conducteur ou câbles à géométrie axi-symétrique	pouvant être Etalonnées	longueur et nécessite la présence d'une couronne métallique cylindrique pour y déposer l'énergie induite
Liants chargés au carbone	tout type de brins, conducteurs ou câbles	facilité d'utilisation, adaptabilité	non calibré, mauvaise reproductibilité des mesures, difficulté à maîtriser la résistance de contact et nécessité de faire circuler le courant de la chaufferette à travers le conducteur
Tip-heater	brins	bonne reproductibilité des mesures	difficulté de mise en oeuvre, très peu d'application
Jauges de contrainte	rubans, et quelques conducteurs à géométrie rectangulaire ou circulaire mais de large diamètre comparé à la jauge	produit commercialisé	calibrage, adaptabilité, contrôle de l'interface jauge de contrainte et échantillon

considérée équivalente à l'énergie nécessaire pour augmenter la température du conducteur de sa température initiale à la température de partage du courant. Lorsque le conducteur est refroidi par de l'hélium liquide, il existe une température, T_{mpz} , située entre la température de partage du courant et la température critique pour laquelle il y a transition. Cela rejoint la condition de Maddock [3] dans le cas d'un modèle d'échange avec bain d'hélium en régime établi.

Pour pouvoir estimer aussi bien la zone minimale de transition que l'énergie minimale de transition, il est nécessaire de respecter certains critères spatiaux et temporels. Figure I.2 (page 25) montre l'évolution de la zone transitée et de l'énergie de transition ("Quench Energy", QE) en fonction de la longueur de la zone chauffée et de la durée de la perturbation. En effet, en dessous de certaines valeurs (≥ 3 mm et $\geq 100 \mu s$ pour les supraconducteurs à basse température critique), le pseudo-plateau de l'énergie minimale de transition se dessine.

Vitesse de propagation (Normal Zone Propagation Velocity, NZPV) : la vitesse de propagation est définie comme la vitesse du front normal de propagation.

Dans le cas adiabatique, la vitesse de propagation est approximée par la relation suivante :

$$\nu_{\text{ad}} \simeq \frac{1}{C_w} \sqrt{\frac{G_c \lambda_m}{T_{\text{cs}} - T_{\text{op}}}} \quad [\text{m/s}] \quad (\text{I.1})$$

où G_c est la puissance dissipée par unité de volume à T_c , T_{cs} est la température de partage du courant, λ_m est la conductivité thermique de la matrice métallique, et C_w est la capacité moyenne du conducteur. Dans la majorité des cas, on peut considérer que ces deux derniers paramètres physiques ont des valeurs indépendantes de la température. La vitesse de propagation dépend ainsi du rapport entre ce qui est dissipé et ce qui est accumulé. Dans le cas d'un refroidissement convectif, un coefficient multiplicatif doit être appliqué qui tient compte des caractéristiques du transfert thermique avec le réfrigérant.

Deux méthodes permettent de déterminer cette vitesse : la méthode dite de la pente (slope method) et la méthode du "temps de vol" (Time flight) [1]. Elles utilisent des tensions enregistrées le long du conducteur. Les prises de tension doivent être suffisamment éloignées de la zone chauffée pour ne pas subir l'influence de cette dernière. Ces méthodes sont présentées dans le chapitre III, paragraphe III.4 (page 94) et chapitre IV, paragraphe IV.5.3.4 (page 157).

I.1.2 Revue sur les systèmes de chaufferette

Dans cette partie, nous présentons une revue relativement exhaustive de tous les systèmes de chaufferette existants. A l'issue de notre recherche bibliographique, il nous est apparu que la plupart de ces systèmes souffraient aussi bien d'un manque de reproductibilité que de calibrage. Hors, pour pousser plus loin la technologie des aimants à fort champ magnétique actuels et futures, il est nécessaire d'obtenir une meilleure précision au niveau des mesures. Cette objectif alors atteint permettra de construire un modèle de stabilité incorporant une meilleure description de l'influence de l'hélium [4]. La première étape est l'étude d'un simple constituant tel qu'un conducteur pour construire pas par pas une étude complète des phénomènes d'instabilités. Par la suite, des efforts aussi bien théoriques que pratiques devront encore être menés afin de comprendre l'origine des transitions survenant dans le bobinage d'aimants supraconducteurs à forte densité de courant. Il sera ainsi possible d'éclaircir la relation reliant la stabilité du conducteur au comportement global de l'aimant.

Quatre principaux systèmes de chaufferette existent à l'heure actuel :

- les bobines inductives [5],
- les liants chargés au carbone [6],
- le tip-heater [4],
- les jauges de contraintes [7].

Chacun de ces systèmes présente des avantages et des inconvénients. Le tableau suivant, Table I.1 (page 26), résume leurs domaines d'application et leurs principales qualités.

I.1.3 Développement de nouvelles technologies

Nous distinguons les études menées sur les supraconducteurs à basse température critique de celles menées sur les supraconducteurs à haute température critique. En effet, les collaborations sont indépendantes et bien que le sujet général reste identique, les buts fixés et les conditions expérimentales sont différents.

I.1.3.1 Supraconducteurs à basse température critique

Suivant la famille de supraconducteur, nous avons testé différents systèmes de chauffe-rette. Dans un premier temps, nous avons tenté d'améliorer les technologies existantes pour ensuite proposer une technologie innovante : une diode laser. Cette technologie est apparue simple d'utilisation, consommant peu d'énergie, ne demandant pas de maintenance particulière. De plus, elle nous a permis de répondre partiellement au cahier des charges que nous nous étions fixés. En effet, la possibilité de calibrer l'énergie de transition a été démontrée à travers une pré-étude, et bien que la reproductibilité des mesures doit encore être démontrée, nous avons atteint une très bonne répétabilité.

I.1.3.2 Supraconducteurs à haute température critique

Dans un premier temps, nous avons utilisé une technologie éprouvée, une jauge de contrainte. Toutefois, il nous est rapidement apparu que cela ne conviendrait pas pour l'étude d'un ruban Ag/YBaCuO en raison de sa grande fragilité mécanique. Il est nécessaire de presser la jauge de contrainte sur l'échantillon afin d'améliorer le contact thermique ce qui dégrade le fin ruban supraconducteur. Nous avons alors développé une chauffe-rette résistive à base d'un fil de NiCr. Contrairement à la jauge de contrainte, cette technologie nous est apparue satisfaisante pour mener à bien la première phase de l'étude. Cette phase s'est attachée à construire et à valider un nouveau système expérimental pour effectuer l'étude sous vide de la stabilité de rubans Ag/YBaCuO. Cette expérience se poursuit actuellement et fait preuve de continues améliorations [8].

I.2 Chapitre III : chaufferette résistive

Après avoir introduit le cadre de l'étude, ce premier chapitre présente une première tentative de chaufferette dont la technologie s'inspire du tip-heater et des époxies chargées au carbone.

Cette chaufferette, appelée chaufferette résistive, a été utilisée pour caractériser la stabilité thermoélectrique de brins nus Cu/NbTi de type LHC-02 fournis par Alstom/MSA (France).

I.2.1 Description du dispositif expérimental

Nous avons utilisé pour cette étude le cryostat GELOTTE dans lequel des mesures de courant critiques sur brins Nb₃Sn et NbTi ont été menées. Ce cryostat, équipé d'un aimant pouvant fournir jusqu'à 12 T, accueillait un porte échantillon de type VAMAS supportant l'échantillon bobiné sur un mandrin en titane. Nous avons adapté sur ce dernier un système mécanique permettant de guider la chaufferette et de la presser sur le brin. Ce système était constitué de deux bagues en aluminium supportant un morceau de G-10 dont le centre était percé d'un trou circulaire pour recevoir la chaufferette. Un ensemble de rondelles Belleville assurait le contact mécanique entre la chaufferette et le brin au cours du refroidissement. Ce support chaufferette fut amélioré tout au long des essais pour permettre un meilleur positionnement de la chaufferette sur le brin.

La chaufferette est constituée d'une vis creuse en G-10 dans laquelle est collée un fil de cuivre émaillé de 2/10 mm. En bout de vis, un trou d'environ 1 mm de diamètre pour 0.5 mm de profondeur accueille une petite boule de résine Eccobond® 60L chargée au carbone. Le fil de cuivre dépassant très légèrement du fond du trou, permettait d'alimenter en courant la résine pour y dissiper la chaleur nécessaire à la transition du supraconducteur. Le courant circulait alors par la chaufferette et le brin pour revenir à l'alimentation impulsionnelle. Figure I.3 (page 30) montre une des chaufferettes testées, la chaufferette numéro 2. Environ une dizaine de chaufferette a été réalisée.

Technologie peu fiable, la majorité des chaufferettes se sont endommagées lors des différents essais de résistance de contact ou durant les tests de stabilité.

I.2.2 Contrôle de la résistance de contact

Quelques études sur le contrôle et le maintien de la résistance de contact entre la chaufferette et l'échantillon ont été menées. Utilisant le montage pour l'étude de la stabilité, nous avons mesuré à température ambiante et à température cryogénique la résistance de contact des chaufferettes aux différents stades de leur écrasement sur le brin. Nous avons ainsi atteint des résistances de contact d'une dizaine d'Ohms à quelques milli-Ohms à basse température. Seules les chaufferettes dont la résistance fut inférieure à l'Ohm ont pu être utilisées (en dessous de la charge limite admise par l'alimentation impulsionnelle).

Pour la chaufferette numéro 4, nous avons mesuré l'évolution de la résistance de contact en fonction du temps lors d'une campagne de mesures de stabilité. Figure I.4 (page 31) montre le résultat obtenu. La résistance de contact varie très peu au cours des différents tests. Nous n'avons pu ultérieurement trouver de corrélations évidentes entre la variation de la résistance de contact et la reproductibilité des

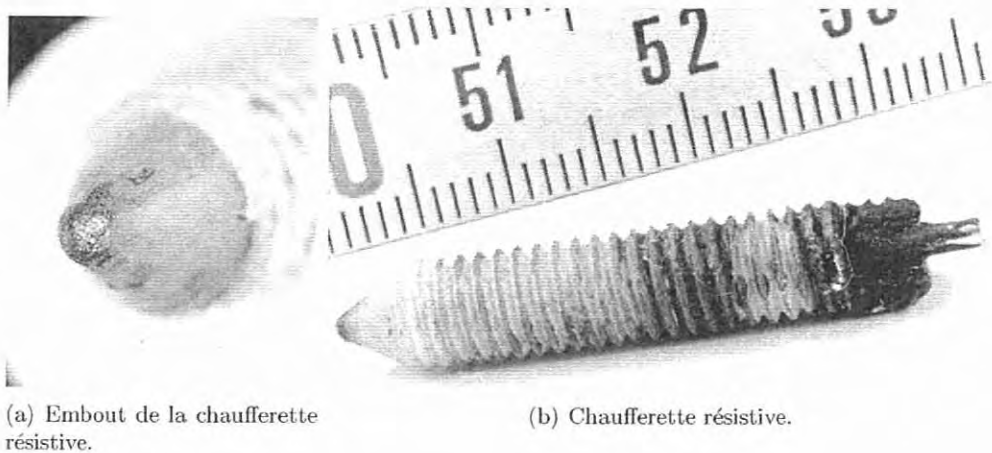


Figure I.3: Photos de la chaufferette numéro 2: (a) embout de la chaufferette dans laquelle nous avons polymérisé de l'Eccobond[®] 60L, (b) photo de la chaufferette entière usinée dans du G-10.

mesures d'énergie minimale de transition. En effet, la résistance de contact apparaît relativement constante alors que l'énergie minimale de transition varie fortement d'une mesure à l'autre, en particulier pour de faibles durées de pulse ($\leq 150 \mu\text{s}$).

I.2.3 Mesures de stabilité

Des campagnes de tests ont été menées avec quelques chaufferettes. Pour ces tests, le brin fut équipé de deux paires de prises de potentiel :

- de part et d'autre de la zone chauffée, V_1 ,
- le long du brin, V_2 .

La distance entre les prises de potentiel V_1 couvre ~ 93 mm du brin, celle des prises de potentiel, V_2 , s'étendent sur ~ 43 mm. Nous avons effectué des tests à différents pourcentages du courant critique, pour des durées de pulse allant de $50 \mu\text{s}$ à 1.5 ms à 8 T et 4.2 K en hélium liquide. Figure I.5 (page 31) montre l'une de ces campagnes à 95% de I_c . Comme nous l'avons précédemment mentionné, l'énergie de transition varie fortement à faible durée de pulse pour laquelle nous espérons voir le pseudo-plateau de l'énergie minimale de transition. Aucune justification n'a pu être donnée pour expliquer une telle variation.

Des essais ont également été menés pour déterminer l'influence de la valeur de la résistance de contact sur l'énergie de transition. Bien qu'aucune relation claire existe entre la reproductibilité de l'énergie minimale de transition et les variations de la résistance de contact, il nous est apparu toutefois que cette énergie dépendait à la valeur de la résistance de contact, en particulier pour des valeurs de quelques dizaines de milli-Ohms (voir figure III.18, page 100 dans le chapitre III).

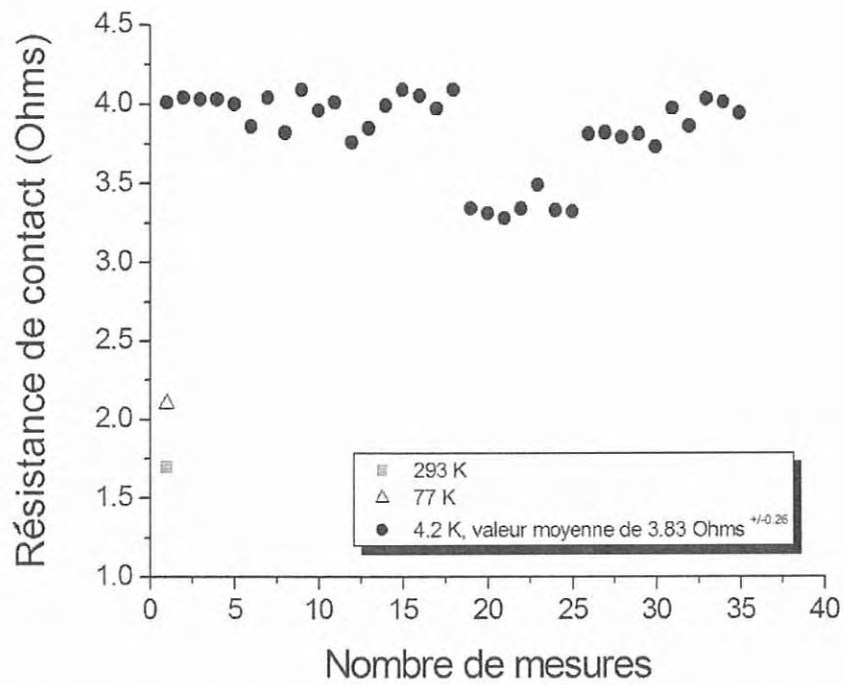


Figure I.4: Evolution de la résistance de contact de la chaufferette numéro 4 durant une campagne de tests de stabilité.

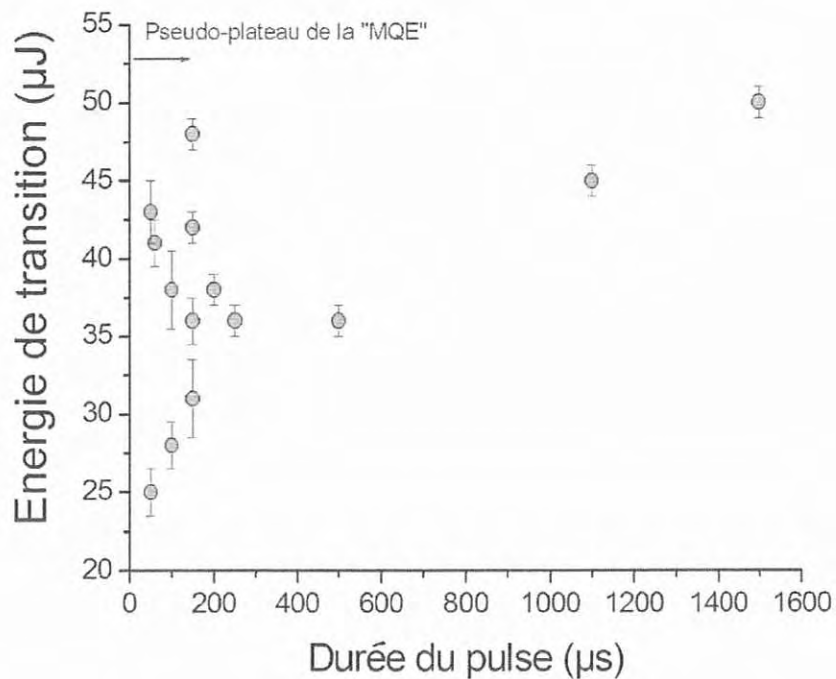


Figure I.5: Energie de transition en fonction de la durée du pulse à 8 T, 4.2 K et 95% de I_c .

I.2.4 Discussion et conclusion

De nombreuses difficultés se sont posées avec le montage décrit précédemment. De ce fait, les résultats obtenus doivent être interprétés avec circonspection. En effet, des problèmes liés au bobinage du brin sur le mandrin en titane (ce dernier étant conducteur électrique) ont pu influencer les résultats expérimentaux. Il est probable que le courant de transport du brin se partage non seulement entre la matrice de cuivre du brin et les filaments supraconducteurs mais également avec le mandrin en titane lors d'une transition. Une telle redistribution a pu entraîner un pseudo-équilibre thermique entre le brin et son environnement bien que ce dernier soit totalement transité. Par conséquent, les vitesses de propagation de l'ordre de 12 m/s (à 8 T, 4.2 K et 95% de I_c) ont pu être sous-estimées. Ce processus d'équilibre semble cependant peu influent car l'ordre de grandeur reste cohérent avec les données fournies dans la littérature [4].

Le contrôle de la résistance de contact n'a pu être obtenu malgré l'ensemble de nos efforts. Des écarts d'un ou deux ordres de grandeurs ont été mesurés sur l'ensemble des chaufferettes réalisées. Néanmoins, cela n'explique pas, aux vues de nos résultats, le manque de reproductibilité des mesures de l'énergie de transition, mais quelques indices laissent apparaître une relation entre l'ordre de grandeur de la résistance de contact et cette dernière énergie. Ainsi, pour de grandes valeurs de la résistance de contact, peu de courant de pulse est nécessaire pour faire transiter le brin. Au contraire, de faibles valeurs de la résistance de contact nécessitent de plus grands courants de pulse. Ces derniers, s'additionnant ou se retranchant au courant de transport, changent la marge en stabilité du brin.

Aux vues des difficultés liées à la mise en oeuvre de la chaufferette, du manque de contrôle de la résistance de contact, du manque de reproductibilité des mesures d'énergies de transition, nous avons abandonné ce système de chaufferette au profit de technologies alternatives telles que la diode laser et la chaufferette inductive.

I.3 Chapitre IV : diode laser et chaufferette inductive

Dans ce chapitre, nous décrivons un tout nouveau dispositif expérimental dédié à l'étude de stabilité de brins supraconducteurs en NbTi ou Nb₃Sn. Notre première tentative de chaufferette, décrite dans le chapitre précédent, nous a permis d'acquérir l'expérience nécessaire pour mettre en oeuvre dans les meilleures conditions la diode laser et la chaufferette inductive.

Bénéficiant d'un aimant à large ouverture (~ 96 mm) pouvant fournir jusqu'à 7 T à 4.2 K, nous avons dessiné un porte échantillon de forme en U pouvant accueillir les deux nouvelles chaufferettes. Nous avons changé entièrement de dispositif expérimental car nous n'aurions pas pu insérer la chaufferette inductive (bobine de 3 mm de long et de 2 mm de diamètre extérieur) dans le montage de type VAMAS, du fait du faible rayon de courbure du mandrin.

Dans ce présent chapitre, nous ne détaillons pas la chaufferette inductive. En effet, nous n'avons pas pu obtenir, jusqu'à présent, de résultats exploitables avec cette technologie. En raison des variations rapides du champ magnétique généré par la chaufferette, la forme des tensions enregistrées le long du brin est fortement déformée.

I.3.1 Echantillon oxydé de Cu/NbTi

Après une série de tests préliminaires sur des brins nus, il est apparu que la puissance laser n'était pas suffisante pour faire transiter l'échantillon à de courtes durées de pulse ($\leq 100 \mu s$). En effet, le cuivre nu absorbe très peu de lumière dans le proche infra-rouge. Notre laser émettant à 807 nm, seule une faible fraction de l'énergie est donc absorbée. Sur les recommandations de S. Calatroni, travaillant au CERN, nous avons fait oxyder, à l'atelier des traitements de surface TS-MME-CEM/CERN, nos échantillons.

Une couche superficielle de quelque microns de CuO et Cu₂O se forme à la surface du brin. Ce dernier étant traité sur toute sa longueur (environ 70 cm), une grande partie de la couche d'oxyde semiconductrice fut par la suite enlevée chimiquement pour ne laisser apparaître qu'une portion de quelque millimètres de long (~ 3 mm) au centre du brin.

I.3.2 Description de la chaufferette laser et de la fibre optique additionnelle

La chaufferette laser se présente sous la forme d'un petit coffret en cuivre Cu-c2 qui permet moyennant l'utilisation d'un élément peltier de la refroidir de manière homogène. Une fibre optique est pré-couplée à la diode laser de marque Spectra-physics (USA). Cette dernière fournit une puissance continue de 1.2 W pour une faible consommation de courant (≤ 2 A). Du fait de ses faibles dimensions et de sa robustesse, cette technologie peut être adaptée sur de nombreux systèmes expérimentaux. La photo I.6 (page 34) montre la diode laser commercialisée avec une fibre optique mesurant environ 30 cm. La chaufferette laser étant située en haut de l'insert de mesure, il nous a fallu alors connecter à la fibre optique existante une deuxième fibre pour guider la lumière le long des 2 m séparant la diode laser de l'échantillon. L'embout de cette fibre optique additionnelle a été modifié pour permettre l'éclairage complet du brin. Cet embout est constitué d'un guide en matière plastique dans

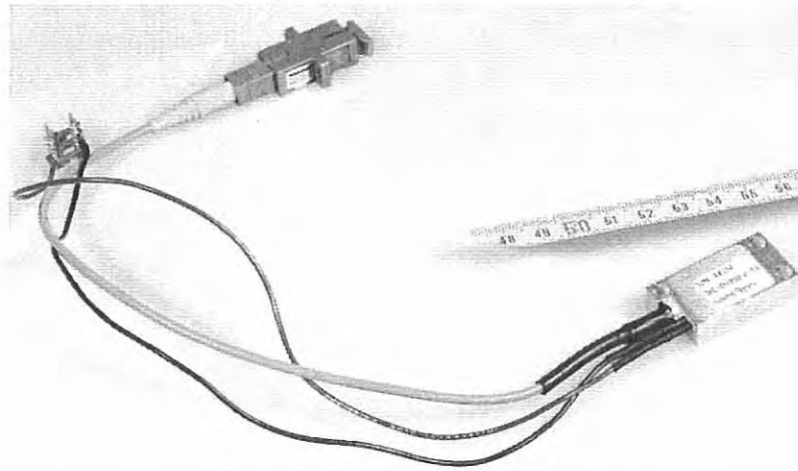


Figure I.6: Diode laser et sa fibre optique.

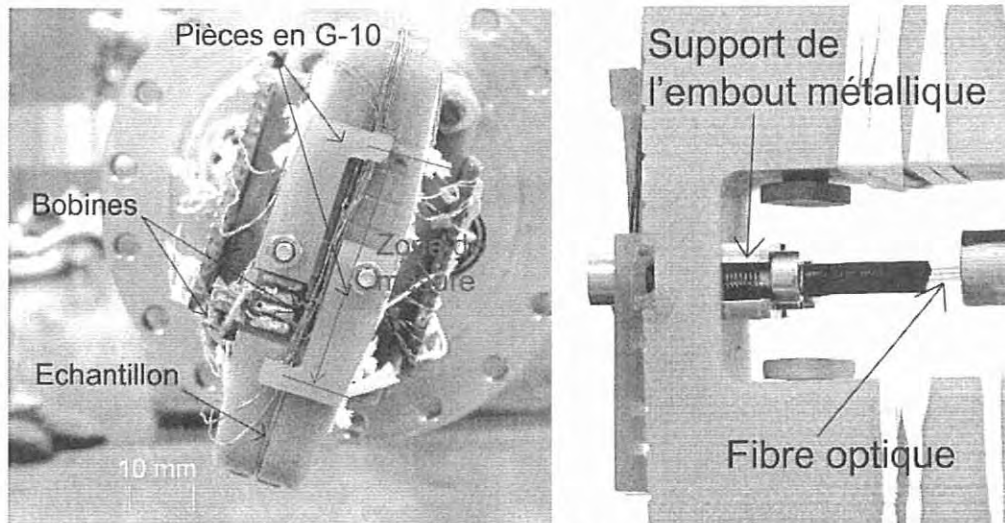
Table I.2: Caractéristiques de la diode laser mono-mode et de la fibre optique additionnelle à 293 K (utilisés au CEA/Saclay).

Puissance optique maximale (W)	1.35
Courant maximale (A)	2
Longueur d'onde centrale (nm)	807.4 ± 10
Diamètre du corps de la fibre optique,	$150 \mu\text{m}$
Ouverture numérique de la fibre	13°

lequel a été inséré une petite aiguille métallique creuse. Dans cette aiguille de diamètre intérieur de l'ordre de $300 \mu\text{m}$ est collée la partie optiquement active de la fibre optique. Le tableau suivant, Table I.2 (page 34), résume les principales caractéristiques de la diode laser et de la fibre optique additionnelle.

I.3.3 Description du support échantillon

Une attention toute particulière a été apportée au maintien de l'échantillon et à celui de l'embout de la fibre. En effet, il est important d'obtenir une distance reproductible entre l'embout de fibre optique et la surface de l'échantillon afin de garantir la répétabilité/reproductibilité des mesures. Cette distance est d'au plus 1 mm pour assurer que le cône de lumière sortant de la fibre optique éclaire totalement le brin. Figure I.7 (page 35) montre deux photos du support échantillon en G-10. Figure I.7(a) (page 35) est une vue de dessous montrant deux pièces en G-10 permettant de maintenir l'échantillon au fond d'une gorge en V pour éviter son déplacement sous l'action de la force de Lorentz. Au milieu du support, deux méplats de $\sim 5 \text{ mm}$ de côté et de moins de 1 mm de profondeur ont été usinés pour permettre d'insérer deux pièces en G-10 positionnant et maintenant la partie oxydée de l'échantillon en face de l'embout de fibre optique. Figure I.7(b) (page 35) mon-



(a) Vue de dessous du support échantillon.

(b) Montage mécanique de l'embout de fibre optique.

Figure I.7: (a) Vue de dessous du support échantillon, 6 prises de potentiel ont été soudées sur le brin, 2 pièces en G-10 permettent de plaquer le brin au fond de sa gorge; (b) vue de côté du support échantillon avec la fibre optique additionnelle et le montage mécanique permettant de maintenir son embout proche de la surface de l'échantillon.

tre une vue de côté du support échantillon. Le système mécanique permettant le maintien de l'embout de fibre optique y apparaît.

I.3.4 Equipements électriques et système d'acquisition des tensions

Trois prises de tension ont été soudées sur le brin : V_1 , V_2 et V_3 . V_1 , dont la distance entre les prises de potentiel est de l'ordre de 5.9 mm, permet d'acquérir les premiers instants de croissance de la zone normale au sein du brin. V_2 et V_3 permettent de déterminer la vitesse de propagation de la zone normale. La distance entre les prises de potentiel de V_2 et V_3 sont respectivement de 7.2 mm et 7.3 mm, une erreur de plus ou moins 0.5 mm peut être commise.

Un oscilloscope numérique nous a permis d'obtenir ces tensions avec une fine résolution temporelle ($\pm 10 \mu\text{s}$). Une prise de tension supplémentaire, V_{cc} , fut utilisée lors des mesures de courant critique. Ces mesures nous ont permis de délimiter la zone de mesure (voir figure I.7(a), page 35). En effet, c'est la zone pour laquelle la caractéristique $V - I$ de l'échantillon ne présente pas de partie résistive résultant de la forme en U du porte échantillon. En effet, le courant de transport se redistribue en partie dans la matrice de cuivre du au changement relatif de direction entre le champ magnétique extérieur et ce même courant ce qui fait apparaître une résistance non nulle aux bornes du supraconducteur.

Différents équipements électrotechniques ont été utilisés pour protéger l'échantillon (alimenté par une alimentation continue de 1000 A), et ses aménages de courant. Un pilote de diode laser fournit des pulses de courant de l'ordre de la microseconde à la milliseconde afin de faire transiter le brin.

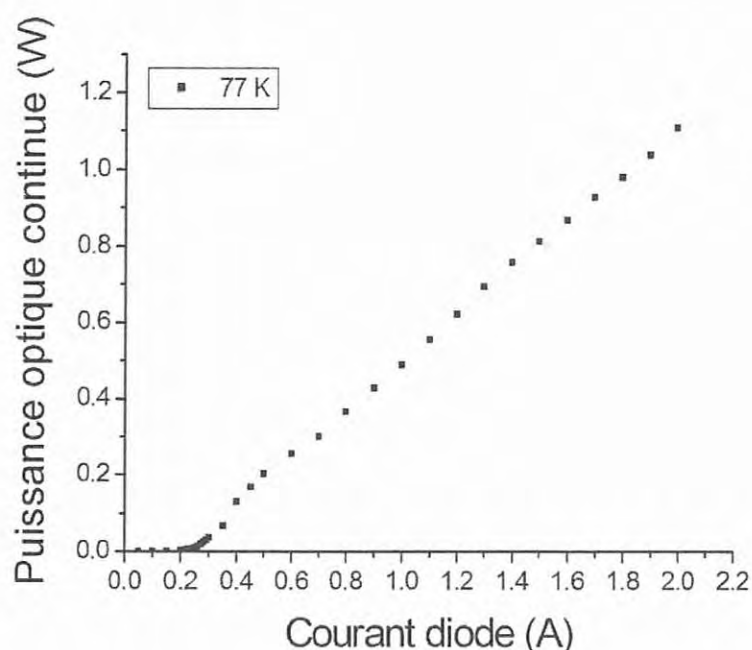


Figure I.8: Caractéristique puissance optique/courant de diode pour une température de la diode laser de 293 K avec 2/3 de la fibre optique baignant dans l'azote liquide à 77 K.

I.3.5 Caractérisation de la diode laser équipée de sa fibre additionnelle

Une série de tests a été menée pour déterminer l'influence des conditions expérimentales sur les pertes de puissance optique de la diode laser et de sa fibre additionnelle. Pour ces tests, un puissance-mètre couplé à un détecteur optique a été utilisé pour tracer la caractéristique puissance optique/courant de la chaufferette laser. Dans un premier temps, nous avons pu ainsi mettre en évidence l'influence de la température de la diode laser sur sa caractéristique $P-I$. Par conséquent, pour le reste de cette étude, nous avons fixé cette température à 293 K grâce à un élément Peltier. Dans un deuxième temps, nous avons quantifié les pertes dues à la présence du connecteur. Ces pertes s'élèvent à environ 16%. Nous avons également mené des études relatives à l'influence de l'environnement cryogénique sur la fibre optique additionnelle. 2/3 de la fibre ont alors été plongés dans de l'azote liquide à 77 K et la caractéristique $P-I$ a été relevée (voir figure I.8, page 36). Cette dernière caractéristique a finalement été retenue pour estimer l'énergie de pulse délivré par la diode laser frappant la surface du supraconducteur. Connaissant la forme du pulse de courant délivré à la diode et sa caractéristique $P-I$, nous avons calculé le pulse de puissance optique en sortie de l'embout de fibre. En intégrant la puissance sur la durée du pulse, nous en avons déduit l'énergie de pulse.

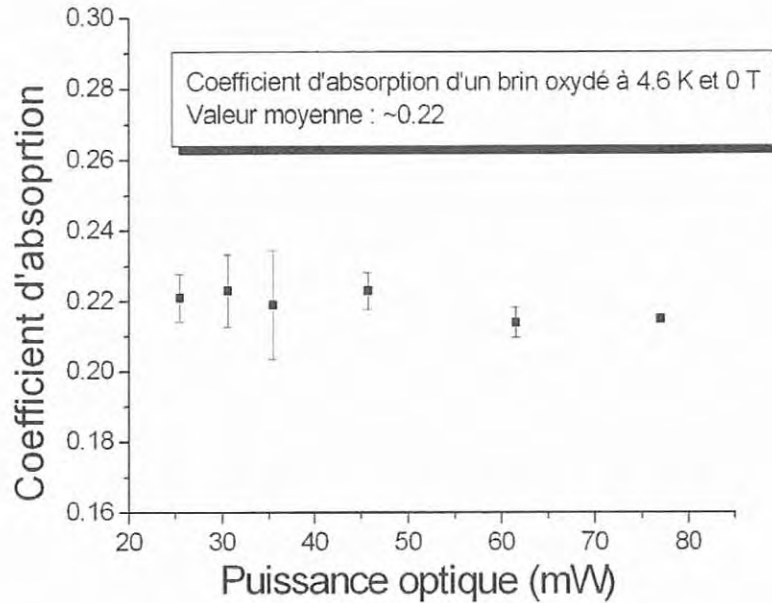


Figure I.9: Evolution du coefficient d'absorption en fonction de la puissance du laser.

I.3.6 Calibrage de l'énergie absorbée par le brin

Ce calibrage a été effectuée au CNRS/CRTBT de Grenoble. A l'origine, le dispositif expérimental devait s'adapter au montage pour l'étude de stabilité du CEA/Saclay. Toutefois, des problèmes de fuite au niveau du support de boîte à vide n'ont pu être résolus. Aussi, nous nous sommes limités à démontrer la faisabilité d'une méthode de calibrage basée sur une mesure bolométrique.

Deux bolomètres en Cuivre Cu-c2 ont été étudiés : un bolomètre clos et un brin. Les tests ont été effectués avec un dispositif expérimental différent de celui du CEA/Saclay, avec une diode laser de caractéristique différente (diode laser fournie par F. Ayela du CNRS de Grenoble) et en l'absence de champ magnétique extérieur. Il est également probable que la distance entre l'embout de fibre optique couplé à cette diode laser et l'échantillon ait pu être différente malgré les précautions prises. Toutes ces différences définissent le caractère préliminaire de ce calibrage. Des études menées *in situ*, utilisant l'acquis de cette pré-étude, permettra d'obtenir des mesures précises de l'énergie minimale de transition. Celles-ci pourront être réalisées en menant une première campagne de tests de stabilité sur un échantillon suivie d'une campagne de calibrage sur ce même échantillon.

Montage expérimental : le bolomètre étudié est situé dans une boîte à vide. Il est attaché à un support en cuivre à l'aide d'une tige en acier. Un ensemble de drains thermiques en cuivre permet d'adapter sa constante de temps et sa sensibilité. Sur ce bolomètre, est attaché un thermomètre de faible dimension pour mesurer son élévation de température.

Une première série de tests a été menée sur le bolomètre clos. Cela nous a per-

mis de caractériser thermiquement les drains thermiques, connaissant par ailleurs l'énergie délivrée par la diode laser alors utilisée. Nous avons donc relevé la température du bolomètre clos à l'équilibre thermique en fonction de la puissance optique, P_{opw} . L'équation d'équilibre thermique est donnée par :

$$\frac{A_{TD}}{L_{TD}} \int_{T_0}^T \lambda_{TD} dT = \epsilon P_{opw} \quad [W] \quad (I.2)$$

où A_{TD} et L_{TD} sont respectivement la section et la longueur du drain thermique, λ_{TD} est la conductivité thermique du drain et ϵ est le coefficient d'absorption optique. Dans le cas du bolomètre clos, $\epsilon \simeq 1$.

Nous avons mené ensuite les mêmes tests sur le brin, mesurant la température d'équilibre thermique pour chaque puissance, P_{opw} . Dans ce cas, le coefficient d'absorption est inférieur à 1 car une partie de la puissance est réfléchiée. A partir de la connaissance de la conductivité thermique du drain thermique fournie par les mesures effectuées sur le bolomètre clos, nous en déduisons le coefficient d'absorption optique :

$$\epsilon = \frac{1}{P_{opw}} \frac{A_{TD}}{l_{TD}} \int_{T_0}^T \lambda_{TD} dT \quad (I.3)$$

La figure I.9 (page 37) présente l'ensemble des résultats obtenus en fonction de la puissance optique du laser. Comme nous l'attendions, ϵ est indépendant de la puissance optique. Toutefois, sa valeur apparaît relativement faible de l'ordre de 0.22 ± 0.007 . Nous espérons un coefficient représentant plus de 60% de l'énergie absorbée. Néanmoins, l'échantillon, le montage expérimental, la diode laser, les conditions de mesures étant différents de celui du test de stabilité, les résultats ne peuvent que conclure à la faisabilité du procédé.

I.3.7 Résultats expérimentaux

De nombreuses mesures ont été effectuées sur un unique brin oxydé. Dans le temps qui nous fut imparti, nous n'avons pas pu mesurer différents brins pour estimer le niveau de reproductibilité de l'expérience. Toutefois, nous avons déterminé sa répétabilité à l'issu de plusieurs semaines de test. Celle-ci est très bonne comme l'indique la figure I.10 (page 39). Cette dernière résume l'ensemble des mesures effectuées à différentes inductions magnétiques, à 85% de I_c , et à 4.2 K dans de l'hélium liquide. Ces mesures ont également été menées à 80%, et 95% du courant critique. Pour la plupart de ces résultats, nous avons relevé les tensions V_1 , V_2 et V_3 pour une transition et dans certains cas une récupération de l'état supraconducteur.

Nous avons aussi relevé les vitesses de propagation dont les résultats sont donnés par la figure I.11 (page 39). L'ordre de grandeur de la vitesse correspond à une dizaine de mètre par seconde comme nous avons trouvé avec la chaufferette résistive.

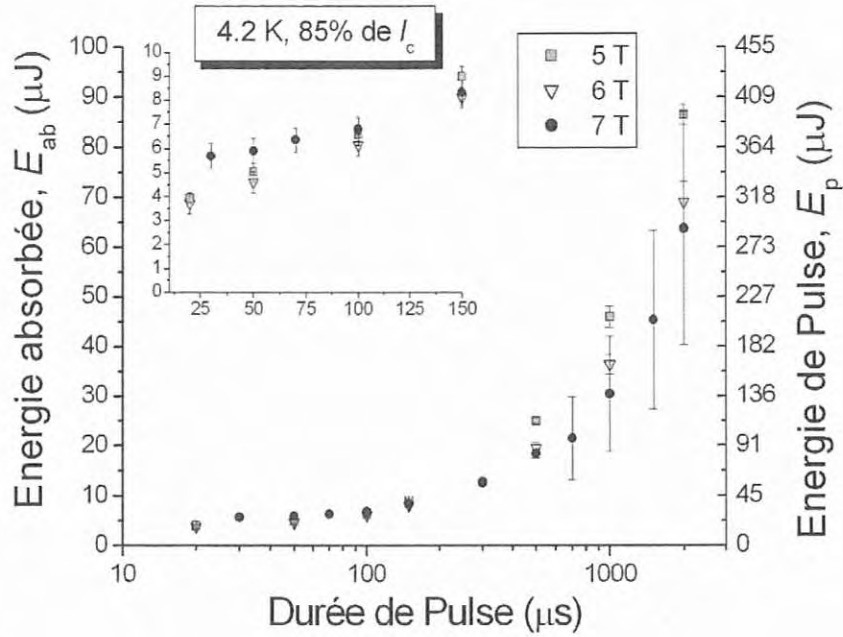


Figure I.10: Evolution de l'énergie de transition en fonction de la durée du pulse à différentes inductions magnétiques, à 4.2 K, et à 85% du courant critique.

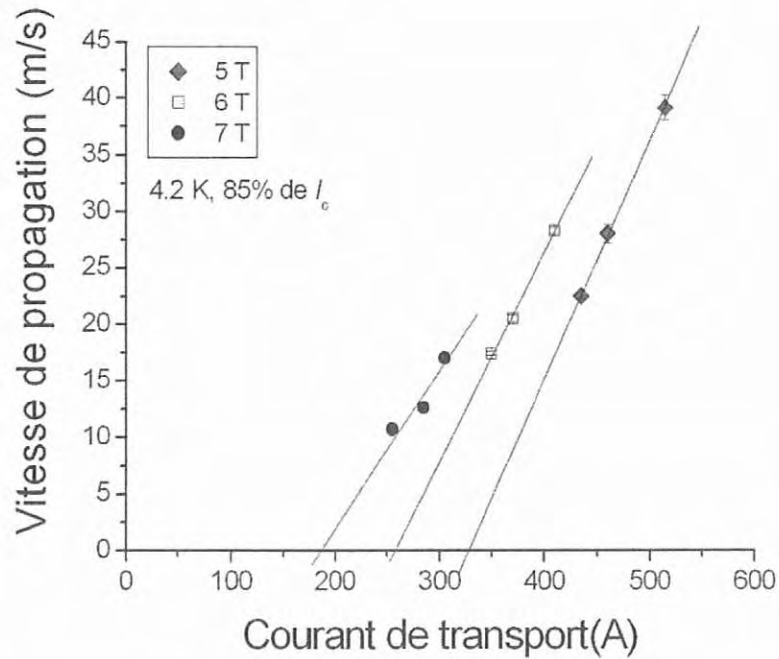


Figure I.11: Evolution de la vitesse de propagation en fonction du courant de transport du brin à différentes inductions magnétiques, à 4.2 K, et à 85% du courant critique.

I.4 Chapitre V : simulations numériques

Dans ce chapitre, nous analysons, au moyen d'une simulation numérique, certains des résultats expérimentaux. Nous avons ainsi choisi d'étudier finement les données obtenues à 7 T pour un courant de transport correspondant à 85% du courant critique. La simulation numérique a été menée sous le logiciel CAST3M du CEA. Nous avons amélioré et modifié un programme existant développé par F.J. Juster (CEA/Saclay, DSM/DAPNIA/SACM).

Ce programme moyennant des paramètres d'entrée résout l'équation différentielle suivante :

$$C_w(T) \frac{\partial T}{\partial t} - \frac{\partial}{\partial x} \left[\lambda_w(T) \frac{\partial T}{\partial x} \right] - G(T) - Q(t) + H(T, t) = 0 \quad [\text{W/m}^3] \quad (\text{I.4})$$

avec :

- $C_w(T)$: la capacité calorifique du brin en $\text{J/m}^3\text{K}$,
- $\lambda_w(T)$: la conductivité moyenne du brin W/m-K ,
- $G(T)$: la puissance volumique dissipée par effet Joule,
- $Q(t)$: la perturbation initial d'énergie,
- $H(T, t) = \frac{p}{A_w} h(T - T_0)$: la puissance échangée avec le bain (p , périmètre mouillé).

Les données physiques du problème ont été moyennées sur la section droite du brin. Le programme résout le profil de température à chaque pas de temps.

I.4.1 Géométrie modélisée, conditions initiales et limites

Un quart d'une section droite du brin a été modélisé. Les conditions de flux nuls ont été imposées dans le brin et à son extrémité et un coefficient d'échange avec l'hélium, h , a été imposé sur la surface mouillée du brin. La température initiale du brin est fixée à 4.2 K.

I.4.2 modélisation du coefficient d'échange avec l'hélium

Nous avons fondé notre modélisation du coefficient d'échange sur les travaux de C. Schmidt [9]. Nous proposons ainsi un modèle transitoire. Dans ce modèle, nous comparons l'énergie nécessaire à la création d'un film de vapeur d'hélium, E_f , à l'énergie transférée de l'échantillon à l'hélium, E_t . Ces deux énergies ont pour expression :

$$E_f(x, t) = \eta [t - t_0(x)]^n \quad [\text{J/m}^2] \quad (\text{I.5})$$

$$E_t(x, t) = \int_0^t h(T - T_0) dt, \quad [\text{J/m}^2] \quad (\text{I.6})$$

où η est un paramètre numérique que nous faisons varier et t_0 est le temps à partir duquel on chauffe l'hélium. n est choisi égale à 0.6 d'après les estimations de C. Schmidt. La fonction, h , relève d'une forme plus complexe qui dépend de la comparaison entre E_t et E_f en chaque point de la surface mouillée à l'abscisse x .

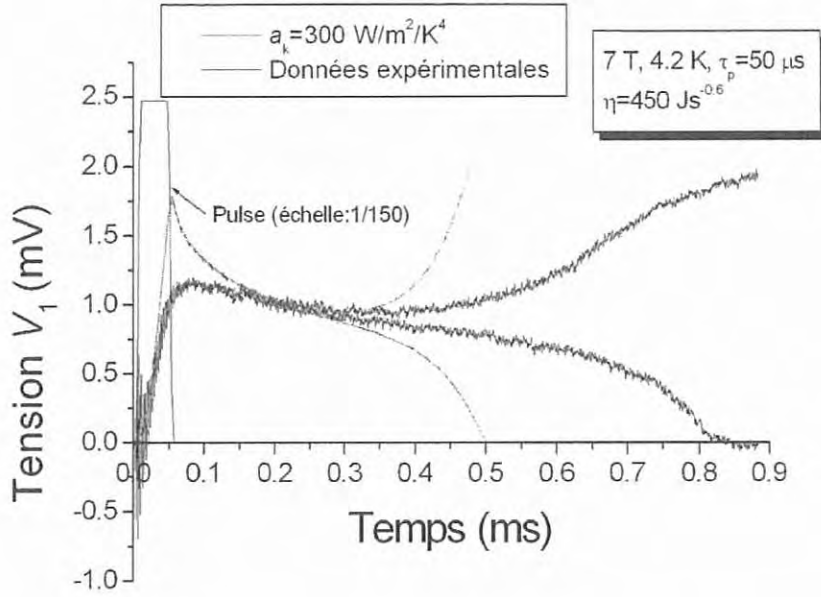


Figure I.12: Evolution de la tension V_1 , estimée numériquement, et des résultats expérimentaux en fonction du temps pour $\eta = 450 \text{ Js}^{-0.6}$ et $a_k = 300 \text{ W/m}^2/\text{K}^4$.

$E_t < E_f$: l'hélium reste dans sa phase liquide et on modélise le coefficient h sur la base d'un régime de résistance de Kapitza :

$$h(T, t) = h_k = a_k(T + T_0)(T^2 + T_0^2) \quad [\text{W/m}^2/\text{K}] \quad (\text{I.7})$$

où a_k est équivalent au coefficient de Kapitza. Il est considéré ici comme un paramètre numérique, il prend les valeurs entre $100 \text{ W/m}^2/\text{K}^4$ et $1000 \text{ W/m}^2/\text{K}^4$.

$E_t \geq E_f$: nous basculons en régime de film de vapeur pour lequel le coefficient h est dégradé :

$$h(T, t) = h_{\text{film}} \simeq 250 \quad [\text{W/m}^2/\text{K}] \quad (\text{I.8})$$

A chaque pas de calcul, nous comparons ces deux énergies pour déterminer le long du brin la valeur du coefficient h qui est ensuite réintroduit dans la résolution de l'équation différentielle au pas suivant.

I.4.3 Résultats de calculs et comparaison avec les données

Une étude de l'influence des paramètres numériques a_k et η a été menée. Nous avons montré que le paramètre η apparaît comme le paramètre influant sur l'énergie minimale de transition et la zone minimale de propagation, le paramètre a_k étant très peu influant. En augmentant la valeur du paramètre η , la phase liquide de l'hélium dure plus longtemps, il nous faut donc avoir une énergie initiale plus importante pour créer le film de vapeur d'hélium. Lorsque le film de vapeur est créé, la conduction

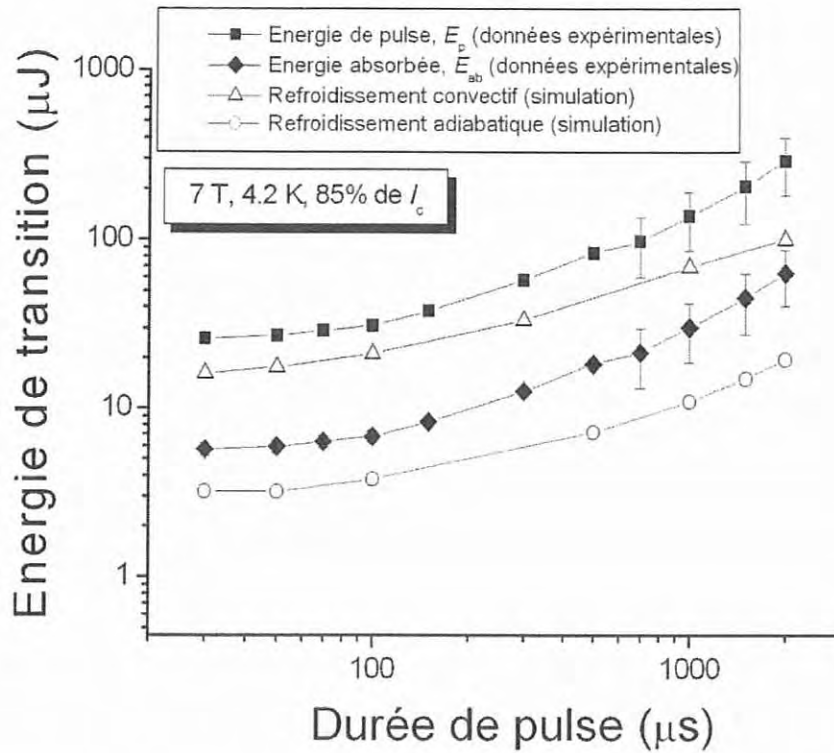


Figure I.13: Evolution de l'énergie minimale de transition numérique en fonction de la durée du pulse comparée aux résultats expérimentaux à 7 T, 4.2 K, et 85% du courant critique, pour $\eta = 450 \text{ Js}^{-0.6}$ et $a_k = 300 \text{ W/m}^2/\text{K}^4$.

de chaleur devient le processus prédominant du refroidissement du brin. Ainsi, les conditions sont requises pour qu'une transition puisse se produire. Le film de vapeur apparaît avant même que la perturbation d'énergie initiale ait disparu expliquant la très faible influence du paramètre a_k .

Détermination des coefficients a_k et η : nos données expérimentales correspondent aux courbes de tension enregistrée sur l'oscilloscope numérique. Nous avons alors estimé le jeu de paramètres a_k et η permettant de simuler les niveaux de tension V_1 de notre expérience. Nous avons trouvé par essais successifs :

- $\eta = 450 \text{ Js}^{-0.6}$.
- $a_k = 300 \text{ W/m}^2/\text{K}^4$.

Comparaison avec les résultats expérimentaux : la figure I.12 (page 41) montre une sortie numérique de la tension V_1 comparée aux résultats expérimentaux. Nous retrouvons pour notre jeu de paramètres, l'ordre de grandeur de la tension. Toutefois, les résultats expérimentaux ne reflète pas exactement la réalité. En effet, nous avons modélisé le champ électrique dans la zone de partage du courant comme linéairement dépendant de la température, ce qui n'est qu'une première approximation. Le calcul de la tension est réalisé à partir du maximum de puissance

Joule dissipé dans le brin. Une nouvelle version du programme permettra d'intégrer le champ électrique le long du brin dans la zone pour laquelle la température est supérieure à la température de partage. Cette dernière méthode conduira à une meilleure modélisation de la tension le long du brin.

Figure I.13 (page 42) montre les résultats de calcul de l'énergie minimale de transition en fonction de la durée du pulse obtenus à 7 T, 4.2 K et 85% du courant critique. Nous donnons également le résultat numérique dans le cas adiabatique. Le résultat numérique s'éloigne de notre estimation de l'énergie absorbée du brin. Toutefois, comme nous l'avons mentionné précédemment le calibrage de l'énergie absorbée par le brin n'a pas été réalisée *in situ*. De ce fait, la différence entre les conditions expérimentales à Saclay et au CNRS/CRTBT de Grenoble peuvent être responsable du faible niveau d'énergie trouvé. D'après les résultats de calculs numériques, 60% de l'énergie devrait être absorbée au lieu de seulement 22%.

I.5 Chapitre VI : supraconducteurs à haute température critique

Nous ne résumons que très brièvement ce chapitre. Ce travail s'est déroulé aux U.S.A. dans le laboratoire des champs magnétiques intenses de Floride. Notre mission fut de développer un système expérimental d'étude sous vide de la stabilité de rubans en YBaCuO. Dans une première phase, un certain nombre de tests a été mené sur des rubans de Bi-2212 et Bi-2223 pour lesquelles nous avons utilisé une jauge de contrainte comme chauffelette. Nous avons alors effectué des mesures dans l'hélium gazeux sur les rubans de Bi-2212 et dans de l'azote gazeux sur les rubans de Bi-2223.

Par la suite, nous avons développé un nouveau système de chauffelette à base d'un fil de NiCr. Ce système nous est apparu plus souhaitable que les jauges de contrainte pour étudier les rubans d'YBaCuO très sensibles aux déformations mécaniques. Des études en azote gazeux ont alors été mené sur un ruban d'YBaCuO avant de faire des tests sous vide à l'aide d'un cryogénérateur.

I.5.1 Description de l'expérience

Chaufferette en fil de NiCr : la photo I.14 (page 45) montre la chauffelette utilisé pour faire transiter les rubans en YBaCuO. Cette chauffelette est faite à partir d'un fil de NiCr commercialisé d'un diamètre de 0.14 mm pour une longueur de ~ 43 mm. La résistance par unité de mètre de cette chauffelette est pratiquement indépendante de la température, de l'ordre de $55 \Omega/\text{m}$.

Echantillon et expérience : nous ne décrivons que l'expérience relative au cas adiabatique. Nous avons dessiné un support en cuivre Cu-c2. Ce support de forme circulaire se visse sur le second étage du cryogénérateur. L'échantillon, soudé à deux aménages de courant (ces dernières étant reprises sur le premier et second étage du cryogénérateur), mesure entre 20 cm et 25 cm. Il est constitué de différentes couches de matériaux : un substrat en nickel, un buffer, le ruban d'YBaCuO (quelque microns d'épaisseurs) et un stabilisant l'argent (quelque microns d'épaisseurs). Nous avons équipé cet échantillon de prises de potentiel de part et d'autre de la chauffelette afin de déterminer l'homogénéité de la vitesse de propagation dans les deux directions. Ces prises de potentiel ont été soudées sur la couche d'argent. 5 prises de tension ont donc été utilisées. Nous avons réalisé des mesures à différentes températures pour différents pourcentages du courant critique. Du fait de la faible vitesse de propagation des supraconducteurs à haute température critique, nous avons utilisé des voltmètres Keithley[®] 2001 pour relever les tensions. Une alimentation impulsionnelle fut utilisée pour alimenter la chauffelette. Une alimentation continue de courant fournit plusieurs centaines d'ampères aux échantillons.

L'ensemble des expériences a été réalisé dans le même cryostat.

I.5.2 Comparaison entre les différentes mesures

La figure I.15 (page 46) montre une compilation de résultats obtenus à ~ 80 K en champ propre dans le cas adiabatique et convectif pour le ruban d'YBaCuO et de Bi-2223. Le ruban d'YBaCuO apparaît moins sensible aux perturbations extérieures. En effet, bien que l'échantillon d'YBaCuO ait une densité de courant plus élevée

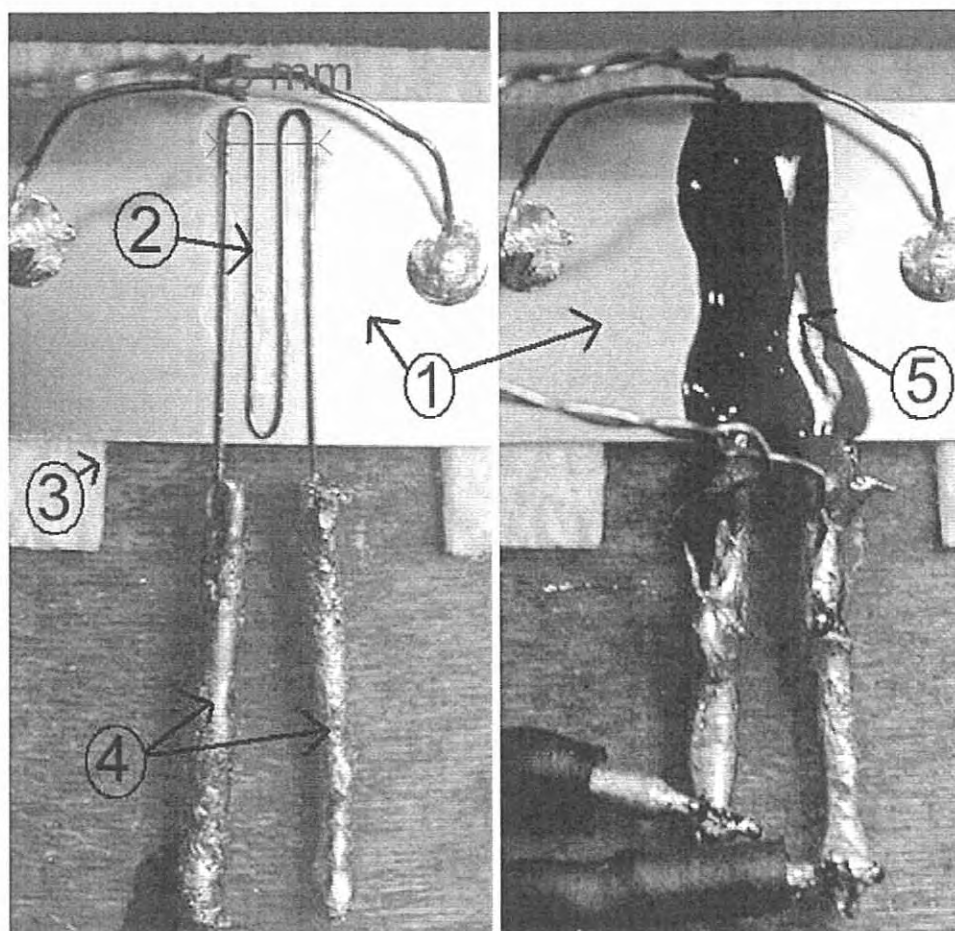


Figure I.14: A gauche, fil de NiCr collé sur la surface du ruban d'YBaCuO. A droite, la même chaufferette recouverte de Stycast[®] 2850FT.

- 1- Ruban d'YBaCuO monté sur un support en G-10.
- 2- Forme en zigzag de la chaufferette.
- 3- Tissu épais pour protéger l'échantillon lors du refroidissement.
- 4- Amenées de courant de la chaufferette.
- 5- Chaufferette recouverte de Stycast[®] 2850FT.

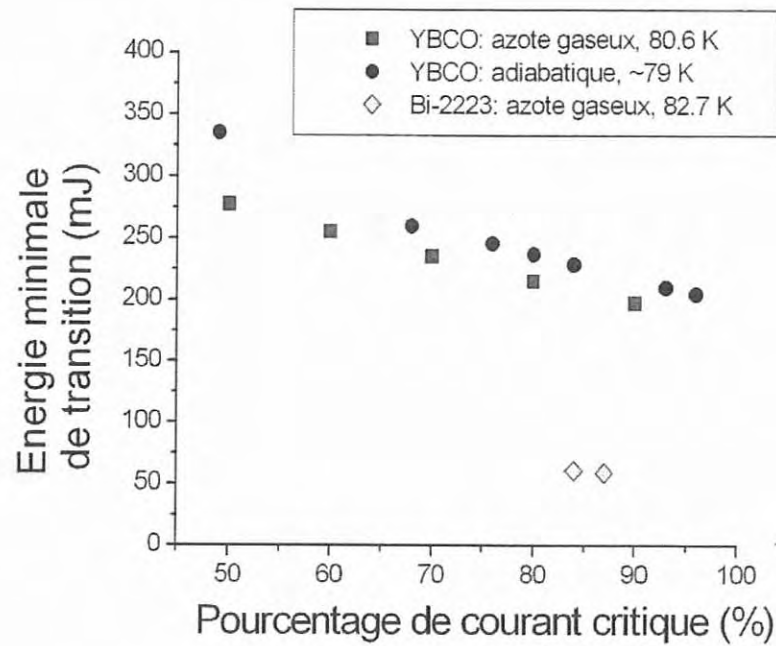


Figure I.15: Evolution de l'énergie minimale de transition en fonction du pourcentage de courant critique en champ propre, à environ 80 K.

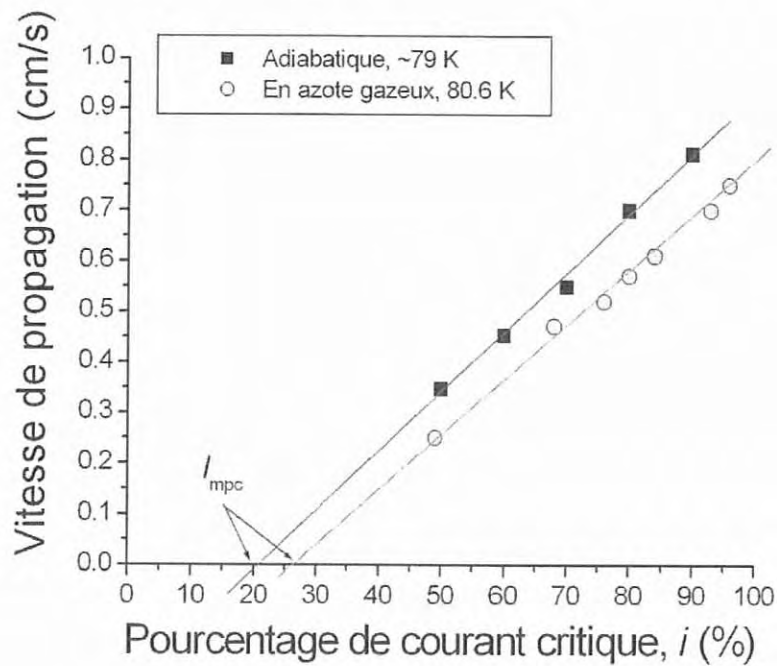


Figure I.16: Evolution de la vitesse de propagation en fonction du pourcentage de courant critique en champ propre, à environ 80 K.

et une section de stabilisant plus faible, il transite pour des niveaux d'énergie de l'ordre de quelques centaines de milli-Joule alors que le Bi-2223 transite en dessous de 100 mJ. La présence du substrat en nickel pourrait apporter la stabilité nécessaire au ruban d'YBaCuO pour expliquer un tel résultat [8].

Si nous comparons le comportement des différents supraconducteurs, nous pouvons distinguer trois cas : un cas où la chaleur diffuse et la zone normale ne propage pas (Bi-2212), un cas mixte entre propagation et diffusion (Bi-2223) et un cas de propagation (YBaCuO, NbTi et Nb₃Sn). De manière surprenante, le comportement du ruban d'YBaCuO tend à ressembler à celui du NbTi. Toutefois, la vitesse de propagation du NbTi apparaît deux ordres de grandeur supérieurs. Figure I.16 (page 46) montre l'évolution de la vitesse de propagation d'un ruban d'YBaCuO en champ propre pour une température de ~ 80 K en fonction du pourcentage de courant critique. La vitesse de propagation reste inférieure au centimètre par seconde. Inversement, l'énergie minimale de transition du NbTi est d'environ 5 ordres de grandeur inférieures à celle des supraconducteurs à haute température critique (la capacité calorifique des matériaux diminuant avec la diminution de la température). En ne considérant pas que les propriétés physiques des matériaux sont différentes¹, cette différence résulte donc des températures d'opération respectives des échantillons. En effet, dans nos expériences, les rubans d'YBaCuO ont été mesurés à ~ 80 K alors que les brins NbTi ont été mesurés à 4.2 K. Finalement, les échantillons en YBaCuO apparaissent plus stables.

Nous ne présentons pas de résultats sur les rubans en Bi-2212 car ces derniers n'ont pu être transités à des niveaux d'énergie en dessous du Joule ce qui a entraîné la destruction de la plupart des chaufferettes. Dans le cas où une zone normale apparaît dans le conducteur, la température s'élève alors très localement autour du point chaud et la chaleur diffuse lentement ce qui peut entraîner la dégradation irréversible et très rapide de l'échantillon.

¹Alors que pour les supraconducteurs à basse température critique, les propriétés physiques ont fait l'objet de nombreuses études, il est difficile de trouver des données fiables pour les différents supraconducteurs à haute température critique dont les propriétés physiques dépendent de la fabrication.

I.6 Chapitre VII : conclusion générale

L'ensemble du travail présenté dans cette thèse est très expérimental. Différentes expériences ont été réalisées et de nombreux systèmes de chaufferette testés.

Dans le cas des supraconducteurs à basse température critique, nous avons recherché une technologie de chaufferette qui soit facile à mettre en oeuvre, qui puisse être étalonnée et puisse fournir des énergies minimales de transition reproductibles. Nous avons suggéré une manière de mener le calibrage de l'énergie absorbée par le brin à travers une étude de faisabilité. Nous avons également mené des études de répétabilité de l'expérience. Toutefois, nous n'avons pas pu tester dans le temps qui nous était imparti d'autres échantillons.

Pour valider le programme numérique, des expériences menées dans des conditions adiabatiques nous paraissent nécessaire. Cela permettra de mettre en lumière, grâce à un calibrage *in situ* de l'énergie absorbée, les critères de transition d'un brin supraconducteur multifilamentaire.

Nous avons effectué des tests préliminaires sur un brin Nb_3Sn fourni par notre partenaire industriel Alstom/MSA. Aucune dégradation n'a été observée lors des mesures de stabilité.

Dans le cas des supraconducteurs à haute température critique, les études se poursuivent en Floride. L'expérience a été améliorée et de nouveaux échantillons recouverts d'un stabilisant électrique et mécanique en cuivre, en plus de la couche d'argent, ont été testés. L'évolution temporelle et spatiale de la température le long des rubans a été mesurée. De plus, des études complémentaires ont été menées pour déterminer l'influence du substrat sur la stabilité des rubans.

Bibliography


- [1] A. Devred *et al.* *Quench Localization in Full-Length SSC R&D Dipoles*, pages 73–83. Plenum Press, New York, 1989.
- [2] Y. Iwasa. *Case Studies in Superconducting Magnets, Design and Operational Issues*. Plenum Press, New York, 1994.
- [3] B.J. Maddock, G. James, and W.T. Norris. Superconductive composites: heat transfer and steady state stabilization. *Cryogenics*, pages 261–273, August 1969.
- [4] P. Bauer. *Stability of Superconducting Strands for Accelerator Magnets*. PhD thesis, Technische Universität Wien, 1998.
- [5] D.E. Baynham, V.W. Edwards, M.N. Wilson. Transient Stability of High Current Density Superconducting wires. *IEEE Transactions on Magnetics*, 17(1):732, January 1981.
- [6] K. Seo, M. Morita, S. Nakamura, T. Yamada, and Y. Jizo. Minimum Quench Energy Measurement for Superconducting Wires. *IEEE Transactions on Magnetics*, 32(4):3089, July 1996.
- [7] S.B. Kim, Y. Ueno, A. Ishiyama. Experiment and Numerical Analysis of Normal Zone Propagation Properties in Ag Sheathed Bi-2223 Superconducting Tapes. *IEEE Transactions on Magnetics*, 32(4):2822, July 1996.
- [8] X. Wang, R.C. Caruso, M. Breschi, G. Zhang, U.P. Trociewitz, H.W. Weijers, and J. Schwartz. Normal Zone Initiation and Propagation in Y-Ba-Cu-O Coated Conductors with Cu Stabilizer. *IEEE Applied Superconductivity*, 15(2):2586–2589, 2005.
- [9] C. Schmidt. Review of the steady state and transient heat transfer in pool boiling helium. *International Institute of Refrigeration, Commission A1/2-Saclay (France)*, (6):17, 1981.

Chapter II

General Introduction

Contents

II.1 Collaborations and objectives of the thesis	51
II.1.1 First collaboration: LTS conductors	51
II.1.2 Second collaboration: HTS conductors	52
II.2 Overview on stability	52
II.2.1 Quench precursors in superconducting magnets	52
II.2.2 Disturbance spectrum and scope of this thesis	53
II.3 Notions of composite conductor stability	54
II.3.1 Current sharing regime and heat generation	54
II.3.2 Minimum Quench Energy and Minimum Propagating Zone concepts	57
II.3.3 Normal Zone Propagation velocity	59
II.4 Review on the various means to simulate quench pre- cursors	60
II.4.1 Inductive heaters	60
II.4.2 Heaters based on resistive heaters	62
II.4.3 Laser and diode laser	70
II.4.4 Summary of the review	70
II.5 Our choice of heater technologies	71
II.5.1 Low temperature superconductors	71
II.5.2 High temperature superconductors	72

his chapter introduces the framework of this thesis. The concept of "quench" and a few notions of stability against local energy releases are introduced. Subsequently, heater technologies to simulate quench precursors in superconducting magnets are reviewed. Finally, a new type of heater, based on a diode laser, is presented.

II.1 Collaborations and objectives of the thesis

The present work was carried out under the auspices of two collaborations. These collaborations, conducted independently from one another, cover the study of the thermo-electric stability of Low Temperature Superconductors (LTS) and High Temperature Superconductors (HTS). They deal with the development of new heater technologies to simulate local heat disturbances of short durations, which are known to occur in superconducting magnets. New experimental setups have especially been designed for these new heaters.

Our objective was to find a new heater which meets the following requirements:

- easy to use,
- adaptable to any configurations,
- calibrated,
- leading to reproducible and accurate data.

II.1.1 First collaboration: LTS conductors

The first collaboration between the "Commissariat à l'Energie Atomique" CEA (France) and an industrial partner, Alstom/MSA (France), was initiated to develop high current density Nb_3Sn conductor for superconducting electromagnets. The scientific program covers the thermo-electrical characterization of the conductors and the prototyping of a Nb_3Sn quadrupole magnet model for the next generation of particle accelerators. Our contribution was focused on the development of a new and reliable heater technique to study the stability of superconductors. Various techniques already exist. However, most of them exhibit a poor reproducibility and suffer from a lack of calibration. To address these issues, three different systems have been developed and a completely new experimental setup has been designed. These systems are:

- resistive heater based on carbon-charged epoxy,
- small induction coil,
- diode laser.

Only the diode laser heater proved to be easy to handle, reliable, and to yield reproducible and calibrated results.

Although the CEA/Alstom collaboration deals mainly with Nb_3Sn , most of our work was carried out on NbTi wires. Indeed, our objective was to develop a reliable technology producing reproducible measurements. NbTi wires were chosen to validate the experimental setup since they have been thoroughly characterized in the framework of the Large Hadron Collider (LHC) and are easier to work with. Of course, after validation of the technology on NbTi conductors, it can be subsequently applied to the characterization of Nb_3Sn conductors.

II.1.2 Second collaboration: HTS conductors

The second collaboration was a joint-project between the MIT Francis Bitter Magnet Laboratory and the National High Magnetic Field Laboratory (NHMFL) at Florida State University in the US. This combined initiative was divided into different tasks which covered various practical studies on YBCO conductors. The primary objective was to address the stability and protection issues related to HTS magnets [1]. General understanding of these issues is necessary to design safe and reliable commercial devices.

In this context, our work was dedicated to the design of an innovative experiment to study the stability of YBCO tapes in a vacuum and, later, in a background magnetic field. In the time frame of this work, a new experimental technique was developed and experiments were carried out on Bi-2223 tapes to validate the experimental setup and, subsequently, on YBCO tapes. The measurements were carried out in nitrogen gas cooling and in vacuum using a cryocooler.

II.2 Overview on stability

In the market of applied superconductivity, two main commercial applications coexist: medical and physics instruments. In human health field, the reliability of devices such as RNM and MRI magnets is an important factor. So, to achieve this requirement over hours of operation, the current density flowing into the magnets is kept relatively low by over-stabilizing the conductors [2]. On the contrary, for physics applications, very high current density superconducting magnets are needed. Engineers and scientists work then at the edge of the conductor technology to reach the highest achievable magnetic field. Therefore, the amount of superconducting filaments is increased while the cross-section of stabilizer is decreased reducing the safety margin to its minimum [3]. Before dealing with our main topic, it must be pointed out that our work targets this last family of very high current density magnets for nuclear and particle physics.

In this section, we shall briefly introduce the origin of instabilities in superconducting electromagnets and the general scope of this thesis. Superconducting magnets are usually wound from high current density superconducting multifilament composite conductors, which are designed to operate safely and reliably. Some basic notions of these conductors and their stability will be presented. A thorough review of heating systems to simulate quench precursors will follow, leading us to the choice of technologies that we have made for our experimental setup.

II.2.1 Quench precursors in superconducting magnets

Thus, high current density superconducting magnets are prone to a phenomenon called a "quench", which corresponds to the sudden transition of the winding from the superconducting state to the normal resistive state. Then, all the stored magnetic energy is released in a short time scale. Large heat dissipation follows because of the conjunction of a large transport current and of the normal-state resistivity of the magnet. The temperature increases and mechanical forces appear within the winding which are transmitted to the whole structure. In terms of reliability, this is a damaging situation that the designer wishes to avoid.

Such a phenomenon is often encountered when the magnet is ramped for the first

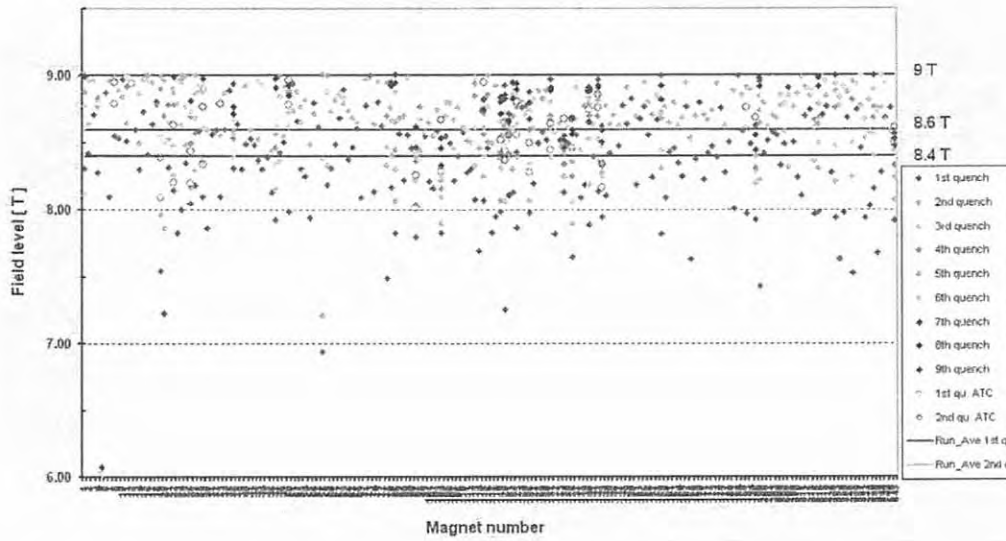


Figure II.1: Quench performances of LHC superconducting magnets (courtesy Alstom/MSA).

time. Thus, at currents well below its operating current, a superconducting magnet can undergo unexpected quenches and may require to be energized several times before reaching its nominal current to produce the desired magnetic field. This is illustrated in Figure II.1 (page 53) which shows a compilation of quench performances of LHC magnets. This gradual improvement in performance is referred as "training", a well-known behavior of any LTS magnets. Investigations over years concluded that local release of energies within the magnet are likely to be the cause of such quenches. A section of conductors switches back to the normal-resistive state and a normal zone propagates throughout the rest of the winding.

The main origins of local energy releases or disturbances are often mechanical, induced by the Lorentz's force. However, other mechanisms can play a non-negligible role in the stability of magnets. Here is a non exhaustive list of possible causes:

- relative motions of conductors [4],
- insulation cracks in impregnated magnets [1],
- fracture and plastic deformations,
- AC losses,
- flux jumps,
- failure of the cryogenic system, or heat leak....

These are all quench precursors, which input heat onto the winding and drive a section of the magnet into its normal resistive state.

II.2.2 Disturbance spectrum and scope of this thesis

Quench precursors can be sorted through the the concept of disturbance spectrum. This concept was first introduced by S.L. Wipf in 1978 [5]. It encompasses all the possible forms of energy disturbances which can occur in the winding of superconducting magnets. Four extreme cases are presented in Table II.1 (page 54). In time,

Table II.1: Disturbance spectrum [6].

Time	Localized disturbances	Distributed disturbances
Transient	<i>Energy (J)*</i>	<i>Energy density (J/m³)</i>
Steady-state	<i>Power (W)</i>	<i>Power density (W/m³)</i>

*Our domain of study.

the energy disturbance can be continuously released as in the case of a bad joint or suddenly as in the case of insulation cracks. In space, its extension can be of the size of the conductor as in the case of friction between wires or extended over a large portion of the magnet as in the case of a heat leak.

Apart from flux jumps, which can be addressed by subdividing the superconductor into a multifilament composite structure [6], transient disturbances of mechanical origins appear to be the most serious source of troubles for which no obvious solutions have been found. Besides, the correlation between disturbance origins and actual magnet performance is not always obvious, and some other mechanisms may come into play.

In the following study, we focus on transient localized disturbances (a few millimeters long) and of short durations (a few milliseconds at most) applied to a single wire. A single wire is the simplest cell upon which can be built a coherent description of quench origin and propagation in high current density magnets. However, in addition to the difficulties of characterizing the stability behavior of a single wire, the task remains outstandingly difficult to relate magnets performance to the performance of their conductors. Such a work has not been done in the present thesis.

II.3 Notions of composite conductor stability

Before describing the different systems which have been used so far to simulate quench precursors in superconducting magnets, cables or single conductors, let us introduce some basic notions on the normal-zone transition of a multifilament composite conductor. These notions are:

- current sharing and heat generation,
- Minimum Quench Energy (MQE) and Minimum Propagating Zone (MPZ),
- Normal Zone Propagation Velocity (NZPV).

II.3.1 Current sharing regime and heat generation

Phenomenology: Practical conductors are made-up of superconducting filaments embedded in a high thermal conductivity and low resistivity metallic matrix. Due to the physical characteristics of superconductors, this composite structure is necessary and cannot be avoided. Indeed, in the absence of such a matrix, a pure superconductor is likely to burn out as soon as it undergoes a quench. The normal-state

resistivity of a superconductor is very large resulting in unmanageable power dissipations by the Joule effect. Even if the presence of the matrix lowers the engineering current density of the conductor, it brings essential thermal and electrical stabilities to the system in addition to a mechanical stability. As a result, the conductor becomes less sensitive to heat disturbances. Indeed, if a heat disturbance cannot be handled by the superconductor, the fraction of transport current that exceeds its maximum transport capability, can be transferred into the metallic matrix which starts to dissipate heat. Then, depending on the amplitude of heat generation and on cooling efficiency, the conductor can undergo a quench or recover.

This redistribution of current between superconducting filaments and matrix occurs only if the transport current exceeds the critical current of the superconductor. Figure II.2 (page 56) schematically introduces the principle of current sharing in a composite conductor. We assume a linear critical current versus temperature characteristic of a composite conductor obtained at a given background magnetic field. The behavior of the composite conductor can be divided into three domains referred to A, B and C. In domain A, the superconductor, initially at the operating temperature, T_{op} , is in the superconducting state and carries the whole transport current, I_t . If heat is deposited onto the conductor, its temperature will rise according to its thermal properties up to the so-called current sharing temperature, T_{cs} , at which the transport current is equal to the critical current. From the operating temperature to the current sharing temperature, the superconductor stays fully in the superconducting state and no heat dissipation occurs. At T_{cs} , the conductor leaves domain A to enter the current sharing regime of domain B. Then, the current is shared between the superconductor, which carries the critical current, $I_c(T)$, at the temperature, T , while the metallic matrix carries the exceeding current $I_m(T) = I_t - I_c(T)$, accompanied with heat dissipation. If the temperature increases further and exceeds the critical current T_c , the transport current property of the superconductor vanishes and the whole transport current flows into the metallic stabilizer (domain C).

Differences between HTS and LTS conductors: The superconducting properties of HTS and LTS conductors are different (see the large differences in the critical temperatures in Table II.2, page 57), and their critical current versus temperature characteristics differ. Figure II.3(a) (page 56) compares the critical current evolution of two generic HTS and LTS conductors. It shows that the normal state transition of LTS conductors takes place over a narrow temperature range of the order of few Kelvins. Then, the transition from the superconducting state to the normal state occurs quickly with a sudden surge of heat dissipation and the propagation of a normal front.

In the case of HTS conductors, the transition to the normal state occurs over a large temperature range, extending from 10 to 30 K [7]. The operating temperature being larger, the heat capacity of the material is also larger. Consequently, the normal zone transition is very progressive and the current sharing zone can spread over a large section of conductor where the temperature ranges from the current sharing temperature to the critical temperature.

Figure II.3(b) (page 56) shows the typical evolution of the heat dissipation of HTS and LTS conductors. In the case of LTS conductors, the heat dissipation increases sharply till the whole conductor is entirely in the normal-resistive state. The critical temperature of LTS conductors is below ~ 25 K, for which the resistivity of

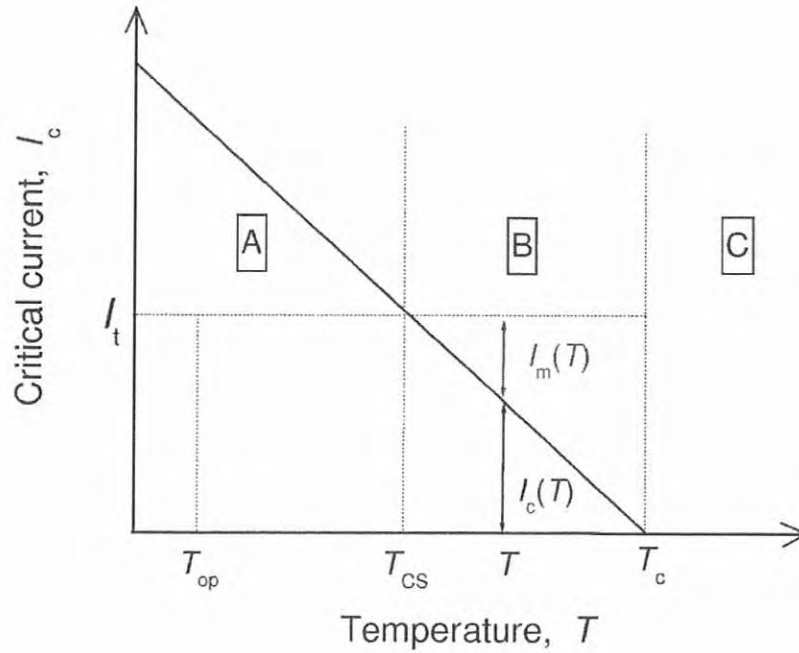
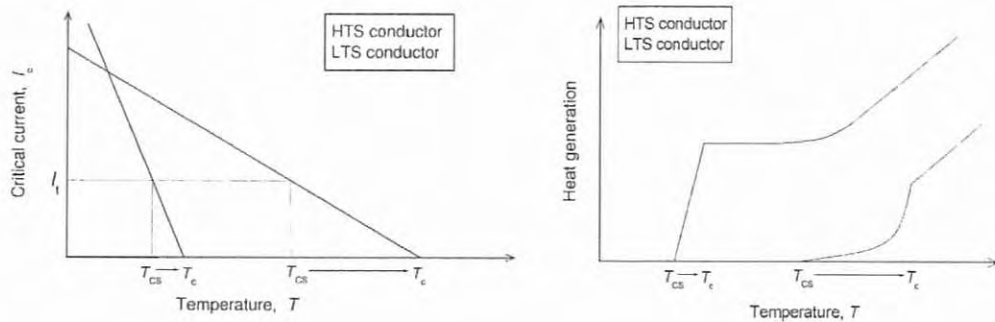


Figure II.2: Linearized critical current characteristic of a superconducting multifilament composite at a given background magnetic field: [A], the current flows entirely into the superconducting filaments ; [B], the conductor enters the current sharing zone and the current is shared between the superconducting filaments and the metallic matrix. [C], the superconducting filaments can no longer carry any current and the transport current flows entirely in the matrix.



(a) Critical current versus temperature characteristics. (b) Heat generation versus temperature characteristics.

Figure II.3: Schematic plots of HTS and LTS characteristics: (a) critical current versus temperature characteristics. (b) heat generation as a function of temperature.

Table II.2: A few generic physical properties of HTS and LTS conductors.

Conductors (Type)	$T_c(0 T)$ (K)	C_p (J/kg-K)	λ (W/m-K)	Normal-state resistivity (Ωm)
Bi-2212 (Ox- ide)	110	2 (77 K)	$< 2 \times 10^{-5}$ (77 K)	
Bi-2223 (Ox- ide)	80	2 (77 K)	$< 2 \times 10^{-5}$ (77 K)	
YBCO (Oxide)	95	90 (77 K)	5.75 (77 K)	0.57×10^{-5} (77 K)
NbTi (Metallic alloy)	9.2	0.6 (4.2 K)	0.2 (4.2 K)	6.5×10^{-7} (6 T, 4.2 K)
Nb ₃ Sn (In- termetallic compound)	19	0.04 (4.2 K)	0.2 (4.2 K)	
MgB ₂ (In- termetallic compound)	39 [8]	0.7 J/mol-K (37 K) [9]	13 (20 K, 0 T) [10]	

normal metal as copper or silver remains constant, and the heat generation function is usually assumed to increase linearly as a function of temperature, T . For HTS conductors, the current sharing temperature is greater than ~ 25 K, for which the resistivity of normal metals increases with increasing temperature, and the heat generation evolves as a function of the square of temperature, T^2 (see Appendix A, page 234).

II.3.2 Minimum Quench Energy and Minimum Propagating Zone concepts

Minimum Propagating Zone (MPZ): The Minimum Propagating Zone theory was first introduced to model the stability of a LTS magnet by S.L. Wipf in 1978 [5]. It extended the stability model suggested by B.J. Maddock *et al.* based on a steady-state thermal equilibrium [11]. This theory states the existence of a non-uniform localized steady profile of temperature that is unstable against small perturbations [12]. This profile, named here, T_{mpz} , defines the MPZ. Normal zones greater than the "MPZ profile" are expected to propagate into a quench while normal zones smaller than the MPZ profile are expected to shrink and to lead to a full recovery of the superconducting state. Consequently, a conductor can undergo a local normal zone transition and subsequently recover the superconducting state [13]. Wilson suggested a simple estimation of the adiabatic MPZ extension in a LTS magnet [14]. The MPZ is determined at the thermal equilibrium between the heat generated inside the conductor and the evacuated power. To apply the resulting equation to composite conductors, we consider that all the current flows into the matrix at the critical temperature, T_c , and that the thermal conductivity is isotropic (a mathematical demonstration can be found in reference [15]). These are rough estimations which lead to conservative values. Finally, the longitudinal extension of

the MPZ, L_{mpz} , is:

$$L_{\text{mpz}} \simeq 2\pi \sqrt{\frac{(1+r)\lambda_{\text{m}}(T_{\text{c}} - T_{\text{cs}})}{r\rho_{\text{m}}J_{\text{w}}^2}} \quad [\text{m}] \quad (\text{II.1})$$

where λ_{m} is the thermal conductivity of the matrix, T_{cs} is the current sharing temperature, ρ_{m} is the resistivity of the matrix in which flows a current density J_{m} ; r is the copper-to-non-copper ratio and J_{w} is the average current density over the cross-section of the composite. Therefore, the length of the MPZ is the result of a competition between conduction cooling and heat generation. Larger heat conduction lead to larger MPZ's while larger resistivities lead to smaller MPZ's. In cooling conditions, the task is complicated by the difficulties to simulate the heat transfer to the helium. At the thermal equilibrium, the heat balance equation is:

$$\lambda_{\text{m}} \frac{d^2T}{dx^2} = G(T) - H(T) \quad [\text{W/m}^3] \quad (\text{II.2})$$

where $G(T)$ is the heat generation function at temperature T , and $H(T)$ is a cooling function modeling the heat transfer between the helium and the surface of the conductor. This last function is the corner-stone of stability models in bath cooling environment. Rough assumptions can be made to solve the previous equation to yield analytical expressions of the MPZ [12]. The case is often treated in steady-state conditions for which the problem can be simplified. Numerical simulations are now preferred for a better understanding of the MPZ concept, especially while transient processes are considered (≤ 100 ms). Then, this function is usually described in terms of Kapitza conduction till the onset of film boiling [16].

Experimentally, it is not easy to measure the temperature evolution of the conductor since most thermal sensors have a large time constant compared to the quench phenomena induced by local release of energy. As we shall see, an empirical criterion cannot be used to determine the MPZ from the local minimum exhibited by the voltage across the heated zone. However, this would appear to be a reasonable assumption if the temperature of the superconductor was superior to T_{c} since the voltage depends only on the resistivity of the metallic matrix and the transport current (see chapter IV, section IV.5 page 149).

Minimum Quench Energy (MQE): It is customary to compute the MQE as the enthalpy content of the Minimum Propagating Zone [13]. This definition is somewhat arbitrary and has no solid mathematical grounds. However, it is consistent with the definition of the Minimum Propagating Zone. Let ϑ_{mpz} and T_{mpz} designate the volume and the temperature profile of the MPZ, the MQE can be written as:

$$MQE \simeq \vartheta_{\text{mpz}} \int_{T_{\text{op}}}^{T_{\text{mpz}}} C_{\text{w}} dT \quad [\text{J}] \quad (\text{II.3})$$

where C_{w} is the average heat capacity of the multifilament composite conductor. Practically, it corresponds to the minimum energy that needs to be deposited onto the conductor to trigger a quench. Below this Minimum energy, the conductor recovers. Above this energy, it unconditionally quenches.

This energy is related to the MPZ whose existence is determined by a time and space criterion. Therefore, the MQE can only be estimated for disturbances of duration

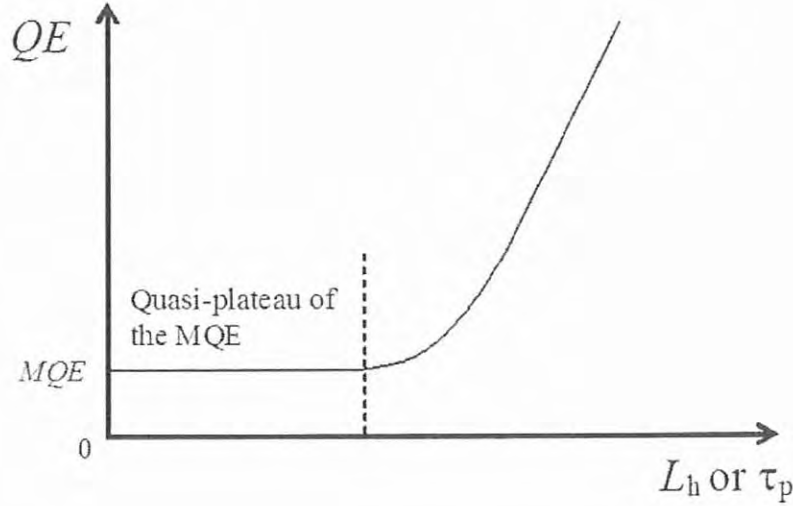


Figure II.4: Typical evolution of the Quench Energy as a function of pulse durations, τ_p , or heat disturbance lengths, L_h .

inferior to the time of creation of the MPZ and of spatial extension smaller than the spatial extension of the MPZ.

When these criteria are satisfied, the quench energy becomes quasi-independent of the pulse duration or disturbance length. Figure II.4 (page 59) shows a typical plot of MQE versus pulse duration or disturbance length. The plot shows a quasi-plateau at short pulse duration and small heat disturbance length. As long as the spatial extension and duration are respected, the MQE can be estimated from the quasi-plateau at infinitely short time and small length disturbance.

II.3.3 Normal Zone Propagation velocity

After the energy disturbance has fled away and the MPZ has been reached, the normal zone grows at a steady velocity referred as the Normal Zone Propagating Velocity (NZPV) [17]. In adiabatic conditions, this velocity roughly depends on the ratio between heat generation and cooling capacity as follow:

$$\nu_{ad} \simeq \frac{1}{C_w} \sqrt{\frac{G_c \lambda_m}{T_q - T_{op}}} \quad [\text{m/s}] \quad (\text{II.4})$$

where G_c is the maximum heat generation reached at T_c , T_q is a temperature between T_{cs} and T_c , λ_m is the thermal conductivity of the matrix, and C_w is the average heat capacity of the conductor (note that in Equation II.4 (page 59), λ_m and C_w are both temperature independent).

For LTS conductors, a fraction of the power generated by the Joule effect near the transition edge diffuses into the superconducting zone and heats it up to the transition temperature leading to the propagation of a "normal front". However, due to the large heat capacity of HTS conductors, the current sharing zone extends over a

large section of conductor thereby smoothing the transition front and lowering the Normal Zone Propagation Velocity.

The Normal Zone Propagation velocity is one of the key-parameters which characterizes the quench behavior of superconductors and must be taken into account when designing a magnet. Indeed, the normal state transition is not harmful as long as the normal zone, created by the disturbance, expands quickly enough to avoid the formation of a hot spot. If the normal zone remains localized over a small volume, there is a risk that a significant amount of stored energy be dissipated in this small volume, leading to irreversible conductor damage. This is particularly critical for HTS conductors for which the velocity of the normal zone expansion is a few orders of magnitude lower than for LTS conductors.

II.4 Review on the various means to simulate quench precursors

In this section, we review previous stability experiments presented in the literature. The general principle consists in releasing a known energy onto a superconducting conductor or cable in controlled environmental conditions (cooling, applied magnetic field and transport current). Then, the Normal Zone Propagation Velocity (NZPV) and the minimum energy triggering a normal zone transitions or Minimum Quench Energy (MQE) are estimated. To estimate accurately the Minimum Quench Energy, it is necessary to choose a heater, which is small and fast enough with respect to the temporal and dimensional criteria enounced above. In the various designs considered until now, a few problems, which include the thermal insulation and the control of the size of the heated zone, have not been entirely solved.

II.4.1 Inductive heaters

The first attempt at carrying out a stability experiment using an inductive heater was performed by Goll and Turowski in 1978 [19]. A constantan wire (see section II.4.2, page 62) and an induction coil (10 mm in length and diameter) were used to generate fast magnetic flux variations at their surface and to trigger normal zone transitions in superconducting wires. The field sweep was 4 ms long. In this experiment, no calibration was carried out. Only the influence of the external flux disturbances on the stability was studied.

In the early 1980's, a transient induction heating technique was developed by D.E. Baynham, *et al.*, to assess the Quench Energy Margin (QEM) of NbTi and Nb₃Sn strands [20]. An induction coil was wound around a silica tube with a 40 mm diameter, which covered 100 mm of wire samples. A switch and a capacitor in series with the coil completed the circuitry. The discharge of the capacitor with a time constant of $\sim 100 \mu\text{s}$ induced eddy-currents in the metallic outer shell of the wires which dissipated heat. The measurements were done in vacuum and liquid helium environment at 4.2 K under a background magnetic flux density of 5.5 T. They were the first comparative results between NbTi and Nb₃Sn strands. As expected, Nb₃Sn samples appeared more likely to endure larger distributed input energies than NbTi samples because of their larger critical temperature.

Almost twenty years later, a similar experiment was pursued on LHC strands [18]. The Silica tube was replaced by an alumina one (see Figure II.5, page 61). Each

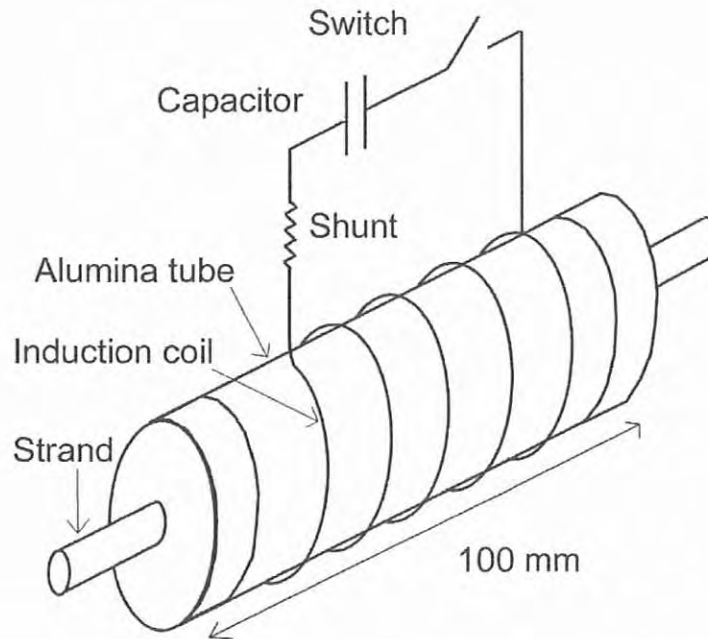


Figure II.5: Schematic drawing of induction coil wound around an alumina tube [18].

end of it was closed by a copper ferrule reducing the helium cooling path. The experimental conditions were supposed to match the operating conditions of LHC magnets, *i.e.* an operating temperature of 1.8 K, in a background magnetic field up to 8 T. The time discharge of the capacitor ranged from $\sim 20 \mu\text{s}$ to $100 \mu\text{s}$. The measurements showed the influence of surface coatings and of helium channel lengths on the stability margin. The induction coil was self-calibrated by soldering the ferrules to the strands creating adiabatic conditions around the heated zone. The subsequent results on Quench Energies (QE) were compared to the calculated enthalpy necessary to raise the temperature of the samples from operating temperature to current sharing temperature. However, this method did not seem to be fully satisfactory. Indeed, discrepancies at low and high transport currents between measurements and calculations could not be explained. In addition, no absolute calibration could be achieved at the time.

A few attempts at calibrating induction coils have been carried out relying on electric and calorimetric techniques. For instance, Kurado *et al.* relied successfully on the "boil-off" method to calibrate the energy dissipated in a full-size Cable-In-Conduit Conductor. However, this calorimetric technique is only relevant as long as the size of the conductors is big enough so as to generate enough heat to boil a sizable quantity of helium liquid. More recently, K. Seo used a coil that was 30 mm long [21]. Temperature and electrical measurements were respectively done on the conductor and the inductive heater. It appeared that the electrical measurement was not suitable for a calibration test. Most of the energy was dissipated inside the winding of the coil. So, litz wires instead of plain copper wires were suggested as the best candidate to improve the design.

The transient induction heating technique has given important results on stability. In addition, on the contrary to most of the other heating techniques, attempts were made to calibrate the experiments. However, they proved to be difficult, often, leading to overestimations of the Quench Energy Margin. No attempt at measuring the Minimum Quench Energy has been made ; the longitudinal dimension of the induction coils were always too long to achieve such a goal.

II.4.2 Heaters based on resistive heaters

The following paragraph has been split in different subsections. It does not necessary respect the chronological order since we prefer to introduce the heater technologies by their affinities. Except for the first two subsections, the reader can refer to Bauer's thesis for a thorough review on paste heaters, clamp heaters and point heaters [22].

Ceramic resistor chips: To measure Minimum Quench Energies, it is necessary to rely on point-like heaters. In the early 1990's, a technique based on a ceramic resistor cut from a commercial ceramic resistor tube was developed [23]. It relied on a 1 mm x 1.5 mm x 0.5 mm chip soldered onto a Cu/NbTi square-shaped wire (see Figure II.6, page 63). Two voltage taps across the heater and a thermocouple were used to detect quenches. The setup, sample plus heater, was thermally insulated with epoxy (10 mm thick) to simulate adiabatic conditions. The pulse durations were quite long (of the order of milliseconds with a repetition rate of 1 min). No attempt to calibrate the heater was made, and no estimation of the influence of the epoxy and of the thermocouple was carried out. However, the low time response of the thermocouple did not enable a fair and accurate measurement of the sample temperature during the initial thermal runaway of quenches. Minimum Quench Energies were calculated from pulse characteristics (current and voltage traces). Good repeatability of the Quench Energies was reported by the author for a given quality of contact resistance between heater and sample.

This experiment demonstrated the feasibility of small heaters. Furthermore, it gave a first hint of the difficulties related to the control of the contact between heaters and samples.

Ohmic wires: One of the most interesting experiment to study the stability of superconducting wires was carried out by C. Schmidt in 1978 [24]. An insulated manganin wire of 0.03 mm of diameter covered by epoxy resin was bifilarly wound around 1 mm of a NbTi superconducting wire in order to avoid inductive effects. Pulses of 20 μ s to near 1 ms were applied to the sample. So, both spatial and time criteria, which are necessary to assess the Minimum Quench Energy, were respected. The wires were characterized in boiling liquid helium and in a vacuum at 4.2 K. The results showed that the presence of liquid helium enhanced the Quench Energy by a factor 3 to 6. These last authors used a technology similar to W. Goll and P. Turowski's one based on an insulated constantan wire of 30 cm long and a diameter of 0.1 mm. This wire was embedded in silicone rubber to insulate it from helium cooling [19]. The pulse duration was 20 ms, thus significantly longer than in C. Schmidt's experiment. According to C. Schmidt, the difference can be explained by the longer diffusion time of the W. Goll and P. Turowski's heater and the longer pulse duration which is larger than the maximum heat pulse duration corresponding

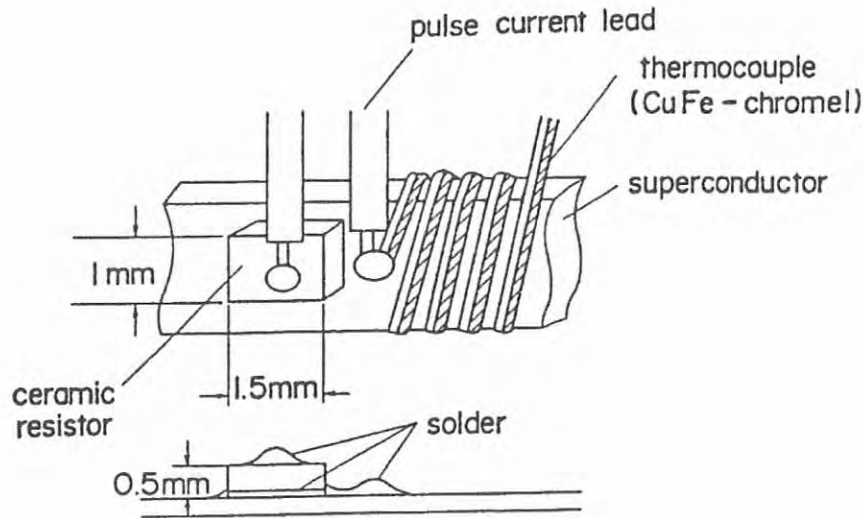


Figure II.6: Schematic drawing of ceramic resistor chip heater [23].

to the end of the quasi-plateau of the Minimum Quench Energy.

At the time, the experiment led by C. Schmidt was the most detailed. However, the estimation of the Minimum Quench Energy remained uncertain due to a lack of calibration of the heater. This is evidenced by the fact that the experimental results measured in adiabatic conditions were a factor 2 larger than the prediction of the corresponding numerical simulation. The simulation was thoroughly checked and cross-checked using independent codes, and no reason for such a discrepancy could be found. One possible explanation could be that the heater and its embedding epoxy resin were not simulated.

Because of the ease and the possibility of miniaturization of this technique, further experiments were performed with it. Thus, a year later, W. Nick *et al.* used a manganin wire of $50\ \mu\text{m}$ wound around 2 mm of a NbTi superconducting wire in the same bifilar way [25] (see Figure II.7, page 64). However, the heating wire was first glued to the sample with high thermal conductive resin and then covered by Stycast[®], again, to prevent direct helium cooling at the surface of the heater. The influence of the cooling environment on quench energies and propagation velocities were assessed on a NbTi wire and compared to a numerical simulation.

The same year, O.P. Anashkin *et al.*, tried similar measurements with constantan wires of different lengths: 1 mm, 3 mm and 10 mm (0.006 mm of diameter). Their goal was to study the behavior of various stabilized NbTi wires and to determine the influence of the length of the heated zone on the magnitude of the Quench Energy [26]. They showed that increasing the heater length brought the Minimum Quench Energy closer to the enthalpy necessary to heat the composite superconductor to its critical temperature. The pulse durations ranged from $3\ \mu\text{s}$ to $300\ \mu\text{s}$. For this range, no influence of the epoxy-silicone glue used to imitate the conditions of an impregnated winding was apparent. The data also showed that the magnitude of the Quench Energy decreases when the resistivity of the metallic stabilizer increases and its thermal conductivity decreases. This can be readily understood

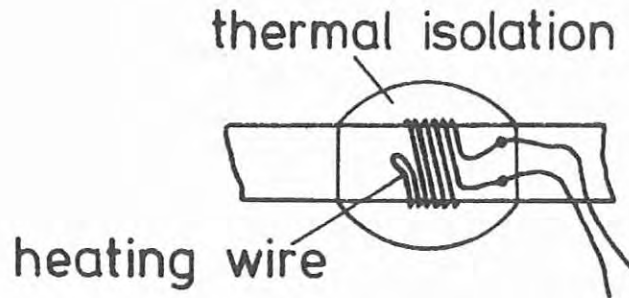


Figure II.7: Schematic of an ohmic wire [25].

when considering that the conduction cooling is reduced while the heat generation gets larger, thereby helping the temperature rise around the normal zone.

Most of the studies on stability concerned Low Temperature Superconductors (LTS). The reason is historical. LTS, such as NbTi and Nb₃Sn, have been discovered and commercialized in the late 1960's, long before ceramic based superconductors discovered in the late 1980's. However, the availability of High Temperature Superconductors (HTS) in long lengths has increased within the past decade. So, based on the experience acquired on LTS, a few experiments have been conducted on ceramic-based superconductors. In 2002, A. Sugawara *et al.* got a first glance at the development of normal zone transitions inside a manufactured HTS conductor cooled by solid Nitrogen [27]. The pulses were surprisingly long: between 10 s and 600 s. The range of pulse duration is far larger than from any reported experiments on the subject. It might be explained by the small power dissipation of the heater and the large thermal heat capacity of the materials at temperatures from 20 to 55 K. In 2003, C. Wu *et al.*, studied Bi2223/Ag multifilament tapes in nitrogen gas cooling at 77 K [28] [29]. They found that the magnitude of the Quench Energy was affected by the embedding and the insulation of the heater.

More recently, the superconducting properties of MgB₂ has been accidentally discovered, causing excitement in the applied superconductivity community. The first investigations on the magnitude of its Minimum Quench Energy and Normal Zone Propagation Velocity were carried out by M. Fu *et al.* on a Cu-Ni sheathed monofilament MgB₂ tape [30]. The results were compared to those of Low and High Temperature Superconductors. The Minimum Quench Energy was found to be larger than for NbTi or Nb₃Sn conductors, and significantly smaller than for Bi2223 and YBCO conductors. The heater was 2 cm long, which is longer than the Minimum Propagating Zone for most superconductors. Nevertheless, it appears that MgB₂ is likely to have a large Minimum Propagating Zone owing to its large thermal conductivity. It was approximatively calculated as 2 orders of magnitude larger than the Minimum Propagating Zone of NbTi or YBCO conductors in adiabatic conditions.

Manganin and Constantan wires are small and relatively easy to install on round wires. They have been broadly used in stability experiments. However, the necessity of epoxy embedding brings additional uncertainties on the measurement of the Minimum Quench Energy. So, epoxy volume and its porosity, plus the quality of

the binding between the ohmic wire and the samples are unknown parameters that can highly vary from one assembly to another.

Carbon paste heaters: In the 1990's, a vast campaign of experiments on superconducting wires and cables has been conducted within the framework of the LHC magnet Research and Development program. They included stability studies carried out at KEK (Japan) on NbTi Rutherford-type cables (A. Kimura [31] [32] and S.W. Kim's team [33]), who used a cured carbon paste spot heater of 3 mm long glued on one of the strands of a cable. The heater was covered by a copper strip, and the current flew through the paste and the strand. A few years later, N. Amemiya *et al.* [34] showed that the efficiency of the heater depended on the thermal properties of its thermal insulation as it was the case for heating wires. For fine measurements, it can cause large errors in the assessment of the Minimum Quench Energy. Carbon paste heaters are still applied in the studies of cable stability [35]. The reason for this is its ease of application on single strands bundled in a Rutherford-type cable.

Kapton[®] Sandwich heater: At Brookhaven National Laboratory, A.K. Ghosh *et al.*, pursued a series of characterizations of LHC cables [36] and single wires [37]. For their campaign of measurements, they covered strands and wires with Eccobond[®] 60L paste over a length of ~ 1 mm long at different locations. This compound gave the most reproducible resistance. Resistances of 1Ω to 5Ω were achieved by controlling the pressure applied on the heater during curing. The pulses were $20 \mu\text{s}$ to $500 \mu\text{s}$ long corresponding to the quasi-plateau of the Minimum Quench Energy. The dissipated energy was calculated by integrating over time the product of current and voltage across the heater. In contrast to past procedures, the samples were systematically quenched to reset the current distribution after each try.

In the case of single wire measurements, the variations of the Minimum Quench Energy per strands for the different heaters appeared to be in the 10 to 20% range. Further experiments were carried out on single strands at 4.2 K and 1.9 K as well [38]. The samples were mounted into a square-shaped groove and covered by a Kapton[®] tape (see Figure II.8, page 66). A drop of Eccobond[®] 60L paste was deposited on the sample through a small cutout in the tape (1 mm^2). A copper foil, covered by an additional Kapton[®] layer, overlapped the assembly. It was then slightly clamped with an Aluminum ring pressing the heater onto the sample. The results showed that the copper-to-superconductor ratio was the main parameter determining the stability margin of the strands. The Minimum Quench Energy increases with higher ratio. At low transport current, cooling parameters such as helium volume and fraction of wetted perimeter affect the stability whereas, at high transport current, the enthalpy of the conductor is the dominant factor. Consequently, at 1.9 K, the plot of the Minimum Quench Energy versus normalized current presents a kink corresponding to the enhancement of the stability margin at low transport current, below 80% of the critical current. A similar behavior was observed by D.E. Baynham, *et al.* (see section II.4.1, page 60). The variation in measured MQE's for the various heaters was estimated to be of the order of $\sim 20\%$. In one case, the variation reached a maximum of $\sim 50\%$. The reason for such a lack of reproducibility was attributed to the change in local cooling conditions and to the surface quality of the strands. P. Bauer suggested that the MQE results obtained with this technique were likely

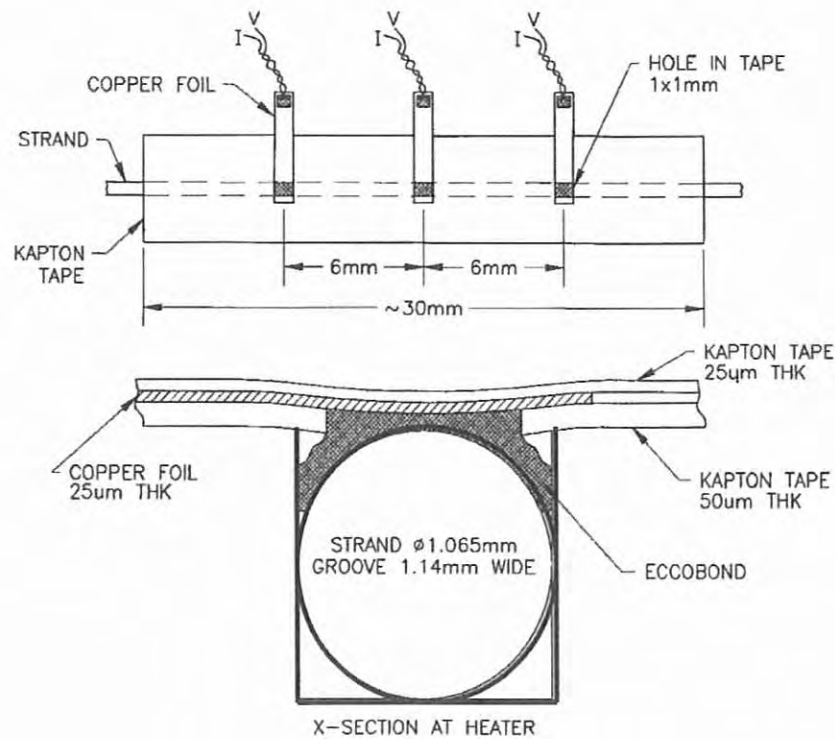


Figure II.8: Schematic of a Kapton[®] sandwich heater [38].

to reflect quasi-adiabatic conditions, *i.e.*, the sample was not sufficiently wetted by liquid helium.

Reproducibility of the measurements seemed to be good. However, the glueing of the heater onto the sample was difficult to control. Consequently, the contact resistance varied from heater to heater and may even vary during the measurements¹. An even better reproducibility may have been achieved with a better control of the contact. Positioning and maintaining of heaters onto samples proved to be difficult making this technique more complicated than the ones already described.

Clamped heaters and tip-heater: To address the main issue of controlling pressure and positioning, assemblies squeezing the heater together with the sample were tried. This idea was first tried on superconducting wires by K. Seo, *et al.* in the late 1990's [39]. The heater, resembling a ceramic chip (see section II.4.2, page 62), was made of a thin layer of carbon of $\sim 20 \mu\text{m}$ thick plastered on the superconducting wire and covered by a thin copper strip sputtered on a Kapton[®] tape. The diffusion time of such a thin setup was fast enough to measure the Minimum Quench Energy. Pulses ranging from few hundreds of microseconds to few tens of milliseconds were generated. To simulate adiabatic conditions, the whole assembly was cast in epoxy. The results obtained were compared to measurements done with an ohmic wire (see

¹This aspect will be discussed in chapter III (page 77) while studying charged point heaters.

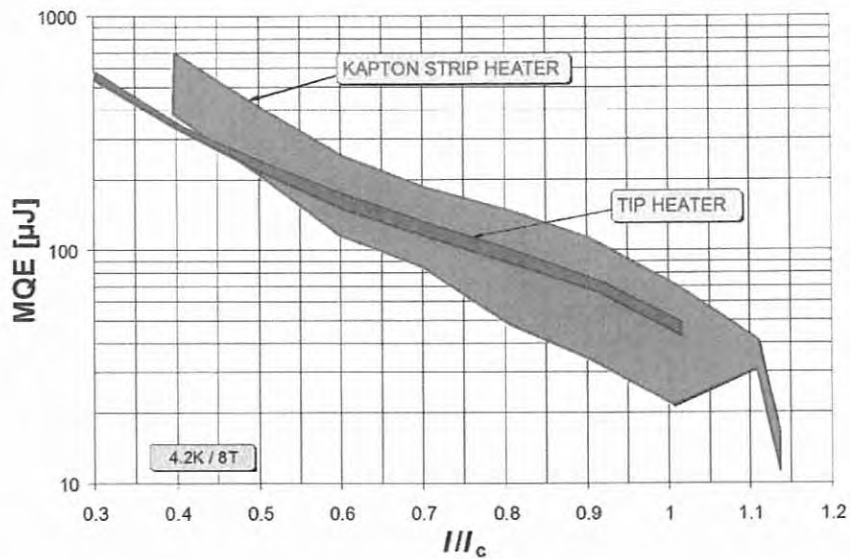


Figure II.9: Comparison of carbon paste heater and tip-heater reproducibilities (modified from the original [22]).

section II.4.2, page 62). The results showed that the clamped paste heater gave lower Minimum Quench Energies (below milli-Joules) than the heating wire. According to the authors, the thermal diffusion time of heat across the heater was too long for the measurement of the Minimum Quench Energy. The latter was calculated as the mean value between the minimum energy triggering a quench and the maximum energy allowing a recovery. The sensitivity of the measurements was relatively poor as differences of several percent existed between those energies.

Despite the complexity of the setup and the obvious improvement of the heater compared to the ohmic wire, it could not give full satisfaction. Indeed, the incertitudes on the contact resistance remained and may have been responsible for the poor sensibility of the measurements.

In the context of LHC cable and strand studies, an improvement of this technique, called clamp-heater was tried by P. Bauer [22]. The strand was squeezed between two Kapton[®] insulated stainless steel pieces in which the paste heater was located. Two screws mounted with springs allowed to control the pressure of the heater onto the wire. In spite of these efforts, the technique did not give reproducible results. Among difficulties, the change in contact resistance during the measurements could not be overcome. This first solution was then abandoned for an alternative and more successful one, the tip-heater [40] [41] (see Figure II.10, page 68). A cylindrical Maccor[®] tip of very small dimensions (a round tip of 0.6 mm of diameter for a length of 1.75 mm), sputtered with silver, was designed to receive a thin layer of charged paste (Epoteny[®] E300) on its tip. Two screws allowed to maintain the heater onto the sample. One of these screws was equipped with a spring. A better control of the applied pressure was achieved with a pressure up to 10 MPa. The pulse duration was of the order of 10 μ s. At first, a thermo-retractable sleeve was used to thermally insulated the sample around the heated zone. The author found

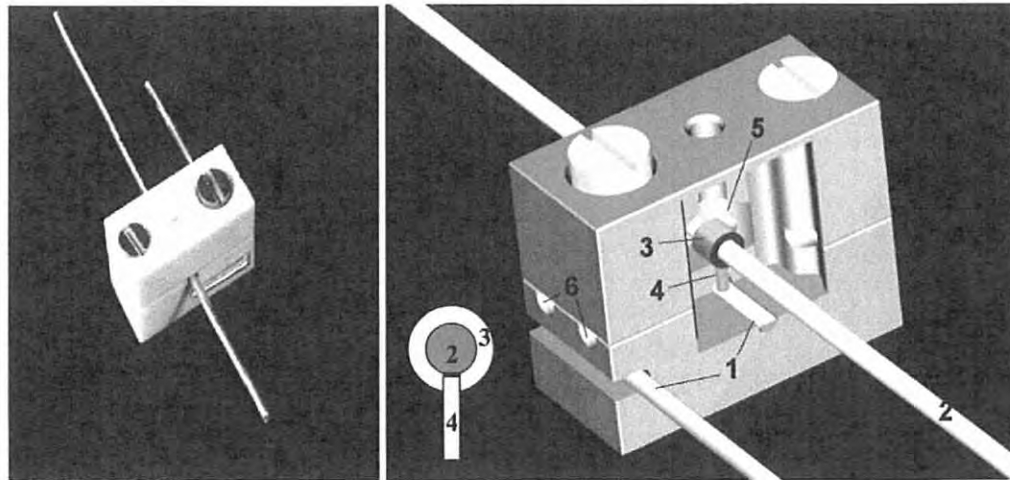


Figure II.10: Tip-heater [22]. Left is a picture of the whole assembly (7.5x16x13 mm) allowing the positioning and clamping of the tip-heater on wire samples. Right is a 3D view of this assembly:

- 1- Heater current lead.
- 2- NbTi sample.
- 3- Thermo-sleeve.
- 4- Tip of the heater.
- 5- Helium reservoir.
- 6- Helium channel.

The tip of the heater is squeezed between the sample and the heater current lead as depicted on the small sketch.

that its presence affected the Minimum Quench Energy without leading to truly adiabatic conditions. The results obtained were in fair agreement with A.K. Ghosh and K. Seo's results.

The tip heater gave numerous and interesting results with a reproducibility down to 10% (see Figure II.9, page 67). However, its fabrication is rather difficult and time consuming.

Although it was not experimentally calibrated, it has certainly been the most reliable and the most performant resistive heater ever made so far.

Strain gages: One of the first experiments on commercial HTS tapes dates back to the mid 1990's. S.B. Kim *et al.*, managed to characterize the behavior of Bi-2223/Ag single-core and multi-filament tapes undergoing a normal zone transition in self-field [42]. They used as heater a small strain gage glued to the silver stabilizer of the tape. The normal zone propagation velocity was found to be 1 to 3 orders of magnitude slower than the propagation velocity of LTS. The minimum heat pulses to initiate quenches were 3 to 4 orders of magnitude larger. These differences in orders of magnitude are the combinations of a remarkable critical temperature (around 110 K), a much larger heat capacity and a lower thermal conductivity. However, to converge to real adiabatic conditions, the sample must be long enough to eliminate the cooling influence of the cryocooler on the measurements. The thermal

properties of this family of superconductors differ wildly from LTS. Due to a large heat capacity and a low thermal conductivity, a hot spot, which barely expands, is likely to appear around the heater. So, in addition to a possible burnout of the sample, a large temperature gradient may develop along the voltage taps recording the normal zone expansion. Consequently, a non-negligible thermoelectric voltage may interfere with the measured signal, and it is necessary either to measure the voltage rises away from the heater or to take into account this phenomenon in the assessment of the normal zone propagation velocity. Although this slow normal zone propagation creates some difficulties, it gives the opportunity to measure in-situ the thermal runaway of the sample by the means of thermocouples. This measurement is almost impossible for LTS since the quench propagation velocity is far too rapid for the thermal time response of commercial thermal sensors. Sensors, with thermal response times in the range of tens of microseconds, would be required.

In 1998, S.B. Kim's experiment was adapted to measure transverse normal zone propagation velocities. A sandwich of one strain gage, Bi-2223/Ag tapes and Kapton[®] insulation tapes was slightly pressed by two Fiberglass Reinforced Plastic (FRP) blocks. For such a setup, the transverse normal zone propagation velocity appeared 1 to 2 orders of magnitude slower than the measured propagation velocity in the longitudinal direction.

Strain gage technology seems to be suitable for HTS characterizations because the conductors often present themselves as tapes. However, a series of stability measurements on CuNb reinforced Nb₃Sn conductors in liquid helium and in a vacuum has proved that such a technology may be applied to LTS wires as well. The ultimate goal was to design a safe, cryocooler-cooled, low temperature superconducting magnet [43]. The samples, covered by grease to avoid mechanical displacement, were separately wound on a FRP bobbin for liquid helium cooling conditions and on an aluminum nitride bobbin for adiabatic conditions [44][45][46]. A strain gage was glued with varnish on the surface of the samples. The heater was pulsed with durations between 500 μ s and 13 ms. The authors showed that the temperature margin is the relevant parameter to define the stability margin of the conductors in cryocooler-cooled conditions, while it is the heat generation due to Joule effect which prevails in liquid helium cooling conditions [47]. In vacuum, the conductor unconditionally quenches as soon as the sharing temperature is reached. In liquid helium, the cooling capacity of the helium pushes further the margin since it can absorb a part of the energy dissipated by Joule effect in the outer stabilizer.

Besides Bismuth-based conductors, one of the most promising HTS is YBCO. It has been recently available in suitable lengths (from several tens of centimeter to several tens of meters) to allow characterizations. The superconductor is grown on an insulated substrate and covered by additional layers of stabilizer and mechanical reinforcement. Very few studies on the normal zone propagation development have been led so far. In addition to the study presented in this document, a few other scientists such as A. Ishiyama *et al.*, worked on the subject [48]. They assessed Minimum Quench Energies at different temperatures: 55 K, 60 K and 65 K. The temperature was controlled using a cryocooler in a background magnetic field of 5 T. Since YBCO tapes show unevenness of the critical current along their length due to non-uniform material properties, the strain gage was located in the center of the tape and voltage taps were carefully soldered on both sides. The Minimum Quench Energy values were several orders of magnitude larger than in LTS.

Strain gages are the predominant heaters used to characterize HTS tapes. They are relatively simple to apply, but, need to be clamped on the sample to improve thermal contact. This operation appears always risky when one deals with fragile tapes such as YBCO conductors. The non-reinforced conductors are often covered by a very thin layer of silver stabilizer. This layer can be easily deformed, inducing defects in the superconductor. These defects can lead to a degradation of superconducting properties.

This technique, which has been successfully tried, is very similar to ohmic wires, and is characterized by the same issues (see section II.4.2, page 62).

II.4.3 Laser and diode laser

Publications relating the thermal interaction of Laser and commercial superconductors are not common in scientific and technical literature. They mainly concern theoretical studies on thin films [49], and the only available technical literature deals almost exclusively with superconducting switches.

At the end of the 1980's, an interesting experiment was led by T.L. Francavilla *et al.*. As part of their study of a NbN superconductor switch, they measured the level of radiant energy necessary to trigger a quench versus the percentage of normalized current density [50]. The losses due to the optics, the geometric factors and liquid helium scattering (bubbles and vortices) were estimated at 60% of the total incident light. A few tens of microJoule were necessary to quench the sample at 4.2 K in self-field.

In 1992, B. Cabrera reported a physics experiment using a YAG (based on $Y_3Al_5O_{12}$ crystals) and a diode laser to pulse energy through an optical fiber on a niobium thin film. One year later, F. Ayela *et al.*, showed the feasibility of a very fast switch using a fibered diode laser for SQUID applications. They pointed out the importance of the temperature control of the diode and the necessity to target precisely the surface of the superconductor to reduce the uncertainties on the measurements [51] [52].

Lasers and Diode Lasers have already been used in applied superconductivity. However, their use was restricted to a specific area revolving around thin film superconducting switches mainly for SQUID application. Surprisingly, nobody attempted to characterize commercial High or Low Temperature superconductors.

II.4.4 Summary of the review

This review has introduced to the reader various heater technologies. The reason for such numerous trials was a lack of reproducibility of the measurements and the difficulty to determine accurately the real amount of energy deposited onto the samples.

Each heater type is optimized for a particular application:

- inductive heaters: Cable-In-Conduit conductors and round wires,
- carbon paste heaters: wires, strands and Rutherford type cables,
- tip-heaters: exclusively wires and strands,
- strain gages and Clamped heaters: tapes, wires and strands.

Table II.3: Domain of applications of the different heaters and their main advantages/drawbacks.

Heater technologies	Usefulness	Advantages	Drawbacks
Induction coils	wire, conductors or cables of round geometry	calibration	larger than the MPZ, necessity of an metallic outer sheath to dissipate the magnetic energy
Carbon charged epoxies	any wires, conductors or cables	easy to apply, adaptability to any configurations	non calibrated, poor reproducibility of the measurements, difficulty to control the contact resistance and necessity to flow the current pulse through the sample
Tip-heater	round wires	very good reproducibility of the results	difficulty of the assembly, calibration, adaptability
Strain gages	tapes, and rectangular conductors and a few round conductors of a larger diameter compared to the dimensions of the strain gage	commercial product	calibration, adaptability, control of the bonding with the sample

covering a broad range of conductors. This variety gives the experimentalist the possibility of choosing among different heater technologies. As each of them shares advantages and disadvantages, the characteristics and limitations of the chosen heater have to be evaluated for the given geometry of the samples and the objectives of the study.

Table II.3 (page 71) gives a summary of the usefulness, advantages and drawbacks of these technologies.

II.5 Our choice of heater technologies

II.5.1 Low temperature superconductors

For our application, we decided to trigger quenches by the means of a diode laser and a small induction coil. A first experiment based on a tip heater was also carried out. This technology was appealing since it conjugated a relatively good reproducibility with a spatial extension and duration corresponding to actual localized transient disturbances. Unfortunately, numerous difficulties were encountered in the preparation of the heaters. The assembly adapted to a VAMAS-type sample holder

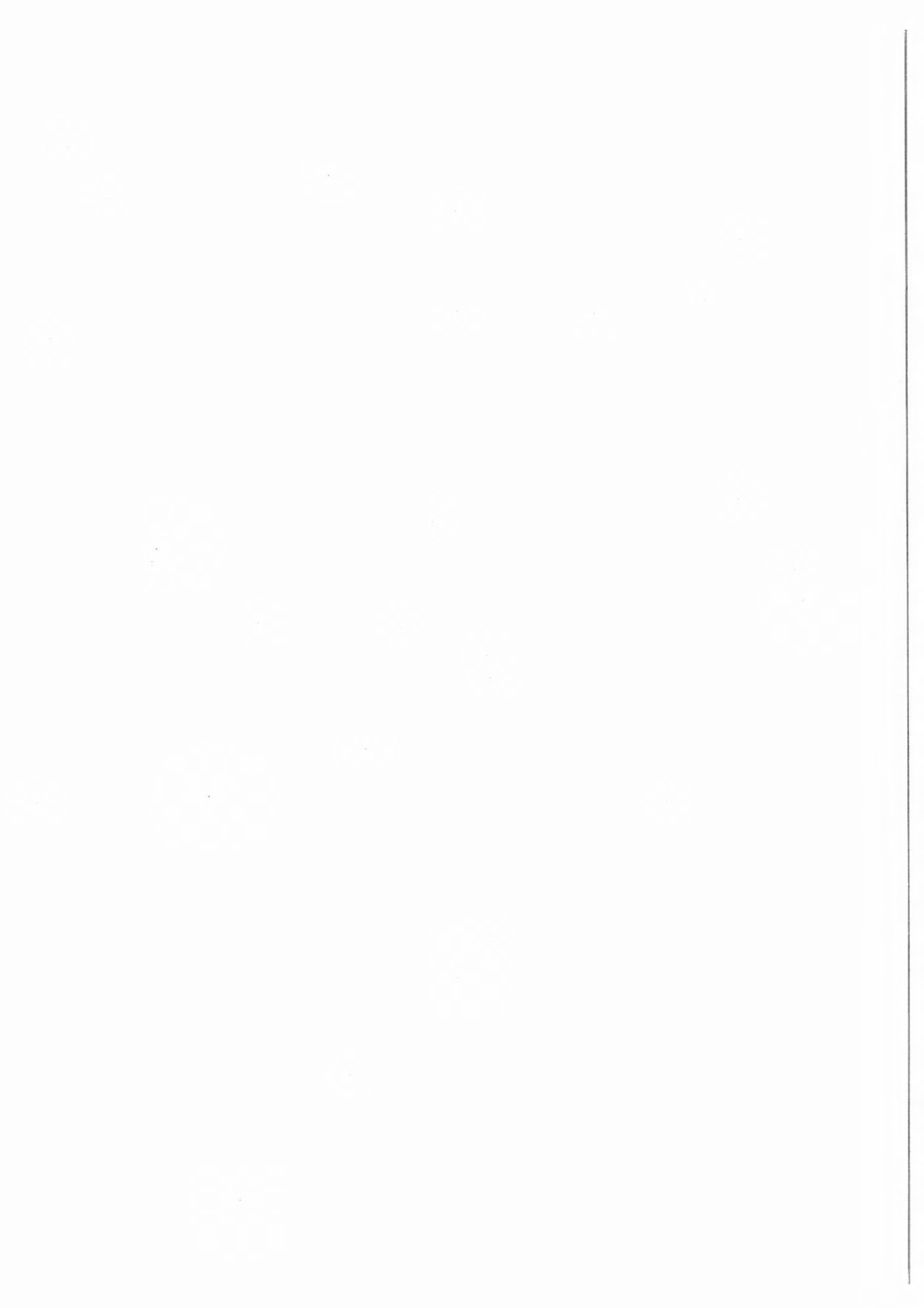
for critical current measurements was difficult to handle and the results were not reproducible in spite of various design modifications. After unsuccessful trials, we finally decided to abandon this technology to focus on laser and inductive heaters. Induction coils have already been used for stability characterizations induced by distributed spatial disturbances. However, a new design relying on a small coil of few millimeters long has been developed to characterize the response of the wires undergoing localized heat disturbances. On the other hand, laser heating has never been attempted. The best candidates among laser systems appeared to be diode lasers. They can supply more than 1 W of continuous power with a low electrical power consumption. Their miniaturization makes them very adaptable and practical for any experimental configurations.

Various issues were encountered with the induction coils. Their large inductances could not be accommodated by our power supply which made the estimation of the energy dissipated into the wire a very tedious task to manage. The exploitation of the voltage traces appeared also very difficult because of inductive voltage distorting the form of the voltage traces. Consequently, stability parameters such as the Quench Decision Time or Normal Zone Propagation Velocity could not be estimated. Continuous efforts are being carried out at CEA/Saclay to improve this technology. But in the context of this thesis, we will not discuss the induction coils further. On the contrary, we will concentrate on the diode laser which gave the most interesting and exploitable data. In particular, it appears as the most promising heater technology since it leads to reproducible data and can be calibrated.

II.5.2 High temperature superconductors

After a few trials using strain gages to trigger normal zone transitions in HTS conductors, we switched to an alternative system based on a NiCr wire. This wire was shaped into a zigzag pattern and glued onto the surface of HTS tapes. Such a system proved to be easier to prepare and a lot more reliable than strain gages. However, it suffers as well from a lack of calibration. At the time of the experiment, only a few preliminary tests had been carried out on the thermo-electric stability of HTS tapes. The literature was limited to a few articles on the study of Bi-2223 tapes. Then, our goal was to design a reliable experiment to carry out measurements in a vacuum at various background magnetic field.

This experiment is briefly described in the second part of this thesis (chapter VI, page 196). It has been further improved and recent results were presented by X. Wang *et al.* in 2004 [53].



Bibliography

- [1] Y. Iwasa. *Case Studies in Superconducting Magnets, Design and Operational Issues*. Plenum Press, New York, 1994.
- [2] B. Seeber, editor. *Handbook of Applied Superconductivity*, volume 2, pages 1213–1248. Institute of Physics Publishing, 1998.
- [3] G. de Rijk, M. Bajko, M. Cornelis, M. Durante, P. Fessia, J. Miles, M. Modena, G. Molinari, J. Rinn, F. Savary, K. Schirm, F. Simon, D. Tommasini, T. Tortschanoff, and J. Vlogaert. Status Report on the LHC Main Magnet Production. *IEEE Transactions on Applied Superconductivity*, 15(2), June 2005.
- [4] A. Devred *et al.* *Quench Localization in Full-Length SSC R&D Dipoles*, pages 73–83. Plenum Press, New York, 1989.
- [5] S.L. Wipf. Stability and Degradation of Superconducting Current Carrying Devices. Technical report, Los Alamos Scientific Laboratory, 1978. Report LA-7275.
- [6] A.H. Wilson. *The theory of metals*. Cambridge at the university press, 1958.
- [7] T.P. Sheahen. *Introduction to High-Temperature Superconductivity*. Plenum press, New York, 1994.
- [8] J. Nagamatsu, N. Nakagawa, T. Muranaka, Y. Zenitani, and J. Akimitsu,. Superconductivity at 39 K in magnesium diboride. *Nature*, 63-64(410):1541–1543, March 2001.
- [9] D.N. Nguyen, and Q.M. Doan. Superconductivity in MgB₂. <http://garnet.acns.fsu.edu/~dnn9636/hw15.pdf>.
- [10] E. Bauer, Ch. Paul, St. Berger, S. Najumdar, H. Michor, M. Giovannini, A. Saccone, and A. Bianconi. Thermal conductivity of superconducting MgB₂. *Journal of Condensed Matter*, 13:L487–L493, 2001.
- [11] B.J. Maddock, G. James, and W.T. Norris. Superconductive composites: heat transfer and steady state stabilization. *Cryogenics*, pages 261–273, August 1969.
- [12] L. Dresner. *Stability of Superconductors*. Plenum Press, New York, 1995.
- [13] M.N. Wilson and Y. Iwasa. Stability of superconductors against localized disturbances of limited magnitude. *Cryogenics*, pages 17–25, January 1978.
- [14] M.N. Wilson. *Superconducting Magnets*, pages 79–84. Oxford University press, 1983.

BIBLIOGRAPHY

- [15] F.P. Juster. Etudes de stabilité: influence du RRR et de la porosité. Technical report, CEA, June 1998. Note CEA/Saclay DSM/DAPNIS/SACM: 5-2650N-1300 003 98.
- [16] C. Schmidt. Review of the steady state and transient heat transfer in pool boiling helium. *International Institute of Refrigeration, Commission A1/2-Saclay (France)*, (6):17, 1981.
- [17] M.N. Wilson. *Superconducting Magnets*, pages 204–208. Oxford University press, 1983.
- [18] D.E. Baynham, D.A. Cragg, R.C. Coombs. Transient Stability of LHC Strands. *IEEE Transactions on Applied Superconductivity*, 9(2):1109, June 1999.
- [19] W. Goll and P. Turowski. Quenching of technical superconductors by heat and magnetic field pulses. *Cryogenics*, 18(2):103, February 1978.
- [20] D.E. Baynham, V.W. Edwards, M.N. Wilson. Transient Stability of High Current Density Superconducting wires. *IEEE Transactions on Magnetics*, 17(1):732, January 1981.
- [21] K. Seo, K. Takahata, T. Mito, H. Hayashi, K. Terazono, T. Semba and K. Miyashita. Calibration of Inductive Heater for Stability Test of Cable in Conduit Conductor. submitted at the Applied Superconductivity Conference, October 2004.
- [22] P. Bauer. *Stability of Superconducting Strands for Accelerator Magnets*. PhD thesis, Technische Universität Wien, 1998.
- [23] K. Yoda and M. Morita. Minimum Quench Energy measurements of NbTi wires using a small ceramic heater. *IEEE Transactions on Magnetics*, 27(2):2159, March 1990.
- [24] C. Schmidt. The induction of a propagating normal zone (quench) in a superconductor by local energy release. *Cryogenics*, 18(10):605, October 1978.
- [25] W. Nick, H. Krauth, G. Ries. Cryogenic stability of composite conductors taking into account transient heat transfer. *IEEE Transactions on Magnetics*, 15(1):359, January 1979.
- [26] O.P. Anashkin, V.E. Keilin, V.V. Lyikov. Stability of Compound superconductors under localized heat pulses. *Cryogenics*, 19(2):77, February 1979.
- [27] A. Sugawara, H. Isogami, B.J. Haid, Y. Iwasa. Beneficial effect of solid nitrogen on a BSCCO-2223/Ag composite tape subjected to local heating. *Physica C*, 372-376:1443–1446, 2002.
- [28] C. Wu, Z. Bai, J. Li, J. Wang. Minimum quench energy studies on Bi-2223/Ag tape operating at nitrogen atmosphere. *Physica C*, 386:162–165, 2003.
- [29] C. Wu, Z. Bai, J. Li, J. Wang. Normal-zone propagation velocities in Bi-2223/Ag superconducting multifilament tape. *Physica C*, 386:166–169, 2003.

- [30] M. Fu, X. Xu, Z. Jiao, H. Kumakura, K. Togano, L. Ding, F. Wang, J. Chen. Minimum quench energy and normal zone propagation velocity in MgB₂ superconducting tape. *Physica C*, 402:234–238, 2004.
- [31] A. Kimura, N. Kimura, Y. Makida, A. Terashima, T. Shintomi, H. Hirabayashi, Y.Z. Lei. Influence of Curing on AC Losses of Cables for Superconducting Accelerator Magnets. *IEEE Transactions on Magnetism*, 30(4):2515, July 1994.
- [32] A. Kimura, S.W. Kim, N. Kimura, Y. Makida, T. Shintomi, H. Hirabayashi, T. Mito, A. Iwamoto, J. Yamamoto. Stabilities of the Rutherford with Cu Matrix and CuMn Barrier. *IEEE Transactions on Applied Superconductivity*, 5(2):385, June 1995.
- [33] S.W. Kim, A. Kimura, T. Shintomi, N. Kimura, Y. Makida, H. Hirabayashi, T. Mito, A. Iwamoto, J. Yamamoto. Experimental Studies on Stabilities of Rutherford Cables for Superconducting Accelerator magnets. *IEEE Transactions on Magnetism*, 32(4):2784, July 1996.
- [34] N. Amemiya, H. Yonekawa, N. Tsuchioka, O. Tsukamoto. Experimental Study on Current Re-Distribution and Stability of Multi-Strand Superconducting Cables. *IEEE Transactions on Applied Superconductivity*, 7(2):943, June 1997.
- [35] A. Kawagoe, F. Sumiyoshi, T. Mito, T. Kawashima. Compact stranded superconducting conductors with both low ac loss and high stability II. Experiment to confirm fundamental performance. *Cryogenics*, 44:623–630, 2004.
- [36] A.K. Gosh, W.B. Sampson, S.W. Kim, D. Leroy, L.R. Oberly, M.N. Wilson. Stability Measurements on Cored Cables in Normal and Superfluid Helium. *Physica C*, 310:335, 1998.
- [37] A.K. Gosh, W.B. Sampson, M.N. Wilson. Minimum Quench Energy of Rutherford Cables and Single Wires. *IEEE Transactions on Applied Superconductivity*, 7(2):954, June 1997.
- [38] A.K. Gosh, W.B. Sampson, P. Bauer, L. Oberli. Minimum Quench Energy Measurements on Single Strands for LHC Main Magnets. *IEEE Transactions on Applied Superconductivity*, 9(2):252, June 1999.
- [39] K. Seo, M. Morita, S. Nakamura, T. Yamada, and Y. Jizo. Minimum Quench Energy Measurement for Superconducting Wires. *IEEE Transactions on Magnetism*, 32(4):3089, July 1996.
- [40] P. Bauer, R. Wolf, L. Oberli, M.N. Wilson. Minimum Quench Energies of LHC Strands. *IEEE Transactions on Applied Superconductivity*, 9(2):1137, June 1999.
- [41] P. Bauer, J. Donnier, L. Oberli. Tip Heater for Minimum Quench Energy Measurements on Superconducting Strands. *IEEE Transactions on Applied Superconductivity*, 9(2):1141, June 1999.
- [42] S.B. Kim, Y. Ueno, A. Ishiyama. Experiment and Numerical Analysis of Normal Zone Propagation Properties in Ag Sheathed Bi-2223 Superconducting Tapes. *IEEE Transactions on Magnetism*, 32(4):2822, July 1996.

- [43] T. Kurusu, M. Ono, S. Hanai, M. Kyoto, H. Takigami, H. Takano, K. Watanabe, S. Awaji, K. Koyama, G. Nishijima, K. Togano. A cryocooler-cooled 19 T superconducting magnet with 52 mm room temperature bore. *IEEE Transactions on Applied Superconductivity*, 14(2):393–396, 2004.
- [44] T. Kaneko, T. Seto, T. Nanbu, S. Murase, S. Shimamoto, S. Awaji, K. Watanabe, M. Motokawa, T. Saito. Stability of Nb₃Sn Wires with CuNb Reinforced Stabilizer on Cryocooled Superconducting Magnet. *IEEE Transactions on Applied Superconductivity*, 10:1235, March 2000.
- [45] K. Watanabe, S. Awaji, M. Motokawa, T. Kaneko, T. Seto, S. Murase, S. Shimamoto, T. Saito. Quench behavior of Nb₃Sn wires in a cryocooled superconducting magnet. *Advances in Cryogenics Engineering*, 46:951, 2000.
- [46] S. Murase, T. Murakami, T. Seto, S. Shimamoto, S. Awaji, K. Watanabe, T. Saito, G. Iwaki, S. Meguro. Normal Zone Propagation and Quench Characteristics of Nb₃Sn Wires with Jelly-Roll and In-Situ Processed CuNb Reinforcements. *IEEE Transactions on Applied Superconductivity*, 11:3627, March 2001.
- [47] T. Yamamoto, Kenji Watanabe, S. Murase, G. Nishijima, Kazuo Watanabe, A. Kimura. Thermal stability of reinforced Nb₃Sn composite superconductor under cryocooled conditions. *Cryogenics*, 44:687–693, 2004.
- [48] A. Ishijama, M. Yanai, T. Morisaki, H. Ueda, Y. Shiohara, T. Izumi, Y. Lijima, T. Saitoh. Normal transition and Propagation Characteristics of YBCO Tape. *IEEE Transactions on Applied Superconductivity*, 15(2):1659–1662, 2004.
- [49] L.R. Testardi. Destruction of Superconductivity by Laser Light. *Physical review B*, 4(7):2189, October 1978.
- [50] T.L. Francavilla, H.H. Nelson, A.P. Baronavski, S.A. Wolf, D.U. Gubser. Further Studies of a Laser quenched superconducting opening switch. *IEEE Transactions on Magnetics*, 25:1996, March 1989.
- [51] F. Ayela, J.L. Bret, J. Chaussy. High frequency thermal modulation of superconducting NbTi thin film by use of laser diode. *Cryogenics*, 34(7):597, March 1994.
- [52] F. Ayela, J.L. Bret, J. Chaussy. Absolute magnetometer based on the high-frequency modulation of the kinetic inductance of a superconducting thin film. *Journal of Applied Physics*, 78(2):1334, July 1995.
- [53] X. Wang, R.C. Caruso, M. Breschi, G. Zhang, U.P. Trociewitz, H.W. Weijers, and J. Schwartz. Normal Zone Initiation and Propagation in Y-Ba-Cu-O Coated Conductors with Cu Stabilizer. *IEEE Applied Superconductivity*, 15(2):2586–2589, 2005.

Chapter III

Preliminary LTS experiment using a carbon point heater

Contents

III.1 LHC-type NbTi wire samples, batch NbTi-1	78
III.1.1 Overview on LHC-type Cu/NbTi multifilament composite wire	78
III.1.2 Description of samples	78
III.1.3 Critical current measurements on batch NbTi-1	79
III.2 Experimental setup incorporating a point heater	80
III.2.1 Description of point heaters	80
III.2.2 Description of the experimental setup	82
III.2.3 Heater holder mounted on VAMAS-type mandrel	82
III.3 A few results on contact resistance	86
III.3.1 Presentation of the experimental protocol	86
III.3.2 Comparisons between contact resistance and applied pressure	87
III.3.3 Evolution of the contact resistance over a series of stability tests	90
III.3.4 Conclusion on contact resistance measurements	90
III.4 Voltage trace recordings and phenomenology of the nor- mal zone transition	92
III.5 Results on Quench Energies	97
III.5.1 Estimation of the Quench Energy	97
III.5.2 Quench Energy measurements at a given contact resistance	97
III.5.3 Quench Energy at different contact resistances	99
III.6 Conclusions on carbon paste point heaters	101

THIS CHAPTER describes a preliminary experimental setup used to study the stability of superconducting wires undergoing a localized transient heat disturbance. The setup is based on a VAMAS-type sample holder and the quench precursor is simulated by a charged point heater pressed onto a superconducting wire sample.

Various difficulties were encountered, which were assumed to be related to the lack of control of the contact resistance between heater and sample.

This experiment outlined the issues related to resistive heaters and led to the design of a new experimental setup which will be described in the subsequent chapter IV (page 103).

III.1 LHC-type NbTi wire samples, batch NbTi-1

III.1.1 Overview on LHC-type Cu/NbTi multifilament composite wire

Our first issue was to determine what kind of superconducting multifilament composite wires would be the best candidate to validate our experimental setup. Among the various superconductors available on the market, LHC-type NbTi wires appeared as the best choice. We implicitly assumed that their various physical properties have been well-established after being thoroughly studied in the framework of the ongoing Large Hadron Collider (LHC) project at CERN. LHC-type, Cu/NbTi, multifilament composite wires were designed to meet the requirements of high current density dipole and quadrupole magnets. They are made-up of thousands of NbTi filaments surrounded by a low resistivity OFHC-copper stabilizer. Filaments of about $6\ \mu\text{m}$ in diameter are distributed over the entire wire cross-section to reduce flux jumps (see Figure III.1, page 79). Thermal and mechanical processes [1], first studied at the university of Wisconsin at Madison in the early 1980's, are now mastered by several manufacturers around the world. They yield long enough batches of high current density wires with a low breaking rate. These batches are used to form cables which are subsequently wound into high field magnets [2].

Despite the abundance of engineering parameters, the detailed micro-structure of the wires is kept secret. Each manufacturer has its own process, designed to achieve the best performances at the optimum cost.

III.1.2 Description of samples

For our application, two batches of LHC-02-type Cu/NbTi multifilament composite wires were supplied by Alstom/MSA¹. LHC-type NbTi wires used in magnets are generally tinned. In our experiment, we only relied on bare wires.

These batches were respectively named NbTi-1 and NbTi-2². Samples NbTi-1 were wound on VAMAS-type sample holders for transport current and stability characterizations using a resistive heater. Samples NbTi-2 were assembled on the new experimental setup for which a diode laser was used as heater. These samples and the new experimental setup are described in chapter IV (page 103).

¹Alstom/MSA is the leading subcontractor of CERN and was awarded about 50% of the total contract of LHC cables.

²We identified the samples from the name of their original batch. For example, samples NbTi-1 were cut from batch NbTi-1, and so on.

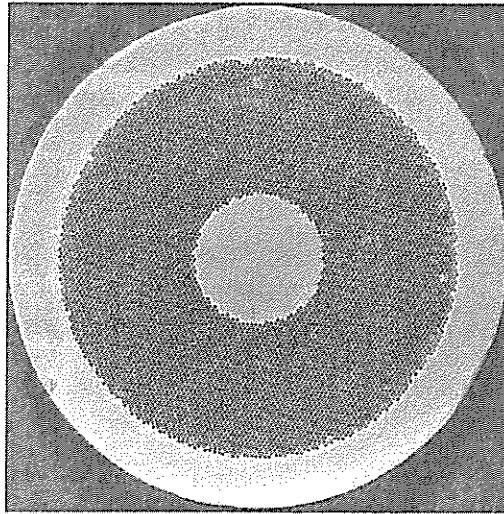


Figure III.1: Cross-sectional view of a generic LHC-type Cu/NbTi multifilament composite wire used in accelerator magnet technology (courtesy Alstom/MSA).

Table III.1: Salient parameters of NbTi-1 wires.

Diameter	0.825 mm
Twist pitch (filaments)	~15 mm
Ratio: Cu/Sc	1.87
RRR	187
Critical current density at 7 T, 4.2 K, J_C	1570 A/mm ²

No special treatment was applied on samples NbTi-1. Their salient parameters are given in Table III.1 (page 79).

III.1.3 Critical current measurements on batch NbTi-1

Critical current measurements have been performed on NbTi-1 samples at various background magnetic flux densities. The critical current was measured anew before each stability test. Then, the transport current was fixed as a percentage of this measured critical current for stability tests.

All the characterizations undergone on LHC-type wires were conducted at 4.2 K in liquid helium at atmospheric pressure. Figure III.2 (page 80) shows the results of the measurements. No error bars are reported since the error was inferior to 1%.

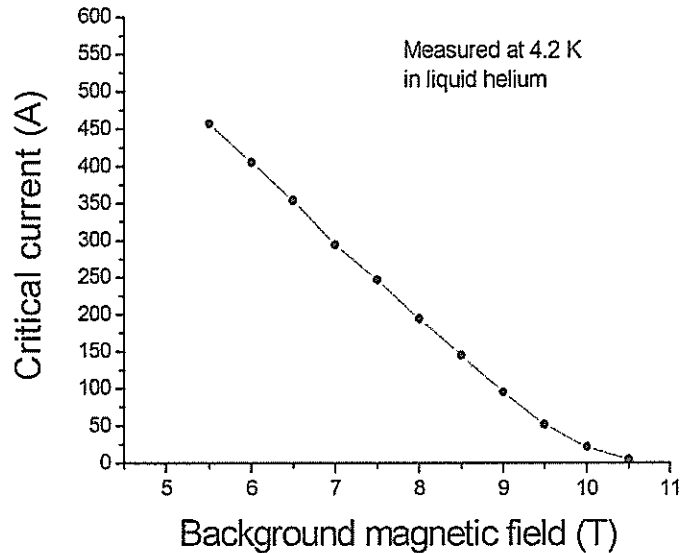


Figure III.2: Critical current versus background magnetic flux density at 4.2 K in liquid helium and atmospheric pressure for samples NbTi-1.

III.2 Experimental setup incorporating a point heater

This section introduces the preliminary results obtained with charged point heaters in addition to the nitty-gritty difficulties related to such a technology.

Their design was inspired from a mix concept between the tip-heater and the Kapton[®] sandwich heater.

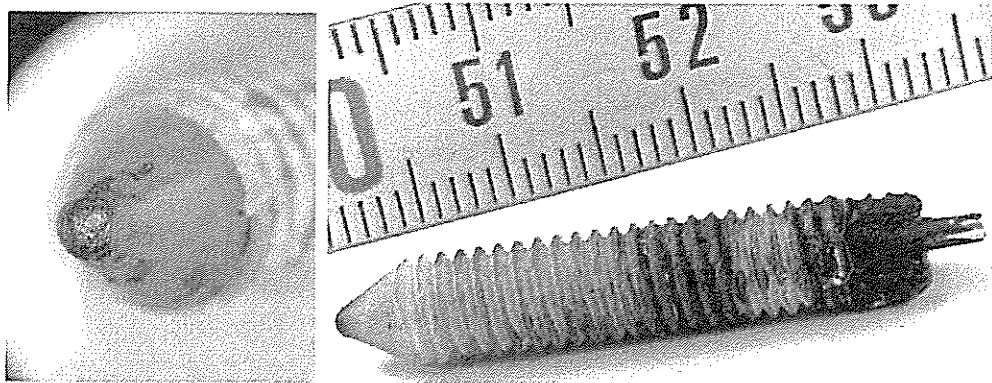
In this work, our primary objective was to achieve a good reproducibility of the contact resistance between samples and heaters. Indeed, we assumed a priori that it would give a better reproducibility of the Quench Energy measurements. So, a particular experimental setup was developed to adjust the contact pressure and consequently the value of the contact resistance. This contact resistance was expected to range from tens of milli-Ohms to hundreds of milli-Ohms at low temperature at low temperature.

A few tests have been carried out on the contact resistance to estimate its degradation in time during the stability experiments or its relationship with the values of Quench Energies. In addition, a series of Quench Energy measurements, at pulse durations ranging from 50 μ s to 1.5 ms, have been carried out to unveil the pseudo-plateau of the Minimum Quench Energy.

III.2.1 Description of point heaters

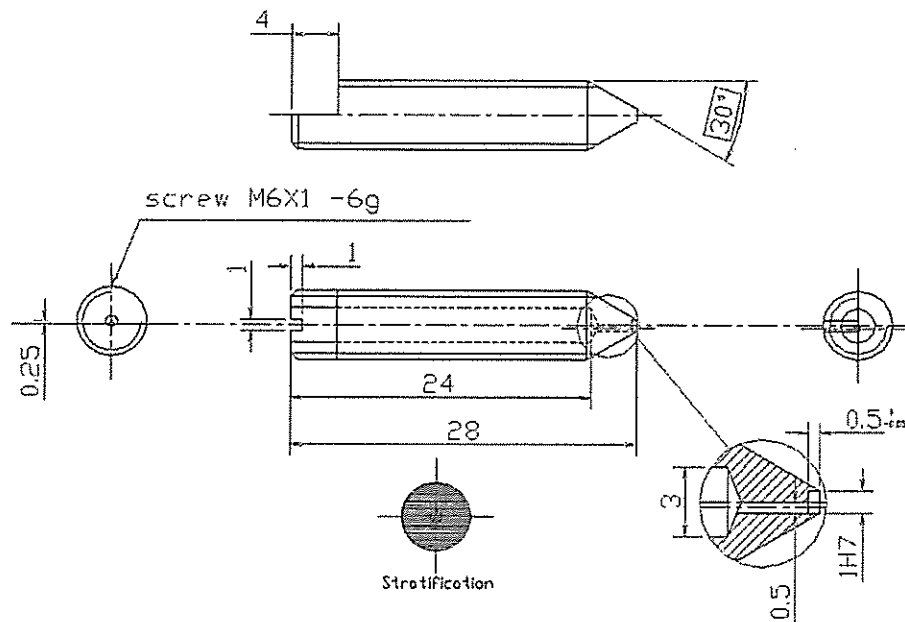
In this preliminary work, a series of heaters was designed on the basis of the tip and the Kapton[®] sandwich heaters [4] [5]. A small hollow screw of 28 mm long and 6 mm in diameter, made up of G-10, was slightly voided at its tip to receive a little drop of carbon filled epoxy paste adhesive, Eccobond[®] 60L (Emerson & Cuming).

III.2. EXPERIMENTAL SETUP INCORPORATING A POINT HEATER.



(a) Tip of the charged point heater.

(b) Charged point heater.



(c) Cad drawing.

Figure III.3: Pictures of charged point heater 2: (a) tip of the heater covered with Eccobond[®] 60L, (b) Picture of the hollow G-10 screw, inside which is glued a copper wire soldered to a small connector. (c) Cad drawing of the G10 screw holding the charged resin [3].

Table III.2: Contact resistances of charged point heaters at 4.2 K.

heater 1	unused
heater 2	failed
heater 3	failed
heater 4	1.7 Ω
heater 5	5 to 55 m Ω
heater 6	failed
heater 7	15 Ω

A copper wire of 0.2 mm in diameter, on which was soldered a connector, was inserted into the screw and glued with Stycast[®] 2850FT (see Figure III.3, page 81). A little section of it was previously painted with silver lac to improve the electrical contact with the charged epoxy paste. The wire was long enough to come out at the pit of the small hole. This hole, having a diameter of 1 mm and a depth of 0.5 mm, was filled up with the charged epoxy paste. Finally, the whole assembly was cured for 24 hours at room temperature. The heater, when fully pressed onto the sample, led to a contact surface of 0.79 mm² at least.

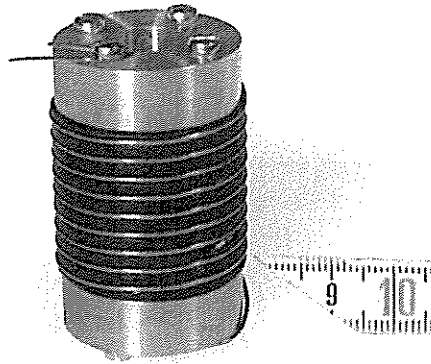
About ten heaters have been made. However, most of them did not lead to actual measurements as they burnt out either during the contact resistance measurements or the stability tests. The only exception was heater 7, which could not give exploitable data because of its too large resistance at 4.2 K. The power supply, used to feed the heaters, was not powerful enough to supply pulse currents to loads over a few Ohms. Table III.2 summarizes the average contact resistances measured at 4.2 K. The reliability of the technology appears rather poor. Nevertheless, a few heaters, for which the value of the average contact resistance is given, have been used in stability characterizations.

III.2.2 Description of the experimental setup

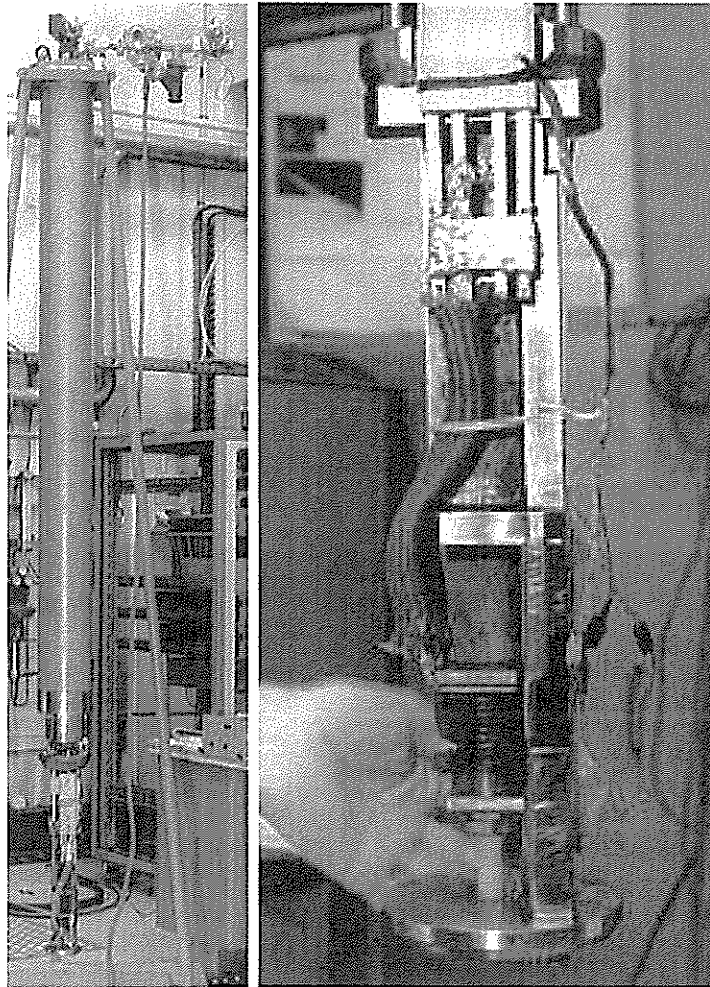
At the time, the stability study was carried out in the cryostat GELOTTE. It was originally used to measure the critical currents of NbTi and Nb₃Sn wires at different background magnetic flux densities ranging from 5 to 12 T and bath temperatures of 4.2 K and 1.8 K [6]. Bare wire samples, from batch NbTi-1 having a length of 1.1 m, were tightly wound in the groove of a graphite coated TiAlV mandrel according to the Versailles project on Advanced MAterials and Standards (VAMAS) recommendations [7]. Figure III.4 (page 83) details the entire probe (Figure III.4(b)), and the sample holder (Figure III.4(c)) at the bottom of which was located the mandrel (Figure III.4(a)).

III.2.3 Heater holder mounted on VAMAS-type mandrel

On the mandrel, we adapted a heater holder, which was slightly modified during the different series of stability tests [3]. Basically, no mechanical modifications were done on the different parts of it. However, two different assembly procedures were applied. These assemblies are subsequently named Assembly 1 and 2.



(a) VAMAS-type mandrel.



(b) Entire probe.

(c) Sample holder.

Figure III.4: Pictures of the experimental setup: (a) copper rings and titanium alloy barrel, onto which a multifilament composite wire is wound, (b) one of the two probes and (c) zoomed view of the sample holder located at the bottom of the probe.

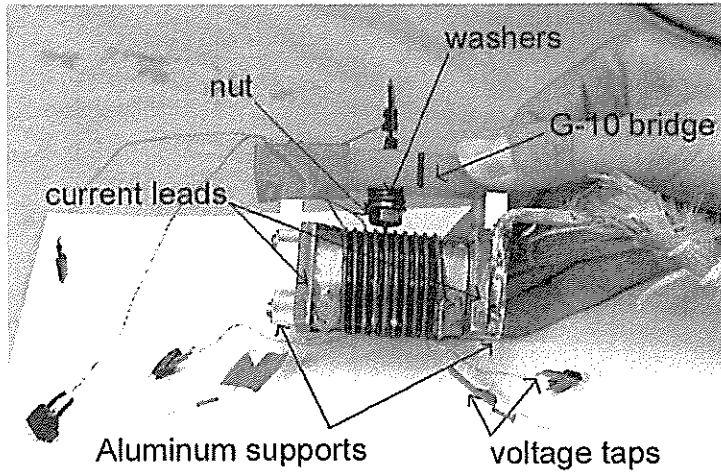


Figure III.5: Picture of the heater holder mounted on a titanium alloy mandrel (assembly 1). The tip of the charged point heater is pressed onto the sample at the center of the mandrel.

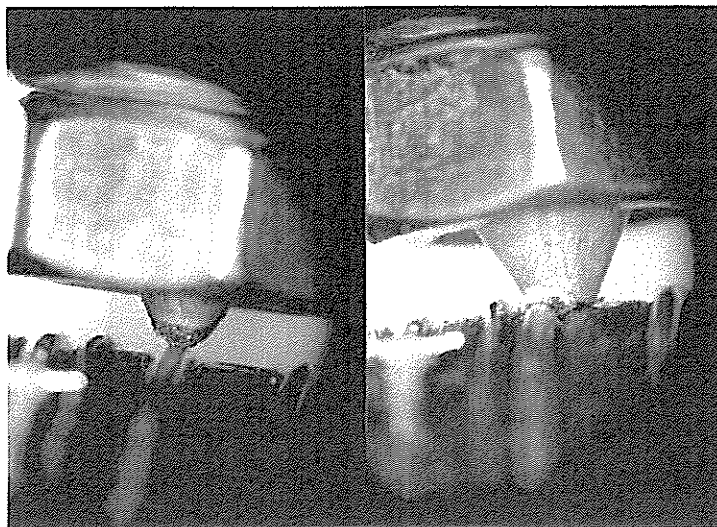


Figure III.6: Zoomed views of the tip of heater 2: left, the heater is simply positioned and no pressure is applied ; right, the heater, at its final position (strongly pressed onto the sample), does not fully cover the sample despite its large contact area compared to the sample.

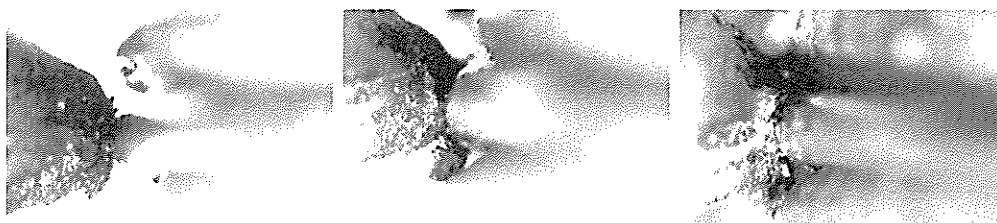


Figure III.7: From left to right, three different pictures taken while heater 5 was pressed onto the sample. The tip of the heater remains fully in contact with the sample throughout the manipulation.

Assembly 1: Figure III.5 (page 84) shows Assembly 1. Two aluminum rings, supporting a G-10 bridge, were screwed on each current lead of the sample. The G-10 bridge was drilled at its center and a metallic pin was inserted by force to guide the charged point heater. Oblong holes were machined at the extremities of the bridge to position accurately the tip of the heater with respect to the sample. In this first assembly, the heater was radially pressed onto the wires owing to a single nut stacking a set of 6 copper-beryllium (CuBe) washers³ (see Figure III.5, page 84). These washers are slightly conical and show a remarkable mechanical elasticity at low temperatures. If they are assembled up side down, the whole stack of washers act as a spring. In this configuration, it can compensate the differential thermal shrinkage of the various parts of the assembly by springing back the heater onto the sample during the cooling down of the experiment.

However, this first assembly procedure did not appeared convenient. Indeed, the tip of the heater tended to slide off the surface of the sample with increasing contact pressure (see Figure III.6, page 84). It made the mounting of heaters onto the sample a tedious task and led to inaccuracy in the measurements as both titanium mandrel and sample were heated at once. Therefore, a second assembly procedure was developed to address this issue.

Assembly 2: A simple modification of the mounting procedure allowed to solve the previous issue. Indeed, by first attaching the heater to the G-10 bridge and then installing washers between this bridge and the aluminum rings and, finally, by pressing the whole assembly onto the sample, the maintaining and guiding of the heater was greatly improved. No axial rotation was permissible any more and ensuing tip degradations were prevented (see Figure III.7, page 85) [8].

In the subsequent subsections, we will present data on heaters 2, 4 and 5. For the first two heaters, the former procedure to mount heaters onto samples was applied. For the last heater, we used the newest procedure. Table III.3 (page 86) summaries the different heaters that were used with their corresponding assembly.

³Supplied by Scherdel (Germany) under the name of Belleville disk springs.

Table III.3: The different heaters used in the experiment and their corresponding assembly.

heater 2	Assembly 1
heater 4	Assembly 1
heater 5	Assembly 2
heater 7	Assembly 2

III.3 A few results on contact resistance

Before concentrating on stability results, we shall first introduce some results obtained on contact resistance in our experimental setup.

III.3.1 Presentation of the experimental protocol

Figure III.8 (page 87) shows schematically the electrical circuitry used to assess the average contact resistances between charged epoxies and samples. As depicted, the contact resistance, R_{CR} , was estimated as the ratio of voltage drop, V_{CR} , and the DC current, I_{CR} , flowing through the heater. The voltage, V_{CR} , is taken between a voltage tap placed on the connector at the heater top and another one soldered to the wire downstream from the heater. We previously checked that the total resistance of the copper stabilizer plus the resistance of the electric wire glued into the G-10 screw were negligible compared to the heater resistance. It was evaluated between 1 m Ω and 2 m Ω at 4.2 K. For most of the cases, we could neglect this total resistance. However, there was one exception: heater 5, for which a bottom resistance of about 5 m Ω was achieved. Therefore, a correction to the average contact resistance had to be done.

The contact resistance was estimated as follow:

$$R_{CR} = \frac{V_{CR}}{I_{CR}} \quad [\Omega] \quad (\text{III.1})$$

Measurements were carried out at 293 K and 77 K, where most of the thermo-mechanical deformations have already taken place. The average contact resistance was calculated as the mean value of measurements at various I_{CR} currents. After the measurements, the electrical copper wire could be slightly visible through the resin. So, this wire may have been directly in contact with the sample during the tests.

In addition to average contact resistance, the corresponding applied pressure exerted on the heater versus the compressional strain per washer were assessed. This compressional strain per washer refers here to the relative change in height of the entire set of washers divided by the number of washer. The contact pressure was roughly calculated from the average force applied onto the whole stack of washers at 293 K divided by the surface of the tip of the heater ($\sim 0.79 \text{ mm}^2$). Indeed, due to the difficulties to measure accurately the compressional strain of the set of washers, the errors on the estimation of the contact pressure can exceed 30%. The average applied force was estimated by confronting the compressional strain per washer to their mechanical stress-strain characteristics provided by the manufacturer.

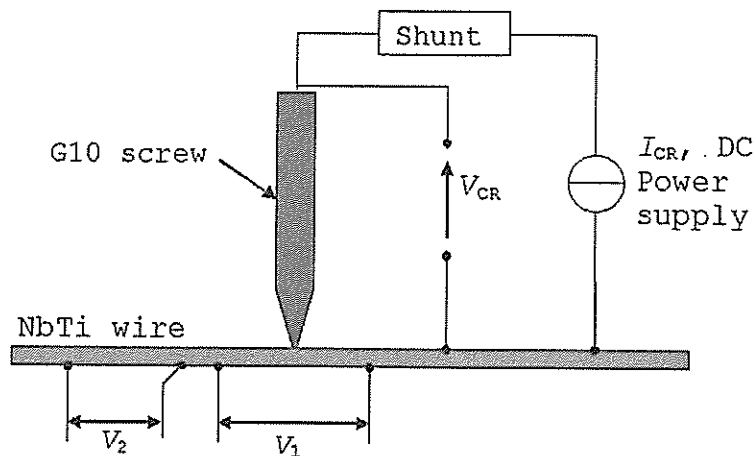


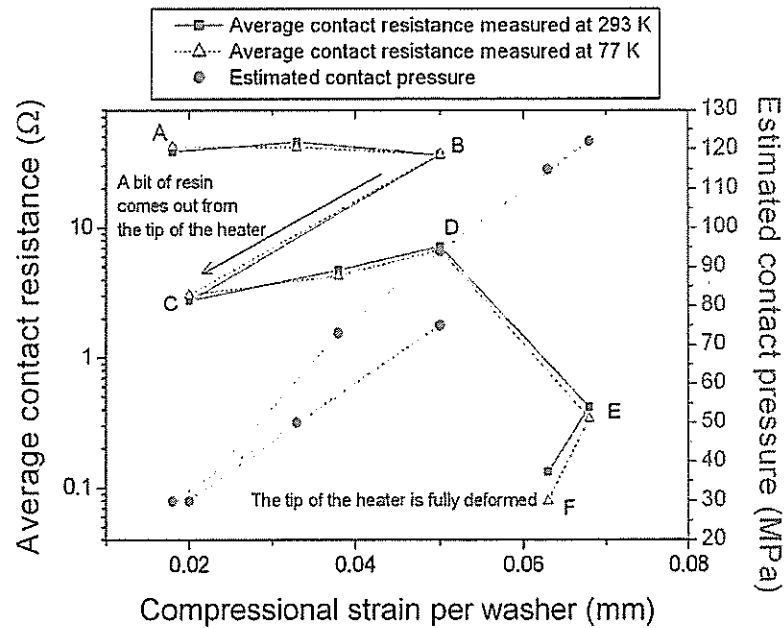
Figure III.8: Electrical sketch for contact resistance measurements. The voltage drop, V_{CR} , was measured across the heater. the voltage drops, V_1 and V_2 , were measured respectively across the heated zone and along the wire. The shunt in series with the heater was used to measure the DC current, I_{CR} , flowing through the heater.

It must be noted that the estimated contact pressure can be overestimated due to the underestimation of the contact surface. Furthermore, large errors can be done in the estimation of the cumulative compressional strain measured owing to a caliper. However, despite the uncertainty on the results, tendencies could be derived from the measurements.

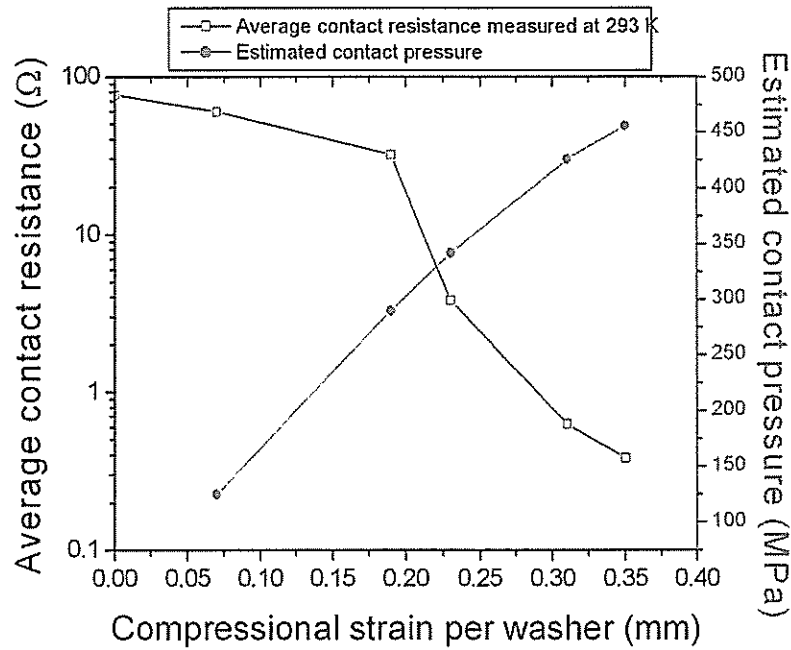
III.3.2 Comparisons between contact resistance and applied pressure

Figure III.9(a) (page 88) shows the behavior of point charged heater 2 under applied force. Based on this Figure, let us describe the different stages in the evolution of the contact resistance starting from the top left corner of the plot, and moving toward increasing pressure.

From A to B, nothing happened on the magnitude of the resistance and the mechanical deformation remained elastic. The variation in the contact resistance was smooth and the ball of charged epoxy just deformed under the applied pressure. At point (B), the structure collapsed expelling bits of resin and the average contact resistance lost one order of magnitude passing from about ten of Ohms to a few Ohms at point (C). This sudden drop in the contact resistance appeared around a compressional strain per washer of 0.05 mm (or 0.3 mm for the whole stack of washers). Simultaneously, the mechanical load stressing the washers was released. As a spring, they extended and the contact was maintained. If the pressure was further increased (from C to D), the contact resistance remained unchanged till a second drop occurred later on. This drop appeared smoother than the previous one. The volume of heater decreased till the tip was fully squeezed (D to E) taking the form of the sample and covering a little less than half of the wetted perimeter. At last, the contact resistance reached a steady value (F), and a thin film of resin remained



(a) Heater 2.



(b) Heater 5.

Figure III.9: Average contact resistance and contact pressure versus compression strain per washer measured for heater 2 and heater 5. (a)-Heater 2, at point (B), the ball of charged epoxy collapsed under the applied pressure. Then, the washers sprang back and maintained the contact with the sample, explaining thereby the decrease of both the contact resistance and the compression strain. (b)-Heater 5, here, a better mechanical behavior of the charged epoxy and consequently of the contact resistance has been achieved.

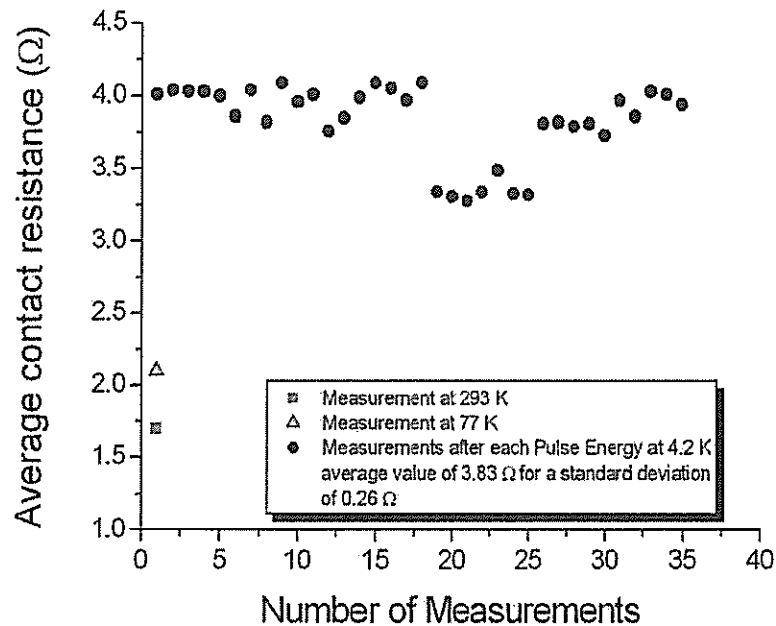


Figure III.10: Evolution of the average contact resistance of heater 4 over a series of stability measurements at 4.2 K and 8 T for a given pulse duration of 150 μ s. For comparison, the value at 77 K and 0 T is: 2.1 Ω , and that at 293 K and 0 T is: 1.7 Ω .

at the interface of the heater and the sample.

On this figure, the contact resistance did not seem to change from room temperature to low temperatures. Actually, the physical properties of the resin loaded with carbon particles vary as a function of temperature. Indeed, carbon material being semiconductor, its electrical resistance increases with decreasing temperatures. It is thought as an artifact of the experimental setup. It is likely that both the differential thermal shrinkage of the assembly and the increase of in the contact resistance may have worked together to yield a similar contact resistance before and after cool down.

These different stages appeared smoothed for heaters 4 and 5 (Figure III.9(b), page 88), showing a constant increase in the applied pressure all along the compression. For heater 5, Assembly 2 was used. So, two stacks of 5 washers were placed at each extremity of the G-10 bridge. The compressional force applied onto the heater was consequently larger than the one of Assembly 1 for the same compressional strain per washer resulting in a lower contact resistance. The change in the slope of the contact resistance versus the compressional strain per washer occurred at ~ 0.2 mm (four times larger than for heater 2 and 4). In this case, the charged epoxy showed a better mechanical behavior under deformation.

III.3.3 Evolution of the contact resistance over a series of stability tests

Figure III.10 (page 89) shows the evolution of the average contact resistance of heater 4 over a whole series of stability measurements for a pulse duration of $150 \mu\text{s}$, an operating temperature of 4.2 K and a background magnetic flux density of 8 T. The average contact resistance remained relatively stable all through the measurements with an average value of 3.83Ω and a standard deviation of 0.26Ω . No error bars are reported here since the series of measurements were not systematically repeated. For comparison, single measurements at 293 K and 77 K at 0 T are given in Figure III.10 (page 89). The contact resistance increases with decreasing temperature as expected with carbon charged resin. In this case, the contact pressure could not fully compensate the increasing resin resistance with decreasing temperature as it was speculated for heater 2.

III.3.4 Conclusion on contact resistance measurements

Despite the efforts taken in maintaining and positioning the tip of the heater onto the sample, we could not reach a reproducible value of average contact resistance from one heater to another. The thickness of the resin, remaining at the interface between the heater and the sample, and the distribution of the actual contact areas were undoubtedly different each time. This assumption could not be checked in detail. Indeed, neither the thickness of the remaining layer of epoxy nor the actual contact surface could be assessed due to the difficult nature of such measurements. A similar issue is encountered in metal to metal contacts [9]. The current path is constricted and the current flows through limited contact areas, which might be smaller than the apparent contact area. The size of those areas is mainly determined by the physical properties of the electrical contacts, the hardness of the materials and the magnitude of the applied mechanical load. In a first approximation, it is proportional to the contact surface and inversely proportional to the hardness of contacts. In our case, the problem is more complicated. Indeed, charged pastes are made-up of carbon powder and resin. Their structure is granular and they are crumbly in nature. As a bulk, they are dominated by their heterogeneous structure and are highly friable. But as a film, the mechanical deformation becomes plastic. Consequently, the shape of the contact cannot be predicted.

It seems that even a hard contact may not enable a good control of the contact resistance. P. Bauer [10] tried this type of technology obtained by sputtering Germanium onto a metallic tip which was strongly pressed onto flat samples. However, he could not achieve reproducibility as well.

At this point, it is implicitly assumed that a reproducible contact resistance will lead to a better reproducibility of Quench Energies measurements. This assumption is somehow arbitrary since no clear evidence can be unveiled from our measurements or can be found in the literature. As it will be shown in the subsequent section III.5 (page 97), the steadiness of the contact resistance value did not lead necessary to reproducible Quench Energies.

However, before presenting the results on Quench Energies and the influence of the contact resistance on these measurements, we will introduce the phenomenology of normal zone growth and some issues related to the electric titanium mandrel.

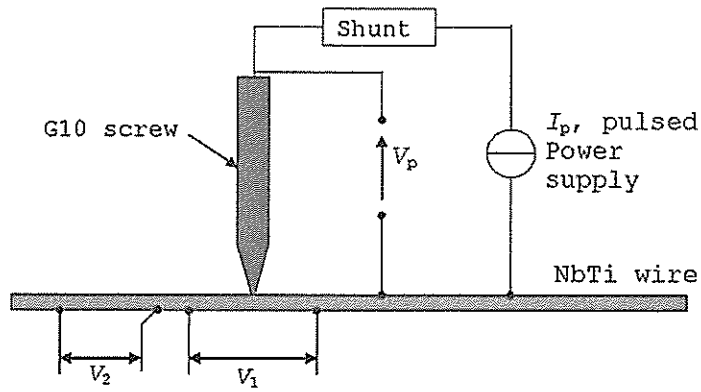


Figure III.11: Electrical sketch of the stability experimental setup. The voltage drop across the heater, V_p , the voltage drop, V_1 , across the heated zone and the voltage drop, V_2 , along the wire were recorded on a digital oscilloscope.

Table III.4: Voltage drops and the corresponding distance between their voltage taps.

Voltage drop	Distance (mm)
V_1	$L_1=93$
V_2	$L_2=43$

III.4. VOLTAGE TRACE RECORDINGS AND PHENOMENOLOGY OF THE NORMAL ZONE TRANSITION

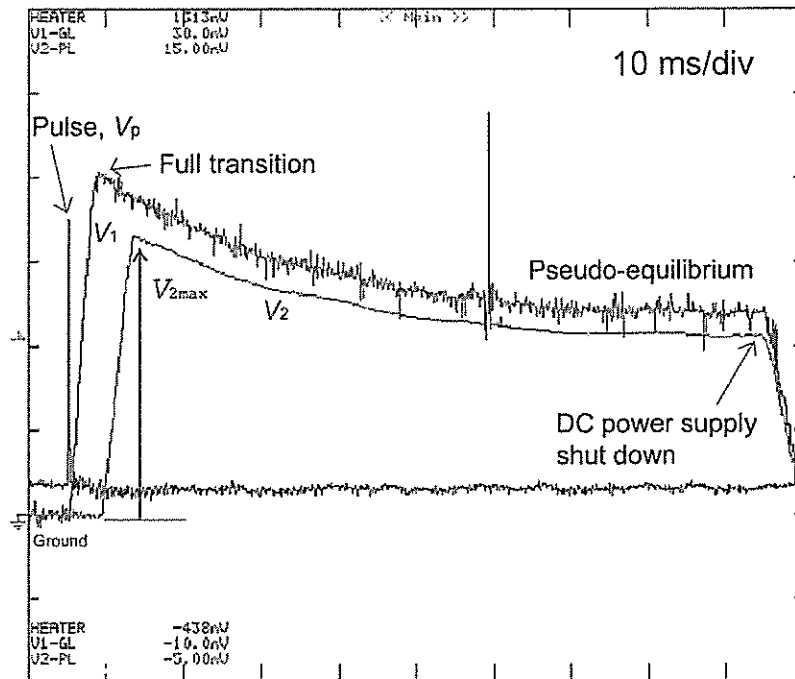


Figure III.12: Voltage traces (magnified by 2.28) recorded during a quench on a digital oscilloscope at 4.2 K, 8 T and 95% of I_c and a pulse duration of 150 μ s.

III.4 Voltage trace recordings and phenomenology of the normal zone transition

In this subsection, some voltage traces, recorded on a digital oscilloscope, are presented. The localization of the voltage taps corresponding to these traces are depicted in Figure III.11 (page 91), and the distance between these voltage taps are summarized in Table III.4 (page 91).

The different Figures, presented hereinafter, show different voltage outputs obtained for a pulse duration of 150 μ s at 8 T, 4.2 K and 95% of I_c (183 A). For each of them, the following voltage traces are given:

- V_p (black trace): across the heater.
- V_1 (red trace): across the heated zone.
- V_2 (blue trace): further away along the sample.

A small offset due to the current supply appears on voltage trace V_p . This offset has been compensated to estimate the magnitude of the quench energy (see next section III.5, page 97).

Let us now describe the different plots in detail.

Figure III.12 (page 92): This plot shows the development of a quench until the DC power supply of the sample was switched off. The quench energy was calculated to be 27 μ J.

After the V_p pulse vanished, voltage trace V_1 begins to rise linearly till it reaches

III.4. VOLTAGE TRACE RECORDINGS AND PHENOMENOLOGY OF THE NORMAL ZONE TRANSITION

a maximum when the transition to the normal resistive phase is fully completed across the wire section it encompasses. Then, it decreases slowly toward a pseudo-equilibrium. After a delay of a few milliseconds, the same trend is seen by voltage trace V_2 . This delay corresponds to the time it takes for the normal zone to propagate along the wire sample and reach the first tap of V_2 . This behavior was not quite expected. After the full transition is completed, the voltage is expected to increase further instead of decreasing. Indeed, due to heat generation, the temperature of the copper matrix rises till the plateau of residual resistivity of copper is exceeded, which usually takes place for a temperature between 20 and 30 K (see Appendix A, page 234). Then, the resistivity increases and so does the voltage.

From our point of view, the cooling capacity of helium is only partly responsible for the plateau of pseudo-equilibrium exhibited by the voltage traces after the onset of the full transition. On one hand, the dissipated power normalized to the wetted surface between voltage taps of V_1 and V_2 at the maximum peak voltage are respectively 0.14 W/cm^2 and 0.05 W/cm^2 , which is inferior to the minimum film boiling heat flux in steady-state regime and drops down to 0.06 W/m^2 and 0.02 W/m^2 toward equilibrium. So, throughout the normal zone transition, the helium coolant stays in the same nucleate boiling regime providing a good cooling to the sample. It would allow a current redistribution between the copper matrix and NbTi filaments which have turned back superconducting. On another hand, following the experience of predecessors and the results obtained with a new experimental setup described in chapter IV (page 103), it is an unexpected phenomenon. In addition to the above possibility, it is likely that a second process can take place, which helps lowering the heat dissipation into the wire. A plausible explanation appears to be the current redistribution between the wire sample and the titanium mandrel onto which it is wound. This redistribution would lower the current flowing into the copper matrix, decreasing heat generation till a quasi thermal equilibrium is reached.

For this explanation to be true, the resistance of the copper matrix of the wire sample must be of the same order of magnitude than the resistance of the titanium mandrel when the pseudo equilibrium has been reached. If this condition is satisfied, the mandrel plays the role of an electrical shunt. At 4.2 K and 0 T, its average resistance was measured equal to $\sim 2.62 \text{ m}\Omega$. To estimate the resistance R_m of the copper matrix of the wire sample at 4.2 K and 8 T, let us proceed as follows:

$$R_m = \rho_m \frac{(1+r)L_w}{rA_w} \quad [\Omega] \quad (\text{III.2})$$

where r is the copper to non-copper ratio, and A_w , the total cross-section of the wire.

Let $V_{2\text{max}}$ designate the maximum voltage taken at the height of the transition. The transport current, I_t , is assumed to flow through the copper matrix⁴, neglecting the presence of the mandrel for a conservative estimate. Then, it is possible to determine the corresponding resistivity at 4.2 K and 8 T:

$$\rho_m = \left(\frac{r}{1+r} \right) \frac{A_w V_{2\text{max}}}{L_2 I_t} \quad [\Omega\text{m}] \quad (\text{III.3})$$

⁴Voltage trace V_1 was not considered in the following calculation.

III.4. VOLTAGE TRACE RECORDINGS AND PHENOMENOLOGY OF THE NORMAL ZONE TRANSITION

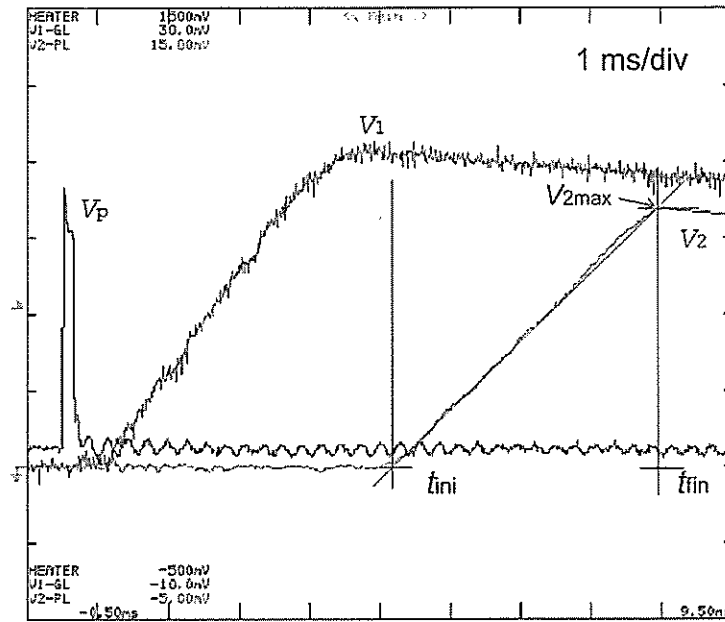


Figure III.13: Zoomed view of the current redistribution and early stage of the normal zone propagation. Voltage traces recorded at 4.2 K, 8 T and 95% of I_C and a pulse duration of 150 μ s for a quench. The data were taken from an other series of measurements than the series of Figure III.12 (page 92).

where L_2 is the distance between the voltage taps of V_2 given in Table III.4 (page 91). By substituting Equation III.2 into Equation III.3, we finally get:

$$R_m = \frac{L_w}{L_2} \frac{V_{2\max}}{I_t} \quad [\Omega] \quad (\text{III.4})$$

From Figure III.12 (page 92), $V_{2\max}$ was equal to ~ 8.44 mV, I_t to 183 A, and the total length of the sample, L_w , to ~ 1.1 m. Subsequently, the resistance of the copper matrix of the wire sample can be estimated to be ~ 1.2 m Ω .

As expected, it is of the same order of magnitude of the resistance of the titanium mandrel. Thus, the current is likely to redistribute itself between the copper matrix and the mandrel leading to a thermal equilibrium between heat dissipation and helium cooling. In the present case, $\leq 2/3$ of the transport current flows in the copper matrix while $\geq 1/3$ flows in the titanium mandrel.

This hypothesis was further verified with the new experimental setup described in the next section where the wire is mounted on a G-10 holder. Then, no such behavior of the voltage traces was recorded after a full transition occurred. As expected, they either disappear when the wire recovers its superconducting state or diverges when it undergoes a quench.

Figure III.13 (page 94): This output, which is taken from a different measurement than the one featured in Figure III.12 (page 92), but which corresponds to the same experimental conditions, details the linear increasing portion of voltage traces, V_1 and V_2 . The transport current being dumped into the copper matrix where

III.4. VOLTAGE TRACE RECORDINGS AND PHENOMENOLOGY OF THE NORMAL ZONE TRANSITION

Table III.5: Slope of the linear increasing part of voltage V_1 and V_2 and the corresponding Normal Zone Propagation Velocity.

Figure	Voltage drop	Number of normal zone propagating front, n	ν (m/s)
Figure III.13	V_1	2	12.9
Figure III.13	V_2	1	10.9
Figure III.12	V_1	2	12.4
Figure III.12	V_2	1	11.4

resistivity remains constant below ~ 20 K, the voltage along the wire increases approximately according to the length of the normal zone developing along the wire (see chapter III, section IV.5.3.2 [page 154] for explanations on the quenched zone estimation). Voltage drop V_1 increases faster than V_2 since its voltage taps are located on both sides of the heated zone thereby encompassing two normal zone propagation fronts.

It is possible from voltage traces V_i ($i \in \{1, 2\}$) to estimate the Normal Zone Propagation Velocity. As we just mentioned, below 30 K, the resistivity of copper, ρ_m , remains steady. So, the voltages V_i ($i \in \{1, 2\}$) evolve according to the length, L_{nz} , of the normal zone developing along the wire encompassed by their respective pairs of voltage taps. In the case of voltage V_1 , the voltage taps are located on both sides of the heated zone. We introduced then the coefficient n_i ($i \in \{1, 2\}$), which corresponds to the number of normal zone propagating front. Based on the voltage slope method [11], we express the Normal Zone Propagation Velocity, ν , as:

$$\nu \simeq \frac{rA_w}{n_i(1+r)\rho_m I_t} \frac{dV_i}{dt}, \quad \forall i \in \{1, 2\} \quad [\text{m/s}] \quad (\text{III.5})$$

Table III.5 (page 95) summaries the values of the slope of V_1 and V_2 and the corresponding Normal Zone Propagation Velocity. We found the expected order of magnitude of tens of meter per second given in the literature [10] despite a possible redistribution of current between the sample and the mandrel. This redistribution leads to an underestimation of the Normal Zone Propagation Velocity in the ratio of the fraction of current flowing through the copper matrix. The differences between the estimation from V_1 and V_2 traces are thought to be related to the error on the estimation of the length between the voltage taps. We do not think that the heater, located between the voltage taps of V_1 , can explain this difference since it covers less than 1% of the total wire surface.

Figure III.14 (page 96): This figure is a zoomed view of the previous Figure III.13 (page 94) on the very early stage of normal zone growth. In spite of the low resolution, it is possible to distinguish a slight bump on V_1 occurring at the end of the heat pulse. It is assumed to be related to the metastable growth of the normal zone before the quench decision time has been reached. The normal zone grows to a maximum, shrinks and takes off toward the full transition as the liquid helium sinks the heat dissipated by the copper matrix till its capacity is overcome and the heat generation finally takes over.

III.4. VOLTAGE TRACE RECORDINGS AND PHENOMENOLOGY OF THE NORMAL ZONE TRANSITION

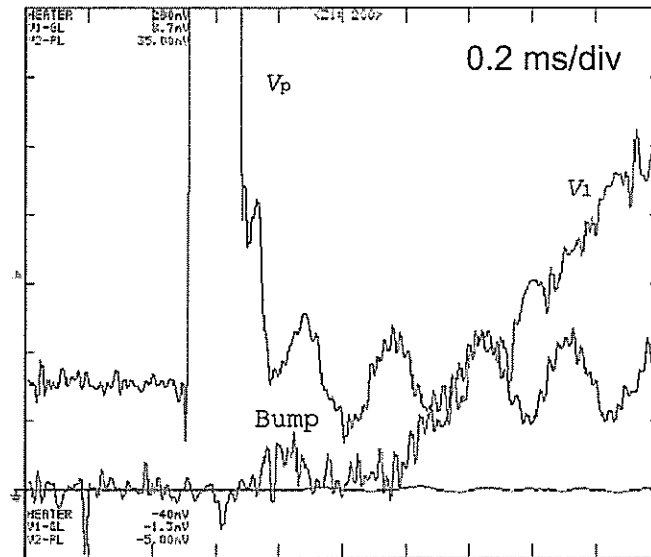


Figure III.14: Zoomed view of the early normal zone creation. Voltage traces (magnified by 12.5 for V_p and by 8 for V_1) measured at 4.2 K, 8 T and 95% of I_C and a pulse duration of 150 μ s. The data correspond to the Figure III.13 (page 94).

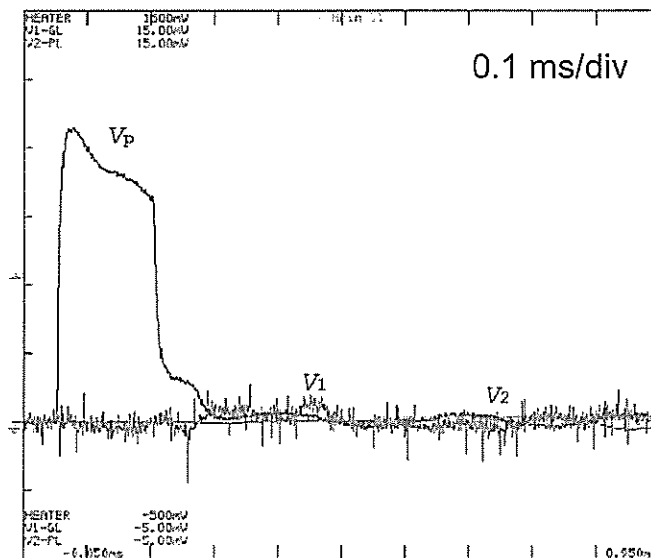


Figure III.15: Voltage traces (magnified by 1.5) recorded at 4.2 K, 8 T and 95% of I_C and a pulse duration of 150 μ s for a recovery.

Figure III.15 (page 96): This plot displays an example of recovery. The corresponding energy was calculated equal to $26 \mu\text{J}$. The previous energy triggering a quench was calculated equal to $27 \mu\text{J}$ thereby demonstrating the good sensitivity of the measurements of the quench energy, around $1 \mu\text{J}$. However, for this level of sensitivity, no clear bump could be distinguished on voltage trace V_1 as it could be seen in the previous figure. We expected to see such behavior since the energy was expected to be close enough to the quench energy for the transport current to redistribute into the copper matrix.

Due to the large distance between the voltage taps, only a few coarse details could be derived from the early growth of the normal zone. It was not possible to see a clear trend in the early stage of quenches and recoveries. In the new experimental setup, the distance between voltage taps were shortened allowing to record with great precision the early growth of the normal zone. It was then possible to see a normal zone growth during a quench and a recovery for the same sensitivity on the quench energy.

Nevertheless, interesting information can be derived from these recordings. It also clearly demonstrated that improvements in the experimental setup were necessary to see greater details on the normal zone growth and its propagation. The new setup, which is described in the next sections, was designed bearing in mind these requirements.

III.5 Results on Quench Energies

In this section, we introduce results on Quench Energies and a few considerations on the relationship between Quench Energy and contact resistance.

III.5.1 Estimation of the Quench Energy

Pulse currents flew through the heater and along NbTi-1 samples as depicted in Figure III.11 (page 91). The pulse durations, τ_p 's, were ranging from $\sim 30 \mu\text{s}$ to more than 1.5 ms . The Quench Energy, which corresponds here to the dissipated energy in the film layer of charged resin, E_p , was calculated as followed:

$$E_p = \int_{\tau_p} (P_p - P_{\text{offset}}) dt \quad [J] \quad (\text{III.6})$$

Since the power supply had a small offset, the total electrical power consumed by the heater, $P_p = V_p \times I_p$, was corrected by subtracting the continuous offset power, P_{offset} , over the pulse duration. A small power was then continuously dissipated onto the sample, which was assumed to be absorbed by the liquid helium.

III.5.2 Quench Energy measurements at a given contact resistance

For an average contact resistance of $\sim 3.83 \Omega$ (see Figure III.10, page 89), we performed with heater 4 different Quench Energies measurements by varying the pulse duration or the fraction of critical current at 4.2 K and 8 T . These measurements are gathered in Figures III.16 (page 98) and Figure III.17 (page 98).

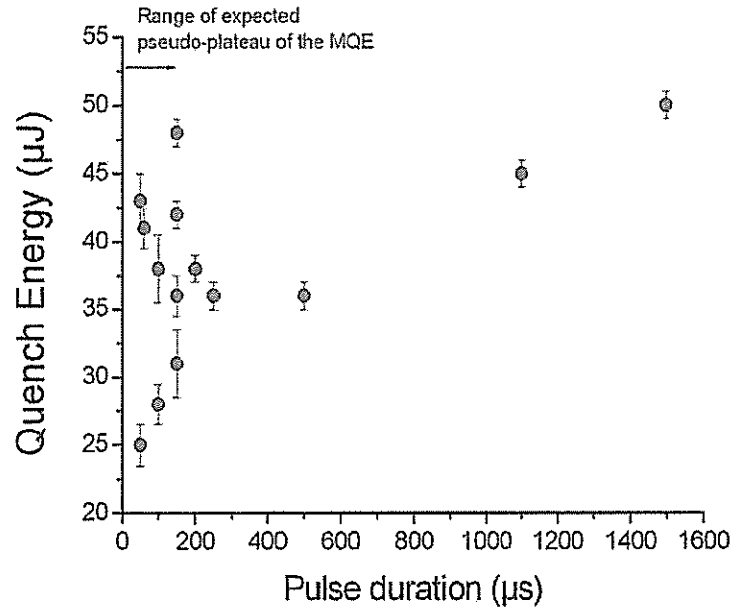


Figure III.16: Energy dissipated by the Joule effect into point charged heater 4 versus pulse duration at 95% of I_c at 4.2 K in liquid helium and 8 T as measured on a NbTi-1 sample. The error bars represent here the sensitivity of the measurement.

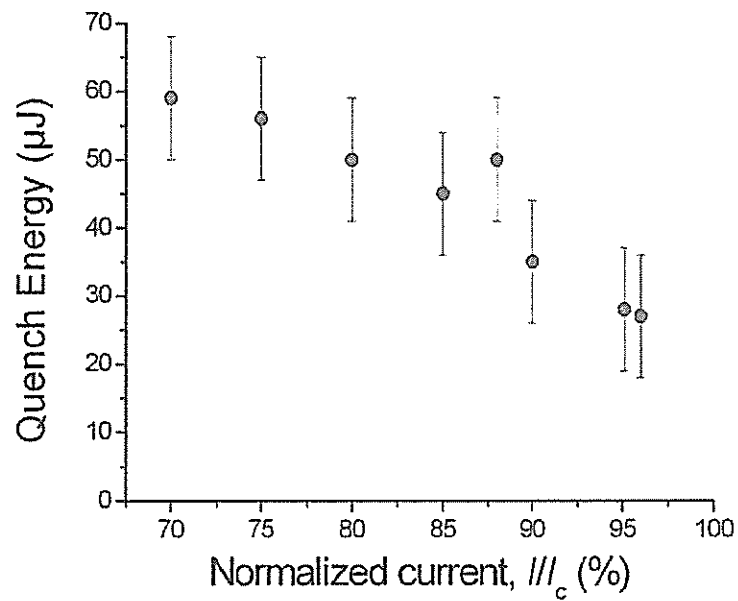


Figure III.17: Energy dissipated by the Joule effect into the point charged heater 4 versus the normalized current for a pulse duration of 150 μs at 4.2 K in liquid helium and 8 T measured on a NbTi-1 sample.

Figures III.16 (page 98): This plot shows the evolution of the Quench Energy obtained with heater 4 versus pulse durations at 4.2 K, 8 T and 95% of I_c . The Quench Energy appears to vary wildly at short pulse durations below a few hundreds of microseconds. It happens despite a quasi-steady average contact resistance (see Figure III.10, page 89) and independently of the order of magnitude of the average contact resistance. Consequently, it is not really possible to distinguish the pseudo-plateau of the Minimum Quench Energy expected at pulse durations below $\sim 100 \mu\text{s}$. The characterization of contact resistances is a difficult issue, especially with a friable material as the charged resin. Some electrical and/or thermal effects, apparent to noise, may have occurred in the transient state, but they could not be identified.

Figure III.17 (page 98): This plot shows the evolution of the Quench Energy obtained with the same heater 4 versus transport current to critical current ratio for a pulse duration of $150 \mu\text{s}$ at 4.2 K and 8 T. In this figure, the error bars are the standard deviation obtained at $150 \mu\text{s}$ from Figure III.16 (page 98).

The value of the Quench Energy decreases with increasing transport current. The tendency is clearly depicted over the range of transport currents despite a large uncertainty on the values of Quench Energies. Then, even if the value obtained at 87.5% of the critical current seems out of the trend, it is likely to come from an error of measurement.

III.5.3 Quench Energy at different contact resistances

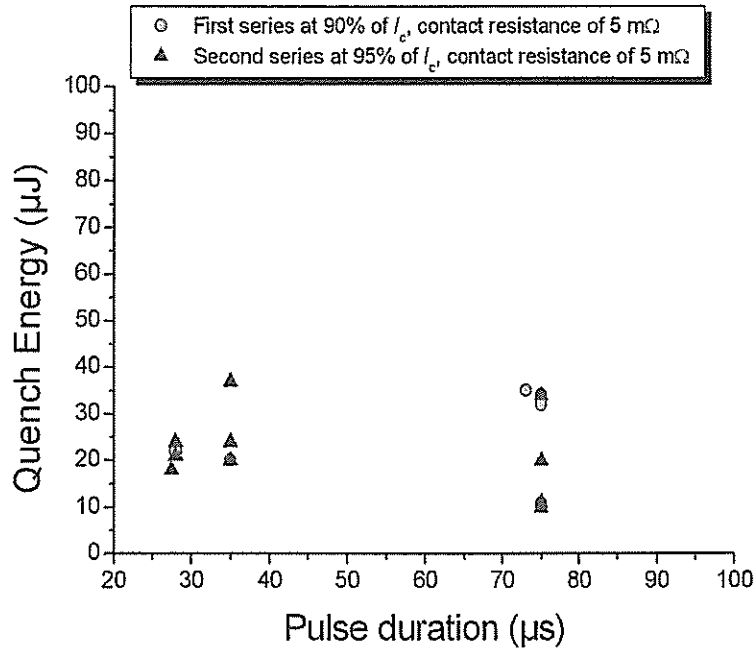
A similar campaign of measurements for two different average contact resistances, at $5 \text{ m}\Omega$ and $55 \text{ m}\Omega$, was carried out with heater 5 (see Figure III.18). To increase the resistance, the pressure exerted on the washers was slightly released. At these values, it was necessary to increase the amplitude of the pulse current to dissipate enough energy at the interface. Doing so, the direction of the pulse current compared to the direction of the transport current affected strongly the magnitude of the Quench Energy. Flowing in the same direction, the pulse current, representing about 5% of the total transport current, adds to the transport current and the stability margin was lowered. Flowing in the opposite direction, the pulse current, representing about 10% of the total transport current, reduced the apparent transport current and the margin increased thereby requiring a larger Quench Energy. For the measurements, we went for the latter setting. At $5 \text{ m}\Omega$, the results remained erratic. We could not distinguish any differences in the magnitude of the Quench Energy between transport currents of 90% and 95% of the critical current. On the contrary, for $55 \text{ m}\Omega$, this magnitude increased with decreasing transport current. As was predicted, at transport currents closer to the critical current, the Quench Energy decreases owing to a larger heat generation inside the wire.

In the end, it is amazing that the order of magnitudes of the quench energies obtained with heater 5 is similar to the one obtained with heater 4 ; especially that the contact resistance of this last heater is several orders of magnitudes larger than that of heater 5.

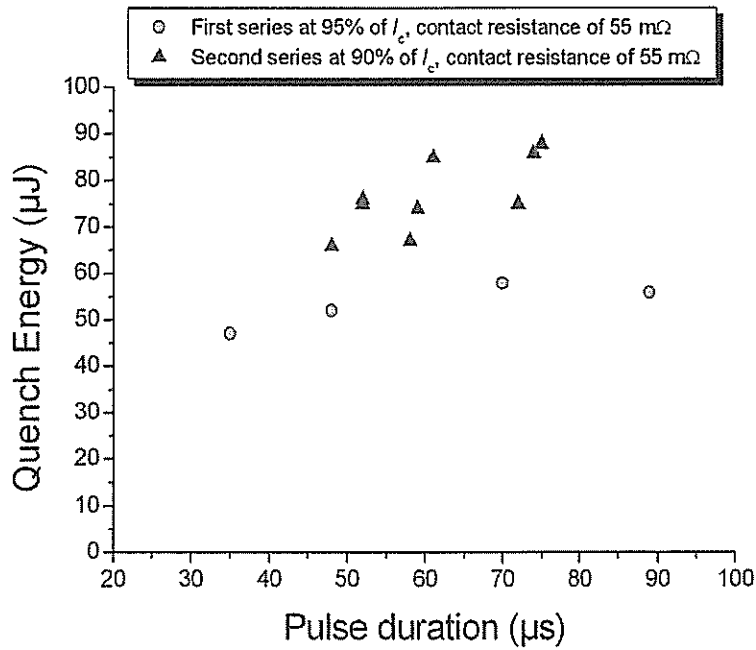
The pulse durations were assumed to be short enough to unveil the pseudo-plateau of the Minimum Quench Energy. However, only the first series of measurements at $55 \text{ m}\Omega$ (see Figure III.18(b), page 100) shows the expected behavior.

No useful results were obtained with heater 7 since the lowest reachable contact resistance was still too large for the capacity of the current supply, which saturated

III.5. RESULTS ON QUENCH ENERGIES



(a) Contact resistance of 5 m Ω .



(b) Contact resistance of 55 m Ω .

Figure III.18: Quench Energy versus pulse duration at 90% and 95% of I_c for different values of contact resistance obtained with heater 5.

at low pulse durations. The setup was further modified, but no improvements were achieved.

III.6 Conclusions on carbon paste point heaters

Our first try based on a mixed technology between the Carbon charged heater and tip-heater did not lead to a noticeable improvement of both technologies. The reliability of our setup was low. Most of the heaters burnt out either during the contact resistance measurements or the stability tests. In addition, the whole assembly was not easy to handle. Especially, it was necessary to use a microscope in order to ensure that the heater stayed in contact with the sample throughout the manipulation. When the heater was in its final position, the average contact resistance ranged from few hundreds of milli-Ohms to a few Ohms. This contact resistance could not be simply adjusted by increasing or releasing the pressure without affecting the measurements on quench energies. Besides, we could not achieve reproducible contact resistances from heater to heater as it was initially planned. No clear correlation was found between the contact resistance value and the Quench Energy. Especially, the large variations of the Quench Energy measurements at short pulse durations do not seem to correlate with the comparatively small variations of the contact resistance for one campaign of tests.

All the above data must be considered with precaution because of a possible current redistribution between the wire sample and its titanium mandrel.

Facing various difficulties related to the positioning of the heater, the presence of the titanium mandrel and the lack of reproducibility of the quench energies, we decided to switch our attention to two different heater technologies: diode laser and induction coil. Contrary to charged paste heaters, they do not require a physical contact to be operated. It was then expected that:

- a better reproducibility could be achieved,
- the pseudo-plateau of the Minimum Quench Energy could be clearly unveiled,
- and more details on the early normal zone development could be seen.

Bibliography

- [1] A. Devred. Supraconducteurs à basse température critique pour électroaimants. Technical report, CEA/Saclay, September 2002. CEA-R-6011.
- [2] F.M. Asner. *High field superconducting magnets*. Oxford Science Publications, 1999.
- [3] M. Dalban-Canassy. Conception et réalisation d'un dispositif expérimental pour déterminer l'Energie Minimum de Quench de brins supraconducteurs, January 2000. CEA note: 5-2650N-2170 001 00.
- [4] K. Seo, M. Morita, S. Nakamura, T. Yamada, and Y. Jizo. Minimum Quench Energy Measurement for Superconducting Wires. *IEEE Transactions on Magnetics*, 32(4):3089, July 1996.
- [5] P. Bauer, J. Donnier, L. Oberli. Tip Heater for Minimum Quench Energy Measurements on Superconducting Strands. *IEEE Transactions on Applied Superconductivity*, 9(2):1141, June 1999.
- [6] F. Trillaud. Mesures de courant critique sur brin supraconducteurs en Niobium-étain (Nb₃Sn), July 1999. CEA note: 5-2650N-2120 021 99.
- [7] VAMAS Technical Party for superconducting materials. VI. Standard method for I_c determination. VI-1: Recommended standard method for determination of d.c. critical current of Nb₃Sn multifilamentary composite superconductor. *Cryogenics*, 35:S105-S112, 1995.
- [8] F. Trillaud. Mise en oeuvre d'un dispositif expérimental pour mesure de stabilité sur brin supraconducteur. Master's thesis, University Paris Orsay, July 2000. CEA note: 5-2650N-2170 002 00.
- [9] R. Holm and E. Holm. *Electric contacts*. Springer-Verlag, 1967.
- [10] P. Bauer. *Stability of Superconducting Strands for Accelerator Magnets*. PhD thesis, Technische Universität Wien, 1998.
- [11] A. Devred *et al.* *Quench Localization in Full-Length SSC R&D Dipoles*, pages 73-83. Plenum Press, New York, 1989.

Chapter IV

New LTS experiment using a diode laser

Contents

IV.1 LHC-type NbTi wire samples, batch NbTi-2	105
IV.1.1 Oxidation treatment of NbTi-2 wires	105
IV.1.2 Critical current measurements on batch NbTi-2 and comparison with batch NbTi-1	106
IV.2 New setup for inductive and laser heaters	106
IV.2.1 Description of the diode laser	108
IV.2.2 Description of the pre-coupled and the optical fiber extension connected to the diode laser	110
IV.2.3 Temperature control system of the diode laser	113
IV.2.4 New Probe for stability tests in liquid helium and in a vacuum	114
IV.2.4.1 Localization of the diode laser	114
IV.2.4.2 G-10 sample holder and maintaining of wire sample	114
IV.2.4.3 Positioning of the heaters onto the sample holder .	116
IV.2.5 Electrical equipments, acquisition system and voltage localizations	118
IV.2.6 Current redistribution and definition of the active zone of measurements	120
IV.3 Determination of the optical energy produced by the diode laser	121
IV.3.1 Description of the experimental setup	121
IV.3.2 Characterization of the diode laser	122
IV.3.3 Setting of powermeter and accuracy of measurements . . .	124
IV.3.4 Influence of the connection between the optical fiber extension and the pre-coupled optical fiber	124
IV.3.5 Influence of the temperature control of the diode laser . . .	126
IV.3.6 Parameters influencing the behavior of optical fibers	126
IV.3.7 Estimation of the optical energy flowing from the optical fiber	129
IV.3.8 Estimation of the energy absorbed by the sample	131
IV.4 Calibration of the optical energy absorbed by the oxidized sample	136

IV.4.1	Experimental setup	137
IV.4.2	Diode laser used for the calibration	137
IV.4.3	Description of the bolometers	138
IV.4.4	Electrical equipments	141
IV.4.5	Experimental results	141
IV.4.5.1	Heat balance equation at the thermal equilibrium and determination of the coefficient of absorption	144
IV.4.5.2	Determination of the thermal conductivity: closed bolometer experiment	146
IV.4.5.3	Estimation of the coefficient of absorption: cylin- drical bolometer experiment	146
IV.4.5.4	Conclusion on the coefficient of absorption	148
IV.4.6	Estimation of the absorbed optical energy by the sample . .	149
IV.5	Stability measurements	149
IV.5.1	Filtering of the voltage traces	149
IV.5.2	Protocol of measurements and examples of voltage recordings	151
IV.5.3	Estimations of the different parameters of the normal zone transition	152
IV.5.3.1	Estimation of the Quench Decision Time	153
IV.5.3.2	Estimation of the length of quenched zones	154
IV.5.3.3	Estimation of Quench Energy and Minimum Quench Energy	156
IV.5.3.4	Estimation of Normal Zone Propagation Velocity .	157
IV.5.4	Influence of various parameters	157
IV.5.4.1	Pulse duration	158
IV.5.4.2	Background magnetic flux density	160
IV.5.4.3	Transport current	164
IV.5.5	Conclusion on Measurements	166

THIS CHAPTER describes a new experimental setup involving two new heater systems: an induction coil and a diode laser. This setup was designed to resolve the lack of reproducibility of quench energy measurements encountered with charged point heaters.

The diode laser exhibits a large improvement compared to past heaters.

Difficulties were encountered with the induction coils, which could not be resolved within the time frame of this work. This technology will not be detailed here.

IV.1 LHC-type NbTi wire samples, batch NbTi-2

In the following experiments, a new batch of LHC-02-type Cu/NbTi multifilament composite wires was supplied by Alstom/MSA. The wires were slightly different from those used in the preliminary study (see chapter III, page 77). They will be detailed in the subsequent section.

IV.1.1 Oxidation treatment of NbTi-2 wires

Samples NbTi-2 were mounted on the new experimental setup using a U-shaped sample holder (see section IV.2.4, page 114). Their salient parameters are given in Table IV.1 (page 106).

As already mentioned, for the previous samples NbTi-1, no special surface treatment was applied to improve the contact resistance at the interface between the resistive heater and the samples. However, with the new experimental setup using a laser source to trigger normal zone transitions, a chemical oxidation treatment was applied to the samples to improve their optical absorptivity. Indeed, previous measurements on the same bare sample showed a poor optical absorption [1].

Figure IV.1 (page 107) shows one of these samples, which was oxidized over a length of 3.52 mm. These oxidation treatments¹ are commonly used to obtain various colors and crystallographic structures in electronic and metal finishing industries [2]. The samples, used in our experiment, were blackened at CERN in the facility for surface treatments². These samples, ~ 1 m long, were soaked into an hydroxide chemical solution of Bondenex[®] products (supplied by Alfachimici in Italy) and deionized water. The whole bucket was heated at ~ 333 K for 20 to 30 min. It is possible to control the penetration depth of the oxidant into bulk copper and the metallography of the oxide layer by adjusting the time of exposure of the samples to the warm bath. Indeed, the rate of cuprous oxide growth (Cu_2O) saturates quickly, and, after a few minutes, cupric oxide (CuO) yielding a genuine black color to the samples grows in a larger quantity [3]. The maximum thickness of oxide is obtained after ~ 20 min. Consequently, a thin layer of the order of few micrometers ($\leq 2 \mu\text{m}$) of cupric oxide and cuprous oxide mixture, which stains the natural reddish color of bare copper with a shiny velvety black coloration, builds up on bulk copper³. Figures IV.1(b) and IV.1(c) (page 107) show the micrographies of similar oxidized wires. It is barely possible to see the oxidized layer in Figure IV.1(c) (page 107), whose thickness remains inferior to the sensibility of the device. It was expected in view of the black

¹Idea suggested by S. Calatroni, CERN.

²Realized by M. Marabella at the "Atelier des traitements de surface", TS-MME-CEM/CERN.

³Additional heat treatments, which were not applied in this case, is expected to improve the adhesion of the oxidation on its substrate. The cuprous oxide decomposes around 1026°C at the atmospheric pressure, which allows to use this coloring process on unreacted Nb_3Sn wires.

Table IV.1: Salient parameters of NbTi-2 wires.

Diameter	0.822 mm
Twist	15.3 mm
Ratio: Cu/Sc	1.96
RRR	194 (150)*
Critical current density at 7 T, 4.2 K, J_c	1720 A/mm ²

*Estimated in situ at CEA/Saclay ; used in the numerical simulation.

reddish color of the sample that a thicker thickness of oxide would grow. On one hand, effects caused by the polishing of the sample may have deformed the edge of the sample cross-section masking a part of the oxide layer. On the other hand, this may explain the low experimental coefficient of optical absorption (see section IV.4, page 136).

With this procedure, the samples are entirely covered by the oxide layer. Then, the excess oxide is chemically removed using a 50% diluted chloridric acid solution, letting only 2 to 5 mm of oxidized copper at the middle of the sample.

IV.1.2 Critical current measurements on batch NbTi-2 and comparison with batch NbTi-1

Figure IV.2 (page 108) shows comparative critical current measurements on batch NbTi-1 and batch NbTi-2 and the corresponding fits⁴ (see Appendix B, page 235). A slight discrepancy appears between the two batches. This discrepancy results from the difference in the design parameters of the samples.

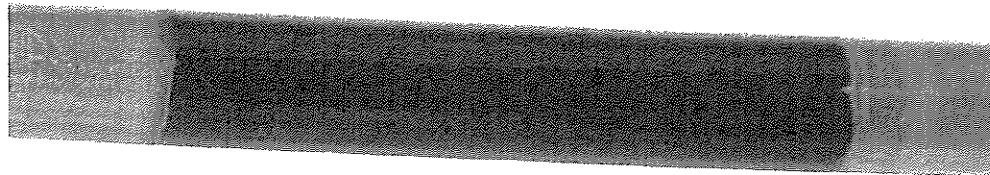
No influence of the oxidation layer was observed on the critical current measurements of samples NbTi-2.

IV.2 New setup for inductive and laser heaters

In the previous chapter, we described a preliminary experimental setup for which we used a charged point heater. For this heater technology, various issues were unveiled. After different modifications of the heater assembly, difficulties inherent to the physical nature of electrical contacts remained unsolved.

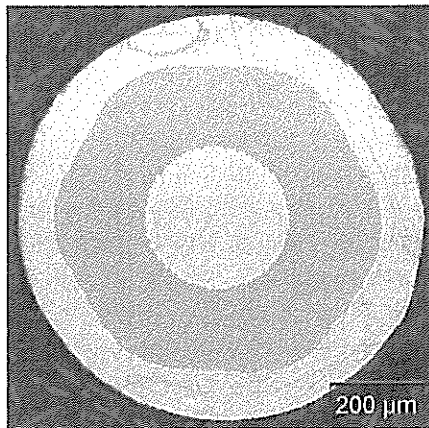
Alternative technologies were tried to address the problem of measurement reproducibility and to improve the simplicity of the overall experiment. Among all possible technologies, induction coil and diode laser, appeared to be the most promising candidates. It was expected that these new heaters would lead to a better reproducibility since their operating principle does not require mechanical bonding to the sample. Then, the energy transferred to the sample depends only on the intrinsic physical properties of the metallic stabilizer sheathing the superconducting wires.

⁴Fits provided by P.P. Granieri, Department of Electrical Engineering, University of Bologna, Italy.

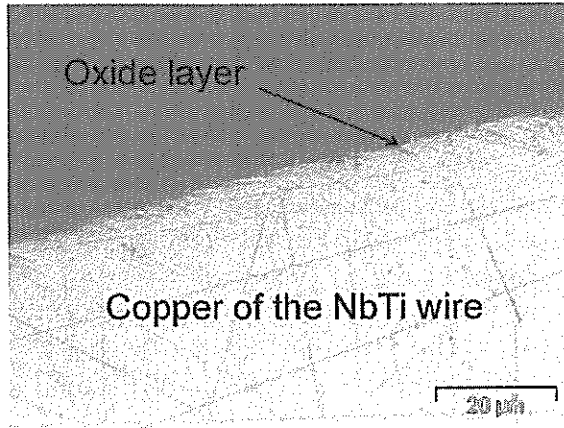


————— **3,5 mm** —————

(a) Oxidized wire.



(b) Cross-section of an oxidized wire.



(c) Zoomed view on the edge of the oxidized wire.

Figure IV.1: View of oxidized Cu/NbTi wire samples. (a) an oxidized portion of a wire ready for stability tests. (b) entire cross-section of a different wire. (c) zoom on the oxidized edge of this previous wire. The resolution of the optical microscope is not good enough to see the oxidized layer, which is inferior to $2 \mu\text{m}$.

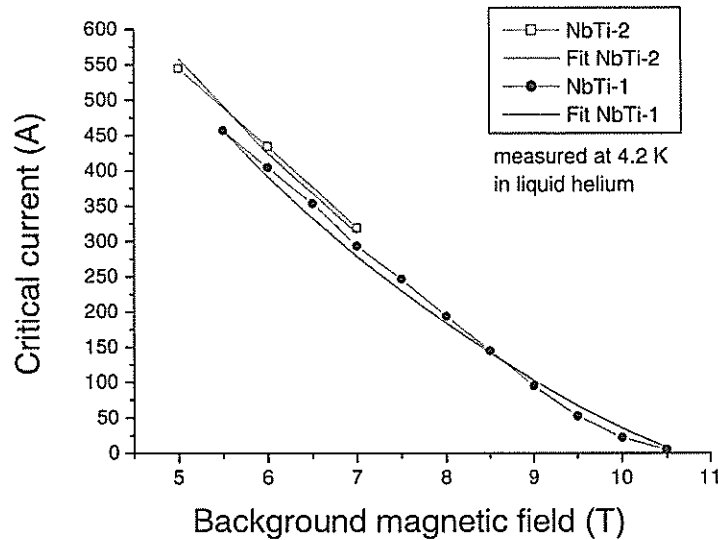


Figure IV.2: Critical current versus background magnetic field at 4.2 K in liquid helium and atmospheric pressure for both samples. No error bars are reported since the error was inferior to 1%.

As it will be shown in this section, our various goals have been partially fulfilled owing to an entirely new experimental setup. This setup is made-up of a new dedicated probe for comparative measurements of the two new heaters. As we have already mentioned, we will not describe the induction coils in this present work since they could not give exploitable data. So, the diode laser, the probe and the heater assemblies are subsequently described and some of their important features are detailed. The feasibility of such a laser technology was demonstrated and reproducible results were achieved. Calibration measurements were also carried out to assess the accuracy of the results.

IV.2.1 Description of the diode laser

Principle of diode lasers: Diode lasers belong to the family of semiconductor lasers. It is schematically a stack of adjacent light emitters. Each one of them is composed of a depletion zone squeezed between a p-n junction (see Figure IV.3, page 109). A current of 10 to 20 mA with a small voltage drop of ~ 2 V per emitter is necessary to pump the diode⁵.

Physically, the applied electrostatic field reduces the potential barrier so that the junction is forward biased allowing electrons of the conduction layer to migrate from the n-doped side to the p-doped side. There, they recombine with positive holes in the valence band by emitting photons. This process is large and fast enough to stimulate the inversion of population in the optically active region with an electro-optical efficiency up to more than 50 % [4]. The photon beams are amplified by

⁵The diode being polarized, it is important to respect the polarization of the current to avoid its destruction.

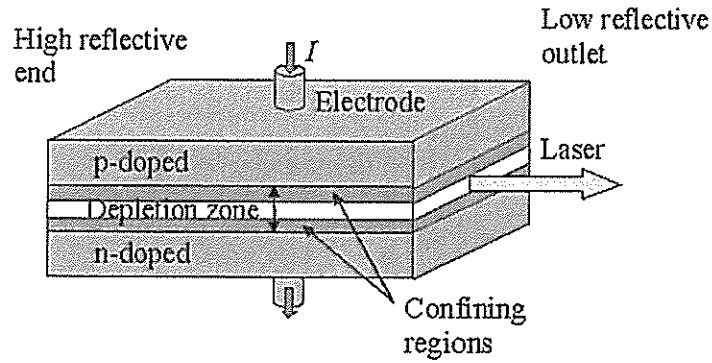


Figure IV.3: Schematic illustration of a laser chip making the diode laser. In a diode laser, the concentration of recombining carriers is large enough to produce stimulated photons for the diode to emit very intense coherent light. To amplify the density of photons, two mirrors, on which they rebound, form a Fabry-Peyrot resonant cavity.

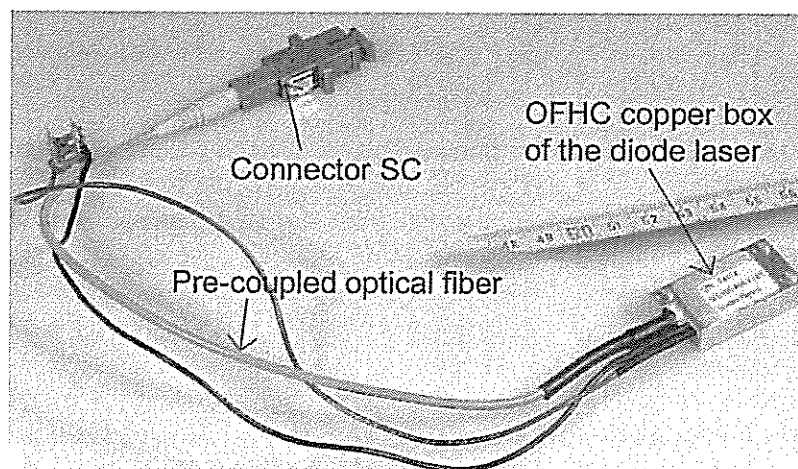


Figure IV.4: Diode laser and its pre-coupled optical fiber.

Table IV.2: Salient parameters of the single-mode diode laser at 293 K (used for stability measurements at CEA/Saclay).

Maximum continuous output power (W)	1.35
Maximum current (A)	2
Numerical Aperture, NA	0.06
Peak wavelength (nm)	807.4 ± 10

reflecting at each end of the diode structure while being confined by guiding layers in the depletion region. Additional optics collimate the photon beam to a coupled optical fiber serving as a wave guide to propagate light from the source to the target. Due to the compactness of the diode, overheating may damage the emitters and the optics. Hence, they are embedded in an OFHC copper shell coupled to a heat sink to maintain a steady temperature during DC operation. Figure IV.4 (page 109) gives an overview of the OFHC copper shell and the pre-coupled optical fiber with its connector attached to it.

In normal operation, the lifetimes of diode lasers are relatively long: more than tens of thousands of hours. Degradation due to overheating and aging can be compensated by increasing the current flowing through the p-n junction or by operating at a lower temperature (see subsection IV.2.3). Nevertheless, it is generally wise to recalibrate the diode after several thousands of operating hours.

Diode laser as heater, a few characteristics: A single-mode diode laser (supplied by Spectra-physics, US) of ~ 1.2 W, pre-coupled with an anti-reflection coated optical fiber of ~ 30 cm long, was used as a pulsed heater. This diode laser was extended by an optical fiber extension to guide the laser beam as close as possible to the sample surface.

Phenomenologically, the beam light strikes locally the surface of the superconducting multifilamentary composite wire. Consequently, the temperature of the sample increases resulting from its interaction with the laser beam. It creates a normal zone inside the bundle of superconducting filaments, which can expand or shrink depending on the balance between dissipated energy and cooling conditions.

Table IV.2 summarizes the essential characteristics of the diode laser implemented in our experiment⁶.

IV.2.2 Description of the pre-coupled and the optical fiber extension connected to the diode laser

Optical fibers are generally used as transceivers to transmit and receive data. So, a large choice of standard optical fibers, used in telecommunications, are available.

⁶The Numerical Aperture is defined as the sinus of the half-angle at the vertex of the cone containing 90% of the light energy. If Θ is this half-angle: $NA = \sin \Theta$.

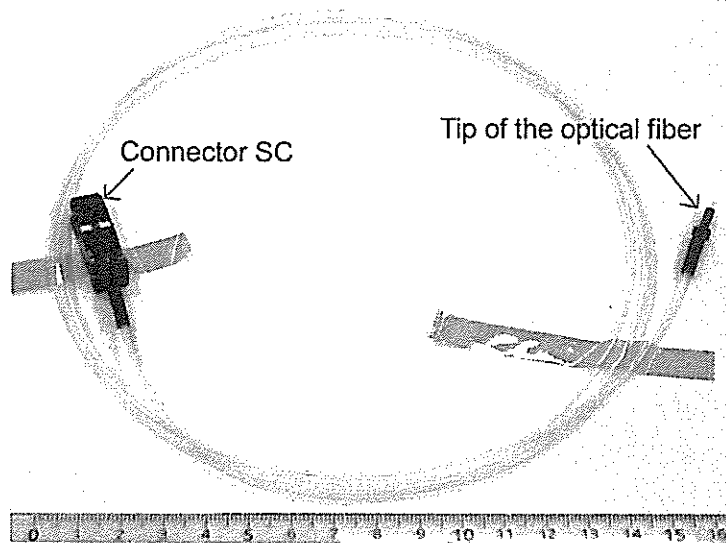


Figure IV.5: Picture of the optical fiber extension.

In our experiment, two standard optical fibers, available for telecommunication applications, were connected in series:

- an optical fiber directly coupled to the diode laser,
- a Silica-Silica optical fiber extending the previous optical fiber.

The optical fiber extension is shown in Figure IV.5 (page 111) while the pre-coupled optical fiber is shown in Figure IV.4 (page 109). The extension was used to guide the laser beam as close as possible to the sample. It propagates powerful light in the visible and near infrared region.

In subsequent paragraphs, after a brief introduction on the principles governing an optical fiber, we will mainly focus on the optical fiber extension whose tip has been customized and whose environmental conditions are unusual for this type of fiber. We will not detail the pre-coupled optical fiber. This standard fiber was supplied with the diode laser. Being located at room temperature, it is used in its normal condition.

Principle: An optical fiber is an electromagnetic wave guide made up of concentric cylinders: a core of high refractive index, a cladding of lower refractive index, and a protective sleeve (Figure IV.6, page 112). This peculiar structure allows guiding the laser light along the fiber length by successive reflection at the interface of its core and its cladding. The resulting wave propagates with low longitudinal losses of the order of 10 dB/km. About 0.5 to 4 % of the light can be back reflected at the outlet or at the entrance of the optical fiber depending on the presence or not of anti-reflection coating.

Optical fiber extension: In our experiment, an extra Silica-silica (SiO_2) low OH^- step index optical fiber (TCL100 supplied by SEDI, France) with a polyimide-coated cladding protected by a Teflon[®] sheath was connected through a connector

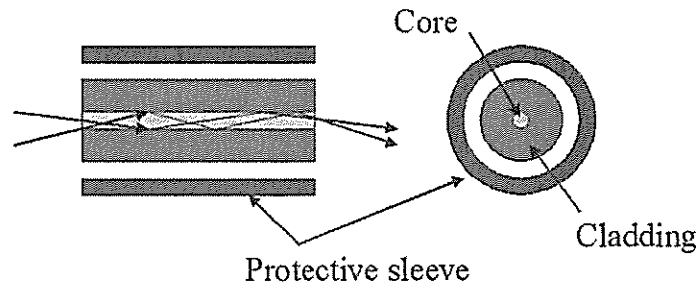


Figure IV.6: Schematic structure of an optical fiber with a protective sheath, a cladding and a coated core.

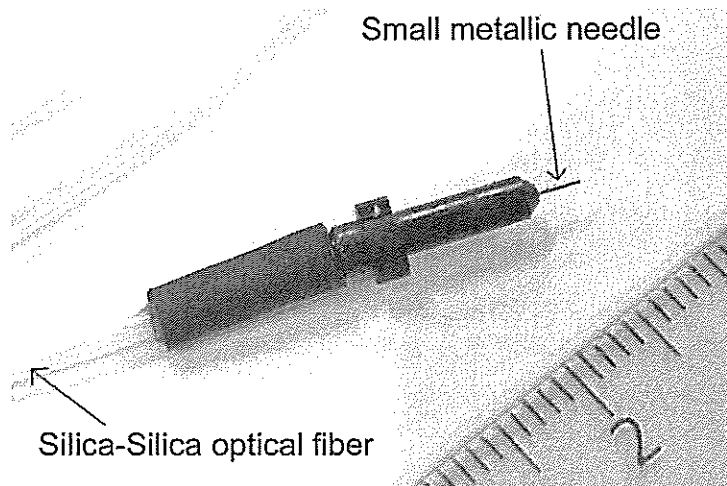


Figure IV.7: Tip of the optical fiber extension, which was customized so that the heated area of the sample be as tiny as possible.

(standard SC) to the fiber pre-coupled to the diode laser. Therefore, the laser beam was guided along 2.048 m measured from the diode located at room temperature to the sample in liquid helium at the bottom of the cryostat, including the length of the pre-coupled fiber. The inner diameter of its core is $100 \mu\text{m}$, which corresponds to a multi-mode optical fiber [5]. Its numerical aperture is $0.22^{\pm 0.002}$. Thus, a cone of light having a half-angle of $\sim 13^\circ$ flows from the tip of the optical fiber.

Customized tip of the optical fiber extension: The tip of the optical fiber extension is made-up of Ultem[®] 1000R into which was glued a hollow metallic needle (inner diameter of $300 \mu\text{m}$) as depicted in Figure IV.7 (page 112). The cladding, corresponding to the outer silica sheath of the wave guide, was glued inside the metallic needle so as to rigidify the whole assembly. The basic idea was to control the lightened area of the sample as much as possible by maintaining the tip of the fiber tightly in place relatively to the sample.

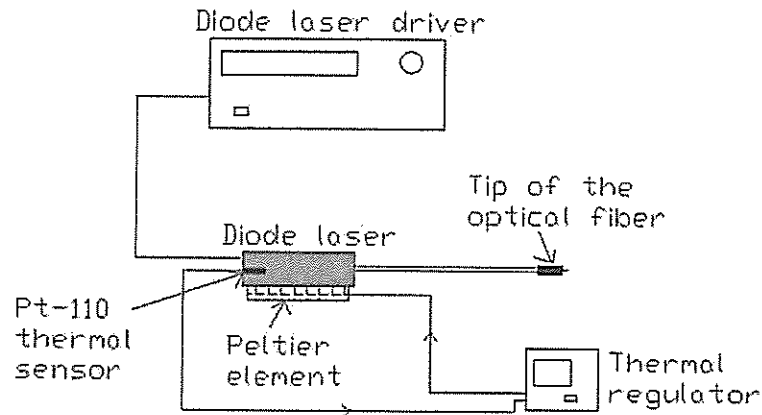


Figure IV.8: Sketch of the thermal regulation system of the diode laser used at CEA/Saclay.

Parameters influencing the behavior of the optical fiber extension: As discussed thereafter (section IV.3.6, page 126), environmental conditions may affect the behavior of the optical fiber. In our case, the environmental parameters are: cryogenic fluid, thermal cycling and background magnetic field. These are harsh conditions surrounding the optical fiber extension. But, contrary to sensor optical fibers which are especially designed to be highly sensitive to their environment, our more conventional optical fiber is expected to be weakly influenced.

IV.2.3 Temperature control system of the diode laser

The diode laser being equipped with the optical fiber extension, a series of preliminary stability experiments for which the wire sample had not been oxidized, has been carried out (see details in reference [1]). The temperature of the diode laser was not controlled at that time. However, its variations were observed with a Pt-110 thermal sensor (supplied by Lakeshore, US) glued with Stycast[®] 2850FT to the OFHC copper shell of the diode laser. The temperature changed during the day according to changes in room temperature. The emission wavelength of the diode laser depending on its operating temperature⁷, its output optical power for the same forward current was likely to change during the day. Later, this phenomenon was also observed while measuring the optical power versus forward current characteristic at different operating temperatures (see section IV.3, page 121). Nevertheless, at a given room temperature and in pulse mode operation, we did not observe any temperature variations for pulse durations up to 1 ms.

For subsequent series of measurements for which a few millimeters of wire sample were oxidized, the temperature of the diode laser was controlled. Figure IV.8 (page 113) shows a sketch of the thermal regulation setup used in our experiment. A thermal regulator was coupled to a Peltier element (Ref: CP0.8-63-0.6, supplied by MELCOR, US). This element was bonded with copper paste to the OFHC copper shell of the diode laser and squeezed between the diode and its support. The

⁷A discrepancy of about -0.3 nm/K is typical.

thermal feedback was provided by the same Pt-110 thermal sensor previously mentioned. Owing to the thermal regulation, we fixed the operating temperature of the diode laser at 293 K for all subsequent stability measurements.

IV.2.4 New Probe for stability tests in liquid helium and in a vacuum

Both the induction and diode laser heater, and their related equipments were incorporated into a new probe dedicated to stability and critical current measurements with an insulating sample holder based on a new design. Indeed, from our first encounter with Quench Energy and Normal Zone propagation study, we anticipated that an experimental assembly based on a VAMAS-type sample holder would not be suitable to try simultaneously the two new heaters on the same setup. Especially, this was a problem for the induction coil since the radius of curvature of the sample wound on its mandrel was a penalizing constraint.

Our intention was to compare results on quench energies for both heaters in the same environmental conditions. The availability at CEA/Saclay of a large bore cryostat of 96 mm in diameter gave us this opportunity, and a complete new probe was designed and assembled to operate easily both heaters.

In this subsection, we introduce the main features of the new probe which aimed at addressing the lack of reproducibility of past experiments. We will only detail here:

- the sample holder,
- the positioning of heaters.

A detailed description of the entire probe is given in Appendix D (page 241). Some parts are numbered. The numbers refer to the nomenclature defined in Appendix D.

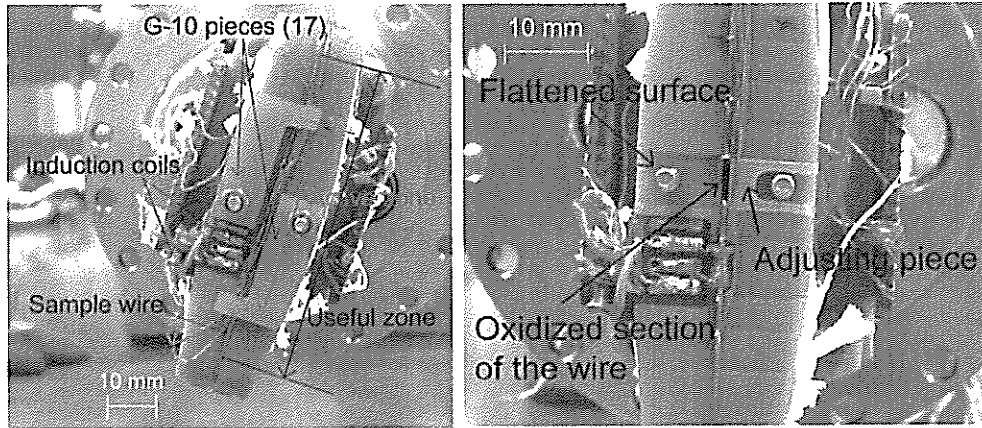
IV.2.4.1 Localization of the diode laser

The diode laser is located at the top of the probe. An optical fiber extension allows to guide the laser beam from the pre-coupled optical fiber to the sample located at the bottom of the probe where is located the sample holder as described.

IV.2.4.2 G-10 sample holder and maintaining of wire sample

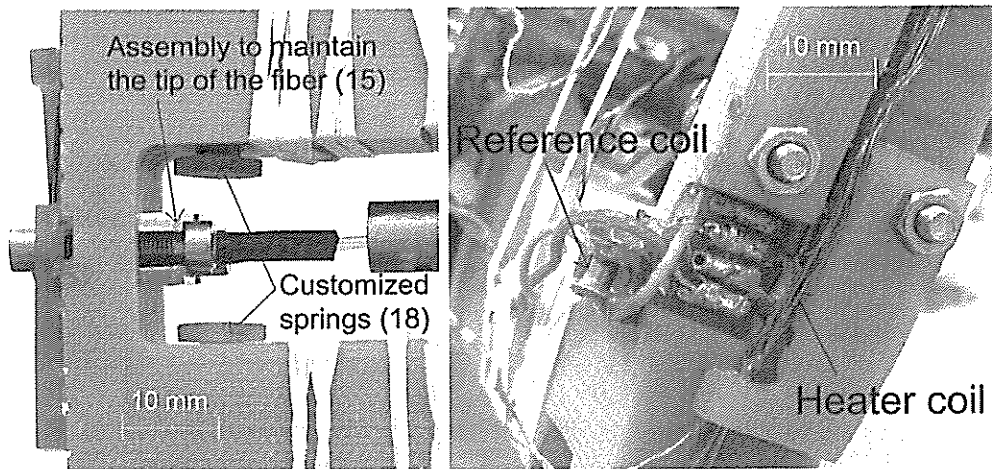
The sample was mounted into a V-shaped groove milled onto a G-10 U-shaped sample holder (see Figure IV.9(a), page 115). The opening angle of the groove is 45° while its maximum depth is 1.5 mm. To avoid any displacements of the sample in its lodging under the Lorentz's force, two G-10 pieces (17) with lugs pushed the wire toward the pit of the groove and two customized springs, made-up of CuBe elastic washers, helped tensioning it (Figure IV.11, page 116). A portion of the sample holder was flattened to receive two adjusting pieces made-up of G-10 (Figure IV.9(b), page 115). These pieces helped to position and maintain the heated portion of the sample in front of the tip of the optical fiber extension.

This assembly was designed to limit the possible displacements of the sample and to control in a reproducible way the distance between the tip of the optical fiber and the surface of the sample.



(a) Bottom view of the sample holder. (b) Flattened part of the sample holder.

Figure IV.9: (a) Bottom view of the G-10 sample holder (20), six voltage taps are soldered to the sample, two G-10 pieces with lug (17) maintain the sample at the pit of the V-shaped groove machined into the sample holder ; (b) flattened part of the sample holder to receive two adjusting G-10 pieces to position the oxidized heated zone in front of the tip of the optical fiber.



(a) Maintaining of the tip of the optical fiber (b) Localization of the coils.

Figure IV.10: (a) metallic assembly to maintain the position of the tip of the optical fiber at a distance of less than 1 mm from the sample to ensure that the entire cone of light strikes the wire surface ; (b) localization of the heater and reference coils.

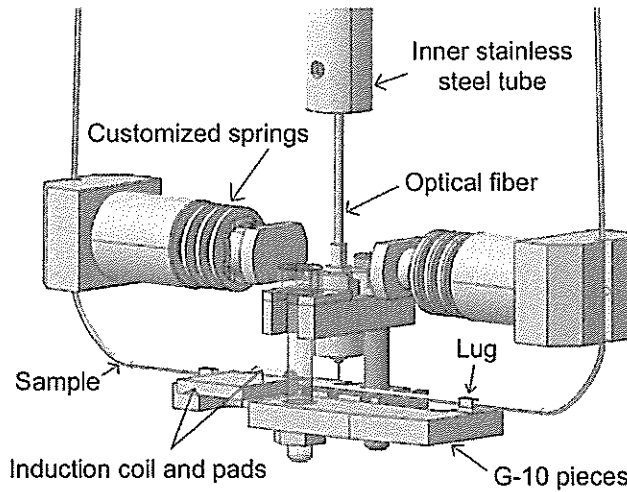


Figure IV.11: Maintaining of the tip of the optical fiber plus the various systems to clamp the sample onto the sample holder. The G-10 sample holder is not shown to better detail the clamping systems.

IV.2.4.3 Positioning of the heaters onto the sample holder

Tip of the optical fiber: A dedicated metallic assembly, depicted in Figure IV.10(a) (page 115), was designed to maintain the tip of the optical fiber in front of the sample at a distance of less than 1 mm. This short distance ensured that the entire cone of light coming out of the fiber illuminates only the wire surface⁸ (see paragraph IV.3.8, page 133). The tip of the optical fiber was located at the center of the active zone of measurements (see Figure IV.9(a) [page 115] and next subsection IV.2.6 [page 120]).

Induction coils: Two induction coils were mounted in series on the sample holder (see Figure IV.10(b), page 115):

- a heater coil (coil 9) with the wire running through it,
- a reference coil (coil 6) with no wire inside.

The heater coil used to excite the wire was located a few millimeters away from the tip of the optical fiber. The reference coil was glued to the sample holder at about ~5 mm above the heater coil (see Figure IV.10(b), page 115). The fixation was necessary to avoid its displacement under the torque developed by the magnetic coupling with the background field. No particular precaution regarding the shielding of the coils has been taken.

Figure IV.11 (page 116) details the different assemblies to position and tension the sample and to maintain the tip of the optical fiber.

⁸As mentioned in the subsection IV.2.2 (page 111), the numerical aperture of the optical fiber extension is 0.22 ± 0.02 corresponding to a cone of light having a half-angle of $\sim 13^\circ$.

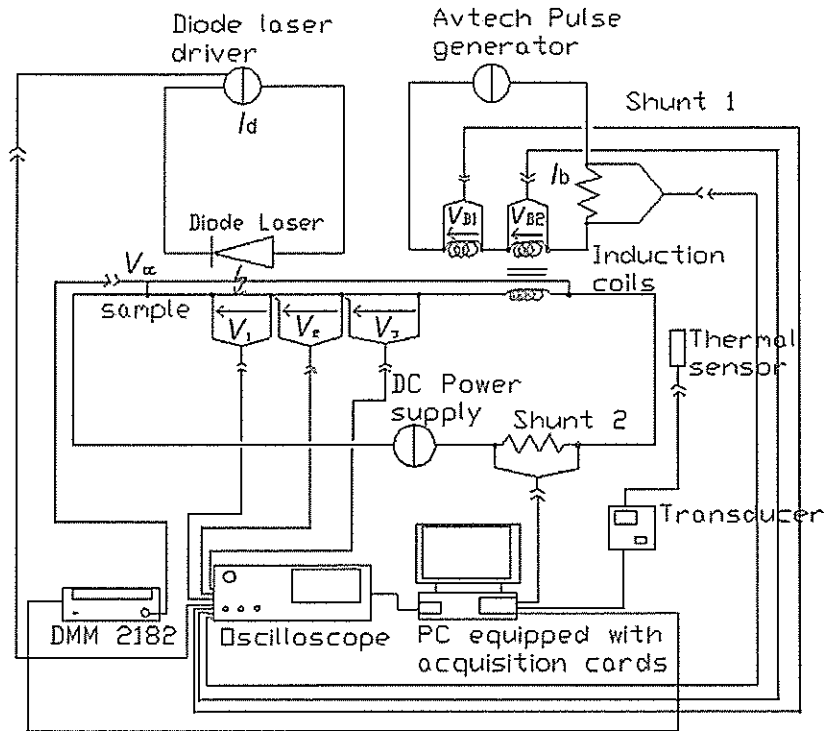


Figure IV.12: Electrical sketch of the acquisition system and the power circuitry. The blue lines correspond to wires for low-voltage measurements, the black lines to power cables and the green lines to RS232 and GPIB cables.

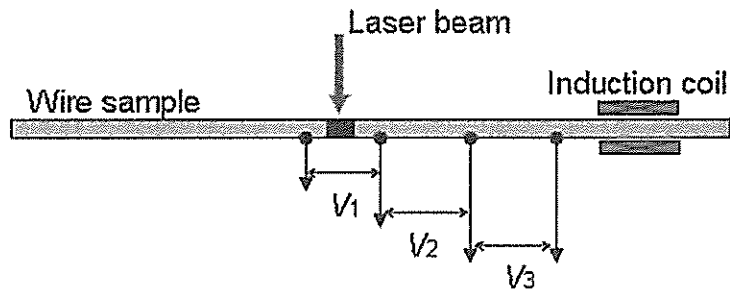


Figure IV.13: Localization of the pairs of voltage taps and of the heaters along the wire sample.

Table IV.3: Distances between voltage taps.

Voltage drops	Distance (mm)
V_{cc}	37
V_1	5.9
V_2	7.2
V_3	7.3

IV.2.5 Electrical equipments, acquisition system and voltage localizations

Figure IV.12 (page 117) shows the electrical sketch of the stability tests. This sketch will be described in the following paragraphs. Details on the localization of the voltage taps, the acquisition system and the various equipments used in the stability tests are also given.

Voltage identification, localizations and data acquisition devices: In addition to the pair of voltage taps, V_{cc} , used for critical current measurements, three other pairs, some with common taps, have been soldered onto the wire, V_i ($i \in \{1, 2, 3\}$), to carry out differential voltage measurements. Voltage drop V_1 records the normal zone generation in front of the tip of the optical fiber while voltage drops V_2 and V_3 are used to assess Normal Zone Propagation Velocity along the sample. Figure IV.13 (page 117) shows the localization of the pairs of voltage taps along the wire sample while Table IV.3 (page 118) gives a summary of typical distances between the pairs of voltage taps. The error on their visual measurements was equal to about ± 0.5 mm. These distances are necessary parameters to estimate the Normal Zone Propagation Velocity from the voltage traces, V_2 and V_3 , and, in some cases, the quenched zone from voltage trace V_1 (see section IV.5.3, page 152). Two additional pairs of voltage taps, V_{B1} and V_{B2} , were also used to record the voltage drops across respectively the reference coil and the heater coil. To calculate the optical energy flowing from the diode laser, the monitored current of the diode laser driver PCX-7410 (Directed Energy, Inc.), I_d , is also recorded through an internal resistance of $50 \text{ m}\Omega$. Similarly, the pulse current of the coils, I_b , supplied by a pulse generator (AV-108A-3-C, Avtech), is measured owing to a calibrated shunt of $50 \text{ m}\Omega$ (shunt 1). Table IV.4 (page 119) summarizes the different voltage drops and their corresponding devices. These devices are detailed in Table IV.5 (page 119). A thermal sensor attached to the bus bars measures through a Voltage-to-Temperature transducer the temperature of the sample during the stability tests. The all set of acquisition equipments is connected to the power network through an isolation transformer.

Electrical power equipments: The transport current, measured with a shunt (shunt 2) in series with the sample, is driven by a water-cooled DC power supply (DRUSH, Germany). This power supply, controlled by an analog ramp generator model A-33 (supplied by Bouhnik, France), can supply up to 1000 A to the sample.

IV.2. NEW SETUP FOR INDUCTIVE AND LASER HEATERS

Table IV.4: Voltage identification, localization, and acquiring devices.

Voltage drop	localization and origin	Use	Acquisition device
V_{cc}	across the wire	critical current measurements	DMM 2182 nano-voltmeter
V_1	across the heated zone	Normal zone generation	Digital oscilloscope DL708
V_2 and V_3	along the wire	Normal Zone Propagation Velocity	Digital oscilloscope DL708
V_{B1}	across the reference coil	energy yielded by the reference coil	Digital oscilloscope DL708
V_{B2}	across the heater coil	energy yielded by the heater coil	Digital oscilloscope DL708
I_b	current of the Avtech power generator	estimation of the two previous energies	Digital oscilloscope DL708
I_d	current of the diode laser driver (monitored current)	estimation of the optical energy	Digital oscilloscope DL708

Table IV.5: Description of the main electrical equipments.

Devices	Brand	Settings
DC power supply	Drush (Germany)	0-1000 A, water cool
Pulse generator AV-108A-3-C	Avtech (Canada)	0-200 A peak (0 to 20 V), squared pulse widths from 1 ns to 1 ms
Laser diode driver PCX-7410	Directed Energy, Inc. (US)	10 mA-10 A (≥ 18 V), squared pulse widths from 1 μ s to 1 ms
DMM 2182 nano-voltmeter	Keithley (US)	integration rate: 83.33 ms, gain: 10^5 , no active filter
Digital oscilloscope DL708	Yokogawa (Japan)	isolated inputs, 10 MS/s, 5 mV/div
Voltage-to-Temperature transducer	Cristel (France)	galvanic isolation, 1.8 K to 77 K at 0-10 V, 1 μ A
Multichannel PC card, RS232	National instrument (US)	PCI-6031E
PC card, GPIB-IEEE 488.2	National instrument	PCI-GPIB

S/s: Samples per second.

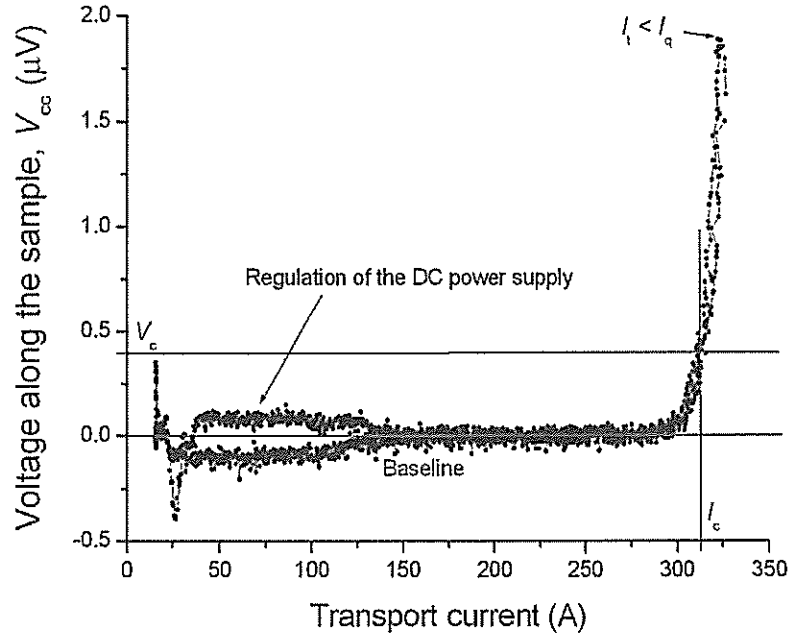


Figure IV.14: V-I characteristic of NbTi sample at 7 T and 4.2 K. The current ramp speed was 65 A/min.

The DMM 2182 nano-voltmeter, the Voltage-to-Temperature transducer, and the voltage taps across the shunt are connected to a multichannel PC card via RS232. A digital oscilloscope Yokogawa DL708 is also connected to the PC via GPIB. The measurements were carried out in differential mode. All devices are controlled by Labview[®] 6.0. The data are subsequently analyzed using Matlab[®] 6.1 and Origin[®] 6.0.

IV.2.6 Current redistribution and definition of the active zone of measurements

At the round edges (having a radius of 8 mm) of the U-shaped sample holder, the current direction, which on the straight vertical parts of the sample holder is aligned with the direction of the background magnetic field, changes. Its direction becomes perpendicular to the field direction over 12.5 mm of sample. In the transition zone, a fraction of the current flows back and forth from the superconducting filaments to the metallic matrix due to inductance shift. This resulting current-transfer causes a slight heat dissipation in the copper matrix of the wire. The $V-I$ characteristic can exhibit a linear region at low transport current until the usual resistive transition is approached.

Our concern was to determine an "active zone of measurements" for which no current-transfer was distinguishable. It would indicate that the redistribution of transport current from the copper matrix into the superconducting filaments is fully completed and that no additional heat sources come into play. Therefore, we arbitrary fixed the distance between the voltage taps at 40 mm out of the 63 mm available. The available length is the useful zone of measurements for which the

direction of the background magnetic field is perpendicular to the wire (see Figure IV.9(a), page 115). For this distance, we checked posteriorly that the shape of the voltage traces during critical current measurements did not present a constant slope at low transport current as it would be expected from current-transfer [6]. Figure IV.14 (page 120) gives an example of such measurements at 7 T, 4.2 K. The voltage was read out from the nano-volmeter while the current was ramped linearly in time [7]. For the first 150 A, some voltage variations appear across the sample. This phenomenon is an artifact of the regulation of the DC current supply. Subsequently, the voltage vanishes and remains zero as long as the voltage transition does not occur and the wire is still superconducting.

In the present case, the critical current is measured equal to 320 A with the electric field criterion of $0.1 \mu\text{V}/\text{cm}$. This value is slightly higher than the value given by Alstom/MSA, thus showing no degradation of the oxidized sample.

IV.3 Determination of the optical energy produced by the diode laser

To determine the real amount of energy absorbed by the sample, it is first necessary to estimate the energy delivered by the diode laser equipped with its optical fiber extension. The following sections will introduce the method used for such a determination. At first, a preliminary series of measurements has been carried out to estimate the influence of the diode laser temperature control, and of the SC connector between the optical fibers on the output optical power.

The diode laser being characterized, a second series of experiments was subsequently carried out to quantify the influence of environmental parameters such as temperature and thermal cycling on the optical transmission of the optical fiber extension. Finally, these parameters were quantified and the optical energy delivered to the sample was accurately estimated.

Before dealing with the influence of these parameters, it is first necessary to describe the optical power versus forward current characteristic of the diode laser and the experimental setup used for its measurement.

IV.3.1 Description of the experimental setup

In addition to a preliminary calibration of the optical energy of the diode laser equipped with its fiber extension carried out at 293 K, a series of measurements for which the temperature of the diode laser was monitored has been also conducted and the results are presented in the next section.

Our goal was to estimate the influence of the temperature of the diode laser on its behavior (see section IV.2.3, page 113).

Figure IV.15 (page 122) shows the experimental setup to carry out these different tests. Current pulses of 100 kHz with a duty cycle of 95% were supplied by the diode laser driver to simulate DC measurements⁹. The optical power was then recorded by a powermeter Fieldmaster¹⁰ and a silicon photodiode disk sensor equipped with

⁹Indeed, it was not easy to replace this driver by a DC power supply in view of our circuitry. It would have led to unnecessary modifications of the experimental setup.

¹⁰This device can also be used as energy meter for pulses ranging from tenths of microseconds to more than 1 s.

IV.3. DETERMINATION OF THE OPTICAL ENERGY PRODUCED BY THE DIODE LASER

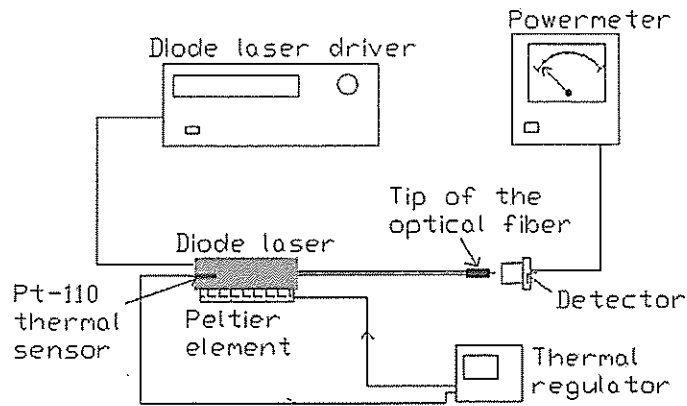


Figure IV.15: Sketch of the experiment to measure the optical power versus forward current characteristic of the diode laser equipped with its optical fiber extension.

a 1000:1 attenuator (all three supplied by Coherent, Inc., US). This attenuator densifies the laser beam before it strikes the semiconductor sensor. Its sensitivity was found independent of its distance to the tip of the optical fiber as long as it was totally illuminated. The best accuracy, which is dependent on the geometrical characteristics of the beam, was reached at the center of the disk.

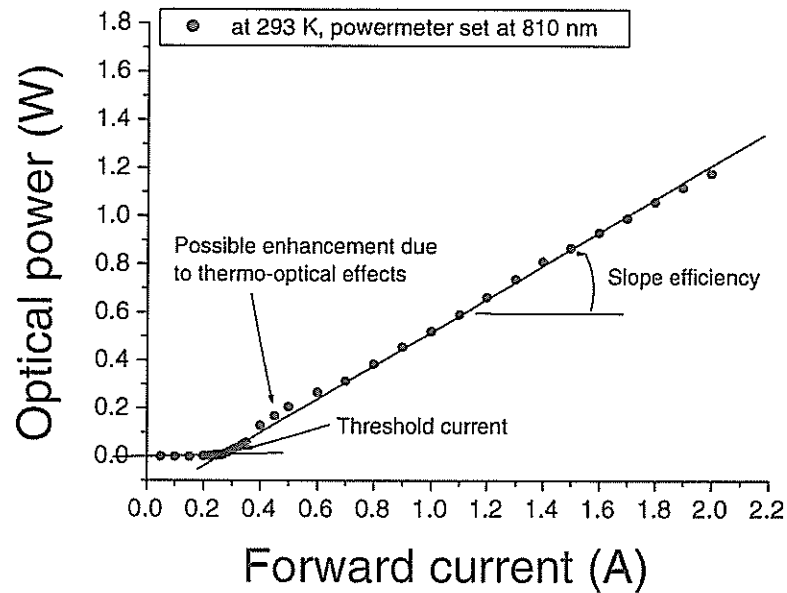
IV.3.2 Characterization of the diode laser

Figure IV.16(a) (page 123) illustrates a typical measurement of the optical power versus forward current characteristic. In this case, it was carried out for a diode temperature of 293 K.

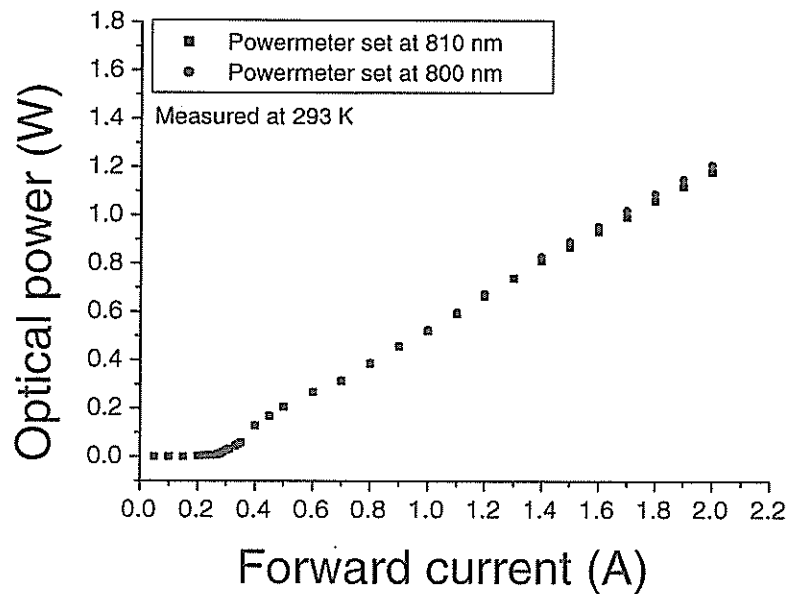
The optical power versus forward current characteristic of diode lasers is constituted of two distinct parts. At first, the diode laser is said to be in a LED phase for which the energy yielded to the junction is not large enough to transit the semiconductor. The emission of light is spontaneous and chaotic resulting in noise and poor efficiency. So, the optical power remains nearly zero at increasing forward current. When this current approaches and passes the so-called threshold current, the creation of photons exceeds the recombinations and the laser effect takes place. Then, there is a boost in the output optical power and the noise level decreases. This boost is intense at first and subsequently decreases slightly with increasing current toward a constant rate of increase. No clear explanation on this slight bumpy shape could be derived from our measurements. It is certainly related to a thermo-optical process which may change the behavior of the quantum cells at increasing current¹¹. According to the manufacturer, a maximum forward current of 10% above the specified maximum current can be used in DC operation, while a larger current can be sustained in single pulse mode [8]. However, this operating mode may age pre-

¹¹A correlated effect would be the appearing of electromagnetic transverse modes in the cavity, which might give a push to the optical power before it disappears at increasing current. However, this interpretation must be taken with cares as no experimental evidences support this hypothesis.

IV.3. DETERMINATION OF THE OPTICAL ENERGY PRODUCED BY THE DIODE LASER



(a) Typical optical power versus forward current characteristic.



(b) Influence of the powermeter settings.

Figure IV.16: Optical power versus forward current characteristic of the diode laser measured at 293 K. (a) typical measurement leading to the determination of the slope efficiency and the threshold current of the diode laser ; (b) influence of the powermeter settings on the optical power measurements.

maturly the diode laser.

From Figure IV.16(a) (page 123), it is possible to estimate the main parameters characterizing the quality of the diode laser. These parameters are: the threshold current and the slope efficiency. The two above mentioned phases, LED and laser, can be approximated by two straight lines of different slopes. In first approximation, the interception of these lines defines the threshold current. We estimate the error in the visual determination of the threshold current at about $\pm 2\%$. From the line of larger slope corresponding to the laser phase, we can derive the slope efficiency. In first approximation, these parameters can be used to calculate the power delivered by the diode laser and, knowing the pulse duration, to estimate the pulse energy. However, it only yields accurate values at large forward currents since the optical power versus current characteristic shows a non-linear behavior near the threshold current. To take into account all the range of forward currents, a different interpolation of the data was implemented, which is further discussed in the section IV.3.7 (page 129).

IV.3.3 Setting of powermeter and accuracy of measurements

To reach the best accuracy on the optical power versus forward current measurements, it is necessary to set the powermeter at a wavelength corresponding to the laser wavelength.

Laser wavelengths shift with temperature. For diode lasers in the range of 800 nm, it is ~ 0.3 nm/K at most [8]. In our case, the temperature of the diode laser was monitored at ± 5 K around 293 K. So, the corresponding variation of wavelength was at most 3 nm inferior to the 807 nm given by the manufacturer at 298 K. This variation is still in the range of ± 10 nm corresponding to the accuracy of the laser wavelength and the sensitivity of ± 10 nm of the powermeter. This statement was checked by performing two measurements at 293 K for two different wavelength values set on the powermeter. The results are given in Figure IV.16(b) (page 123). These values surround the ~ 805.5 nm $[(807-3) \text{ nm/K} \times 5 \text{ K}]$ of the diode laser at this temperature. A different setting of the receptor wavelength leads to a different slope efficiency. This difference was roughly quantified equal to ~ 0.002 W/A/nm, which can be neglected compared to the slope efficiency values given in Table IV.6 (page 126). In addition, for these different settings of the powermeter, no change was observed on the threshold current. Therefore, we fixed the wavelength of the powermeter at 810 nm for all subsequent measurements performed on the diode laser and its optical fiber extension.

IV.3.4 Influence of the connection between the optical fiber extension and the pre-coupled optical fiber

Data from the manufacturer, provided at 298 K, were also compared to our measurements at the same temperature. The results are given in Figure IV.17 (page 125). As expected, the threshold currents correspond. However, a discrepancy of $\sim 16\%$ was estimated between the slope efficiency given by the manufacturer and our estimation. This discrepancy is thought to be related to the presence of the SC connector between the two optical fibers. It is well within the range of typical losses in such connectors (from 10% to 20%) [9].

IV.3. DETERMINATION OF THE OPTICAL ENERGY PRODUCED BY THE DIODE LASER

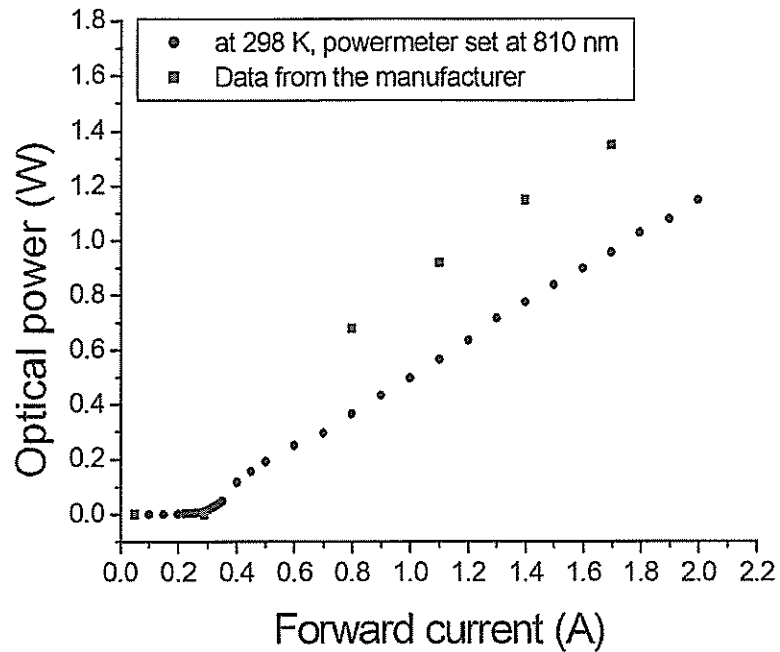


Figure IV.17: Influence of the connector on the optical power versus forward current characteristic of the diode laser.

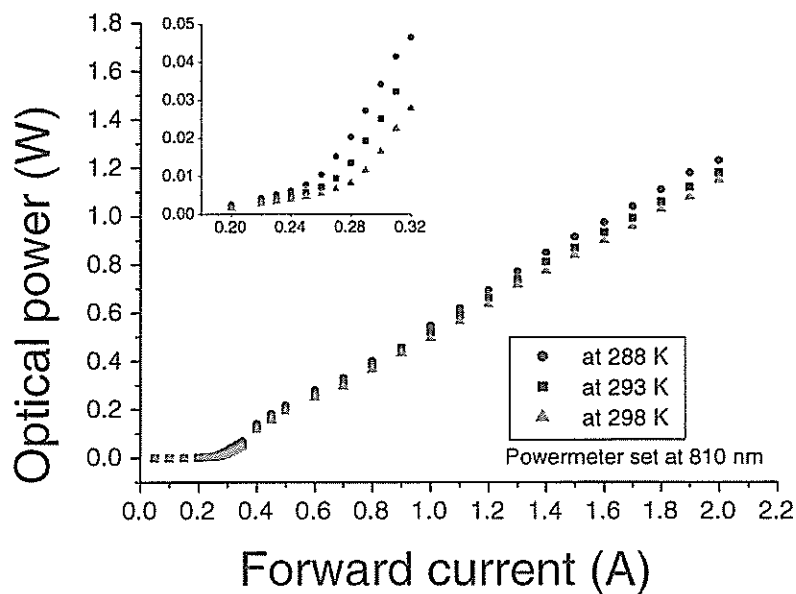


Figure IV.18: Influence of the temperature on the optical power versus forward current characteristic of the diode laser.

IV.3. DETERMINATION OF THE OPTICAL ENERGY PRODUCED BY THE DIODE LASER

Table IV.6: Summary of salient parameters of the diode laser.

Temperature of the diode laser (K)	Wavelength set on the powermeter (nm)	Threshold current (A)	slope efficiency (W/A)
298 ^a	807 (laser wavelength)	289	0.776
288	810	255	0.705
293	810	270	0.690
298	810	280	0.660
293	800	270	0.710
77 ^b	810	270	0.670

^aData provided by the manufacturer.

^bTemperature of the optical fiber extension.

IV.3.5 Influence of the temperature control of the diode laser

Figure IV.3.3 (page 125) summarizes measurements taken at three different temperatures of the diode laser: 288 K, 293 K and 298 K. These temperatures were controlled owing to a Peltier element.

It appears that the slope gets steeper at lower temperatures and that the threshold current decreases slightly. This implies that the laser effect appears at lower forward currents and that larger output optical powers are reached for the same forward current. We estimate the influence of the temperature to be ~ 2.5 mA/K on the threshold current and ~ 4 mW/A/K on the slope efficiency. Table IV.6 (page 126) summarizes the results of the various measurements that were carried out.

In continuous mode operation, for which the temperature can increase by a few tens of degrees, it is necessary to stabilize the temperature of the diode to maintain its beam quality.

IV.3.6 Parameters influencing the behavior of optical fibers

The previous section dealt with various parameters which have to be taken into account for a typical diode laser characterization. In our application, however, additional factors may change the optical power versus forward current characteristic of the diode laser equipped with its optical fiber extension. Indeed, the optical fiber extension is partially immersed into a cryogenic environment which can induce additional transmission losses.

In the following section, we briefly review the different parameters which can influence the behavior of the optical fiber during our tests. These parameters are:

- cryogenics,
- mechanical stress,
- electromagnetic environment.

Except for the subsequent paragraph on the influence of cryogenic environment, we mostly restrain our discussion to general facts. Indeed, very few experiments have been purposely carried out to quantify the influence of the other parameters.

IV.3. DETERMINATION OF THE OPTICAL ENERGY PRODUCED BY THE DIODE LASER

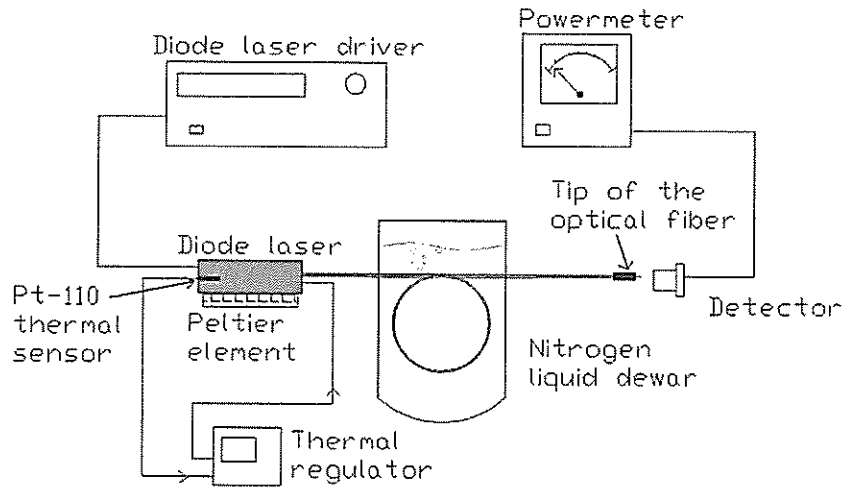


Figure IV.19: Schematic drawing of the test carried out to study the influence of the cryogenic environment on the optical fiber.

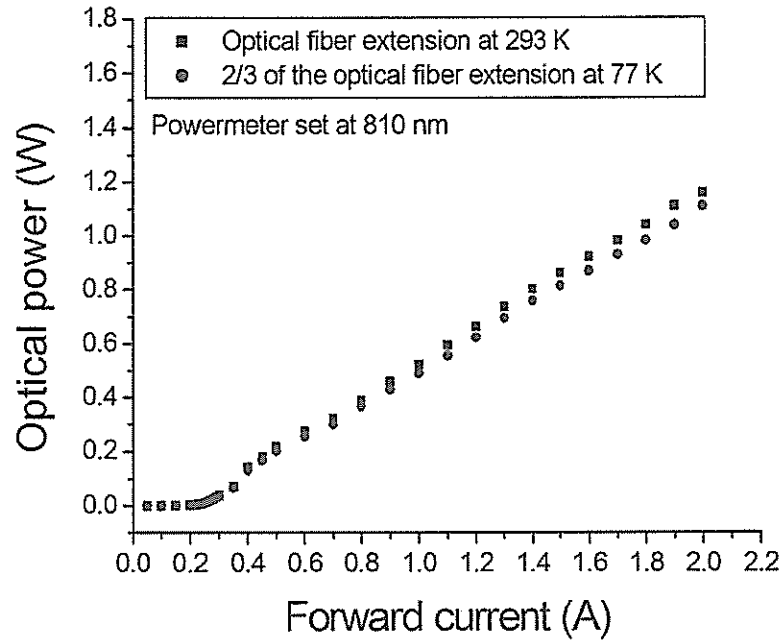
Cryogenic environment: At low temperature, the optical fiber is partly wetted by liquid helium. So, a thermal gradient of about 289 K develops along the fiber. To the best of our knowledge, no thorough investigation of the light transmission of standard glass optical fibers in the presence of a cryogenic fluid has been carried out so far. Consequently, we did the following simple investigation. At first, we performed a simple visual check by dipping the optical fiber extension into liquid nitrogen. No dispersion of the beam was observed. Then, we measured the characteristic of the diode laser with 2/3 of the optical fiber extension immersed into liquid nitrogen (see Figure IV.19, page 127). This wetted length would correspond to the maximum length of the optical fiber in the cryostat for which the temperature is below ~ 110 K.

Figure IV.20(a) (page 128) shows a comparison of the measurements at room temperature and in boiling liquid nitrogen at 77 K. No difference was observed on the threshold current. However, there appears to be a decrease in the slope efficiency of $\sim 5\%$ corresponding to a discrepancy of ~ 0.2 mW/A/K. This discrepancy is likely to be of mechanical origin rather than purely temperature dependent. Following this assumption, since most of the thermal shrinkage happens between room temperature and ~ 100 K, the behavior of the optical fiber must become independent of the temperature below that. Nevertheless, extrapolating the previous value of ~ 0.2 mW/A/K from 77 K to 4.2 K, we find a slope efficiency decrease of ~ 0.015 W/A, which can be neglected compared to the slope efficiency of ~ 0.627 W/A found at 77 K.

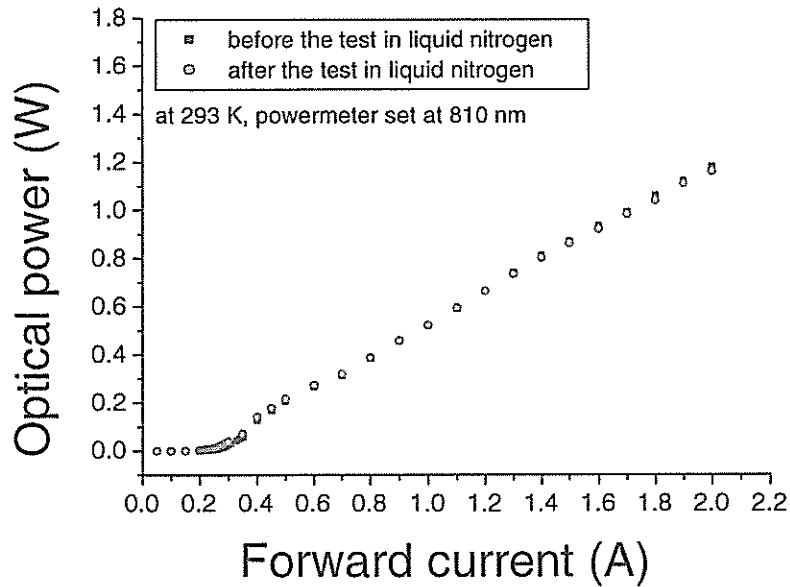
So, it appears relevant to use the optical power versus forward characteristic of the diode laser at 77 K to calculate the optical pulse energy flowing from the tip of the extension optical fiber instead of our preliminary measurements at 293 K.

Mechanical stress and cracks: Optical fibers are highly stress sensitive. Cracks in silica can easily occur thereby modifying the behavior of the entire wave guide. Even if the processes of fabrication reduce most of the defects, some flaws remain

IV.3. DETERMINATION OF THE OPTICAL ENERGY PRODUCED BY THE DIODE LASER



(a) Comparative measurements at 293 K and 77 K.



(b) Reproducibility of the measurements after thermal cycling the optical fiber extension.

Figure IV.20: Influence of the cryogenic environment on the optical fiber. (a) measurements carried out while 2/3 of the optical fiber extension was immersed into boiling liquid helium and at room temperature ~ 293 K. (b) influence of thermal cycling on the optical fiber extension.

which may result in the propagation of cracks due to harsh environments. Bending stresses are likely to be the main origin of aging during storage or operation. For the pre-coupled fiber [9], the minimum radius of curvature at room temperature, recommended by the manufacturer, is ~ 7 cm. It is about 14 cm for the optical fiber extension [10]. These values are lower at cryogenic temperatures as the thermal shrinkage reduces the mechanical toughness of the brittle glass material. In our design, we were very careful to avoid excessive bending by maintaining the fiber straight.

However, this does not prevent the fiber from aging due to thermal cycling. The resulting mechanical cycling can create and propagate cracks as well¹². So, we have left some slack in the mounting of the optical fiber extension so as to accommodate differential thermal shrinkages.

If we refer to the literature, very few mechanical studies in the presence of cryogenic coolant have been performed (see Matthewson's works on the mechanical aging of Silica optical fibers [12]). So, we carried out a simple experiment by cycling a few times the optical fiber to liquid nitrogen. The results are presented in Figure IV.20(b) (page 128). There is a slight difference in the threshold current (~ 10 mA) and the slope efficiency (~ 0.015 W/A). However, it stays within the error of measurements and no conclusion can be reasonably drawn from these results. For a systematic study, further experiments are necessary. For now, we shall neglect the influence of thermal cycling of the optical fiber.

Background magnetic field: Silica being non-magnetic and standard fibers being designed to be weakly sensitive to magnetic disturbances, we did not observe any influences of the background magnetic field during our various stability tests.

IV.3.7 Estimation of the optical energy flowing from the optical fiber

The optical power versus forward current characteristic measured for a diode laser temperature of 293 K and 2/3 of the optical fiber extension wetted by liquid nitrogen is our reference plot to estimate the optical energy. In our experiment, a current pulse is supplied to the diode laser. Then, this current pulse is converted into an optical power pulse that strikes the wire sample. To determine the optical energy that is deposited, we simply have to integrate the time evolution of the optical power pulse calculated from the current pulse using the characteristic.

In this subsection, these different operations are chronologically presented:

- interpolation of the optical power versus DC forward current characteristic,
- conversion of current pulse into optical power pulse,
- Integration of the optical power pulse to estimate the pulse energy.

Interpolation of the optical power: To estimate the optical power flowing out of the tip of the optical fiber following the variation of forward currents, we did not

¹²Possible water condensation on the fiber during warming up of the experiment is not taken into account even if hydroxide ions OH^- participate actively in the growth of cracks and may accelerate consequently the aging of the fiber [11].

IV.3. DETERMINATION OF THE OPTICAL ENERGY PRODUCED BY THE DIODE LASER

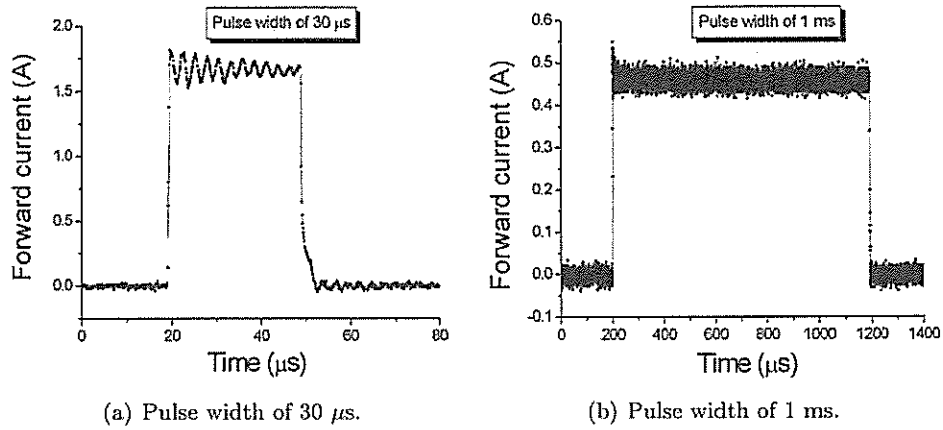


Figure IV.21: Examples of current pulses for two different pulse durations.

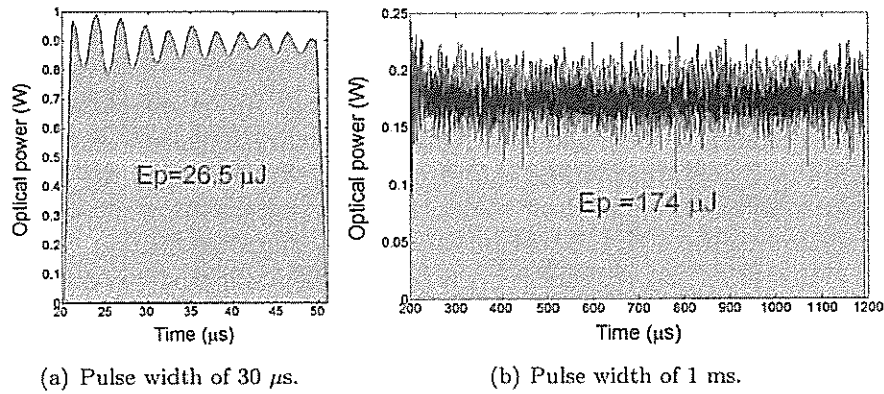


Figure IV.22: Optical power pulses resulting from numerical treatment of the current pulse data of Figure IV.21. Also marked on the plots is the total integrated energy.

IV.3. DETERMINATION OF THE OPTICAL ENERGY PRODUCED BY THE DIODE LASER

Table IV.7: Minimum pulse durations achieved with the diode laser.

	80% of I_c	85% of I_c
5 T	30 μ s	20 μ s
6 T	30 μ s	20 μ s
7 T	40 μ s	30 μ s

use a linear interpolation as could have been suggested by Figure IV.16(a) (page 123). This linear interpolation could not approximate with accuracy the behavior of the diode laser at low forward currents. The best fit, over the all range of forward current, was achieved by a cubic spline interpolation. Further discussions are given in Appendix C (page 238).

Current pulse and resulting optical power: The current pulse used to trigger quenches in wire samples is a square-shaped pulse having a short rise and fall-times of less than 1 μ s. The minimum achievable pulse durations, which depend on the maximum admissible output power of the diode laser, are given in Table IV.7 (page 131)¹³. The maximum pulse duration was up to 2 ms in order to remain within the pseudo-plateau characterizing the Minimum Quench Energy. Two examples of current pulses corresponding to two different pulse durations are given in Figure IV.21 (page 130).

This current pulse is transformed into an optical power pulse using the optical power versus forward current characteristic of the diode laser with the optical fiber dipped into liquid nitrogen at 77 K. Figure IV.22 (page 130) is the resulting output corresponding to Figure IV.21 (page 130). This plot is subsequently integrated to estimate the pulse energy flowing from the tip of the optical fiber.

Calculation of the optical energy: After converting the current pulse into an optical power pulse, P_{opw} , the optical energy pulse, E_p , flowing from the tip of the optical fiber is integrated using a trapezoidal method:

$$E_p = \int_{\tau_p} P_{opw} dt \quad [\text{J}] \quad (\text{IV.1})$$

where τ_p is the pulse duration. The error on the numerical estimation of the pulse energy, which was evaluated by adjusting the time of integration, is less than $\sim 1\%$. This energy pulse is different from the energy really absorbed by the illuminated sample. Only a fraction of this energy is really dissipated ; this point is discussed in the next section IV.3.8 (page 134).

IV.3.8 Estimation of the energy absorbed by the sample

In the following section, we introduce some considerations on light scattering by liquid helium and we briefly deal with the optical behavior of the sample.

¹³95% of I_c is not given since we used the limit estimated at 85% of I_c .

IV.3. DETERMINATION OF THE OPTICAL ENERGY PRODUCED BY THE DIODE LASER

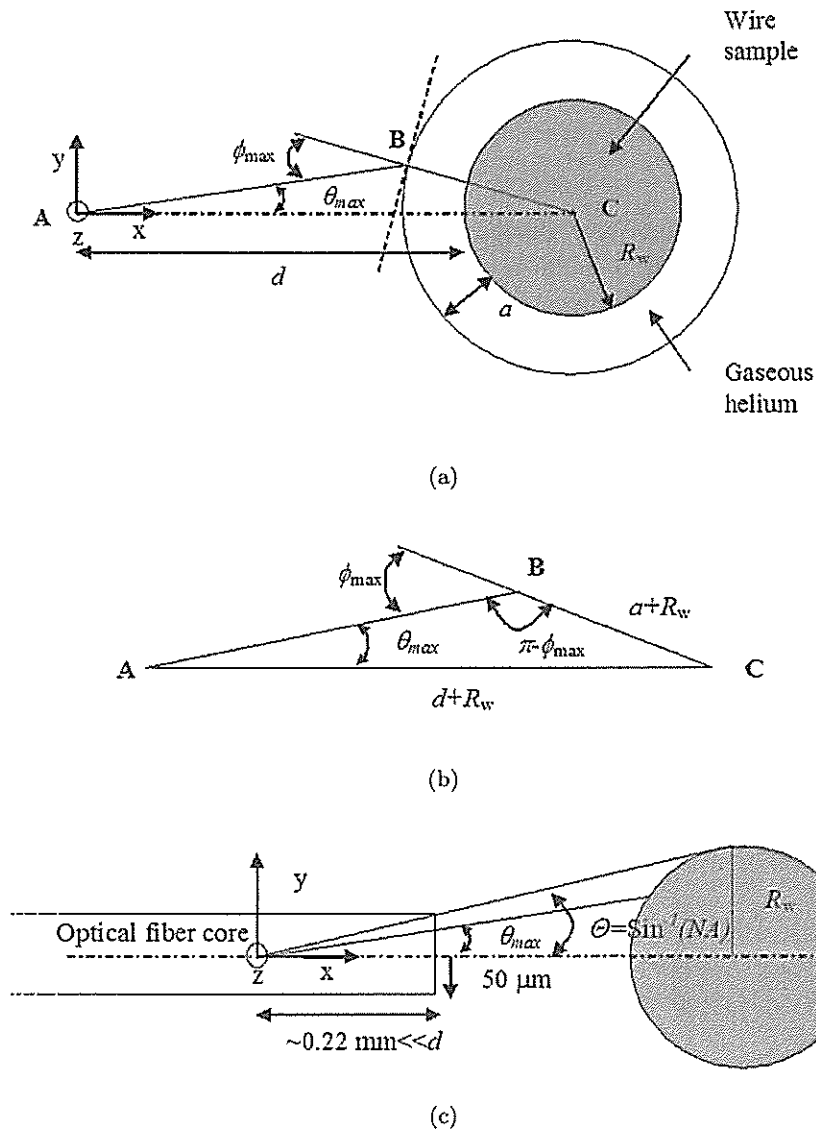


Figure IV.23: Definition of the different parameters to estimate the thickness of gaseous helium resulting in a total reflection of the outer rays of light flowing from the tip of the optical fiber (not to scale). (a) intersection of a ray of light and gas-liquid helium interface, (b) magnified triangle (ABC), (c) representation of the optical fiber extension and sample.

Refractive index of helium and light scattering: For low temperature measurements, the laser beam flowing out of the tip of the optical fiber extension propagates in liquid helium before striking the surface of the sample and interacting with it. The optical properties of this medium may induce some scattering and diffusion. A priori, the liquid helium scattering can be assumed to be relatively weak. The fluctuations of refractive index are due to density fluctuation in the liquid (as vortexes), which turns into light scattering [13]. Therefore, as long as the power dissipated inside the superconducting wire sample does not lead to a phase change in the bulk of helium, the light propagates in the liquid helium with a low diffraction. The refractive index of liquid helium I at 4.2 K is $n_1 \simeq 1.0245$ while the refractive of cold gaseous helium is $n_2 \simeq 1.0034$ [14].

If a film of vapor forms near the surface of the wire sample, the ray of light coming from the liquid will be diffused at the liquid-gas interface. As an example illustrating the influence of gaseous helium, let us consider the geometry illustrated in Figure IV.23 (page 132), which is representative of the actual experimental setup. Starting from Figures IV.23(a) and IV.23(b) (page 132), let us estimate the maximum half-angle θ_{\max} of the cone of light flowing from the tip of the optical fiber extension as a function of the thickness of the vapor film, a , such that the outer rays of light are back reflected at the helium-gas interface. To simplify the model, we assume that all rays of light flowing from the optical fiber tip cross at the apex of the cone of light corresponding to the numerical aperture of the optical fiber extension. In addition, we do not consider the nucleation of helium bubbles (for more information on helium scattering and boiling helium, see reference [15]).

At the liquid-gas interface, Descarte's law yields the maximum angle of incident ray of light, ϕ_{\max} , such that there is total reflection:

$$\phi_{\max} = \arcsin\left(\frac{n_2}{n_1}\right) \quad (\text{IV.2})$$

A numerical application gives a maximum angle of 78° . Using relations in a triangle, we can write:

$$\frac{\sin(\theta_{\max})}{(R_w + a)} = \frac{\sin(\phi_{\max})}{(R_w + d)} \quad (\text{IV.3})$$

In our case, d is the maximum distance between the apex of the cone of light and the sample. This distance is such that the outer rays of the cone of light corresponding to the numerical aperture of the optical fiber strike the wire surface as described in Figure IV.23(c) (page 132), then:

$$d = \frac{R_w}{\tan(\Theta)} \quad [\text{m}] \quad (\text{IV.4})$$

where $R_w \simeq 0.412$ mm is the radius of the wire sample. A numerical application gives $d \simeq 1.8 \times 10^{-2}$ m. In first approximation, this distance can be considered as the distance between the optical fiber tip and the sample since the distance between the apex of the cone of light and the sample (~ 0.22 mm) is negligible compared to d (see Figure IV.23(c), page 132). The different parameters of the calculations can be found in Table IV.8 (page 134).

Finally θ_{\max} is given by:

$$\theta_{\max}(a) = \arcsin\left[\left(\frac{R_w + a}{R_w + d}\right) \sin(\phi_{\max})\right] \quad (\text{IV.5})$$

IV.3. DETERMINATION OF THE OPTICAL ENERGY PRODUCED BY THE DIODE LASER

Table IV.8: Parameters of calculation.

Half-angle corresponding to the numerical aperture of the optical fiber extension, Θ	$\sim 13^\circ$
Distance between the apex of the cone of light and the sample, d	≤ 1.8 mm
Radius of the wire sample, R_w	~ 0.412 mm
Refractive index of liquid helium at ~ 4.2 K, n_1	~ 1.0245
Refractive index of cold gaseous helium, n_2	~ 1.0034
Incident angle for total reflection of the rays of light at the liquid-gas interface, ϕ_{\max}	78°

Figure IV.24 (page 135) shows the evolution of θ_{\max} as a function of a . The line defines the limit between total reflection and penetration of the outer rays of light of the cone of light. The rays of light having a half-angle larger than the limit of total reflection are back reflected while those of smaller half-angles penetrate the helium bubble. θ_{\max} ranges from $\sim 10.5^\circ$ for a thickness of $\sim 1 \mu\text{m}$ to 13° corresponding to the numerical aperture NA of the optical fiber extension for a thickness of $\sim 130 \mu\text{m}$. Then, at $\sim 1 \mu\text{m}$, the rays of light having an angle between $\sim 10^\circ$ and $\sim 13^\circ$ are totally reflected and do not reach the wire sample. For thicknesses over $\sim 100 \mu\text{m}$, all the rays of light flowing from the optical fiber extension cross the liquid-gas interface. Over the range of gaseous helium thicknesses, the variation $\Theta - \theta_{\max}$ is small. Hence, only a small fraction of rays of light are lost at the early stage of vapor helium formation. Practically, we have chosen to reduce as much as technically possible¹⁴ the distance d (as discussed in paragraph IV.2.4.3, page 116). Indeed, reducing this distance increases the number of outer rays of light penetrating the gas-liquid helium interface. For example at a thickness of $\sim 1 \mu\text{m}$, the distance d for which the whole cone of light penetrates the gaseous helium is of the order of 1.4 mm.

At short pulse durations for which the power pulse must be large to trigger a quench, a vapor of gaseous helium is likely to form rapidly over the surface of the sample and light scattering may occur during the deposition of the energy disturbance. However, at longer pulse durations ($\geq 100 \mu\text{s}$ and more) for which the power pulse necessary to trigger a quench is accordingly smaller, a film of gaseous helium may not form during the initial energy pulse release. Nevertheless, helium bubbles are expected to occur early during the initial disturbance which induce light scattering.

A rigorous calculation would be necessary to quantify the real amount of light intensity illuminating the wire surface and effectively absorbed in liquid helium conditions. It was not carried out in this context.

¹⁴To avoid such an issue, it is possible to collimate the laser beam by using a collimating or focusing lens at the outlet of the optical fiber extension.

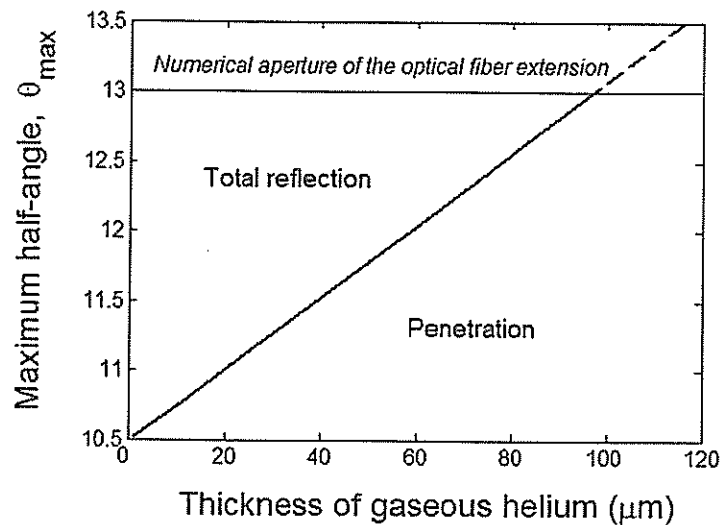


Figure IV.24: Estimation of the maximum half-angle of the cone of light for which the outer rays are totally reflected as a function of gaseous helium thickness.

Optical behavior of the sample and coefficient of optical absorption, ϵ : The energy flowing out of the tip of the optical fiber extension is deposited onto the sample. However, all this energy is not absorbed and a significant fraction of it may be reflected. This section introduces briefly the coefficient of absorption used to quantify the amount of absorbed energy. This coefficient will be determined using a specific experiment which is described in section IV.4 (page 136).

The interaction between laser beam and matter leads to a certain amount of absorbed light. This amount is quantified by a coefficient of absorption, ϵ which ranges from 0 to 1. This coefficient is defined as the ratio between the average absorbed radiant power and the total radiant power. It mainly depends on the physical properties of the material, which are often magnetic field and temperature dependent. It also depends on the surface cleanness and roughness of the material. However, it does not depend on the intensity of coherent light.

In our case, it is quite difficult to estimate a priori this coefficient. Indeed, the thickness of the heterogeneous oxide layer and its crystallographic structure are unknown. Due to the thinness of the oxide layer, the copper material is likely to participate in the absorption and reflection of light.

This oxide layer is composed of different semiconductors ; the optical properties of such materials differ from metals [16] and rely on a specific phenomenology [17]. This issue was not investigated in the present work.

Uncertainties related to sample geometry and proximity of the optical fiber tip: The short distance between the tip of the fiber and the sample [18] and the fact that the fiber is multi-mode (core of 100 μm diameter) [5] lead to a non-homogeneous spatial distribution of the optical power in the material due to optical interferences. Besides, as the laser beam diverges at the outlet of the optical fiber tip, it forms a cone which strikes the surface of the round wire sample. Consequently,

IV.4. CALIBRATION OF THE OPTICAL ENERGY ABSORBED BY THE OXIDIZED SAMPLE

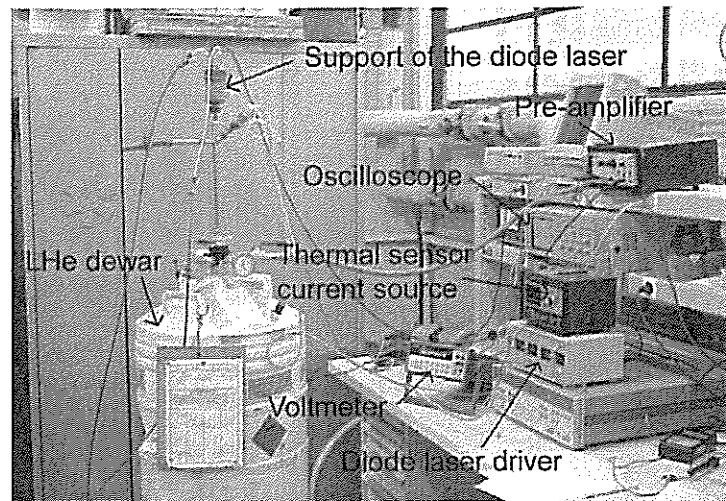


Figure IV.25: Experimental setup used to perform calibration measurements at CRTBT/CNRS with two types of bolometers at 0 T and liquid helium temperature.

the rays of light coming from the optical fiber reach the sample at various angles. It results in an angle distribution between rays of light and normals to the wire surface which ranges from 0° to 90° . At 0° angle, the maximum optical power is absorbed while there is no more absorption at a certain angle depending on the refractive indexes of copper and helium (analogous to the developments carried out in the previous paragraph IV.3.8, page 133).

These parameters must be taken into account to estimate the energy really absorbed by the sample. But, there are no simple ways to model this and, especially, to estimate the refractive index of copper at cryogenic temperature under magnetic field. To circumvent this difficulty, we decided to perform a direct calibration of the coefficient of optical absorption using a calorimetric method.

IV.4 Calibration of the optical energy absorbed by the oxidized sample

This section deals with the experimental determination of the coefficient of optical absorption of the oxidized sample. It is an experimental calibration of the amount of energy really absorbed by the sample. As already mentioned, no attempt on a theoretical study was carried out within the framework of this investigation.

The main issue in our experiment is to assess the amount of energy absorbed by the sample. Various means can be used to perform such a calibration. Among the different possibilities, we have chosen to rely on the technology of metallic bolometers because of its simplicity and its low cost. Bolometers are thermal detectors which belong to the family of optical devices converting the absorbed fraction of incident radiation into a measurable signal through a thermal process. Thus, they convert the incident optical power into heat. Their active part must have a low specific heat capacity to enable a sensitive measurement of temperature variation due to the interaction between light beams and matter. This variation is then transformed into

IV.4. CALIBRATION OF THE OPTICAL ENERGY ABSORBED BY THE OXIDIZED SAMPLE

Table IV.9: Salient parameters of the single-mode diode laser at 298 K used for calibration measurements at CRTBT/CNRS.

Maximum continuous output power (mW)	300
Maximum current (mA)	900
Diameter of the optical fiber (μm)	150
Peak wavelength (nm)	840

a voltage drop, using a thermal sensor that can be easily recorded.

The present work essentially demonstrates the feasibility of such techniques, although the influence of some parameters as background magnetic field and laser wavelength could not be evaluated at the time. Also, the technology could not be used at CEA/Saclay in the setup of the stability experiment since we could not achieve the necessary vacuum.

IV.4.1 Experimental setup

As mentioned above, the bolometer assembly was first designed to be assembled onto the stability experiment to carry out measurements in a vacuum and magnetic field. However, due to heat leak issues, this assembly had to be slightly modified to be incorporated into a different experimental setup.

The probe, on which the bolometers were assembled, was implemented on the original setup designed by F. Ayela at the CRTBT/CNRS in Grenoble [19]. The setup has been modified to house the bolometer. Measurements at 0 T in a vacuum could be carried out at an operating temperature of ~ 4.6 K. This temperature is slightly above the temperature of the sample of ~ 4.2 K during the stability measurements in liquid helium at CEA/Saclay. This difference, which may simply be an artifact due to the quality of the fit used to convert the resistance variation of the thermal sensors into a temperature response, is assumed to have a minor influence on the determination of the coefficient of absorption.

The CRTBT/CNRS probe is made-up of a long stainless steel tube, which connects the support of the diode laser to the vacuum box in which the experiment is carried out. Figure IV.25 (page 136) presents an overview of the experimental setup during one of the bolometer tests. The support of the diode laser was made-up of copper material and included a water exchanger to control the temperature of the diode laser. The vacuum chamber, which is not described here, was drilled to receive two copper rods providing a support to the bolometers and improving its cooling.

IV.4.2 Diode laser used for the calibration

The diode laser, used to estimate the coefficient of absorption of the sample, was water-cooled at a steady temperature of $\sim 15^\circ\text{C}$. The main characteristics of this diode laser, LCW 100F supplied by LaserDiode Inc., are given in Table IV.9 (page 137). It emits in the near infrared region, but, at a laser wavelength of ~ 840 nm, which

IV.4. CALIBRATION OF THE OPTICAL ENERGY ABSORBED BY THE OXIDIZED SAMPLE

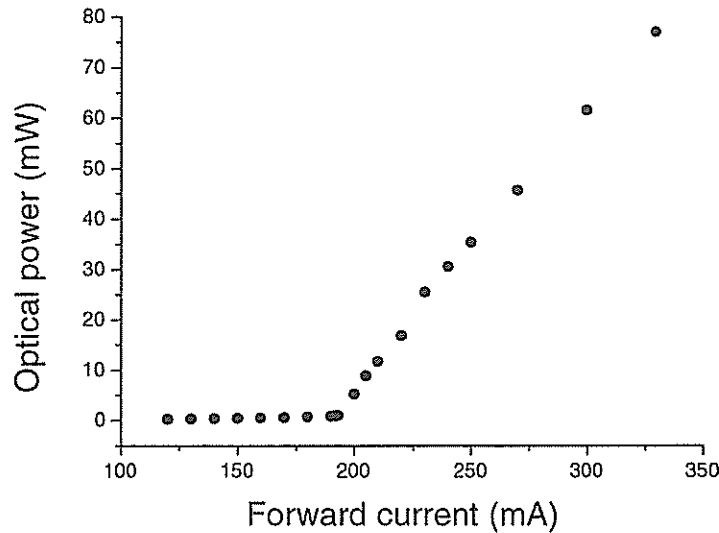


Figure IV.26: Optical power versus forward current characteristic of the diode laser used for calibration measurements at CRTBT/CNRS in Grenoble (Data communicated by F. Ayela).

is about 30 nm larger than for the diode laser used in stability experiment at CEA/Saclay. To be thorough, we would need to study the impact of the wavelength of the laser on the coefficient of optical absorption. It has been shown in the literature that, depending on the thickness of the oxidized layer and its composition¹⁵, it may have some influence [21][22]. In addition, the output optical power of the CRTBT/CNRS diode laser is smaller by one order of magnitude (see table IV.2, page 110). However, as already indicated, the absorption coefficient should not depend on the light beam intensity.

The following Figure IV.26 (page 138) gives the output optical versus forward current characteristic of this diode laser.

IV.4.3 Description of the bolometers

Two different types of bolometers were used for the calibration:

- a closed bolometer (see Figure IV.27(a), page 140),
- a cylindrical bolometer (see Figure IV.27(d), page 140).

The closed bolometer absorbs totally the optical power yielded by the diode laser, while the cylindrical bolometer absorbs only a fraction of this power. The determination of this fraction enables one to evaluate the coefficient of absorption of the sample. This coefficient is subsequently used to determine the amount of energy absorbed by the sample. The geometry of the sample and its physical properties are

¹⁵The spectral localization of the absorption edge, which corresponds to a rapid change in the light absorption of semiconductors [20], depends on the physical properties of the thin oxide film, and on its temperature as well.

IV.4. CALIBRATION OF THE OPTICAL ENERGY ABSORBED BY THE OXIDIZED SAMPLE

Table IV.10: Salient design parameters for the closed bolometer.

Parameters	Notation	Values (units)
Temperature of heat sink and initial temperature	T_0	~ 4.6 K
Average length of the two tinned copper wires set in parallel	l_{TD}	$\sim 4.5 \times 10^{-2}$ m
Average cross-section of the two tinned copper wires (diameter per wires of 0.4 mm)	A_{TD}	2.5×10^{-7} m ²
Total length of stainless steel support	l_{SS}	15×10^{-3} m
Average cross-section of the the stainless steel support for a diameter of 1 mm	A_{SS}	7.9×10^{-7} m ²
Volume of the closed bolometer	ϑ_B	$\sim 10^{-6}$ m ³
Length of the wire sample (see Figure IV.27(d) page 140)	L_w	$\sim 14 \times 10^{-3}$ m

included into this coefficient. The copper material of the bolometers is identical to the one used in the manufacturing of superconducting wires. In addition, to match the properties of the wire surface, the bolometer parts subjected to the light beam have been similarly oxidized at CERN. Subsequent sections will describe the two metallic bolometers whose pictures can be found in Figure IV.27 (page 140).

First experiment, closed bolometer: The design selected for the so-called closed bolometer has been worked out so that the temperature rise of the detector does not extend beyond ~ 30 K. The result is shown in Figure IV.27(a) where the optically-active part and the copper shell can be clearly seen. The tip of the optical fiber, guiding the light from the diode laser located at room temperature to the bolometer, is inserted on top of its copper shell. It is assumed that this closed shape absorbs most of the optical energy. The losses due to the absorption of the metallic tip and possible rays of light coming out of the bolometer, if any reflections occur, are assumed to be negligible. The temperature variations of the optically-active part were measured using a small thermal sensor (cernox[®] bare chip technology [23]). Figure IV.27(b) shows the fully-assembled bolometer. The copper shell is supported by a stainless steel support. Figure IV.27(c) is a side view of the previous picture. It shows the optical fiber glued to the copper shell. This picture shows also a set of tinned copper wires which have been soldered to the copper shell and the thermal sink. They were used as a thermal drain to optimize the time constant and the sensitivity of the bolometer. Figure IV.27(e) (page 140) gives a detailed schematic overview of the closed bolometer.

Table IV.10 (page 139) summarizes salient parameters of the bolometer to achieve a response time of a few seconds with a sensitivity of few milli-kelvins.

IV.4. CALIBRATION OF THE OPTICAL ENERGY ABSORBED BY THE OXIDIZED SAMPLE

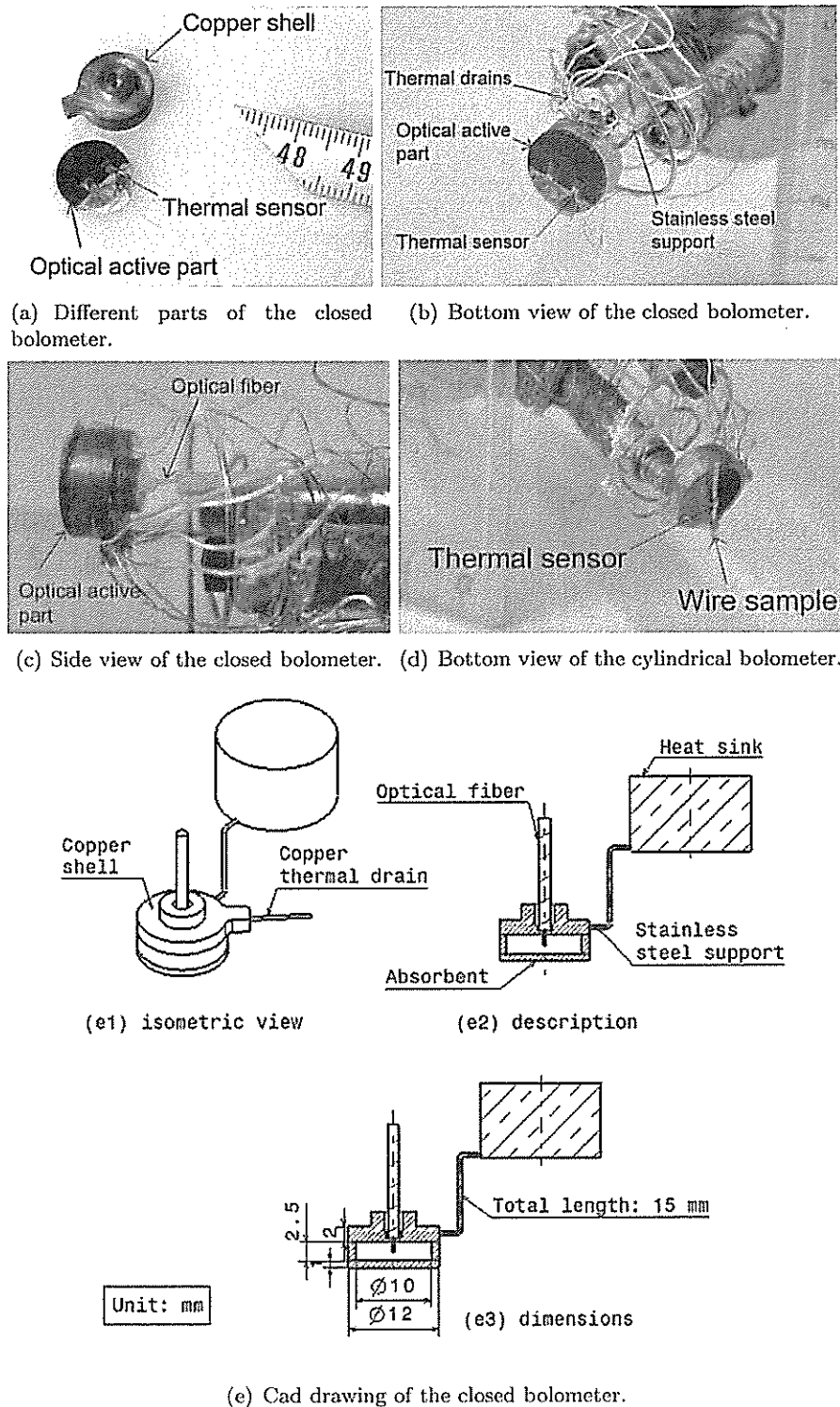


Figure IV.27: The two different bolometers used to estimate the coefficient of absorption of the oxidized samples and implemented into F. Ayela's modified setup at CRTBT/CNRS in Grenoble.

Second experiment, cylindrical bolometer: In addition to the above experiment which aims at the estimation of the total power flowing out of the tip of the fibered diode laser, a second experiment was carried out to reach a better understanding of the interaction between laser beam and wire sample.

This second experiment is based on a so-called cylindrical bolometer whose design was adapted from the closed bolometer. It is simply made-up of a piece of oxidized multifilament composite Cu/NbTi wire¹⁶. This wire sample, mounted on the copper shell in place of the optically-active part, is depicted in Figure IV.27(d) (page 140). The tip of the optical fiber has been positioned as close as possible to the piece of wire sample so that the lighted area has the same illumination as an actual sample used for stability measurements.

IV.4.4 Electrical equipments

A current source supplied a DC current of $\sim 1 \mu\text{A}$ to the thermal sensors. A simple DC current supply was also used as a driver for the diode laser to supply a forward current up to 330 mA. The temperature variations of the thermal sensors bonded to the bolometers were recorded using a voltmeter. It actually measured the voltage across the thermal sensors. This voltage was then converted into a resistance, which was subsequently transformed into a temperature owing to calibration curves such as the one presented in Figure IV.28 (page 142). The oscilloscope and its pre-amplifier were used to monitor the evolution of the temperature till a thermal equilibrium was reached and the ensuing recovery when the diode laser driver was switched off.

IV.4.5 Experimental results

Figure IV.29 (page 143) shows typical examples of time evolution of the resistances of the thermal sensors attached to the closed and cylindrical bolometers. After an initial variation which lasted from 1 s to 2 s, the system appears to reach a quasi-thermal equilibrium. This quasi-equilibrium is achieved when the absorbed power is totally evacuated by the thermal drain. The initial transient regime corresponds to the absorption of energy by the enthalpy of the system. This phenomenon can be described by a simple mathematical model. However, some simplifications must be done to treat analytically the problem. These simplifications are:

- temperature uniform across the bolometer,
- physical properties independent of temperature,
- thermal drain modeled by a linear heat conductance, G_{TD} ,
- the only heat source is the absorbed optical power.

Considering these simplifications, the thermal behavior of the bolometers can be represented by the following ordinary differential equation with temperature-invariant coefficients:

$$C_B \frac{dT}{dt} = \epsilon P_{\text{opw}}(t) - G_{\text{TD}}(T - T_0) \quad [\text{W}] \quad (\text{IV.6})$$

$$C_B = \vartheta_{\text{BCB}} \quad [\text{J}/\text{m}^3\text{K}] \quad (\text{IV.7})$$

$$G_{\text{TD}} = \frac{A_{\text{TD}}}{l_{\text{TD}}} \lambda_{\text{TD}} \quad [\text{W}/\text{K}] \quad (\text{IV.8})$$

¹⁶It would have been preferable to use an oxidized pure copper wire of the same nature. However, this would have required a special product which was unnecessary deemed for this study.

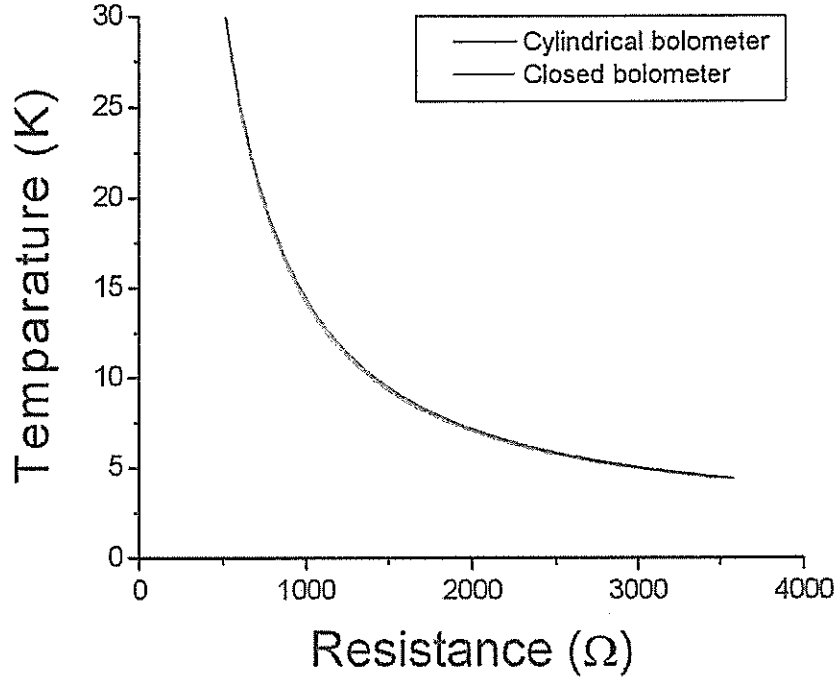


Figure IV.28: Calibration of the thermal sensors used for the cylindrical and closed bolometer. This calibration was carried out at CEA/Saclay.

where T is the temperature of the whole bolometer. ϑ_B and c_B are respectively the volume of the bolometer and its specific heat capacity, ϵ is the optical absorption coefficient, P_{opw} is the optical power delivered by the diode laser, G_{TD} is the thermal conductance of the thermal drain and T_0 is the temperature of the heat sink. In this equation, we considered that the thermal drain was only made-up of tinned copper wires. The presence of additional cooling provided by the stainless steel support is negligible. In addition, in the case of the cylindrical bolometer, we neglected the thermal contact between the wire sample attached to the copper support of the bolometer (see Figure IV.27(d), page 140) and the thermal resistance of the wire sample compared to the thermal resistance of the thermal drain (see Table IV.11, page 144). Consequently, the temperature variation due to heating occurs across the thermal drain, $\Delta T = T - T_0$, and the above equation can be rewritten as:

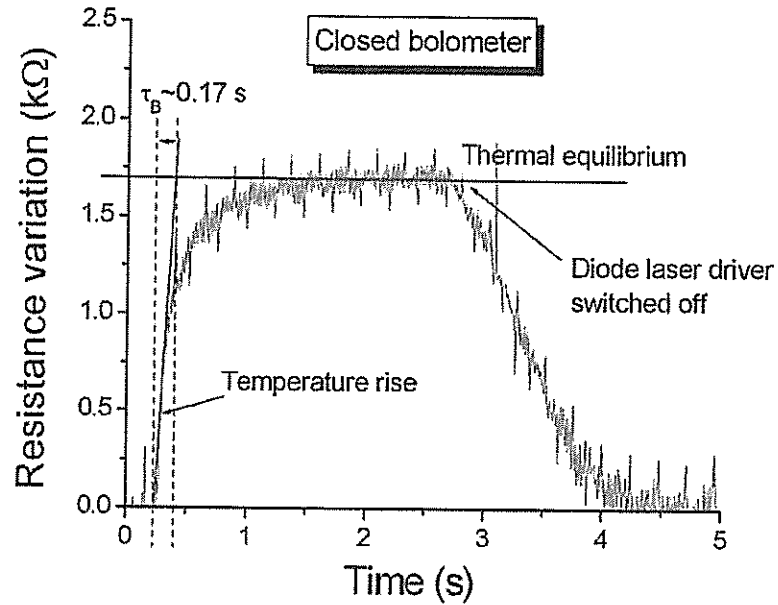
$$C_B \frac{d\Delta T}{dt} = \epsilon P_{opw}(t) - G_{TD} \Delta T \quad [W] \quad (IV.9)$$

To derive a particular solution, let us assume that the optical power function is a Heavyside function with a plateau value P_{opw} . The final solution is:

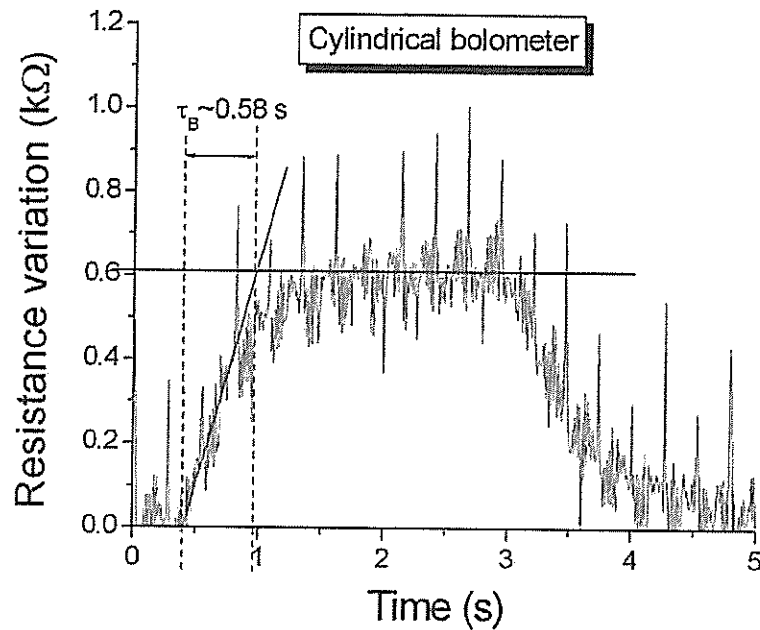
$$\Delta T = \left(\frac{\epsilon P_{opw}}{C_B} \tau_B \right) \left(1 - e^{-\frac{t}{\tau_B}} \right) \quad [K] \quad (IV.10)$$

with a time constant:

$$\tau_B = \frac{C_B}{G_{TD}} \quad [s] \quad (IV.11)$$



(a) Resistance variation recorded on the closed bolometer.



(b) Resistance variation on the cylindrical bolometer.

Figure IV.29: Time evolution of the resistances of thermal sensors attached to the bolometers: $\Delta R_{TS} = |R_{TS}(T) - R_{TS}(T_0)|$, with an initial resistance: $R_{TS}(T_0) \simeq 3000 \Omega$. The data presented here were recorded on the numerical oscilloscope for an optical power delivered by the diode laser of ~ 12 mW. The noise appearing in the recordings is due to the power network cycling at 50 Hz.

IV.4. CALIBRATION OF THE OPTICAL ENERGY ABSORBED BY THE OXIDIZED SAMPLE

Table IV.11: Thermal properties of the thermal drain and the stainless steel support.

Parameters	Notation	Values (units)
Heat capacity of the copper bolometer at ~ 4.6 K	c_B	~ 1 kJ/m ³ K
Conductivity of the thermal drain at ~ 4.6 K	λ_{TD}	~ 400 W/m-K
Thermal conductance of the thermal drain at ~ 4.6 K	G_{TD}	2 mW/K
Thermal resistance of the thermal drain at ~ 4.6 K	L_{TD}/λ_{TD}	$\sim 110 \times 10^{-6}$ m ² K/W
Conductivity of stainless steel at 4.2 K [24]	λ_{SS}	~ 0.25 W/m-K
Thermal conductance of the stainless steel support at ~ 4.6 K	G_{SS}	13 μ W/K
Thermal resistance of the wire sample at ~ 4.6 K	$\sim L_w/(2\lambda_w)$	$\sim 1 \times 10^{-6}$ m ² K/W

The numerical application, using data from Table IV.10 (page 139) and Table IV.11 (page 144), yields for the closed bolometer: $\tau_B \simeq 0.5$ s. With respect to the precision of the calculation and the various simplifications, it is consistent with the measured τ_B 's. The time constant of the cylindrical bolometer is slightly larger than the one of the closed bolometer. It is due to the presence of the NbTi filaments inside the wire sample whose heat capacity are about four times larger than copper at 4.2 K. However, the volume of copper is larger than the volume of NbTi thereby decreasing the influence of NbTi.

The variation of temperature versus time is an exponentially increasing function¹⁷. After a lag of few τ_B 's, it reaches a thermal equilibrium for which:

$$\Delta T \simeq \frac{\epsilon P_{opw}}{G_{TD}} \quad [\text{K}] \quad (\text{IV.12})$$

The thermal equilibrium is mainly determined by the conductance of the thermal drain, G_{TD} . The response time and the temperature variation are also conditioned by G_{TD} . The larger the conductance, the more reactive the bolometer, but the smaller the temperature increase. A trade-off was found between these contradictory requirements in order to reach a time response of a few seconds with appreciable sensitivity of the order of hundreds of milli-Kelvin.

IV.4.5.1 Heat balance equation at the thermal equilibrium and determination of the coefficient of absorption

At the thermal equilibrium, the optical power yielded to the sample is evacuated by the thermal drain. Combining Equations IV.8 (page 141) and IV.12 (page 144)

¹⁷It does not appear clearly in Figure IV.29 (page 143) due to the non-linear relationship between the resistance and the corresponding temperature (see Figure IV.28, page 142).

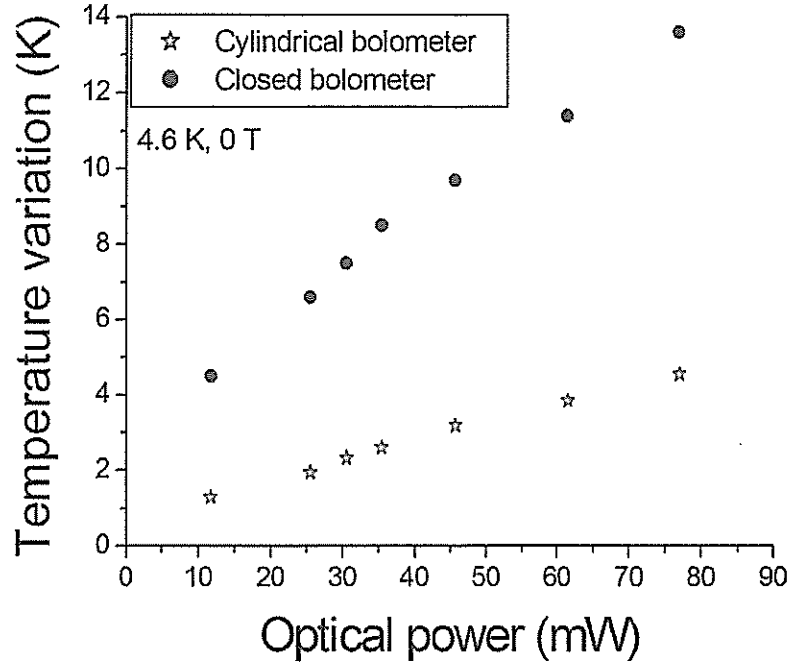


Figure IV.30: Temperature variation recorded on the voltmeter at various optical power at an initial temperature of ~ 4.6 K and a background magnetic flux density of 0 T.

and taking into account of the evolution of the thermal conductivity as a function of temperature, we get:

$$G_{TD}\Delta T \simeq \frac{A_{TD}}{L_{TD}} \int_{T_0}^T \lambda_{TD} dT = \epsilon P_{opw} \quad [W] \quad (IV.13)$$

where A_{TD} and L_{TD} are respectively the total cross-section and the average length of the thermal drain, λ_{TD} is its thermal conductivity, T is the temperature reached by the bolometer at the thermal equilibrium, and $\epsilon \in]0, 1[$ is the coefficient of optical absorption. Hence, this last coefficient is given by:

$$\epsilon = \frac{1}{P_{opw}} \frac{A_{TD}}{L_{TD}} \int_{T_0}^T \lambda_{TD} dT \quad (IV.14)$$

However, this equation can be only solved when the integral of the thermal conductivity across the thermal drain is known. In our case, the dimensions of the thermal drain are fixed and the optical power versus forward current of the diode laser is known. The only unknown parameters are then the thermal conductivity of the thermal drain, λ_{TD} and the coefficient of absorption, ϵ .

IV.4.5.2 Determination of the thermal conductivity: closed bolometer experiment

The thermal conductivity of copper is related to the electrical resistivity at cryogenic temperature through the Wiedemann-Franz law:

$$\lambda_{TD} = \frac{L_0 T}{\rho_{TD}} \quad [\text{W/m-K}] \quad (\text{IV.15})$$

where $L_0 = 2.45 \times 10^{-8} \text{ V}^2\text{K}^{-2}$ is the Lorentz constant, T is the absolute temperature and ρ_{TD} is the resistivity of copper wires. The resistivity of copper depends on the magnetic field, the temperature, the purity and cold work state of copper as described by the Residual Resistivity Ratio, RRR . In our case the background magnetic field is nil. Thus, knowing the temperature of the bolometer, the thermal conductivity is entirely determined by RRR . The RRR value of the thermal drain can be evaluated using the closed bolometer experiment. Indeed, in this case, the coefficient of absorption is equal to 1 since all the optical power is absorbed and Equation IV.14 (page 145) becomes:

$$\int_{T_0}^T \lambda_{TD}(T, RRR) dT = \frac{L_{TD}}{A_{TD}} P_{opw} \quad [\text{W/m}] \quad (\text{IV.16})$$

This yields a table of integral values of thermal conductivity over the range of measured temperatures on the bolometer as a function of optical power. The temperature variation, over which the thermal conductivity is integrated, is determined from the equilibrium plateau observed in Figure IV.29 (page 143). Figure IV.30 (page 145) summarizes the measured temperature variations of the bolometer as a function of optical power. There appears a quasi-linear increase of the temperature as a function of optical power.

We can use these data to estimate the RRR of the thermal drain. For a given optical power, we know what is the temperature of the bolometer. Using the CRYOCOMP software package [25], we can solve the implicit Equation IV.16 (page 146) to determine the RRR . This resolution can be carried out for every data point. Figure IV.31 (page 147) shows the computed RRR values as a function of optical power. The average value of RRR is found equal to ~ 56 with a standard deviation of ± 5.7 . This average value is the one used subsequently to calculate the coefficient of optical absorption.

IV.4.5.3 Estimation of the coefficient of absorption: cylindrical bolometer experiment

Figure IV.29 (page 143) shows, in addition to the temperature variation of the closed bolometer, the temperature variation of the cylindrical bolometer. The discrepancy between both data set is due to the reflection of light onto the surface of the cylindrical bolometer. In contrary to the closed bolometer, the cylindrical bolometer absorbs only a fraction of the optical power delivered by the diode laser. Using the RRR value found above, we estimate the power evacuated by the thermal drain, P_{ab} :

$$P_{ab} = \frac{A_{TD}}{L_{TD}} \int_{\Delta T} \lambda_{TD}(T, RRR = 56) dT \quad [\text{W}] \quad (\text{IV.17})$$

IV.4. CALIBRATION OF THE OPTICAL ENERGY ABSORBED BY THE OXIDIZED SAMPLE

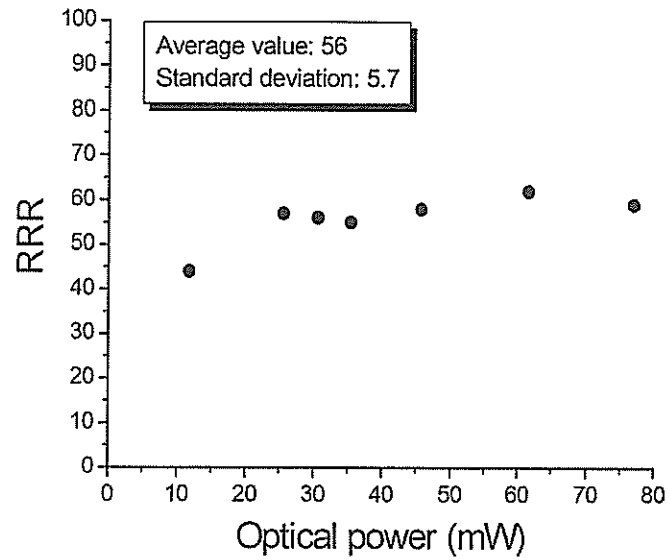


Figure IV.31: Estimated RRR as a function of optical power. An average value of 56 with a standard deviation of ± 5.7 was calculated.

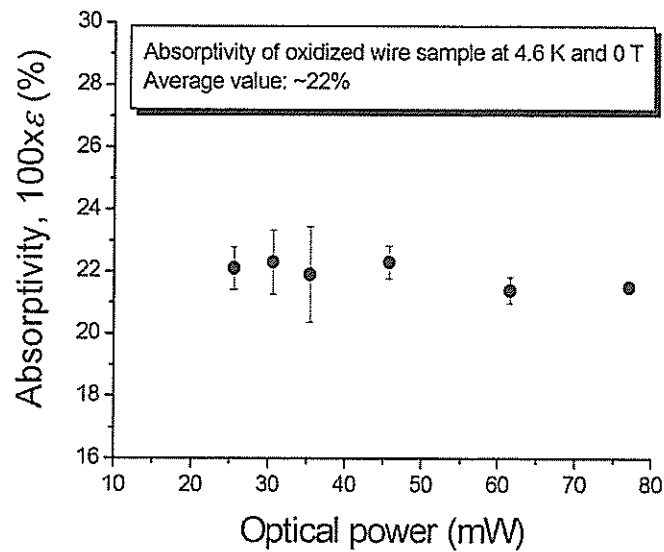


Figure IV.32: Absorptivity as a function of the optical power delivered by the diode laser (at the thermal equilibrium of the bolometer). The average value is equal to $\sim 22\%$ with a standard deviation of $\pm 7\%$. The error bars result from the error on the estimation of the temperature variation of the cylindrical bolometer.

where ΔT is the temperature variation given in Figure IV.30 (page 145) for the cylindrical bolometer at the thermal equilibrium (Figure IV.29, page 143). Subsequently, the coefficient of optical absorption can be estimated for each optical power, P_{opw} , as:

$$\epsilon = \frac{P_{ab}}{P_{opw}} \quad (IV.18)$$

Figure IV.32 (page 147) shows the resulting coefficients of absorption as a function of optical power. As expected, the coefficient of absorption does not depend on the intensity of the optical power.

From the data, an average coefficient of absorption of the oxidized sample can be estimated to be equal to ~ 0.22 with a standard deviation of ± 0.07 at a temperature of ~ 4.6 K and at zero background magnetic field¹⁸. The error bars result from the error on the estimation of the temperature variation of the cylindrical bolometer.

In our analysis, the coefficient of absorption has been implicitly considered as constant over time. This assumption can be reasonably made since no significant temperature variations were observed at the thermal equilibrium (see Figure IV.29, page 143).

IV.4.5.4 Conclusion on the coefficient of absorption

To estimate the coefficient of absorption of the wire sample, a few implicit assumptions have been made:

- same illumination as in the stability experiment at CEA/Saclay,
- coefficient of absorption independent of pulse duration,
- coefficient of absorption independent of background magnetic field.

Following these hypothesis, the coefficient of optical absorption was estimated to be equal to ~ 0.22 which corresponds to 22% of absorbed optical power. For our application, this percentage is large enough to carry out stability study over a large range of pulse durations with an accurate estimation of the Minimum Quench Energy.

Nevertheless, to address some of the previous assumptions, it would have been preferable to carry out the calibration in situ using the experimental setup of the stability experiment. However, heat leak issues could not be solved during the time frame of this work and we could not carry out calibration experiments at CEA/Saclay as it was initially planned.

In this section, we have demonstrated that the calibration of laser heater is feasible. Different bolometric setups can be used, we picked one of them to carry out the calibration of our heater. It must be pointed out that adiabatic conditions are always required. Consequently, the presence of helium bubbles and/or film of gaseous helium during stability tests in liquid helium is not taken into account and a discrepancy may result in the real amount of energy hitting the surface of the wire sample.

¹⁸The measurements were carried out at 0 T. Some variations following the magnitude of the background magnetic field may occur. In further studies, experiments in field will be necessary to estimate the influence of a high background magnetic field on the coefficient of absorption. For now, this influence is not taken into account.

Table IV.12: Values of transport current as a function of percentage of critical current and background magnetic field.

	5 T	6 T	7 T
80% of I_c	~435 A	~350 A	~255 A
85% of I_c	~460 A	~370 A	~270 A
95% of I_c	~515 A	~410 A	~305 A
I_c	~545 A	~430 A	~320 A

IV.4.6 Estimation of the absorbed optical energy by the sample

The coefficient of absorption, which has been previously estimated at 0 T and ~4.6 K from the calibration experiment at CRTBT/CNRS, is subsequently applied to the pulse energy flowing out of the tip of the optical fiber in the stability experiment at CEA/Saclay¹⁹. Hence, the amount of energy absorbed by the wire sample, E_{ab} , is estimated as:

$$E_{ab} = \epsilon \times E_p \quad [\text{J}] \quad (\text{IV.19})$$

where E_p is the pulse energy flowing from the tip of the optical fiber in the stability experiment, integrated over the pulse duration τ_p (see section IV.3.7, page 129), and $\epsilon \simeq 0.22$, the coefficient of optical absorption (see previous section IV.4.5.3, page 146).

IV.5 Stability measurements

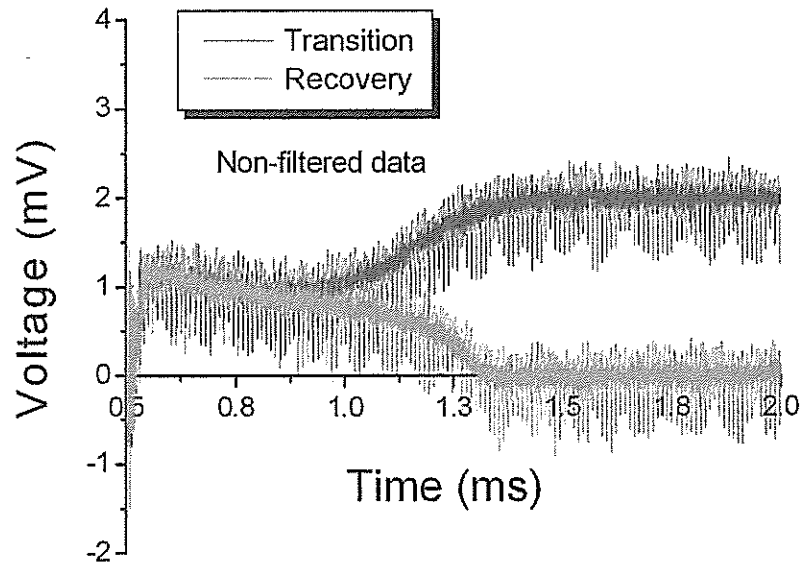
Being well beyond what was achieved with previous heating systems, the data recorded with the diode laser experiment leads to a better understanding of the normal zone growth and propagation. In particular, the early growth of the normal zone can be well studied and reasonable estimations of the Quench Decision Time can be derived. Numerous results have been recorded at different background magnetic flux densities: 5, 6 and 7 T, and different percentages of critical current: 80%, 85% and 95%. All the measurements were carried out at 4.2 K in liquid helium.

Table IV.12, page 149 summarizes the transport current values at which measurements were taken.

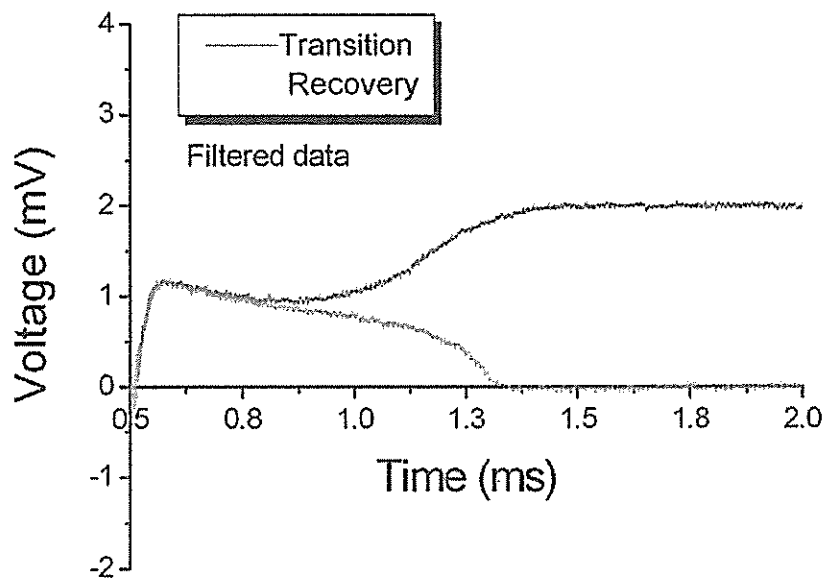
IV.5.1 Filtering of the voltage traces

Before estimating the magnitude of the quenched zone extension, the Quench Decision Time and the Normal Zone Propagation Velocity, it was first necessary to filter the data downloaded from the numerical oscilloscope. We used a discrete time filter (standard function *filter* of Matlab[®] 6.1 [26]). The following Figure IV.33 (page 150) shows a comparison between bare data and filtered ones for voltage trace V_1 across the heated zone. These traces correspond to the overlay of two measurements at 4.2 K, 7 T and 85% of the short sample critical current: a quench (red trace) and a

¹⁹The optical phenomenon of absorption are rapid with respect to thermal processes.



(a) Bare data.



(b) Smoothened data.

Figure IV.33: Comparison of voltage data for a quench and a recovery at 4.2 K, 7 T and 85% of the critical current. (a) bare data. (b) filtered data using a discrete time filter.

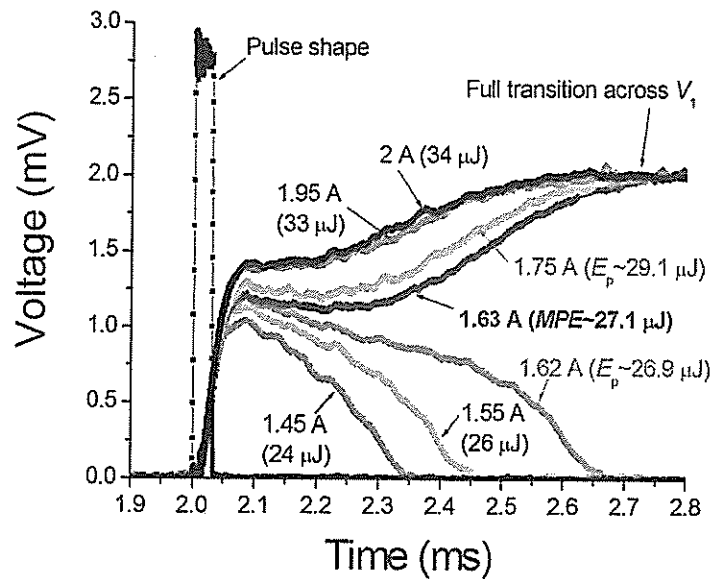


Figure IV.34: Set of recordings of voltage trace V_1 for increasing forward current pulses. Transitions and recoveries are observed at 4.2 K, 7 T, and 285 A (85% of I_C), for a fixed pulse duration of 30 μ s. The red trace shows the first transition after the last recovery (green trace) recorded between cleansing quenches.

recovery (green trace). As it can be seen, the filtering of the data does not distort the shape of the traces and can be confidently used to analyse the data. The bare data exhibit a peak at the beginning of the voltage rise which is concomitant to the optical power pulse. The origin of the peak is not understood. The noise level recorded during the second series of tests for which the wire sample was oxidized was somewhat larger than the one observed during the first series of tests on bare wire [1]. For this too, no explanation could be found.

IV.5.2 Protocol of measurements and examples of voltage recordings

Figure IV.34 (page 151) shows an accumulation of voltage traces V_1 across the heated zone for a series of shots at increasing pulse energy. The measurements were taken in pool boiling helium at 4.2 K, in a 7 T background magnetic flux density (perpendicular to the wire axis), and at 85% of the wire critical current (measured in situ). For this data set, the duration of the pulse current delivered to the diode laser was equal to 30 μ s and its amplitude was progressively increased. After each recovery, the wire was cleansed of persistent magnetization currents by performing an intermediate quench. When the deposited energy is not enough to trigger a full quench, the wire enters the current sharing regime corresponding to an increase in the voltage across the wire, but, the cooling capacity of the helium cryogen is strong enough to enable a recovery of the superconducting state for which the voltage vanishes. However, as soon as the input energy is large enough²⁰ to reach

²⁰In the present case, as soon as the energy pulse reached $\sim 27 \mu$ J.

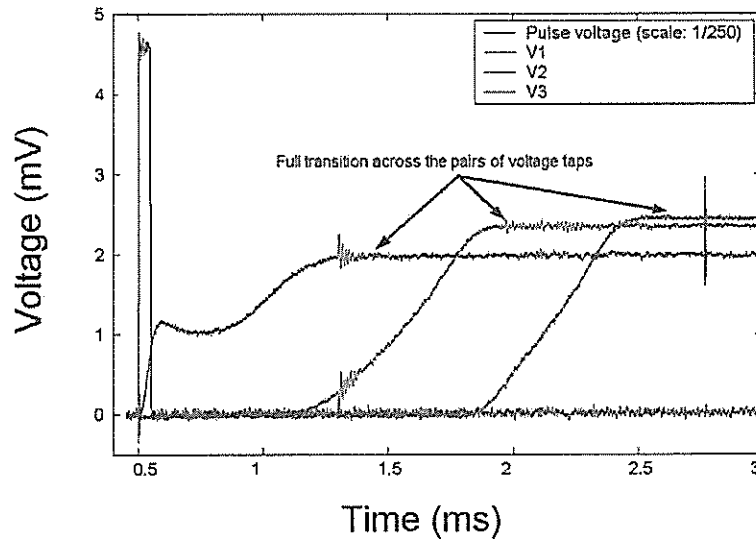


Figure IV.35: Voltage traces downloaded from the numerical oscilloscope. The traces were obtained at 4.2 K, 7 T, and 85% of I_C for a pulse duration of 50 μ s. The data have been previously filtered.

the Minimum Propagating Zone (MPZ), the heat generated by the Joule effect takes over and the sample undergoes an irreversible transition. Then, the voltage increases till it reaches a plateau corresponding to the full transition of the portion of wire located between the pair of voltage taps V_1 . Plots similar to the one shown in Figure IV.34 (page 151) were taken for various pulse durations, various background magnetic flux densities and various fractions of critical current.

In the case of a quench, one can also study the normal zone propagation by looking at voltage traces V_2 and V_3 . This is illustrated in Figure IV.35 (page 152) which shows a quench at 4.2 K, 7 T and 85% of I_C triggered by a 50 μ s-long pulse. We can clearly see the quench developing along the adjacent wire sections. As it has been already explained, the voltage traces V_2 and V_3 increase quasi-linearly which is a good illustration of the fact that the quench propagates at constant velocity. When the wire is fully quenched across each pair of voltage taps, the voltage traces appear constant. It shows that the temperature of the wire is not large enough for the resistance of the copper matrix to exceed the plateau of the residual resistivity (see Appendix A).

Figure IV.36 (page 153) shows a complete non-filtered recording for which the voltage reaches the plateau of the residual resistivity before running away as the resistivity of the copper matrix increases with temperature.

IV.5.3 Estimations of the different parameters of the normal zone transition

In this section, we introduce the way that different parameters, characterizing a normal zone transition in a multifilament composite wire, are estimated. These parameters are:

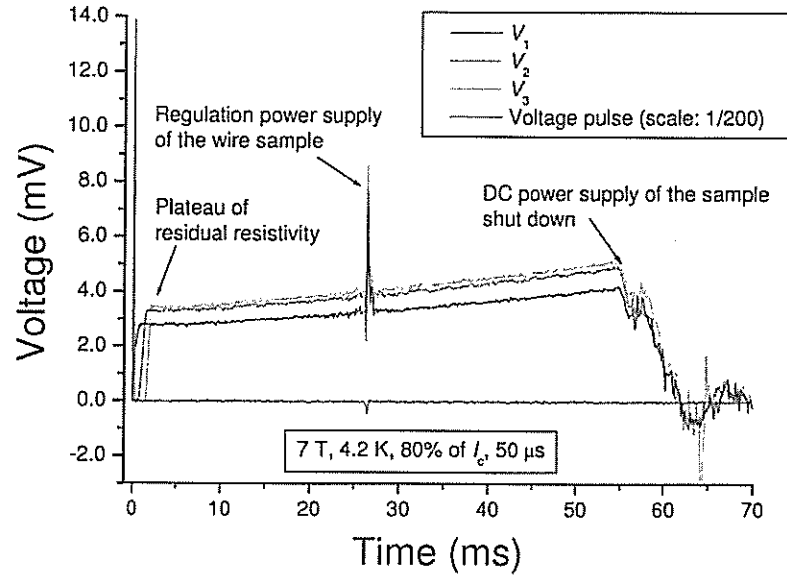


Figure IV.36: Voltage traces obtained at 4.2 K, 7 T, and 80% of I_C for a pulse duration of 50 μ s. The voltage increases according to the temperature evolution of the copper matrix resistance.

- Quench Decision Time (QDT),
- quenched zone extension,
- Quench Energy (QE),
- Normal Zone Propagation Velocity (NZPV).

In view of the numerous amount of data, various Matlab[®] routines, including the filtering, were written to calculate automatically the amplitude of these parameters.

IV.5.3.1 Estimation of the Quench Decision Time

Figure IV.37 (page 154) shows filtered voltage trace V_1 recorded for a quench and a recovery at 4.2 K, 7 T and 85% of the critical current. The current pulse of 50 μ s width, which triggered the quench, is also shown. The recovery and quench recordings were respectively acquired for a pulse energy of 30 μ J and 30.5 μ J. At this sensitivity, it is possible to see clearly that the recovery trace follows the quench one during the first phase of the normal zone growth. At one time, the decision between recovery and quench is made and the normal zone vanishes or expands to cover the distance between the voltage taps of V_1 . Following P. Bauer [27], we refer to this time as the Quench Decision Time. Hence, it is the time lag between the initial time of heat disturbance, t_i and the time of decision, t_q :

$$QDT = t_q - t_i \quad [\text{s}] \quad (\text{IV.20})$$

In our example, the Quench Decision Time is equal to $\sim 190 \mu$ s.

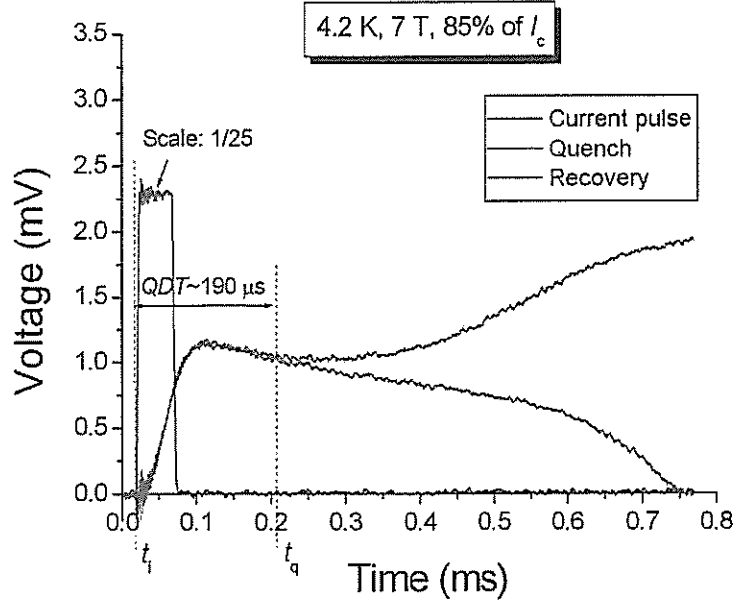


Figure IV.37: Determination of the Quench Decision Time.

IV.5.3.2 Estimation of the length of quenched zones

To estimate the quenched zone extension, it is necessary to treat numerically the voltage trace V_1 . Figure IV.38 (page 155) shows two plots at 4.2 K, 7 T and 85% of critical current for a pulse duration of 30 μs :

- the time evolution of voltage V_1 : Figure IV.38(a),
- the corresponding time evolution of quenched zone: Figure IV.38(b).

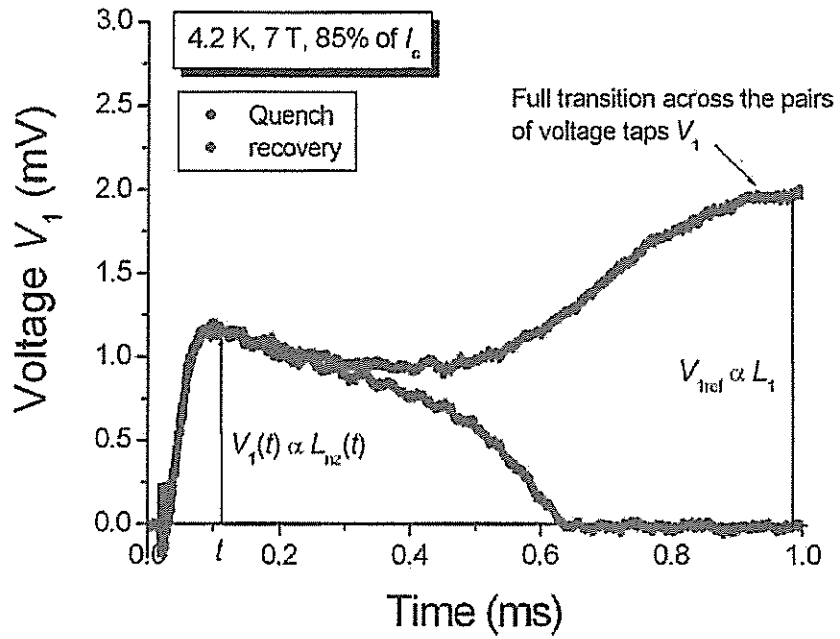
To transform Figure IV.38(a) into Figure IV.38(b), we use the fact that the voltage reaches a pseudo-plateau value, $V_{1\text{ref}}$, when the normal zone extends across the two pairs of voltage taps whose distance, L_1 , is known. Indeed, if we note $V_1(t)$ the voltage across the heated zone at the time t , and $L_{\text{nz}}(t)$ the corresponding longitudinal length of the normal zone, we can write in first approximation:

$$\frac{V_1(t)}{L_{\text{nz}}(t)} = \frac{\rho_m I_t}{A_w}, \quad \forall t \in [t_i, +\infty[\quad (\text{IV.21})$$

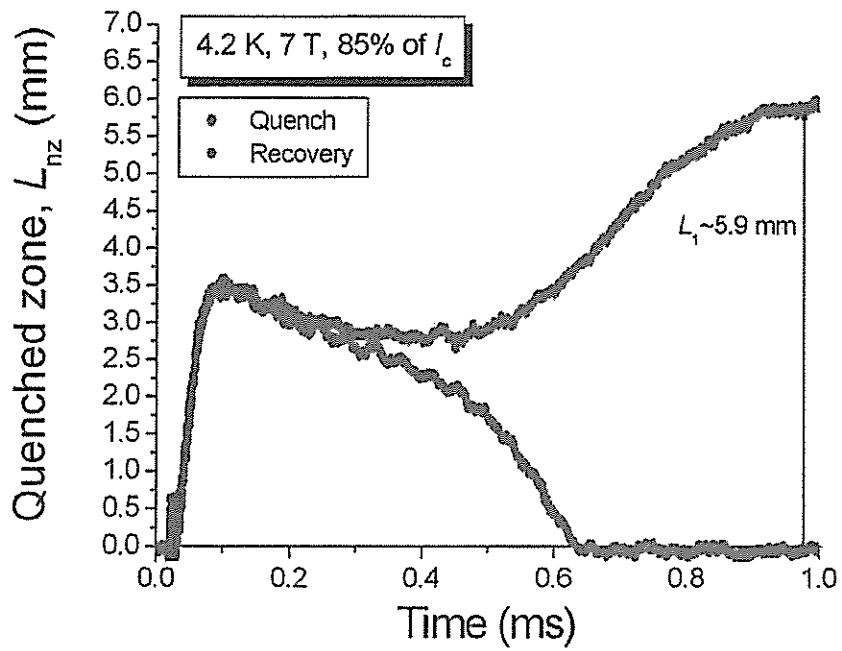
where ρ_m is the residual resistivity of the matrix²¹, I_t is the transport current, and A_w is the total cross-section of the wire sample which are all constants. Consequently, the tendency of the normal zone development is given by:

$$L_{\text{nz}}(t) = \frac{V_1(t)}{V_{1\text{ref}}} L_1, \quad \forall t \in [t_i, +\infty[\quad (\text{IV.22})$$

²¹Using the previous Equation IV.21 applied to voltage $V_{1\text{ref}}$ and length L_1 , we crosschecked the residual resistivity ratio with the one given by Alstom/MSA. It was estimated to ~ 150 compared to 189 given by the manufacturer. In view of the cumulative errors on the measurements of L_1 and $V_{1\text{ref}}$, it can be assumed that $V_{1\text{ref}}$ is consistent with the residual resistivity ratio of the wire sample.



(a) Voltage traces.



(b) Resulting quenched zone.

Figure IV.38: Example of the transformation of voltage traces into a plot of the time evolution of quenched zone.

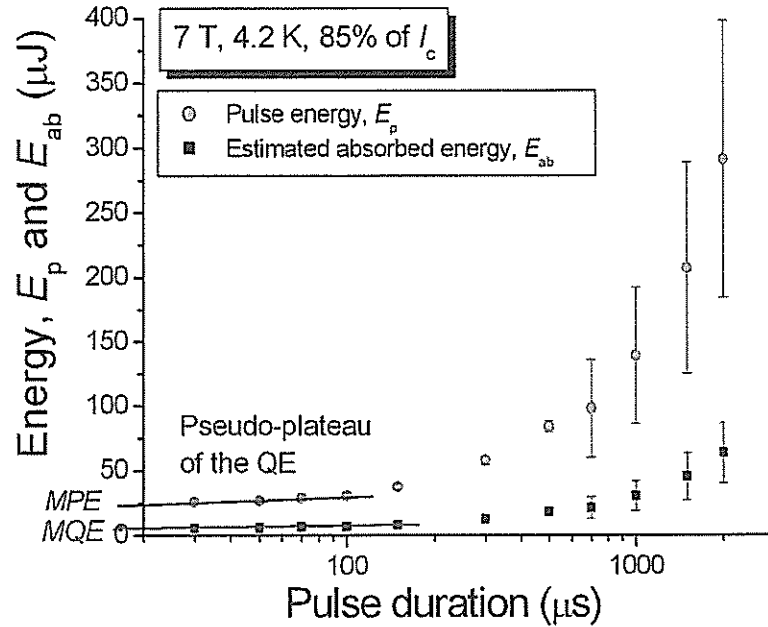


Figure IV.39: Evolution of the Quench Energy as a function of the pulse duration at 7 T, 85% of I_c and 4.2 K. .

This result gives only a tendency of the time evolution of the quenched zone extension. Indeed, in our approach, we did not take into account the current sharing regime for which the actual resistivity of the conductor is a mixed between the copper resistivity and the flux flow resistivity of the superconducting filaments. So, the voltage measured across the heated zone does not only depend on the quenched zone extension, but, depends also on the temperature of the conductor. The above estimation becomes accurate as soon as the critical temperature of the superconductor is exceeded since all the current then flows in the copper matrix. Consequently, it is not practically possible to assess from the voltage traces the Minimum Propagating Zone since the temperature along the sample is unknown. This aspect of the results will be further discussed in chapter V (page 169).

IV.5.3.3 Estimation of Quench Energy and Minimum Quench Energy

As already mentioned in section IV.5.2 (page 151), we adjust the current pulse so as to find the minimum energy triggering a quench at a given pulse duration. Figure IV.39 (page 156) shows the minimum energy flowing from the tip of the optical fiber extension, E_p , triggering a quench and the corresponding minimum energy absorbed by the wire sample, $E_{ab} = \epsilon E_p$ as a function of pulse durations. The measurements were carried out at 4.2 K in liquid helium under a 7 T background flux density at 85% of the critical current.

As expected, the Quench Energy tends toward a pseudo-plateau for pulse durations below $\sim 100 \mu s$. We define the Minimum Pulse Energy, MPE , and the Minimum Quench Energy, MQE , as the values of Quench Energies corresponding to extrapolations of these pseudo-plateaus at 0 pulse duration. In our example, the extrapolated

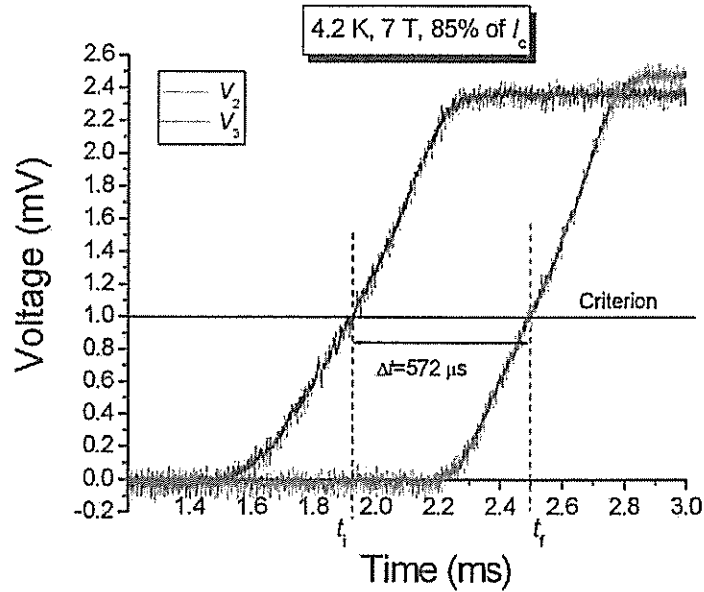


Figure IV.40: Determination of the normal zone propagation velocity.

Minimum Pulse Energy is equal to $\sim 25 \mu\text{J}$ and the Minimum Quench Energy is equal to $\sim 5 \mu\text{J}$.

IV.5.3.4 Estimation of Normal Zone Propagation Velocity

After, the onset of a quench, the normal zone propagates at a constant velocity, resulting in a quasi-linear increase of the voltages recorded along the wire sample. The Normal Zone propagation Velocity can be estimated by two means [28]:

- time of flight,
- voltage slope.

In the case of the time of flight, and as illustrated in Figure IV.40 (page 157), we measure the time lag, Δt , between voltage V_2 and V_3 for a criterion of 1 mV. Using the distance, L_2 , between the corresponding voltage taps, the Normal Zone Propagation Velocity is simply:

$$\nu = \frac{L_2}{\Delta t} \quad [\text{m/s}] \quad (\text{IV.23})$$

In our example, $\nu \simeq 12 \text{ m/s}$.

The voltage slope method has been previously described in chapter III, section III.4 (page 94). Using Equation III.5 (page 95), we calculated respectively for voltage traces V_2 and V_3 $\sim 13 \text{ m/s}$ and $\sim 14 \text{ m/s}$ with an error of $\pm 2.5 \text{ m/s}$. The results are consistent with the previous value found using the time of flight.

IV.5.4 Influence of various parameters

In this section, we present various results for which parameters such as background flux density, transport current, and pulse duration were investigated. We do not

thoroughly analyze all the results presented in this section. A deeper analysis will be carried out in chapter V (page 169) for some of these parameters.

IV.5.4.1 Pulse duration

Quenched zone: Figure IV.41 (page 159) shows time evolutions of the quenched zone for various pulse durations and various background magnetic flux densities. All the measurements were taken at 4.2 K in liquid helium and at 85% of I_c . At 7 T (Figure IV.41(a)), a rapid increase in the normal zone is followed by a clear kink around the Quench Decision Time. The quench plot follows the trend of the recovery plot till the onset of a full normal zone transition. The shape of recovery and quench plots are similar in the range 30 μ s to 100 μ s which corresponds to the pseudo-plateau of the Quench Energy. However, the initial increase of the normal zone is slower at larger pulse durations. Indeed, for the same Quench Energy, the power necessary to quench the sample is larger for a shorter pulse duration. Consequently, a larger dissipation is quickly induced inside the sample²². This tendency is accentuated at 5 T (Figure IV.41(c)) and 6 T (Figure IV.41(b)) for which the transport current is larger. If we compare the different plots at a same pulse duration, the normal zone appears to grow at the same rate. Then, at 7 T, the maximum normal zone length is equal to ~ 3 mm and is reached after less than 100 μ s for a pulse duration of ~ 50 μ s. At 5 T and 6 T, a similar time is needed to reach maximum normal zone lengths of ~ 2 mm and ~ 2.2 mm respectively. However, once the quench decision has been made, the growth of the normal zone seems more aleatory and the different plots at a given background magnetic flux density cross-over. This aleatory behavior may be related to the variation of the heat exchange capacity of helium during the stability tests once the quench is initiated.

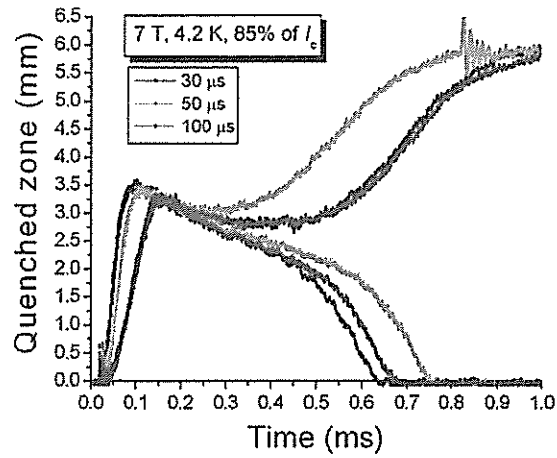
Quench Decision Time: Figure IV.42 (page 160) shows the evolution of the Quench Decision Time as a function of pulse durations at various background flux densities. We only reported QDT's for which the quench and recovery plots split after the quenched zone has passed its maximum from the voltage trace V_1 (see Figure IV.41(a), page 159). In this case, the QDT appears constant within the pseudo-plateau of Quench Energy. The average QDT is equal to ~ 80 μ s at 5 T, ~ 100 μ s at 6 T and ~ 200 μ s at 7 T (at 85% of I_c and 4.2 K).

No error bars are reported at 5 T and 6 T since only one series of measurements was carried out for each magnetic flux density at which recovery and quench voltage traces were recorded.

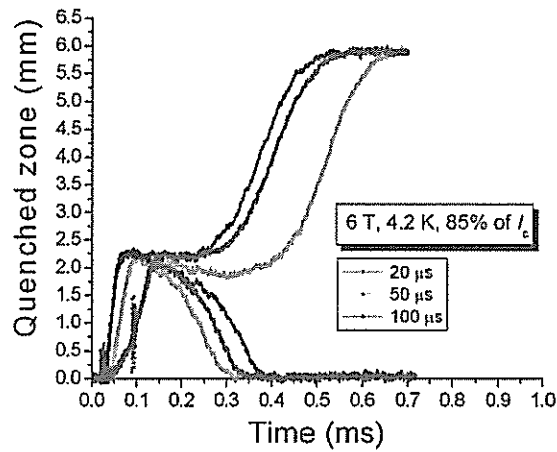
Quench Energy: Figure IV.43 (page 161) shows the estimated Quench Energy as a function of pulse durations at various background magnetic flux densities (at 4.2 K in liquid helium and 85% of I_c). As expected, the Quench Energy tends toward a pseudo-plateau²³ for pulse durations below ~ 100 μ s. As can be seen in the insert, the Quench Energy does not follow a clear trend. Indeed, for pulse durations between ~ 125 μ s and 150 μ s, the plots at different background magnetic flux densities cross over. However, with the error bars on the measurements, the

²²As it will be shown in the next chapter V, page 169, film boiling is triggered before the end of the energy pulse limiting the influence of helium cooling at an early stage of the normal zone transition.

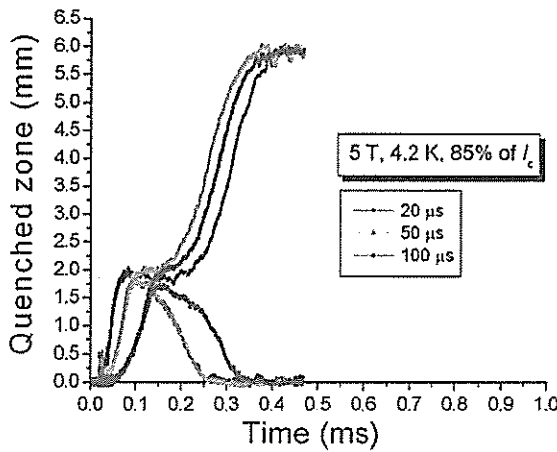
²³The same trend was also seen at 80% and 95% of I_c for the same range of pulse durations.



(a) Quenched zone at 7 T.



(b) Quenched zone at 6 T.



(c) Quenched zone at 5 T.

Figure IV.41: Time evolution of the quenched zone for various pulse durations.

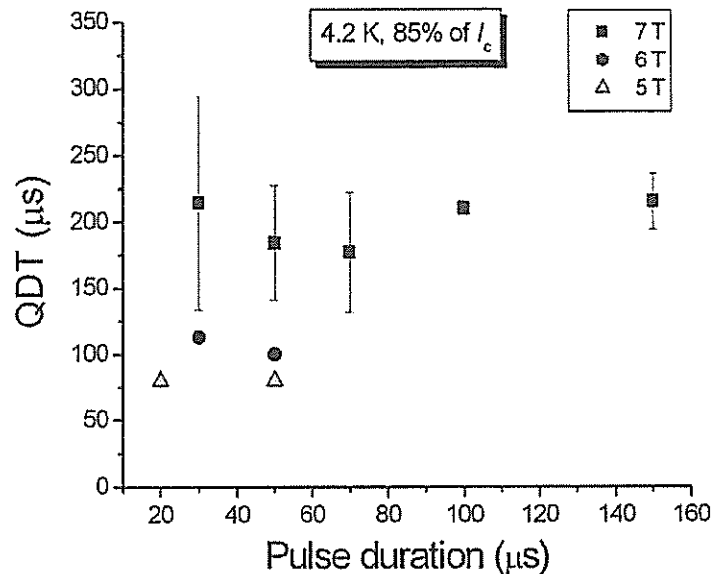


Figure IV.42: Evolution of the Quench Decision Time as a function of pulse durations at various background magnetic flux densities.

Quench Energies obtained at 5 T and 6 T converged toward the same Minimum Quench Energy of $\sim 3.5 \mu\text{J}$ at 85% of I_c .

IV.5.4.2 Background magnetic flux density

Quenched zone: Figure IV.44 (page 161) shows an example of the time evolution of the quenched zone for a quench and a recovery under various background magnetic flux densities recorded at a pulse duration of $50 \mu\text{s}$ and at 85% of I_c . The profile of the quenched zone increases with increasing field. The largest discrepancy occurs between 6 T and 7 T which is consistent with our previous observation. At low background magnetic flux density for the same fraction of critical current, a larger transport current flows in the sample. Consequently, a larger current redistributes into the copper matrix during a quench. It induces a larger heat dissipation inside the wire which turns into a larger temperature increase of the wire. The temperature difference between the wire surface and the bulk liquid helium will be larger and the heat transfer will be enhanced till the onset of film boiling [29]. As a result, the quenched zone shrinks before the final onset of a full transition (see chapter V, page 169). The onset of full transition starts when the energy to form a vapor film has been exceeded. The heat transfer is strongly degraded and the heat generation takes over.

Quench Decision Time: Figure IV.45 (page 162) shows the average Quench Decision Time as a function of background magnetic flux density. It does not seem to be influenced by the percentage of critical current whereas it appears to depend strongly on the background magnetic flux density. The estimation of the QDT is

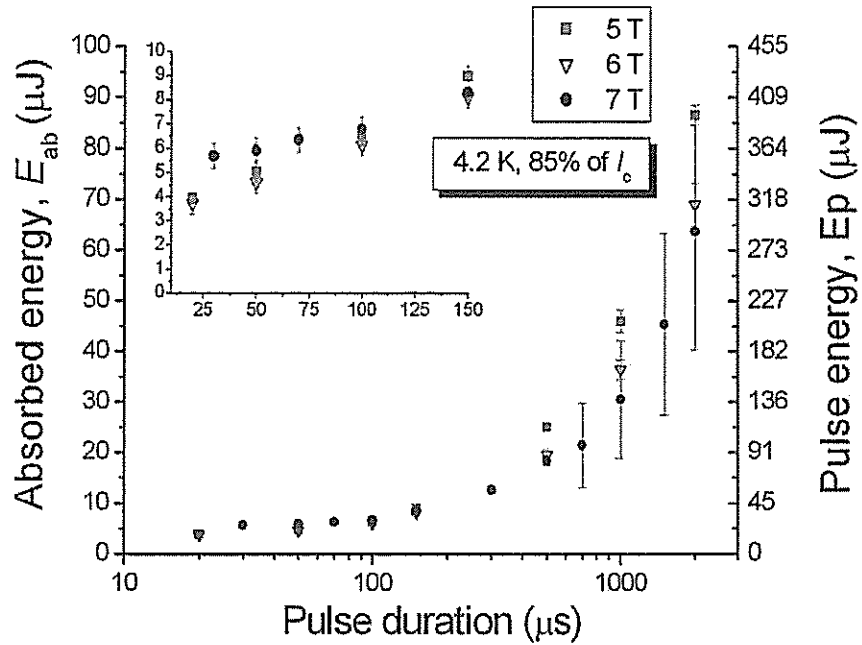


Figure IV.43: Evolution of the minimum absorbed energy and corresponding pulse energy triggering a quench as a function of the pulse duration at different background magnetic flux density, 85% of I_c and 4.2 K. The Quench Energies tend to rejoin towards an equivalent Minimum Quench Energy and crossover passed at a pulse duration between 125 μs and 150 μs .

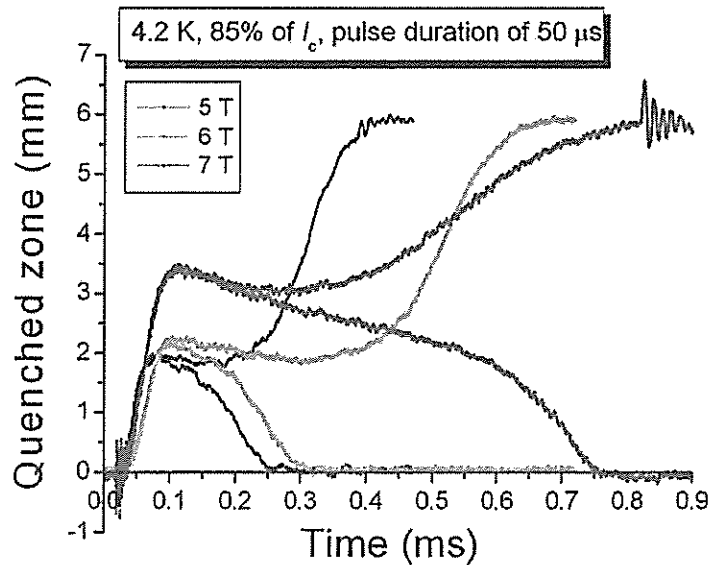


Figure IV.44: Evolution of the quenched zone for various background magnetic flux densities.

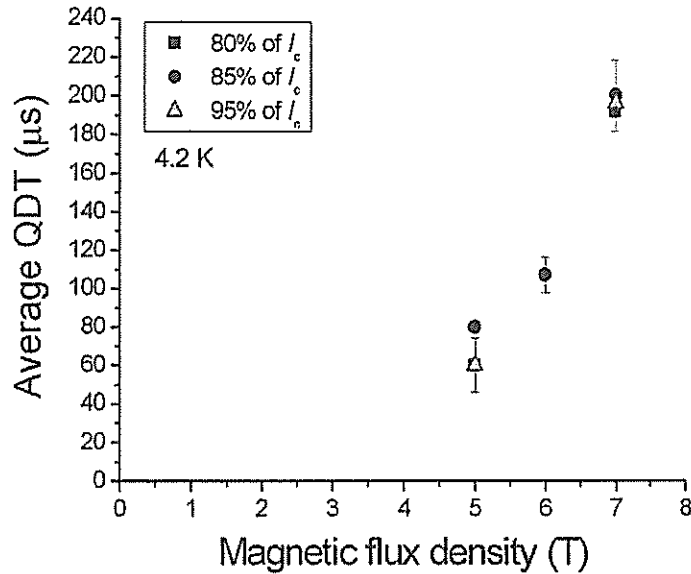


Figure IV.45: Evolution of the Quench decision time as a function of background magnetic flux density at various percentages of critical current.

very dependent on the degree of filtering and the interpretation of the analyst leading to greater uncertainties²⁴.

Quench Energy: Figure IV.46 (page 163) shows the evolution of the Quench Energy as a function of background magnetic flux densities at various pulse durations. For pulse durations longer than those of the pseudo-plateau of Quench Energy, it tends to decrease with increasing field. Conversely, on the pseudo-plateau of the Quench Energy (below $\sim 100 \mu\text{s}$), the Quench Energy decreases toward a quasi-constant value around $5 \mu\text{J}$ for which the effect of the background magnetic field does not appear significant.

Normal Zone Propagation Velocity: Figure IV.47 (page 163) shows the evolution of the NZPV as a function of the background magnetic flux density at various percentages of critical current. The NZPV decreases quasi-linearly with increasing field over the range of measured data. If we linearly extrapolate the NZPV to zero, we find that all the lines cross at $\sim 8.7 \text{ T}$. This result suggests that there is a background magnetic flux density for which the wire becomes cryostable. In this case, the transport current is not large enough to induce heat power dissipation overwhelming the heat capacity of helium coolant and a normal zone unconditionally recovers. Additional measurements at higher magnetic flux densities and a refined model of heat transfer would be necessary to explain the linear decreasing of the NZPV as a function of background magnetic flux densities.

²⁴Errors of more than $50 \mu\text{s}$ can result.

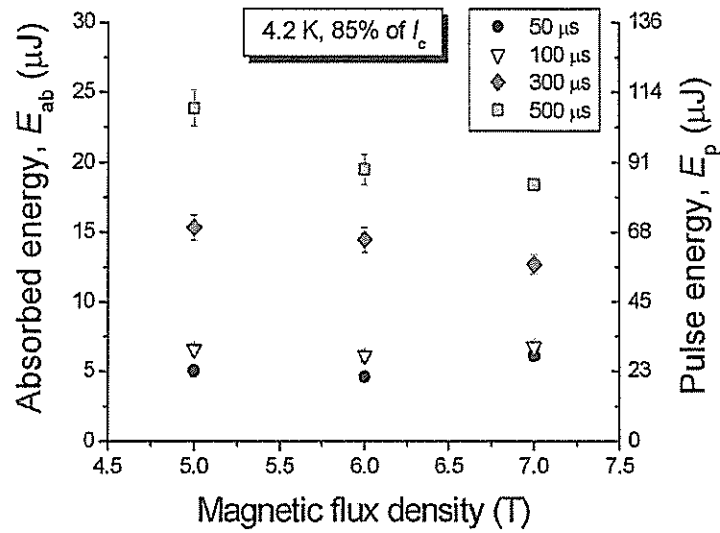


Figure IV.46: Evolution of the Minimum absorbed energy and the corresponding pulse energy triggering a quench as a function of background magnetic flux density at different pulse durations, 85% of I_c and 4.2 K.

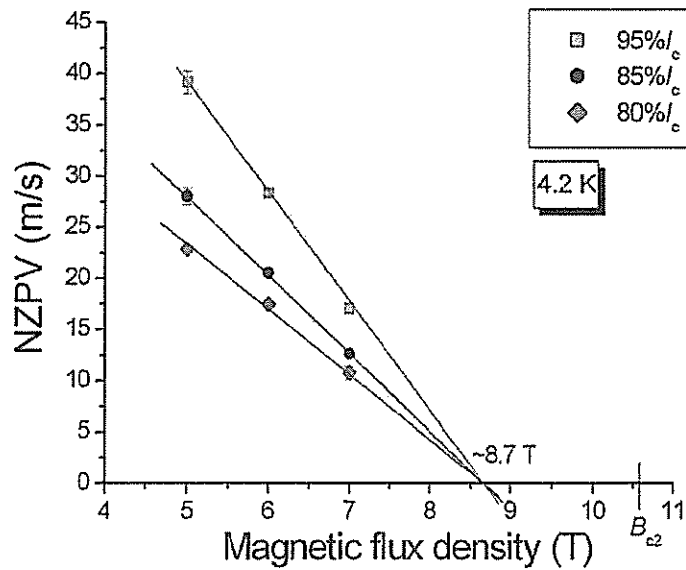


Figure IV.47: Evolution of the Normal Zone Propagation Velocity as a function of background magnetic flux densities.

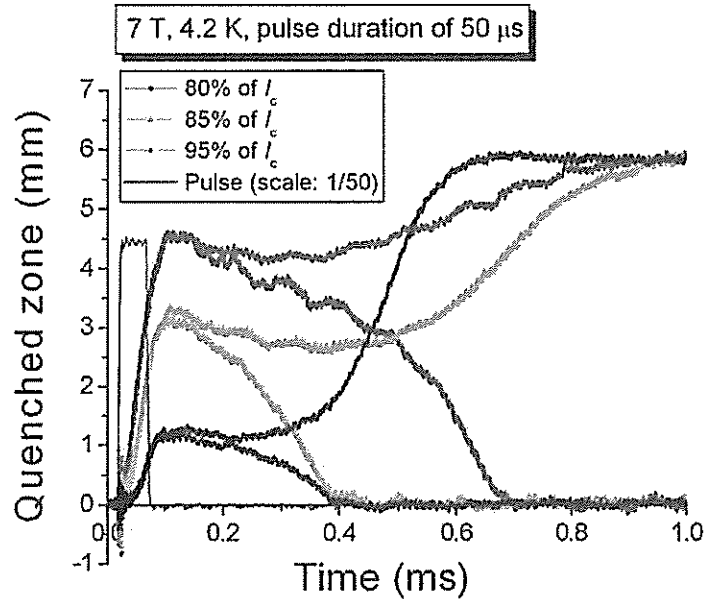


Figure IV.48: Time evolution of the quenched zone at various percentages of critical current.

IV.5.4.3 Transport current

Quenched zone: Figure IV.48 (page 164) shows an example of the time evolution of the quenched zone at various percentages of critical current. The profile of the quenched zone increases with decreasing transport current. The early growth of the quenched zone appears faster at low transport current even if the current density is lower. It is consistent with our previous comment in paragraph IV.5.4.2 (page 160). Indeed, the larger transport current leads to a larger heat dissipation which results in a larger temperature rise of the wire sample. Consequently, the heat capacity of the sample increases and the heat transfer with helium improves restraining locally the propagation of the normal zone.

Quenched zone: Figure IV.49 (page 165) shows the evolution of the MQE extrapolated from Figure IV.43 (page 161) as a function of percentage of critical current. At 5 T and 6 T, the values of MQE's are very close which is consistent with their respective MPZ and QDT. In addition, the curves tend toward the same value of MQE around $1.2 \mu\text{J}$ close to the critical current.

Normal Zone propagation Velocity: Figure IV.50 (page 165) shows the evolution of the NZPV as a function of the transport current at various background magnetic flux densities. As expected [27], the NZPV increases quasi-linearly with increasing transport current. The NZPV is expected to vanish not at zero transport current but at a certain value which depends on the background magnetic flux density, the cooling environment. The transport current, at which the NZPV vanishes, is called Minimum Propagating Current, I_{mpc} . Below this current, the wire sample is cryostable [30]. By extrapolating the slope of the plots, we showed the upper limit

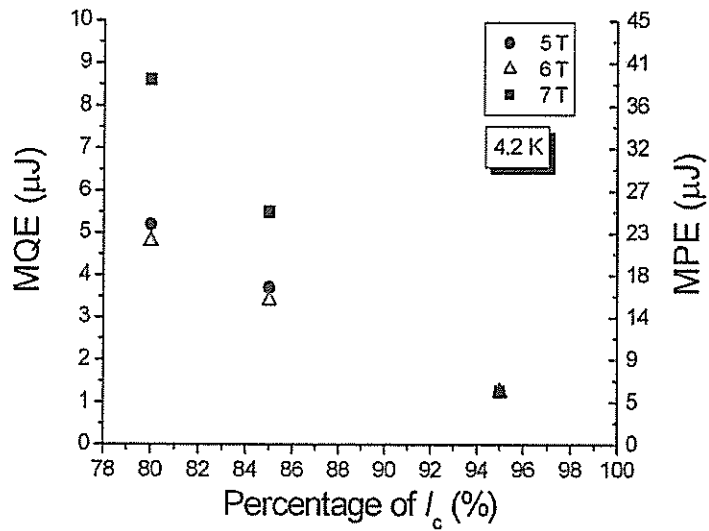


Figure IV.49: Evolution of the Minimum Quench Energy and the corresponding Minimum Pulse Energy as a function of percentage of critical current at different background magnetic flux densities.

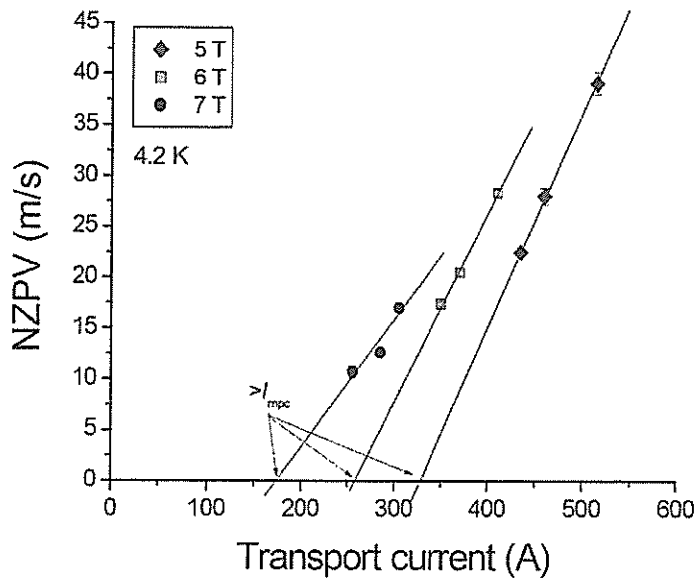


Figure IV.50: Evolution of the Normal Zone Propagation Velocity as a function of the transport current.

of the Minimum propagating Current. The minimum propagating current is inferior to ~ 343 A at 5 T, ~ 272 A at 6 T and ~ 211 A at 7 T.

The order of magnitude of NZPV's ranges between ~ 10 m/s to 40 m/s. It is consistent with the order of magnitude found in chapter III (page 77).

The slopes of the NZVP versus transport current plots differ following the magnitude of the background magnetic flux density. Indeed, it is thought to be related to the decreasing temperature variation $T_c - T_{cs}$ with increasing magnetic field and the increasing magneto-resistance since the NZPV is determined by the ratio of the resistivity of the metallic matrix and the above temperature variation (see Equation II.4, page 59).

IV.5.5 Conclusion on Measurements

From the above presentation, the different measurements show good repeatability and consistency. It must be pointed out that the reproducibility of the measurements has not been checked within the time frame of our work. It is a necessary task to confront the laser heater against past heaters.

During our different tests, we clearly unveiled the expected pseudo-plateau of Quench Energy at various background magnetic fields. At first glance, the MPZ and the MQE seem to be strongly related while the QDT appears somewhat disconnected. To explain the consistency of the results on MPZ's and MQE's, a realistic and refined model of helium cooling must be worked out. An attempt of such a work is given in chapter V (page 169).

The order of magnitude of NZPV's is consistent with data reported in the literature [27]. Tens of meters per second are expected at 4.2 K and in this range of background magnetic flux density. Also, the NZPV appears to vary linearly as a function of background magnetic flux density and as a function of fraction of critical current.

Bibliography

- [1] F. Trillaud, F. Ayela, M. Fratani, A. Devred, D. Leboeuf, and P. Tixador. Quench Propagation Ignition Using Single-Mode Diode Laser. *IEEE Applied Superconductivity*, 15(2):3648–3651, 2005.
- [2] J. Cordani. Optimizing The Oxide Process. *PC FAB*, pages 88–93, January 1989.
- [3] T.M. Tam and R.D. Robinson. Analysis of Factors Controlling Peel Strength of Black Oxide Conversion Coatings. *Plating and Surface Finishing*, pages 74–77, April 1986.
- [4] R. Menzel. *Photonics: Linear and Nonlinear Interactions of Laser Light and Matter*. Springer Edition, 2001.
- [5] S. Ungar. *Fibre Optics, Theory and Applications*. John Wiley & Sons, 1990.
- [6] VAMAS Technical Party for superconducting materials. VI. Standard method for I_c determination. VI-1: Recommended standard method for determination of d.c. critical current of Nb_3Sn multifilamentary composite superconductor. *Cryogenics*, 35:S105–S112, 1995.
- [7] L.F. Goodrich, and A.N. Srivastava. Comparison of Transport Critical Current Measurement Methods. *Advances in Cryogenic Engineering (Materials)*, 38:559–566, 1992.
- [8] Spectra-Physics (US). private communications, 2004.
- [9] Spectra-Physics (US). private communications, 2001.
- [10] SEDI (France). private communications, 2005.
- [11] J.L. Armstrong, J. Matthewson, and C.R. Kurkjian. Humidity Dependence of the Fatigue of High-Strength fused Silica Optical Fibers. *Journal of the American Ceramic Society*, 83(12):3100–3108, 2000.
- [12] M.J. Matthewson, C.R. Kurkjian, C.D. Haines, Navin Venugopal. Temperature dependence of strength and fatigue of fused silica fiber in the range 77 to 473 K. In *Proceedings of SPIE: Reliability of Optical Fiber Components, Devices, Systems, and Networks*, volume 4940, pages 74–79, 2003.
- [13] J.M. Vaughan. Liquid helium, vortices, helices and laser light scattering. *Journal of Physics: Condensed Matter*, 11:7711–7722, 1999.

BIBLIOGRAPHY

- [14] R.D. McCarty. *Thermophysical Properties of Helium-4 from 2 to 1500 K with Pressure to 1000 Atmospheres*, pages 11–15. National Institute of Standards and Technology, 1972.
- [15] L. Augyroun. *Contribution à l'étude des écoulements verticaux d'hélium diphasique*. PhD thesis, Université Pierre et Marie Curie, 1998.
- [16] R.B. Dingle. The anomalous skin effect and the reflectivity of metals. I & II. *Physica*, XIX:311–364, 1953.
- [17] C. Kittel. *Introduction to Solid State Physics-7th ed.* John Wiley & Sons, 1996.
- [18] E. Hecht. *Optics*, pages 421–425. Addison-Wesley, 4th. edition, 2002.
- [19] F. Ayela. *Réalisation d'un détecteur absolu de très faibles champs magnétiques*. PhD thesis, Université Joseph Fourier-Grenoble I, 1993.
- [20] M.L. Cohen and J.R. Chelikowsky. *Electronic Structure and Optical Properties of Semiconductors*, chapter 5. Springer-Verlag, 1988.
- [21] A.E. Rakhshani. Preparation, characteristics and photovoltaic properties of Cuprous oxide-A review. *Solid-State Electronics*, 39(1):7–17, 1986.
- [22] T. Masumi, H. Yamaguchi, T. Ito and H. Shimoyama. New Fine Structures near the Optical Absorption Edge of CuO at Low Temperatures. *Journal of the Physical Society of Japan*, 67(1):67–70, 1998.
- [23] S. Fuzier. Use of the bare chip Cernox thermometer for the detection of second sound in superfluid helium. *Cryogenics*, 44:211–213, 2004.
- [24] R.G. Scurlock. Proceedings of the 2nd Cryogenic Engineering Conf. Brighton 7-10. page 144. Iliffe Science and Technology Pub. Co., May 1968.
- [25] CryoData. CRYOCOMP®.
- [26] A. V. Oppenheim and R.W. Schaffer. *Discrete-Time Signal Processing*, pages 311–312. Englewood Cliffs, 1989.
- [27] P. Bauer. *Stability of Superconducting Strands for Accelerator Magnets*. PhD thesis, Technische Universität Wien, 1998.
- [28] A. Devred *et al.* *Quench Localization in Full-Length SSC R&D Dipoles*, pages 73–83. Plenum Press, New York, 1989.
- [29] C. Schmidt. Review of the steady state and transient heat transfer in pool boiling helium. *International Institute of Refrigeration, Commission A1/2-Saclay (France)*, (6):17, 1981.
- [30] B.J. Maddock, G. James, and W.T. Norris. Superconductive composites: heat transfer and steady state stabilization. *Cryogenics*, pages 261–273, August 1969.

Chapter V

Numerical simulation of the thermal behavior of a Cu/NbTi multifilament composite wire

Contents

V.1	Introduction to the numerical analysis	171
V.1.1	Description of the simulated wire	171
V.1.2	Environmental conditions surrounding the wire	171
V.1.3	Hypotheses of the simulation	171
V.1.3.1	Axi-symmetry	173
V.1.3.2	Uniformity of temperature and homogenization of the physical properties	173
V.1.3.3	Energy disturbance	173
V.1.3.4	Cooling environment	173
V.2	Description of the numerical model	174
V.2.1	Mesh	174
V.2.2	Boundary and initial conditions	174
V.2.3	Heat balance equation	175
V.3	Heat generation in the multifilament composite wire	175
V.3.0.1	Heat generation function, $G(T)$	175
V.3.0.2	Determination of the current sharing temperature, T_{cs}	177
V.4	Initial heat perturbation	177
V.5	Heat transfer coefficient and adiabatic conditions	178
V.5.1	Adiabatic conditions	178
V.5.2	Heat transfer coefficient for pool boiling Helium I	179
V.5.2.1	Determination of E_f and E_t	179
V.5.2.2	Comparison of energies and determination of the heat transfer coefficient	181
V.6	Results on the numerical simulation and comparison with experimental data	182
V.6.1	Influence of the numerical parameters	182

V.6.1.1	Minimum Quench Energy	182
V.6.1.2	Minimum Propagating Zone	184
V.6.1.3	Quench Decision Time	184
V.6.1.4	Time evolution of the maximum temperature of the sample	185
V.6.1.5	Voltage across the heated zone and comparison with experimental data	187
V.6.2	Comparison quenched zone extension and helium film ex- tension	189
V.6.3	Comparison between numerical simulations and experimen- tal data	191
V.7	Conclusion on numerical simulations	194

IN THIS CHAPTER, we will introduce a numerical model based on a Finite Element Method, which aims at simulating the thermal behavior of Cu/NbTi multifilament composite wires undergoing a quench. The numerical program¹ was written under CASTEM[®] v98. It was subsequently modified and upgraded under CAST3M[®] v2003 [1].

The program resolves a non-linear transient heat balance equation and yields the temperature profile along the wire as a function of time. The algorithm used for the resolution is based on a Dupont2 algorithm with a double time step resolution [2] [3].

V.1 Introduction to the numerical analysis

V.1.1 Description of the simulated wire

A composite conductor having the geometry of a Cu/NbTi wire from batch NbTi-2 has been modeled. It is made-up of different materials which are drawn together to form a multifilament structure. NbTi filaments of 5-to-6 μm of diameter are embedded into an OFHC copper matrix. Figure V.1 (page 172) shows a detailed cross-section of such a composite wire. Two distinctive regions can be distinguished:

- a high purity copper region (copper Cu1),
- a multifilament region (copper Cu2 plus NbTi filaments).

For the oncoming analysis, we define as $x_{\text{Cu}1}$ and $x_{\text{Cu}2}$ the fraction of copper Cu1 and Cu2, respectively, and as x_s , the fraction of superconductor such that:

$$x_{\text{Cui}} = \frac{A_{\text{Cui}}}{A_w}, \quad \forall i \in \{1, 2\} \quad (\text{V.1})$$

$$x_s = 1 - (x_{\text{Cu}1} + x_{\text{Cu}2}) \quad (\text{V.2})$$

where A_{Cui} ($\forall i \in \{1, 2\}$) is the cross-sectional area of copper and A_w is the total cross-sectional area of the wire.

The main geometrical parameters of the wire are given in Table V.1 (page 172). The residual resistivity ratio was estimated from the results obtained from the stability measurements with the diode laser (in chapter IV, see footnote page 154).

V.1.2 Environmental conditions surrounding the wire

The wire, in which flows a transport current I_t , is surrounded by liquid helium or vacuum at $T_{\text{op}} = 4.2$ K and atmospheric pressure. The pressure exerted by the volume of liquid helium above the conductor is neglected. A background magnetic field of 5, 6 or 7 T is applied transversally to the axis of the conductor.

V.1.3 Hypotheses of the simulation

Different hypotheses have been made to simplify the numerical model.

¹This program was originally written by F.P. Juster, CEA/Saclay, DSM/DAPNIA/SACM, France.

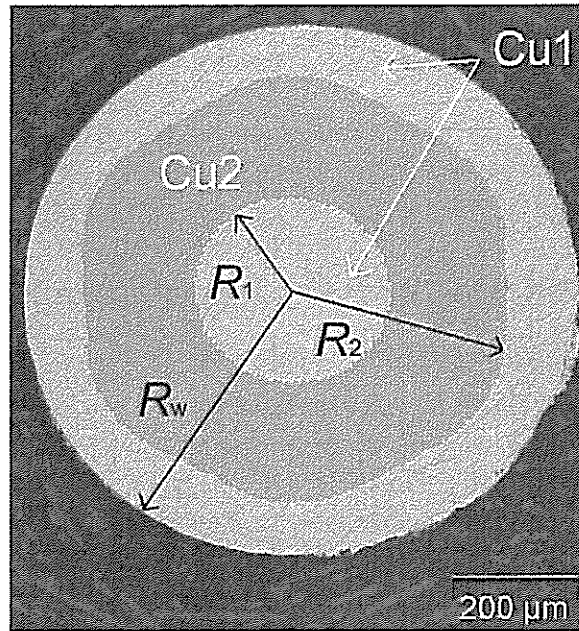


Figure V.1: Micrography of the cross-section of a LHC-type Cu/NbTi multifilament composite wire from batch NbTi-2.

Table V.1: Parameters to model the NbTi-2 wire.

Radius of the wire, R_w	~ 0.412 mm
Inner diameter of the multifilament zone, $R_1^{(*)}$	~ 0.149 mm
Outer diameter of the multifilament zone, $R_2^{(*)}$	~ 0.33 mm
Ratio Cu/non-Cu for the entire cross-section, r_1	1.96
Ratio Cu/non-Cu for the multifilament zone, r_2	0.33
Fraction of pure copper Cu1, x_{Cu1}	~ 0.497
Fraction of degraded copper Cu2, x_{Cu2}	~ 0.172
Fraction of NbTi superconductor, x_s	~ 0.341
Estimated bulk copper RRR	150

(*) Generic information provided by T. Boutboul, CERN.

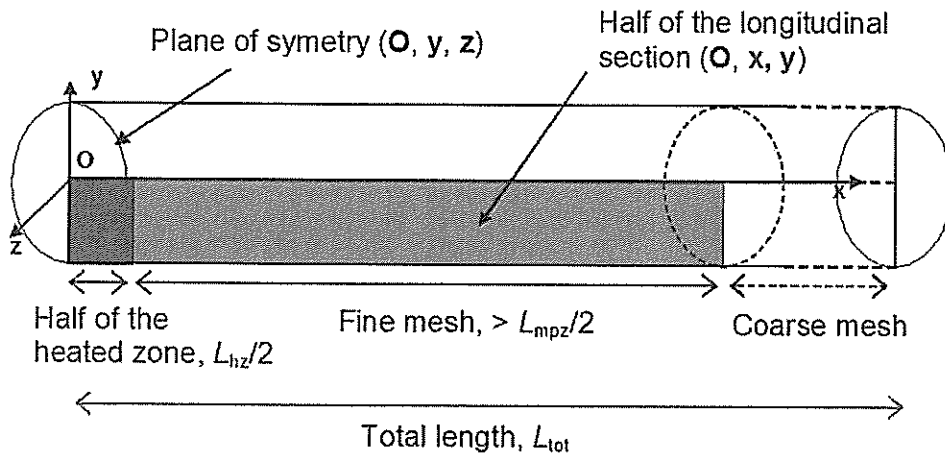


Figure V.2: Definition of the mesh based on an axi-symmetrical model.

V.1.3.1 Axi-symmetry

The geometry of the conductor is cylindrical. The length of the conductor is ~ 60 mm in the active zone of measurements. In view of its small diameter of ~ 0.82 mm, it can be considered as infinitely long compared to its diameter.

V.1.3.2 Uniformity of temperature and homogenization of the physical properties

We consider in first approximation that the temperature is uniform at all times in each cross-section of the wire (see Appendix E, page 246). Thus, the physical properties of the different materials can be averaged over the wire cross-section. These physical properties are:

- heat capacity [$\text{J}/\text{m}^3\text{K}$],
- thermal conductivity [$\text{W}/\text{m}\cdot\text{K}$],
- electrical resistivity [Ωm].

V.1.3.3 Energy disturbance

We did not model the source of energy disturbance. The energy is assumed to be released in the conductor volume over a heated zone of ~ 1 mm. The duration of the energy disturbance is a parameter set by the user.

V.1.3.4 Cooling environment

The cooling environment of the conductor is represented by a heat transfer coefficient. This coefficient is taken equal to zero in a vacuum and is function of temperature, time and distance along the wire when liquid helium cooling is considered.

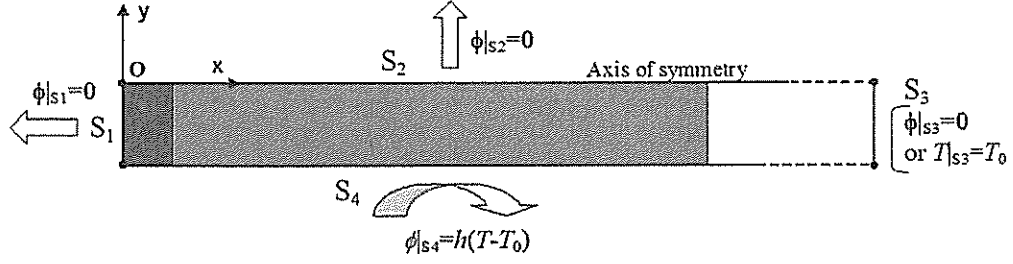


Figure V.3: Definition of the boundary conditions imposed on the model. Φ 's symbolize the fluxes exchanged through the surfaces S_i ($i \in \{1, 2, 3, 4\}$) [bold fonts representing vectors]. Here, T_0 is equal to 4.2 K.

V.2 Description of the numerical model

V.2.1 Mesh

Figure V.2 (page 173) presents a sketch of the mesh used to model the conductor. We consider a cartesian system of coordinates (O, x, y, z) such that (O, x) corresponds to the longitudinal axis of the conductor and (O, y, z) the plane of symmetry at the center of the heated zone. The conductor sections of uniform temperature are parallel to the (y, z) plane.

The mesh corresponds to the discretization of one quarter of the longitudinal section of the conductor included in the (O, x, y) plane. Three parts are distinguished. The first part (red) represents half of the heated zone having a length of $L_h/2$. The second part (blue) covers a distance assumed to be longer than half of the Minimum Propagating Zone, $L_{mpz}/2$, for which the mesh is finely discretized. This distance is adjusted by the user. The third part (white) is taken to be long enough so that the outer radius of the composite wire, R_w , becomes negligible compared to the total length of the simulated wire, L_{tot} . Then, the effects of the boundary condition at its extremity are avoided. In this region, it is not necessary to refine the resolution and a decreasing density of nodes was implemented.

V.2.2 Boundary and initial conditions

Initial condition: At $t = 0$, the temperature of the conductor, T_{op} , is assumed to be uniform at 4.2 K.

Boundary condition: Figure V.3 (page 174) represents the mesh, which is limited by four sides. Each side, referred to as S_i ($i \in \{1, 2, 3, 4\}$), is affected by a boundary condition:

- on sides S_1 and S_2 : the thermal gradients are assumed to be zero, $\varphi|_{S_{1-2}} = -\frac{\partial T}{\partial x} = 0$,
- on side S_3 : either the temperature, $T|_{S_3}$, is set to be constant, equal to 4.2 K or the thermal gradient is nil, $\varphi|_{S_3} = 0$, at all time,
- on side S_4 : we impose a heat transfer coefficient, h (corresponding to helium liquid, $h \neq 0$, or vacuum, $h = 0$).

V.2.3 Heat balance equation

It has been assumed that the temperature is uniform in each conductor cross-section. Consequently, the temperature depends only on two parameters: the distance along the wire, x , and the time, t .

The mesh being defined, the program solves with the appropriate boundary and initial conditions the following non-linear transient heat balance equation governing the thermal behavior of the wire:

$$C_w(T, B) \frac{\partial T}{\partial t} - \frac{\partial}{\partial x} \left[\lambda_w(T, B) \frac{\partial T}{\partial x} \right] - G(T, B) - Q(t) + H(T, t) = 0 \quad [\text{W/m}^3] \quad (\text{V.3})$$

with:

- $C_w(T, B)$: average heat capacity of the wire in $\text{J/m}^3\text{K}$,
- $\lambda_w(T, B)$: average thermal conductivity of the wire in W/m-K ,
- $G(T, B)$: heat generation function,
- $Q(t)$: initial heat disturbance,
- $H(T, t) = \frac{p}{A_w} h(T - T_0)$: the linearized heat power exchanged with the coolant (p : wetted perimeter, and h , the heat-exchange coefficient).

The average thermal properties are detailed in the Appendix F (page 250). The heat generation function, $G(T, B)$, the initial perturbation, $Q(t)$, and the exchanged heat power, $H(T, t)$, are discussed thereafter.

V.3 Heat generation in the multifilament composite wire

V.3.0.1 Heat generation function, $G(T)$

Figure V.4 (page 176) shows a classical linear approximation of the critical current versus temperature characteristic of a multifilament composite wire at a given background magnetic field, B . At the operating temperature, T_{op} , the transport current, I_t , flows entirely in the superconducting filaments with no heat dissipation (see chapter II, page 50). If the temperature of the superconductor increases, the current sharing temperature, T_{cs} , is eventually exceeded. Then, the superconductor can no longer carry the whole transport current, and a fraction of it is shared with the copper matrix. Consequently, heat dissipation occurs which increases further the temperature of the conductor. When the critical temperature is exceeded, the superconductor is in the normal resistive state and no current flows through it. All the current is then dumped into the metallic matrix and the maximum heat dissipation is reached.

Thus, three regimes can be singled out:

- $T < T_{cs}$: superconducting regime,
- $T_{cs} < T < T_c$: current sharing regime,
- $T > T_c$: normal-state regime.

$T < T_{cs}$: In this regime, there is no current flowing in the copper matrix, and the superconductor carries the full current without losses:

$$G(T, B) = 0, \quad \forall T < T_{cs} \quad (\text{V.4})$$

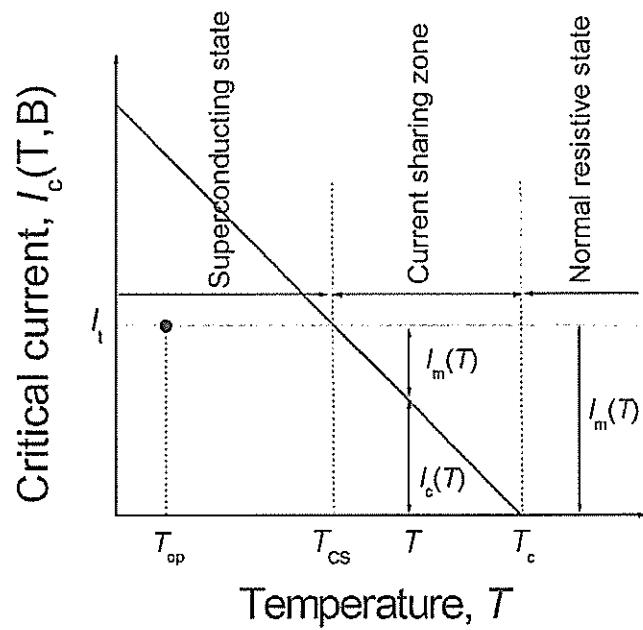


Figure V.4: Typical critical current versus temperature characteristic of a composite wire at a given background magnetic field.

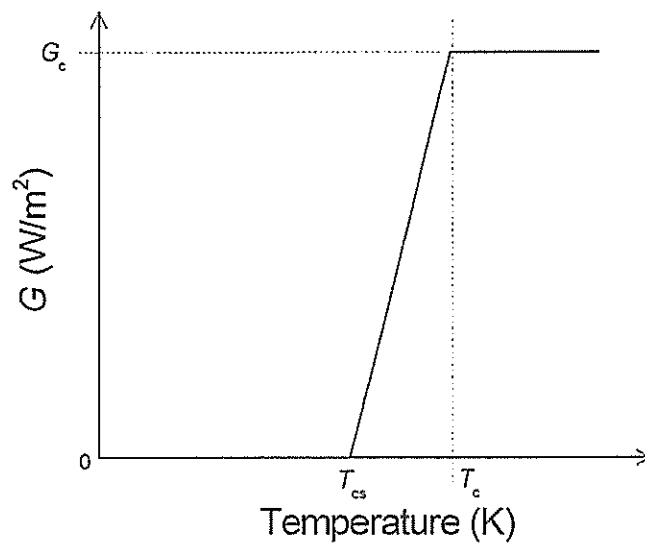


Figure V.5: Heat generation function for a multifilament composite wire.

Table V.2: Current sharing temperatures and critical temperatures.

T_{cs} (K)	80% of I_c	85% of I_c	95% of I_c	T_c (K)
5 T	4.8	4.65	4.35	7.17
6 T	4.7	4.58	4.33	6.7
7 T	4.61	4.51	4.3	6.24

$T_{cs} < T < T_c$: In this regime, we follow the classical description that the excess transport current is carried out by the copper matrix resulting in a linear dependency of $G(T, B)$ with respect to the temperature [4]:

$$G(T, B) = G_c(T, B) \frac{T_{cs}(J_w, B) - T}{T_{cs}(J_w, B) - T_c(J_w, B)} \quad [\text{W/m}^3] \quad (\text{V.5})$$

where,

$$G_c(T, B) = \frac{1+r}{r} \rho_{Cu}(T, B) J_w^2 \quad [\text{W/m}^3] \quad (\text{V.6})$$

and J_w is the current density averaged over the conductor cross-section. G_c represents the maximum density of dissipated power when all the current flows in the copper matrix.

$T > T_c$: In this regime, we simply have:

$$G(T, B) = G_c(T, B) \quad [\text{W/m}^3] \quad (\text{V.7})$$

Figure V.5 (page 176) shows the heat generation function versus temperature.

V.3.0.2 Determination of the current sharing temperature, T_{cs}

Using the simple model illustrated in Figure V.4 (page V.4), the current sharing temperature can be expressed as:

$$T_{cs}(J_w, B) = T_c(J_w, B) - \frac{(1+r)J_w}{J_c(T_{op}, B)} (T_c(J_w, B) - T_{op}) \quad [\text{K}] \quad (\text{V.8})$$

where $J_c(T_{op})$ is the critical current density at T_{op} and B . Table V.2 (page 177) summarizes the different values of current sharing temperatures at various percentages of critical current and background magnetic flux densities.

V.4 Initial heat perturbation

As already mentioned, the source of energy perturbation is not modeled, and we assume that it is released within the conductor.

This energy, whose value is set by the user, is first transformed into a gaussian or trapezoidal heat power perturbation and subsequently divided by the volume of the heated zone, $\vartheta_{hz} = L_{hz} A_w$ to be treated by the numerical program. For the

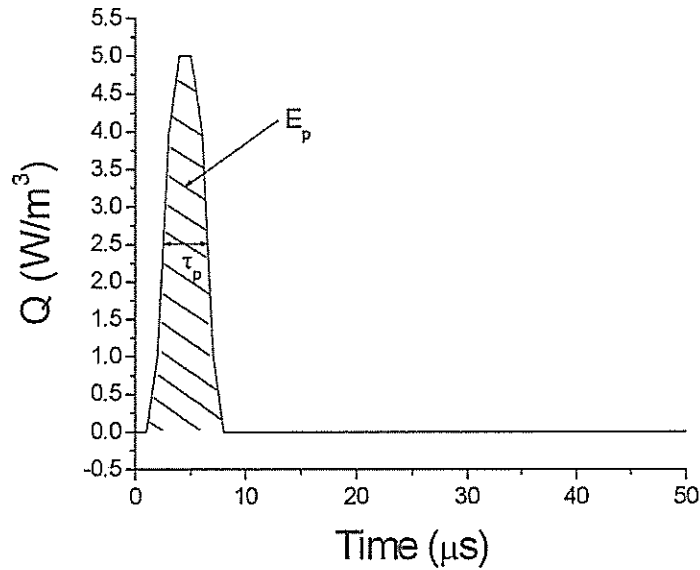


Figure V.6: Shape of the pulse power density implemented in CAST3M. The integral of the pulse power density over the pulse duration τ_p fixed corresponding to the half height of the pulse yields the pulse energy, E_p .

gaussian shape, the transformation is in such a way that the integral of the power perturbation pulse over the pulse duration yields the input energy:

$$E_p = \vartheta_{hz} \int_{\tau_p} Q(t) dt \quad [\text{J}] \quad (\text{V.9})$$

Two shapes of the initial heat perturbation have been tested: a gaussian shape and a trapezoidal quasi-rectangular shape. Figure V.7 (page 179) shows a typical Gaussian shape of the pulse power density while the trapezoidal shape can be seen in Figure V.10 (page 183) in the subsequent section V.6 (page 182). The shape of the pulse weakly influences the numerical result and the error on the computed Minimum Quench Energy is of a few percent at most. For this analysis, we rely on the initial heat perturbations of trapezoidal shape.

V.5 Heat transfer coefficient and adiabatic conditions

V.5.1 Adiabatic conditions

The program allows the user to choose between adiabatic and helium cooling conditions. The choice is determined by the heat transfer coefficient, h , implemented into the program:

- helium cooling: $h = h(T(x), t)$,
- adiabatic conditions: $h = 0$.

In adiabatic conditions, the physical problem is simplified and the number of unknown parameters is reduced. Unfortunately, the results of those runs could not be

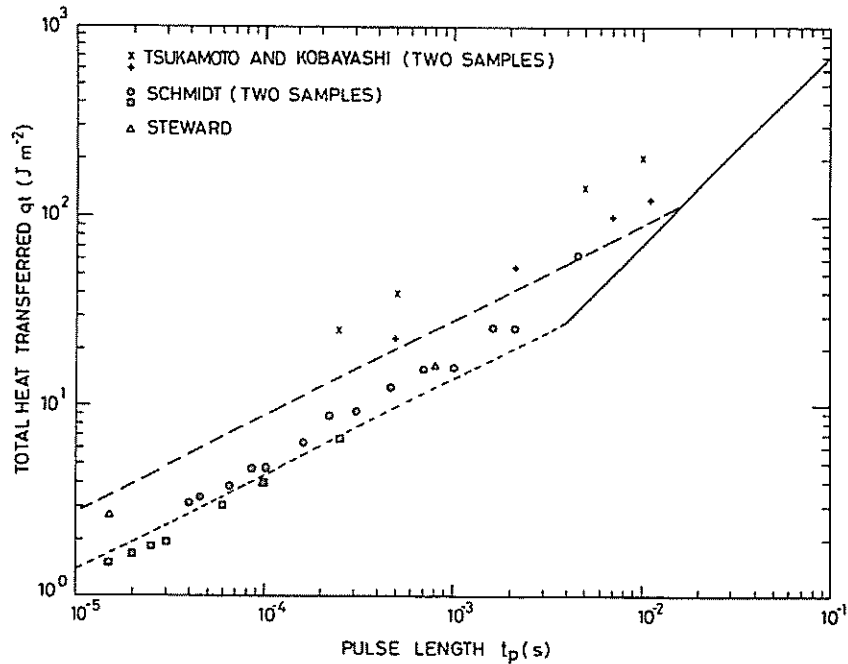


Figure V.7: Transient heat transfer to liquid helium: the maximum heat per unit area which may be transferred by nucleate boiling, shown as a function of heat-pulse duration. Dashed and dotted lines correspond to Equation V.12 (page 180) with $\eta = 900$ and $\eta = 450$ respectively (adapted from [5]).

experimentally validated because of leak problems. Therefore, in the following, we focus on helium cooling conditions.

V.5.2 Heat transfer coefficient for pool boiling Helium I

In the stability experiment involving very short pulse heat perturbations, the thermal phenomena are transient. To study such phenomena, we use a classical approach which aims at comparing the energy transferred from the sample to liquid helium, E_t , to the energy necessary to trigger film boiling, E_f :

- liquid regime: $E_t < E_f$,
- film regime: $E_t \geq E_f$.

Schematically, the numerical program calculates at each time step these energies for each portion dx of the wire and adjust the heat transfer coefficient according to it. The subsequent sections will present the estimation of these energies and the resulting heat transfer coefficient.

V.5.2.1 Determination of E_f and E_t

Energy to trigger film boiling, E_f : In pool boiling helium I, the heat transfer from solid to bulk liquid helium is enhanced during a short period of time before the onset of film boiling [6]. W.G. Steward [7], C. Schmidt [8] and O. Tsukamoto [9]

have carried out different experiments, which aimed at measuring the onset time of film boiling. The experimental setups were based on a resistive heater immersed into an helium bath. A current pulse was driven through the heater and heat was transferred to the bath. By adjusting the amplitude of the current or the width of the pulse, the film boiling regime could be ignited. Then, the total heat transfer per unit area of heater could be estimated as a function of pulse duration. A compilation of their results by M.N. Wilson [5] is presented in Figure V.7 (page 179). To interpret the data, C. Schmidt [10] considered a simple model based on a diffusion process across a thin layer of liquid helium, a (see Appendix E, page 246):

$$a = \frac{\pi}{2} \sqrt{\frac{\lambda_{\text{lh}} t_{\text{dif}}}{C_{\text{lh}}}} \quad [\text{m}] \quad (\text{V.10})$$

where λ_{lh} is the thermal conductivity of liquid helium, C_{lh} is the heat capacity of liquid helium, and t_{dif} is the time during which the energy diffuses into the layer. The heat transfer is efficient as long as the helium coolant remains liquid. The amount of energy to vaporize the layer, a , of liquid helium is:

$$E_f = a\mathcal{L} = \frac{\pi}{2} \sqrt{\frac{\lambda_{\text{lh}}}{C_{\text{lh}}}} \mathcal{L} t_{\text{dif}}^{1/2} \quad [\text{J/m}^2] \quad (\text{V.11})$$

where \mathcal{L} is the latent heat of vaporization of liquid helium. As suggested by M.N. Wilson [5], we can parametrize E_f as:

$$E_f = \eta t_{\text{dif}}^n \quad [\text{J/m}^2] \quad (\text{V.12})$$

where n has been chosen equal to 0.6 as suggested by C. Schmidt [10] and η is given by:

$$\eta = \frac{\pi}{2} \sqrt{\frac{\lambda_{\text{lh}}}{C_{\text{lh}}}} \mathcal{L} \quad [\text{J/m}^2/\text{K}^{-0.5}] \quad (\text{V.13})$$

In our model, the diffusion time has to be evaluated at each nod,

$$t_{\text{dif}} = t - t_{\text{idif}} \quad [\text{s}] \quad (\text{V.14})$$

with $t_{\text{idif}} = t(T > T_0, x_i)$, $\forall x_i \in S_4$, corresponds to the time where heat starts to be transferred to the helium at nod x_i . In the present version of the program, we rely on an artifact. We assume that the diffusion time can be estimated as:

$$t_{\text{dif}} = \left[\frac{(T(x_i, t) - T_0)}{(T_{\text{max}}(t) - T_0)} \right] \times t \quad [\text{s}] \quad (\text{V.15})$$

where $T_{\text{max}}(t) = \max[T(x_i, t)]$, $\forall x_i \in S_4$. Indeed, if the temperature T is equal to T_0 at nod x_i , $t_{\text{dif}} = 0$. However, as soon as T exceeds T_0 , t_{dif} starts increasing, and the maximum value is achieved for T_{max} , which corresponds to the temperature of the center of the heated zone.

Energy transferred from the sample to liquid helium, E_t : The energy transferred by the wire sample to liquid helium, E_t is estimated at each nod x_i of the side mesh S_4 as:

$$E_t(x_i) = \int_0^t h[T(x_i), t](T - T_0) dt, \quad \forall x_i \in S_4 \quad [\text{J/m}^2] \quad (\text{V.16})$$

The determination of the heat transfer coefficient is given by comparing E_t and E_f at each nod and each time step.

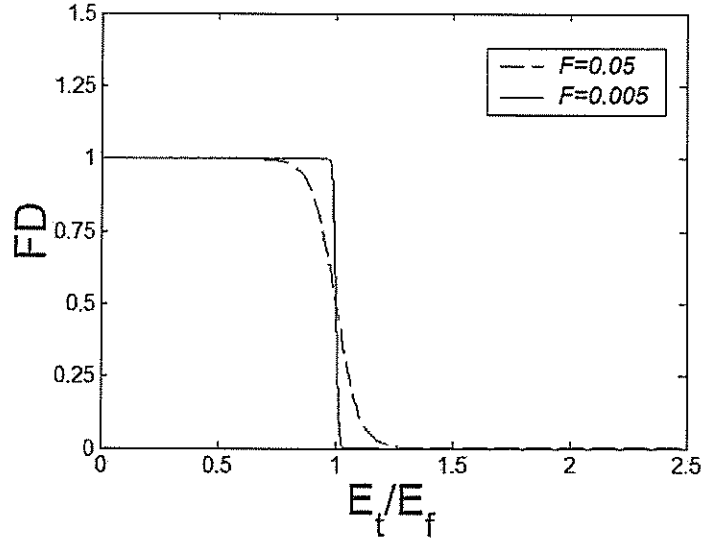


Figure V.8: Fermi-Dirac-like function to smoothen the heat transfer coefficient h for different values of F : 0.05 and 0.005.

V.5.2.2 Comparison of energies and determination of the heat transfer coefficient

To automatically compare both energies E_t and E_f and smoothen the transition from Kapitza regime to film boiling, we used a Fermi-Dirac-like distribution, FD :

$$FD(E_t/E_f) = \frac{1}{1 + e^{\frac{E_t/E_f - 1}{F}}} \quad (\text{V.17})$$

where $F \in]0, 1]$. F has been chosen equal to 0.0005 in the current analysis. Figure V.8 (page 181) shows FD for two values of F . We apply this distribution to the heat exchange coefficient so that:

$$h(T, t) \simeq FD\left(\frac{E_t}{E_f}\right)h_k + \left[1 - FD\left(\frac{E_t}{E_f}\right)\right]h_{\text{film}} \quad [\text{W/m}^2/\text{K}] \quad (\text{V.18})$$

Then, the heat transfer coefficient can be automatically estimated along the the wire length as a function of E_t/E_f .

$E_t < E_f$: We assume that the dominant heat transfer is ruled by Kapitza resistance:

$$h(T, t) = h_k(T, t) = a_k(T + T_0)(T^2 + T_0^2) \quad [\text{W/m}^2/\text{K}] \quad (\text{V.19})$$

where a_k is a parameter which adjusts the magnitude of heat transfer [10]. Typical values of a_k for copper surface ranges from $\geq 100 \text{ W/m}^2/\text{K}^4$ to $\sim 1000 \text{ W/m}^2/\text{K}^4$ [11].

$E_t > E_f$: As soon as the energy to create the film vapor is exceeded, the liquid helium enters the regime of film vapor, and:

$$h(T, t) = h_{\text{film}} \quad [\text{W/m}^2/\text{K}] \quad (\text{V.20})$$

In our simulation, we fixed h_{film} to $250 \text{ W/m}^2/\text{K}$ to restrain the number of parameters.

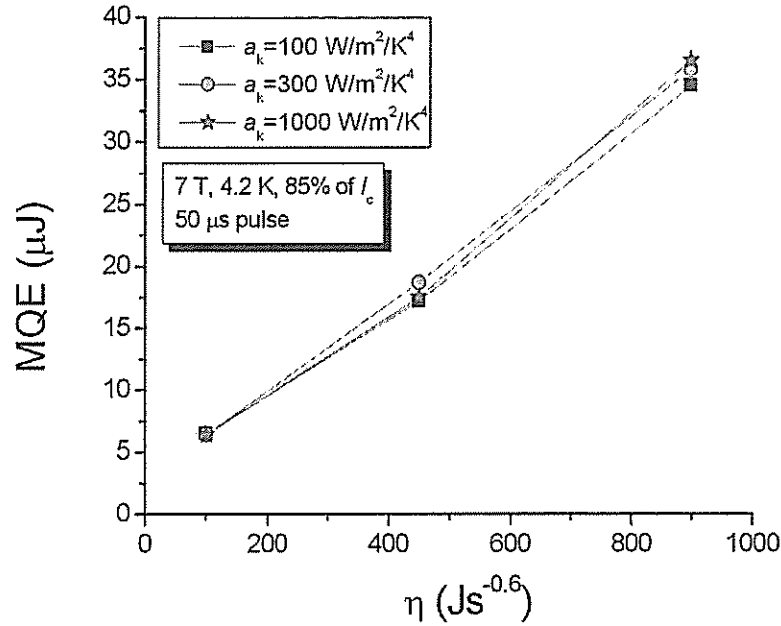


Figure V.9: Evolution of the Minimum Pulse Energy as a function of the parameters η and a_k .

V.6 Results on the numerical simulation and comparison with experimental data

In view of the numerous measurements carried out with the diode laser, we will focus on the simulation of a few main stability parameters at 7 T, 4.2 K and 85% of critical current for a pulse duration of 50 μs . These stability parameters are:

- Minimum Quench Energy (MQE),
- Minimum Propagating Zone (MPZ),
- Quench Decision Time (QDT).

We will study the influence of the numerical parameters:

- η , magnitude of the energy to trigger film vapor,
- a_k , Kapitza coefficient representing the magnitude of the heat transfer,

on the stability parameters, and on other data such as the time evolution of the voltage and maximum temperature of the sample. Subsequently, we will compare some numerical results to a few experimental data for a chosen set of parameters $\eta = 450 \text{ Js}^{-0.6}$ and $a_k = 300 \text{ W/m}^2/\text{K}^4$ which lead to the best agreement between the simulated voltage trace, V_1 , and our measurements.

V.6.1 Influence of the numerical parameters

V.6.1.1 Minimum Quench Energy

To find the Minimum Quench Energy the program increases automatically the pulse energy till a quench is detected. The quench criterion is based on a maximum nor-

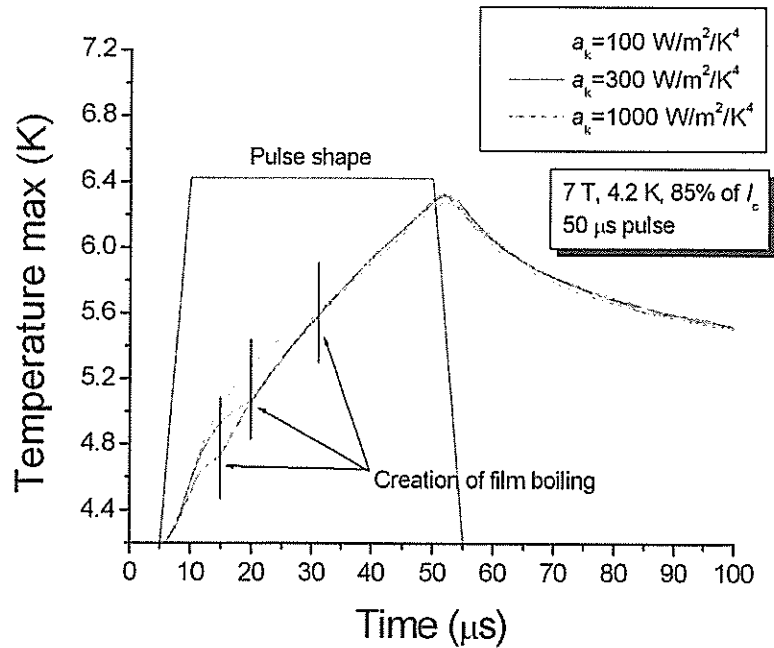


Figure V.10: Time evolution of the maximum temperature along the sample for $\eta = 450 \text{ Js}^{-0.6}$.

mal zone extension fixed by the user. When the calculated normal zone extension is larger than this criterion, the program stops and yields post-treated set of plots. Using this method, we estimated Quench Energies for different set of parameters η and a_k as depicted in Figure V.9 (page 182).

The most sensitive parameter appears to be η , which characterizes the energy necessary to trigger helium film boiling. The Minimum Quench Energy increases with increasing η 's. Indeed, as long as the helium remains liquid the exchanged power is large enough to compensate the initial heat perturbation. This lasts until the onset of the vapor film. Then, the heat transfer coefficient decreases, enabling the heat generation to take over igniting the thermal run away. Decreasing the value of η corresponds to tend toward adiabatic conditions for which the Minimum Quench Energy is lower. On the contrary, parameter a_k , which characterizes the exchange of heat flux between the sample and liquid helium, appears to influence weakly the Minimum Quench Energy: of the order of 3% from 100 to 1000 $\text{W/m}^2/\text{K}^4$.

To understand the influence of this latter parameter, let's have a closer look at the time evolution of the maximum temperature along the sample for $\eta = 450 \text{ Js}^{-0.6}$ and various a_k 's as depicted in Figure V.10 (page 183). The time of the onset of film boiling appears sooner with increasing a_k 's. Indeed, at η constant, *i.e.*, at a fixed energy to trigger film boiling, by increasing a_k , the energy transferred to liquid helium increases faster reaching this first energy sooner. However, as soon as the transition to film boiling occurs, the time evolutions of the maximum temperature tend to follow each other. The slight difference in the time evolutions are responsible for the small discrepancy in the estimated Minimum Quench Energies.

The differences in the Minimum Quench Energies and the temperature profiles being

V.6. RESULTS ON THE NUMERICAL SIMULATION AND COMPARISON WITH EXPERIMENTAL DATA

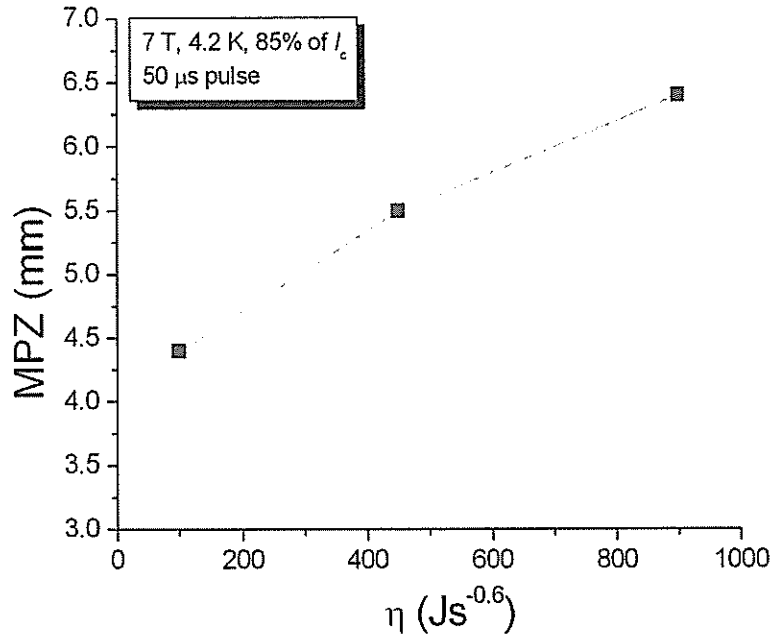


Figure V.11: Evolution of the Minimum propagating Zone as a function of parameters η .

negligible, we set a_k equal to $300 \text{ W/m}^2/\text{K}^4$ in subsequent analysis (value suggested by C. Schmidt [10]).

V.6.1.2 Minimum Propagating Zone

Figure V.11 (page 184) shows the evolution of the Minimum propagating Zone as a function of parameter η . In this case, we do not show the evolution of the MPZ as a function of a_k . Indeed, as the MPZ extension is determined from the temperature profile (see subsection V.6.2, page 189), and the profiles of temperatures in our range of a_k 's are alike, the influence of this parameter is of a few percents at most (within the error of the estimation of the MPZ extensions).

Conversely, the MPZ extension increases with increasing η 's. Indeed, the larger η , the larger amount of energy is required to trigger a quench as it has been discussed previously. Consequently, the temperature increase gets larger, and, the spatial extension of the temperature profile, hence, the MPZ is larger.

As a comparison, the adiabatic MPZ extension was estimated around $\sim 3.5 \text{ mm}$ in the same conditions. As expected, the MPZ extension tends toward the adiabatic limit at small η 's.

V.6.1.3 Quench Decision Time

It is not easy to really distinguish visually the precise time of the quench decision. As for the experimental data, errors can be made. Nevertheless, some trends can be derived in the numerical simulation as it can be seen in Figure V.12 (page 185). At decreasing values of the parameter η , the QDT tends to decrease from $\sim 280 \mu\text{s}$

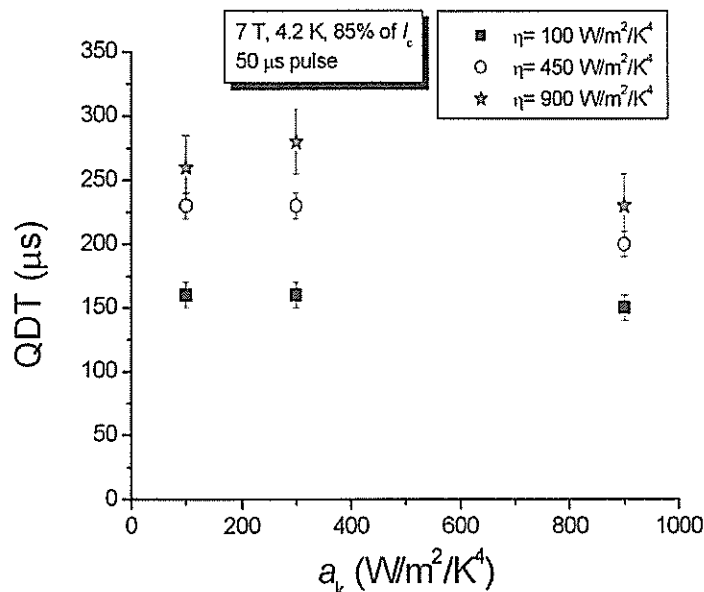


Figure V.12: Estimated Quench Decision times as a function of parameters η and a_k .

for $\eta = 900 \text{ W/m}^2/\text{K}^4$ to $\sim 150 \mu\text{s}$ for $\eta = 100 \text{ W/m}^2/\text{K}^4$. Indeed, at lower η 's, the sample tends to behave as in adiabatic conditions for which the quench decision occurs at a smaller temperature excursion. Conversely, no clear tendency could be revealed regarding the influence of the parameter a_k . The order of magnitude of the computed QDT 's correspond to the experimental data ($\sim 200 \mu\text{s}$) obtained at 7 T, 4.2 K and 85% of I_c for $\eta \simeq 450 \text{ Js}^{-0.6}$.

V.6.1.4 Time evolution of the maximum temperature of the sample

No experimental measurements of the temperature evolution along the wire sample have been carried out. These measurements are difficult to perform in view of the time frame of the thermo-electric phenomena involved in a quench.

Figure V.13 (page 186) shows the computed time evolution of the maximum temperature along the sample for $a_k = 300 \text{ W/m}^2/\text{K}^4$ and for various values of η . The maximum temperature corresponds to the temperature at the center of the heated zone.

The temperature variation gets larger for larger values of η 's. Indeed, by increasing the energy necessary to trigger the film of gaseous helium, the Kapitza regime lasts longer and a larger energy is needed to trigger a quench (see Figure V.9, page 182), which results in a larger initial temperature increase in the heated zone.

As discussed in the previous section, the temperature profile is weakly dependent on a_k 's since the transition to film boiling occurs at a very early stage (see next subsection V.6.1.5, page 187).

If we compare the time evolutions of the maximum temperature to the ones of the adiabatic case where there is no helium (see Figure V.13, page 186), we find the same trend. The reason can be found in Figure V.14 (page 186). It shows a rough

V.6. RESULTS ON THE NUMERICAL SIMULATION AND COMPARISON WITH EXPERIMENTAL DATA

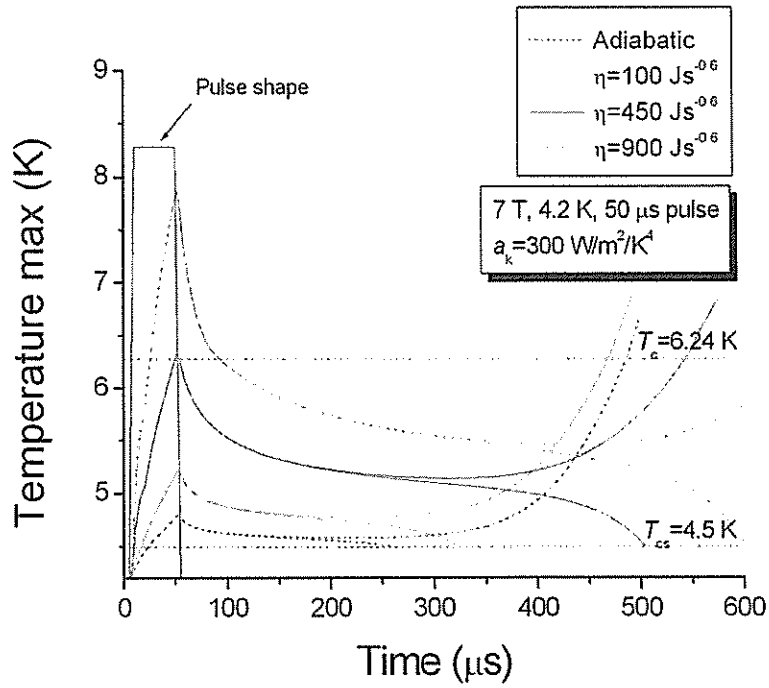


Figure V.13: Time evolution of the maximum temperature of the sample as a function of parameters η .

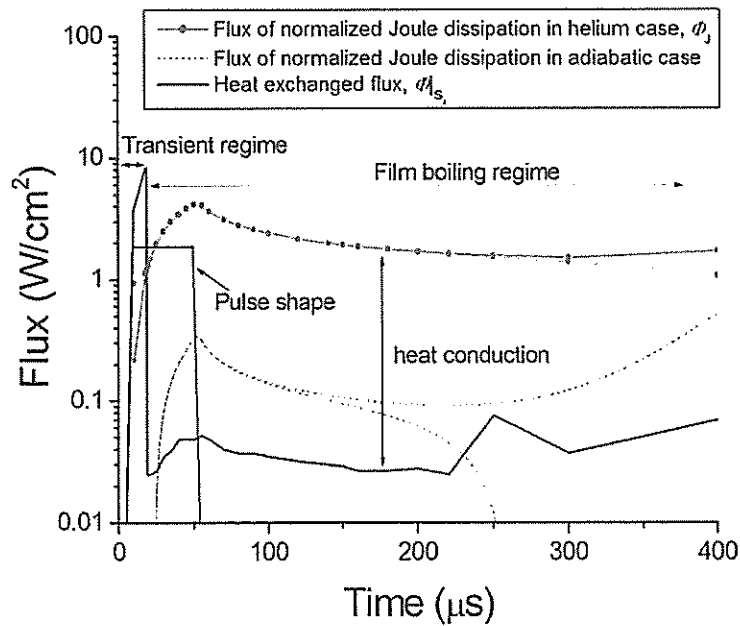


Figure V.14: Comparison between the heat flux exchanged between the sample and liquid helium and the Joule dissipation normalized to the wetted perimeter of the sample obtained at 4.2 K, 7 T, 85% of I_c and for a pulse duration of 50 μ s.

V.6. RESULTS ON THE NUMERICAL SIMULATION AND COMPARISON WITH EXPERIMENTAL DATA

comparison between the time evolution of the heat flux between the sample and the helium at $x = 0$ (in the plane of symmetry ($\mathbf{O}, \mathbf{y}, \mathbf{z}$), $\Phi|_{S_d}$, and the maximum Joule dissipation normalized to the wetted perimeter of the sample, Φ_J . These fluxes are defined as:

$$\Phi|_{S_d} = h[T(x=0) - T_0] \quad [\text{W/m}^2] \quad (\text{V.21})$$

$$\Phi_J = \frac{R_w}{2} \max[G(T, B)] \quad [\text{W/m}^2] \quad (\text{V.22})$$

Thus, in helium cooling conditions, once the film boiling regime has been ignited, the heat conduction becomes the dominant cooling mechanism. So, the thermal process converges toward adiabatic conditions where heat conduction is the only cooling mechanism.

The peak of temperature at the end of the pulse energy is assumed to be related to the heat capacity of the sample.

V.6.1.5 Voltage across the heated zone and comparison with experimental data

Our actual experimental data are the voltage traces recorded along the wire sample. Our goal in the numerical computation was to determine a set of parameters η and a_k leading to a reasonable fit of the voltage traces.

Before comparing computed voltage traces V_1 to experimental data, we shall describe the method used to realize this computation.

Computed voltage, V_1 : We have chosen to derive the voltage trace V_1 from the computed heat generation function $G(T, B)$. So, the voltage across the heated zone can be expressed as follow:

$$V_1 \simeq \int_{L_{nz}} \frac{G(T, B)}{J_w} dx \quad [\text{V}] \quad (\text{V.23})$$

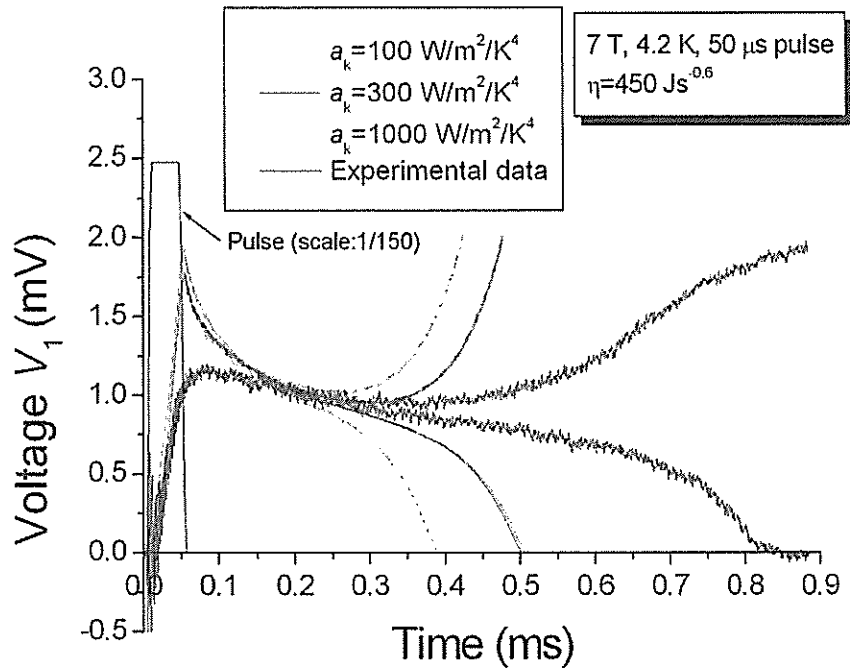
where $G(T, B)$ is the heat generation function defined in subsection V.3.0.1 (page 175) and J_w is the current density of the sample. In this version of the numerical simulation, we have not chosen to use this above expression. Indeed, it is not easy to perform such an integration at each time step. Then, we approximate the previous equation by:

$$V_1 \simeq \frac{\max[G(T, B)]L_{nz}}{J_w} \geq \int_{L_{nz}} \frac{G(T, B)}{J_w} dx \quad [\text{V}] \quad (\text{V.24})$$

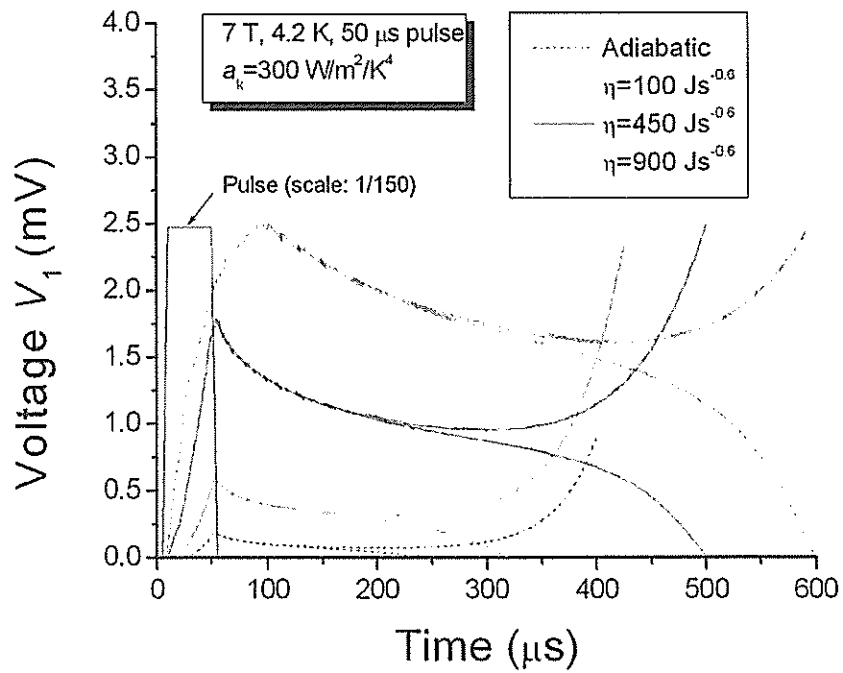
This is a rather crude approximation which overestimates V_1 for temperatures of the sample between T_{cs} and T_c . This expression becomes more accurate once the critical temperature is exceeded (see section V.16(a), page 190).

Comparison with experimental data: Figure V.15 (page 188) shows two plots of the time evolution of the computed voltage V_1 across the heated zone as a function of parameters η and a_k . In Figure V.15(a) (page 188), parameter η has been fixed to $450 \text{ Js}^{-0.6}$ while different plots have been shown for various a_k 's. As discussed for the Minimum Quench Energy and MPZ, the parameter a_k has only a weak influence on the shape of the voltage traces. The experimental voltage traces are also given. The numerical simulation does not fit perfectly the experimental data,

V.6. RESULTS ON THE NUMERICAL SIMULATION AND COMPARISON WITH EXPERIMENTAL DATA



(a) Influence of a_k and comparison with experimental data.



(b) Influence of η .

Figure V.15: Time evolution of the voltage across the heated zone as a function of parameters η and a_k and comparison with experimental data.

especially at the end of the energy pulse, but, it follows the shape of the time evolution of maximum temperature depicted in Figure V.13 (page 186). As for the temperature, the shape of the voltage traces strongly depends on the parameter η as depicted in Figure V.15(b) (page 188). The computed voltage trace follows the increasing temperature profile with increasing η . For small η 's, the shape of the voltage trace follows the time-evolution of the maximum temperature. However, for $\eta = 900 \text{ Js}^{-0.6}$, the temperature raises above the critical temperature and the shape of the voltage trace shows a better similitude to the actual experimental voltage trace as expected. For comparison, we also show the computed voltage trace in the adiabatic case.

To fit the voltage trace V_1 , we adjusted the parameters η and a_k . We found that the best agreement between simulated voltage and real data is obtained for the following set of numerical parameters:

- $\eta = 450 \text{ Js}^{-0.6}$,
- $a_k = 300 \text{ W/m}^2/\text{K}^4$.

These values remain in the range of typical values of copper [6]. They are used in the subsequent discussions.

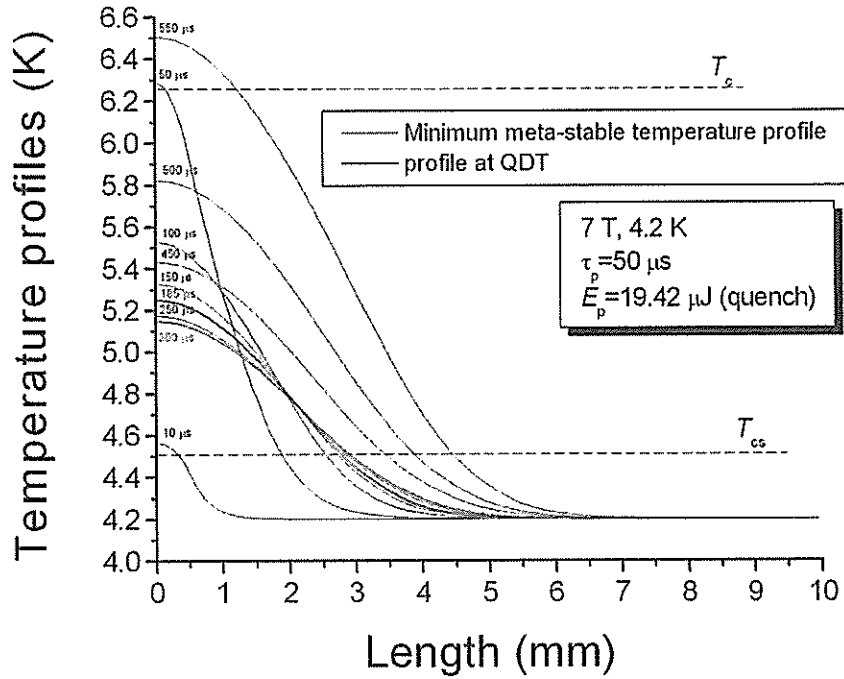
We did not try to adjust the model to fit the voltage traces beyond the quench decision time since we focused on the generation of the Minimum Propagating Zone. Otherwise, the model must be refined to better simulate the recovery or the full transition of the wire.

V.6.2 Comparison quenched zone extension and helium film extension

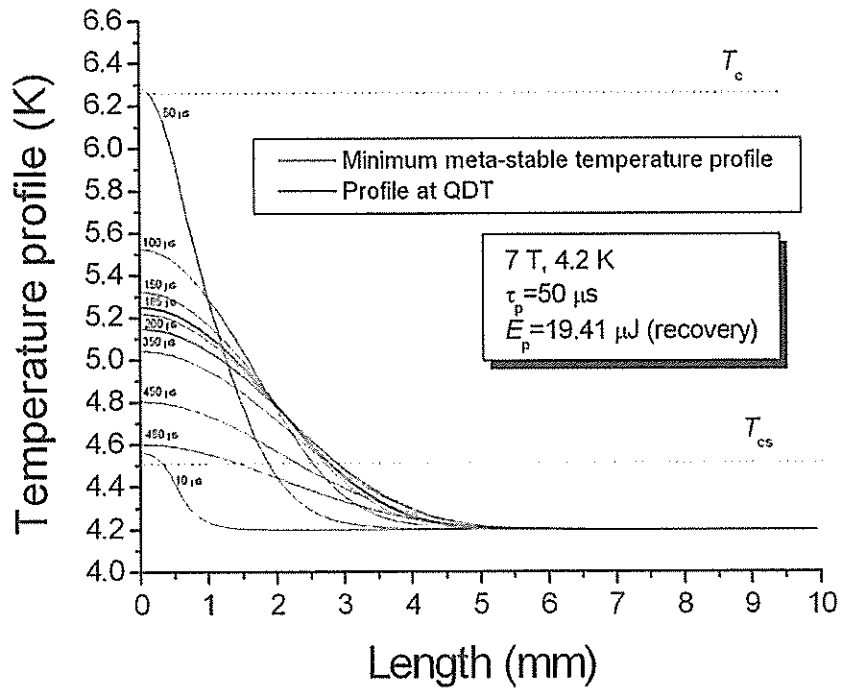
Before comparing the length of the quenched zone to the length of the helium film, it is necessary to introduce the temperature profile along the sample estimated at each time step. This profile is important since it leads to the estimation of the voltage V_1 presented above and of the quenched zone extension. The length of the quenched zone is defined as the length of the mesh for which the temperature is superior or equal to the current sharing temperature: $T \geq T_{cs}$. The length of the helium film is estimated from the evolution of the heat exchange coefficient along the wire sample, and corresponds to the maximum extension of the mesh for which the heat transfer coefficient is equal to h_{film} .

Meta-stable MPZ profile: Figure V.16(a) (page 190) shows the time evolution of the temperature profile along half of the sample obtained at various time steps for a quench while Figure V.16(b) (page 190) shows a similar plot for a recovery at 7 T, 85% of I_c and a pulse duration of 50 μs . The minimum temperature profile close to the MPZ profile and the one at the Quench Decision Time are also given. At first, the maximum temperature at the middle of the heated zone rises quickly and exceeds eventually the critical temperature at the end of the energy pulse. Subsequently, the maximum temperature at the middle of the heated zone drops down rapidly and the temperature profile approaches a minimum profile close to the MPZ profile. The speed of the changing temperature profile slows down. If a quench occurs, the temperature profile grows anew slowly before running away. If a recovery occurs, a meta-stable temperature profile can be clearly observed and

V.6. RESULTS ON THE NUMERICAL SIMULATION AND COMPARISON WITH EXPERIMENTAL DATA



(a) Minimum meta-stable profile close to the MPZ profile.



(b) Temperature profile at recovery.

Figure V.16: Temperature profiles for a quench (a) and a recovery (b) for $a_k = 300 \text{ W/m}^2/\text{K}^4$ and $\eta = 450 \text{ Js}^{-0.6}$.

the temperature profile remains quasi-constant for a lapse of time $\leq 100 \mu\text{s}$ before shrinking and disappearing.

Quenched zone and helium film extension: Figure V.17 (page 192) shows a comparison of the corresponding time evolution of the quenched zone and of the helium film extension for a quench and a recovery (where $\eta = 450 \text{ Js}^{-0.6}$ and $a_k = 300 \text{ W/m}^2/\text{K}^4$). As already discussed, the film of gaseous helium appears rapidly before the end of the energy pulse. At first, the normal zone drags the film of gaseous helium. However, rapidly, the film length exceeds the normal zone extension and the development of the normal zone is governed by h_{film} .

The information drawn from the comparison of the time evolution of the quenched zone and film extension sheds some light on the time evolution of the temperature shown in Figure V.13 (page 186). After the initial temperature rise due to the heat deposited by the pulse (first $50 \mu\text{s}$), the temperature decreases to reach, over the next few hundred microseconds, a pseudo-plateau, located between T_{cs} and T_c . On this plateau, the wire is in the current sharing regime and dissipates a power by Joule effect that can be significantly lower than when the wire is fully quenched (temperature above T_c). Then, the behavior is very similar to the adiabatic case where the Joule power is conducted out of the normal zone until the temperature gradient flattens, reducing the heat conduction and enabling quench propagation. This phenomenology explains the predominant influence of the parameter η . A larger energy to trigger the film of gaseous helium allows a larger temperature difference between the sample and the liquid helium to develop. So, the time to trigger the film is delayed and a larger heat dissipation is induced. The thermal gradient along the sample increases due to a larger temperature difference and the MPZ profile extends over a larger portion of sample.

Some difficulties appeared while performing the numerical simulations. Indeed, the time evolution of the film of gaseous helium exhibits numerical oscillations. These instabilities have been encountered in the computation of the heat transfer coefficient h . However, they are expected to affect our results.

V.6.3 Comparison between numerical simulations and experimental data

Figure V.18 and Figure V.19 (page 192) compare the numerical Minimum Quench Energies to the experimental Minimum Pulse Energies and the corresponding Minimum Absorbed Energies for various background magnetic flux densities. The numerical results correspond to $a_k = 300 \text{ W/m}^2/\text{K}^4$ and $\eta = 450 \text{ Js}^{-0.6}$ for which we had the best agreement between the computed voltage V_1 and the experimental one (see Figure V.15(a), page 188). The numerical results for the adiabatic case are also given. As expected, it corresponds to the lower plot.

The numerical Minimum Quench Energy is located between the Minimum Pulse Energy and the Minimum Absorbed Energy estimated as described in chapter IV, section IV.4.6 (page 149) for an absorptivity of 22%. Our chosen set of parameters η and a_k leads to greater energies than the estimated absorbed energies. This seems to indicate that the coefficient of absorption is somewhat greater. By comparing the computed Minimum Quench Energy to the Minimum Pulse Energy at various magnetic flux densities (see Figure V.19(a) and Figure V.19(b)), we find similar orders of $\sim 60\%$ at 5 T and 7 T, and $\sim 68\%$ at 6 T. This discrepancy can be related to the

V.6. RESULTS ON THE NUMERICAL SIMULATION AND COMPARISON WITH EXPERIMENTAL DATA

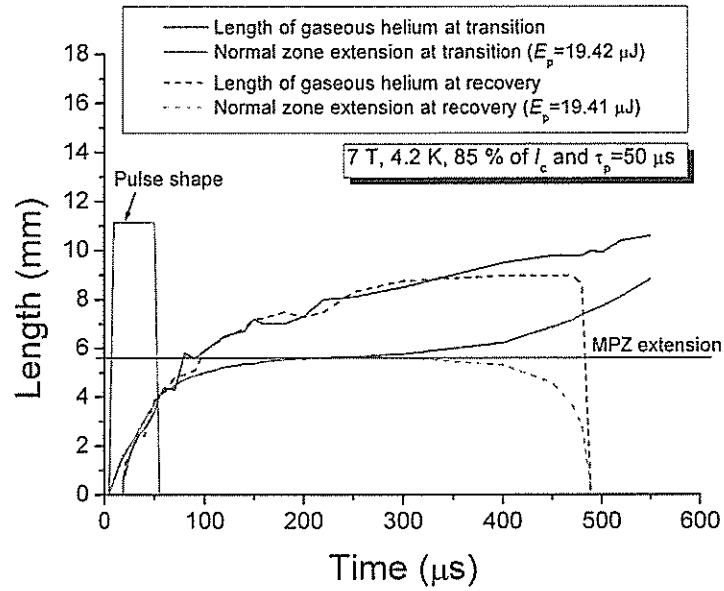


Figure V.17: Time evolution of film of gaseous helium extension and quenched zone for $a_k = 300 \text{ W/m}^2/\text{K}^4$ and $\eta = 450 \text{ Js}^{-0.6}$.

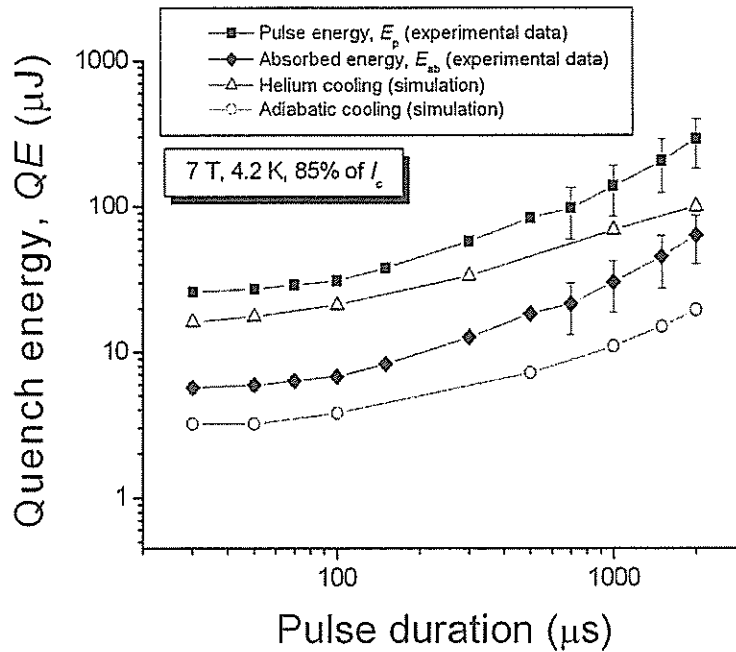
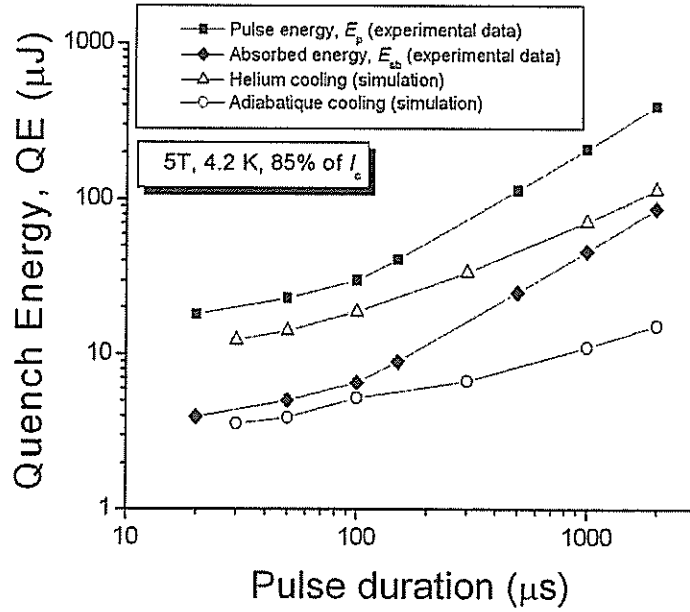
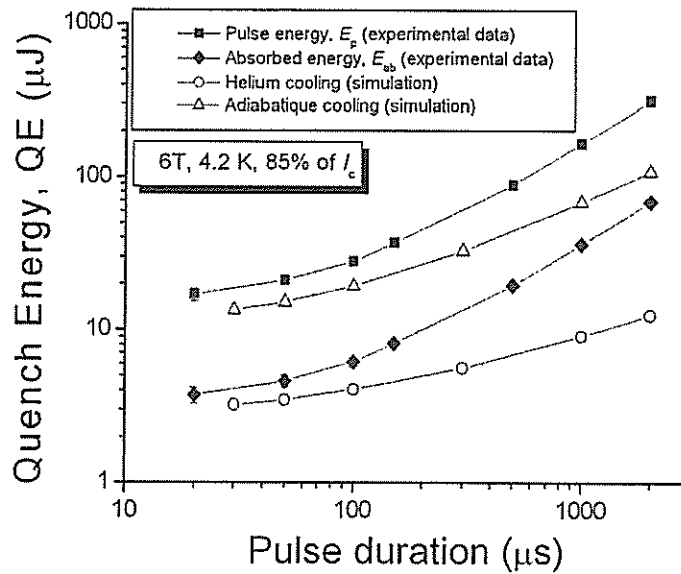


Figure V.18: Comparison of experimental and numerical Quench Energies versus pulse durations at 7 T, 4.2 K and 85% of I_c for $a_k = 300 \text{ W/m}^2/\text{K}^4$ and $\eta = 450 \text{ Js}^{-0.6}$.



(a) Quench Energy at 5 T.



(b) Quench Energy at 6 T.

Figure V.19: Temperature profiles for a quench (a) and a recovery (b) for $a_k = 300 \text{ W/m}^2/\text{K}^4$ and $\eta = 450 \text{ Js}^{-0.6}$.

experimental setup used to calibrate the absorbed energy. Indeed, this experimental setup differs from the one used to study the thermo-electric stability of wire sample. Consequently, the positioning of the tip of the optical fiber facing the wire surface, the presence of the background magnetic field in the stability experiment, the fact that the diode laser used for the calibration had different characteristics than the one used for the stability tests can account for this difference.

Therefore, a calibration in situ, as it was originally planned, is needed and it should clarify the discrepancy between the numerical simulation and the experimental data.

V.7 Conclusion on numerical simulations

The simulation presented here to describe the thermal behavior of a Cu/NbTi composite wire is based on a simplified transient liquid helium heat exchange model, which was adapted from C. Schmidt's works [10]. This preliminary model appears very promising although it does not consider the helium boiling regime and the actual heat diffusion process which takes place through the thin liquid helium layer surrounding the sample². Nevertheless, we were able, at this preliminary stage, to simulate the proper orders of magnitude of the voltage and of the Quench Energies observed experimentally.

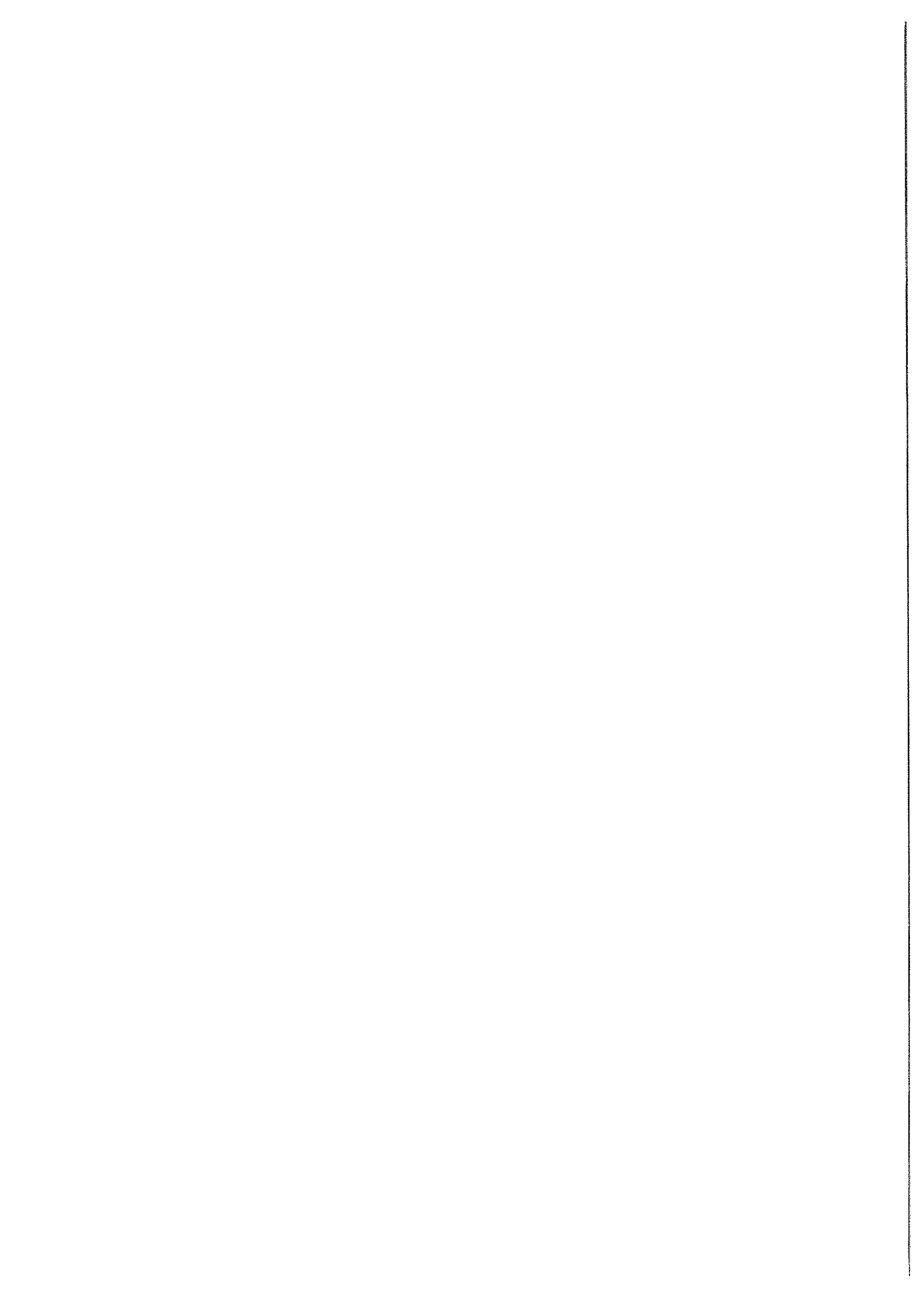
From our first analysis, the quench decision is made when the heat conduction is the dominant cooling mechanism. Thus, the initial pulse perturbation supplies the energy necessary to induce a film of gaseous helium blanketing the sample to set the proper cooling conditions for a quench to occur.

In view of the quantity of data, only a small part of them have been carefully analyzed. A larger campaign would be needed to ensure that the numerical simulation can properly describe the behavior of the sample at various background magnetic fields, percentages of critical current and pulse durations. It may also bring a better understanding on the true nature of the MPZ and on the actual parameter combinations determining a quench and a recovery. However, before performing such a task, the numerical program must be improved. For instance, it is necessary to address the numerical oscillations which have been encountered in the calculation of the heat exchange coefficient, h . In addition, a finer voltage calculation must be implemented to better describe the experimental voltage traces. In spite of all these shortcomings, we are nevertheless able to understand the basic phenomenology of the mechanisms involved and to confirm the soundness of our interpretations of the experimental data.

²The model of heat diffusion can be realized by adding an additional heat transfer coefficient to the one suggested in Equation V.19 (page 181) [6].

Bibliography

- [1] CEA. CAST3M v2003. <http://www-cast3m.cea.fr/cast3m/index.jsp>.
- [2] T. Dupont, G. Fairweather, J.P. Johnson. Three-level Galerkin methods for parabolic equations. *SIAM, Journal of Numerical Analysis*, 11(2):393, 1974.
- [3] A. Segal A.J. Dalhuijsen. Comparison of finite element techniques for solidification problems. *International Journal for Numerical methods in engineering*, 23:1807–1829, 1986.
- [4] A. Devred. *Propagation longitudinale de la zone normale dans les bobinages supraconducteurs à réfrigération indirecte*. PhD thesis, Institut National Polytechnique de Lorraine, 1987.
- [5] M.N. Wilson. *Superconducting Magnets*, page 114. Oxford University press, 1983.
- [6] S. van Sciver. *Helium Cryogenics*. Plenum press, 1986.
- [7] W.G. Steward. Transient Helium Heat Transfer Phase-I Static Coolant. *International Journal of Heat Mass Transfer*, 21, 1978.
- [8] C. Schmidt. The induction of a propagating normal zone (quench) in a superconductor by local energy release. *Cryogenics*, 18(10):605, October 1978.
- [9] O. Tsukamoto and S. Kobayashi. Transient heat transfer characteristics of liquid helium. *Journal of Applied Physics*, 46(3):1359–1364, March 1975.
- [10] C. Schmidt. Review of the steady state and transient heat transfer in pool boiling helium. *International Institute of Refrigeration, Commission A1/2-Saclay (France)*, (6):17, 1981.
- [11] P. Bauer. *Stability of Superconducting Strands for Accelerator Magnets*. PhD thesis, Technische Universität Wien, 1998.



Chapter VI

Preliminary HTS experiments using Ohmic heaters

Contents

VI.1 Description of the samples	198
VI.1.1 Bi-2212 tape	198
VI.1.2 Bi-2223 tape	198
VI.1.3 YBCO tape	198
VI.2 Heaters	199
VI.2.1 Strain Gauge	201
VI.2.2 NiCr wire	201
VI.3 Helium gas cooling: preliminary study using strain gages	202
VI.3.1 Stability of Bi-2212 tapes in helium gas cooling condition .	204
VI.3.2 Stability of Bi-2223 tapes in helium gas cooling condition .	204
VI.4 Nitrogen gas cooling experiment	204
VI.4.1 Experimental setup and G-10 Sample holder	205
VI.4.2 Acquisition system, electrical equipments	205
VI.4.3 Results on Bi-2223 tapes	207
VI.4.3.1 Preliminary studies	207
VI.4.3.2 Voltage-time and temperature-time plots of normal zone transitions and recoveries	208
VI.4.4 YBCO tape	210
VI.4.4.1 Voltage-time plots of normal zone propagations and recoveries	210
VI.4.4.2 Minimum Pulse Energy versus the fraction of critical current	213
VI.4.4.3 Normal Zone Propagation velocity	215
VI.5 Conduction cooling Experiment	216
VI.5.0.4 Description of the experimental setup	216
VI.5.0.5 Electrical equipments, acquisition system	216
VI.5.0.6 Homogeneity of the critical current	218
VI.5.0.7 Normal zone propagation measurements	218

VI.5.0.8	Normal Zone Propagation Velocity versus the fraction of critical current	221
VI.5.0.9	Minimum Pulse Energy versus the fraction of critical current	222
VI.5.1	Conclusion	223

OWING TO THE EFFORTS OF INDUSTRIALS to commercialize High Temperature Superconducting conductors (HTS conductors), long lengths of tapes and wires have been rapidly available for engineers and scientists at a reasonable price. In the 1980's, the possible applications of these conductors were just anticipated ; it needed less than a decade to see the first commercial tapes with relatively high current densities be experimentally characterized in view of designing HTS magnets.

The present chapter completes two articles published in 2003 [1] and 2004 [2] which introduced two experiments conducted on Ag-coated $\text{YBa}_2\text{Cu}_3\text{O}_{7-\delta}$ /Ni-alloy and Bi-2223 tapes. Both experiments used the same cryostat, but one was dedicated to Nitrogen gas cooling study while the other used a cryocooler to carry out quasi-adiabatic measurements on YBCO tapes.

As an introduction to these experiments, a few words will be given on a preliminary study conducted on Bi-2212 and Bi-2223 tapes in helium gas cooling condition. This study used a strain gage as heater. It was subsequently replaced by a NiCr wire. This chapter deals mainly with the latter heater technology, which showed better reliability at that time.

All the measurements were carried out in self-field. No simulations were carried out. The objective was to design a reliable experiment to study HTS conductors.

VI.1 Description of the samples

VI.1.1 Bi-2212 tape

Bi-2212 tapes were cut from batches used to wind pancakes for the 5 T project conducted at the National High Magnetic Field Laboratory. Supplied by Oxford, they were composed of Bi-2212 filaments enclosed in a silver stabilizer (representing commonly $\sim 60\%$ of the total cross-section [3]).

VI.1.2 Bi-2223 tape

Samples of Bi-2223 tapes were supplied by American Conductors, Inc. (US). As Bi-2212 tapes, they are filamentary structures composed of Bi-2223 filaments inside a silver matrix. Their cross-section is 0.173 mm x 3.07 mm.

The average n -value at 4.2 K in self-field is 47. The self-field critical current is 385 A at 4.2 K and 68 A at 77 K, measured using a $1 \mu\text{V}/\text{cm}$ electrical field criterion with a 10 m voltage tap separation on a 60 m length of conductor. The self-field engineering critical current density, J_e , is estimated to be equal to $\sim 723 \text{ A}/\text{mm}^2$ at 4.2 K.

VI.1.3 YBCO tape

The sample is a thin film Ag-coated YBCO conductor deposited on a textured Ni alloy substrate. Figure VI.1 (page 199) depicts a schematic cross-section of layered YBCO tapes. The tape is constituted of a $75 \mu\text{m}$ thick RABiTS type Ni-5at%W substrate, coated with a $2 \mu\text{m}$ Ni layer, a 50 nm thick Y_2O_3 seed layer, a 250 nm YSZ anti-diffusion barrier layer, and a 20 nm CeO_2 layer (composing the buffer layer). A $1 \mu\text{m}$ YbCO layer was then deposited using a TFA based solution process. Subsequently, a $3 \mu\text{m}$ thin Ag cap-layer was laminated on top of the YBCO layer for chemical protection and to facilitate electrical contacts [4]. The resulting overall cross-section was 0.08 mm x 8.9 mm (see Figure VI.1).

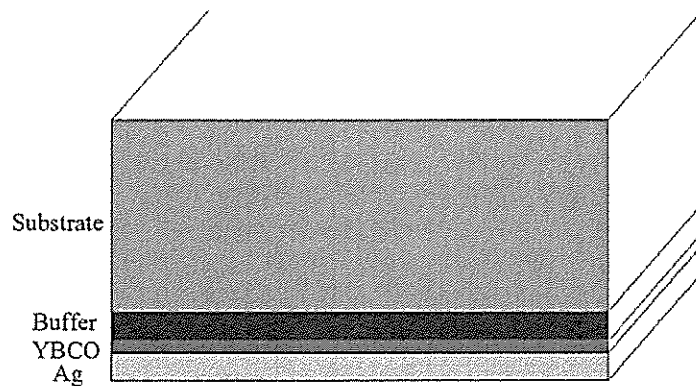


Figure VI.1: Sketch of an YBCO tape (scale not respected).

Table VI.1: Salient features of YBCO tapes.

Total length (mm)	250
Total thickness (mm)	0.08
Total width (mm)	8.9
Ni-substrate (μm)	~ 77
Buffer layer (μm)	~ 0.32
YBCO deposition (μm)	1
Silver stabilizer (μm)	3
I_C [self-field, ~ 77 K] (A)	147

The self-field critical current is 50 A at 77 K. Salient geometric features are listed in Table VI.1.3 (page 199).

VI.2 Heaters

In this section, we will introduce two different heater technologies:

- strain gages,
- NiCr wire.

The strain gages were used as heaters to trigger normal zone propagation on Bi-2212 and Bi-2223 tapes. They were used for a preliminary study of HTS stability in helium gas cooling condition. This technology did not appear convenient for stability studies on YBCO tapes because of the mechanical fragility of this material.

An alternative heater technology, based on a NiCr wire, was successfully tried on Bi-2223 tapes. It was then applied on YBCO tapes in nitrogen gas cooling condition and later in conduction cooling condition. This technology appeared reliable and easy to handle.

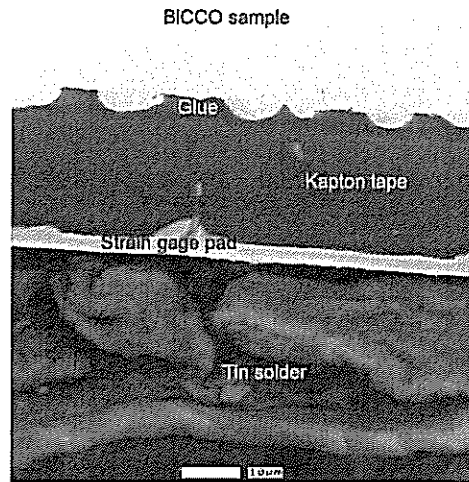


Figure VI.2: Micrography of Bi-2212 tapes on which is glued a strain gage. The volume of Kapton[®] tape is about $20 \mu\text{m}$, which corresponds to a diffusion time of the order of a few microseconds at low temperature.

Table VI.2: Thermal properties of polyimides and Stycast[®] 2850FT at room and low temperatures.

	Heat capacity (J/kgK)	Conductivity (W/m-K)	Diffusivity (m^2/s)
Polyimide [1.42 kg/m ³ [5]]			
Room temperature	1000-1450 [6]	6-12 [6]	$4\text{-}6 \times 10^{-6}$
4.2 K	17 [7]	0.045 [7]	2×10^{-6}
Stycast[®] 2850FT [2.45 kg/m ³ [8]]			
room temperature		1.28 [8]	
4.2 K	0.8 [9]	0.06 [10]	29×10^{-6}

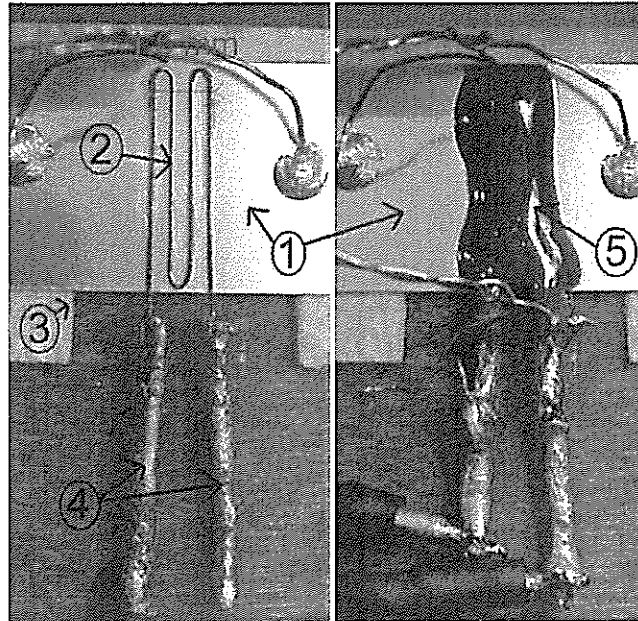


Figure VI.3: Left, NiCr wire glued on the surface of an YBCO tape. Right, the same heater recovered with Stycast[®] 2850FT and equipped with current leads and voltage taps.

- 1- YBCO tape mounted on its G-10 sample holder.
- 2- Zigzag pattern.
- 3- Thick pad of tissue to protect the sample.
- 4- Braided copper wire.
- 5- Zigzag pattern covered by Stycast[®] 2850FT.

VI.2.1 Strain Gauge

In preliminary experiments, strain gages, Vishay[®] EA-06-125BZ-350, were used as the resistive element for locally heating Bi-2212 and Bi-2223 samples in helium gas cooling condition between 10 K and 50 K. These strain gages are made-up of an alloy constantan resistive grid, which has a temperature-independent resistance of 350 Ω . The grid is glued on a 25 μm thick Kapton[®] tape. In order to limit heat sink from the tape (see Figure VI.2, page 200), we reduced its volume by removing the excess of Kapton[®] surrounding the grid.

To obtain an intimate contact between the heater and the sample, the strain gage was gently clamped onto the samples and cured at room temperature. The thermal diffusion across the Kapton[®] tape is relatively fast, of the order of a few hundreds of microseconds at low temperature. Table VI.2 (page 200) gives some thermal properties of generic polyimides and Stycast[®] 2850FT.

The strain gages degraded for pulse energies of a few Joules.

VI.2.2 NiCr wire

YBCO tapes being very sensitive to any mechanical deformations, we moved from strain gages requiring clamping to a new technology based on a silicone-insulated

Table VI.3: Salient parameters of silicone insulated 80%Ni20%Cr "Stablohm650" wire.

Total length (mm)	43
Diameter (mm)	0.14
Resistance (Ω)	2.1
Typical heater range (mJ)	200-350
Pulse height (V)	1-2
Typical pulse duration (ms)	100-400
Failure of the heater (J)	5-10
I_C (self-field, ~ 77 K) (A)	147

80%Ni20%Cr wire. This new heater proved straightforward to prepare and less fragile than the strain gauge. So, sample damage was eliminated and no degradation was seen in the superconducting performances of YBCO tapes. However, the thermal diffusion time across the heater embedded by Stycast[®] 2850FT was larger than for strain gages, of the order of a few tenths of milliseconds (see Table VI.2, page 200, for the thermal properties of Stycast[®] 2850FT).

The resistance per meter of the NiCr wire at 293 K was measured to be equal to $\sim 54.9 \Omega/\text{m}$. Measurements at 4.2 K showed this value to be temperature independent.

Figure VI.3 (page 201) shows a NiCr wire, which is prepared on an YBCO tape. The section of wire that is in contact with the HTS sample was shaped into a zigzag pattern from a 1 cm long piece of wire, giving a resistance of $\sim 2 \Omega$. The total length of the NiCr wire was 4.3 cm. Details of the heater are summarized in Table VI.2.2 (page 202).

After shaping the NiCr wire, the insulation was chemically removed from both end sections to insert two tinned copper sheaths. As it is difficult to solder directly to NiCr material, the sheaths were filled with Sn60%Pb40% solder to encircle the NiCr leads, improving the electrical contact. The ohmic heater was subsequently tacked with SuperGlue to the middle of the sample. It was then covered by blue epoxy Stycast[®] 2850FT with catalyst 24LV and cured for 24 hours at room temperature. The maximum energy that could be dissipated by the NiCr heater before it burned out was ~ 300 mJ at 293 K and between 5 J and 10 J at 80 K. No degradation of the heater was observed after repeated pulses at lower energies.

VI.3 Helium gas cooling: preliminary study using strain gages

In this section, we summarily introduce the very first stability studies conducted on Bi-2212 and Bi-2223 tapes using a strain gage as heater. This preliminary study was carried out to qualify the experimental setup used in the nitrogen gas cooling experiment and to find a proper heater. The setup is then similar to the one described in section VI.4 (page 204).

The results are rather scant and we only give a few comments.

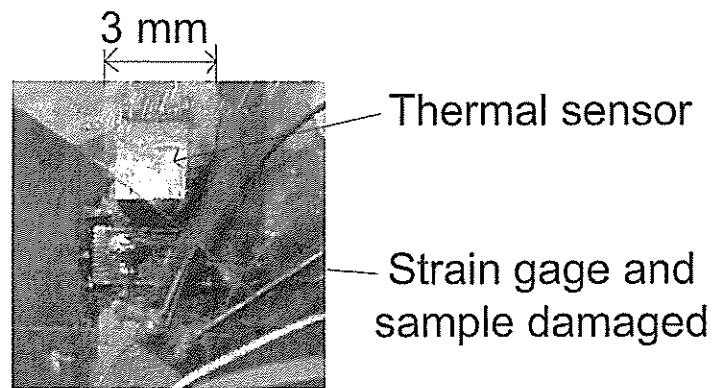


Figure VI.4: Picture of a damaged strain gage while stability tests were carried out on Bi-2212 tape. The sample burnt out before normal zone transition occurred damaging the strain gage.



Figure VI.5: Local destruction of a Bi-2212 tape. The sample and the strain gage burnt out before the normal zone expands inside the superconductor. The order of magnitude of the energy necessary to trigger a transition was of tens of Joules at most.

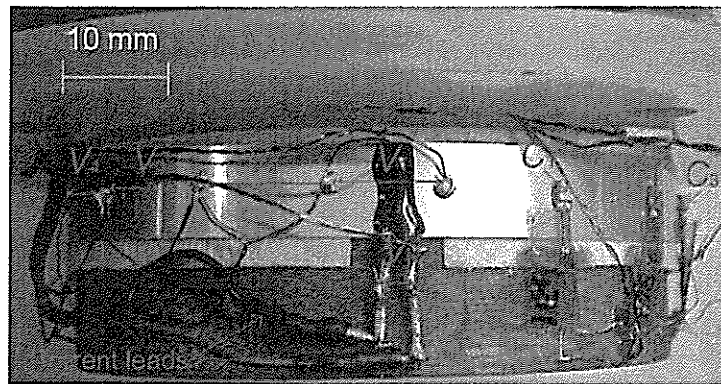


Figure VI.6: Sample holder for stability study in Nitrogen gas cooling conditions.

V_1 , voltage drop across the heated zone.

V_i ($i \in \{2, 3, 4\}$), voltage drops along the sample.

C_i ($i \in \{1, 2, 3\}$), thermal sensors located along the sample on the other side of the heater.

VI.3.1 Stability of Bi-2212 tapes in helium gas cooling condition

Bi-2212 tapes appeared very stable to local disturbances. Most of the strain gages burnt out before the ignition of a distinctive normal zone inside the conductor. Figure VI.4 (page 203) shows one of the strain gages damaged during a stability test. Energies of 1 J to 15 J were delivered to the samples. The normal zone diffused slowly across the conductor and a hot spot occurred very locally which led to the destruction of the tape (see Figure VI.5, page 203).

The stability of these tapes does not appear as an actual issue since releases of a few tens of Joules are necessary to trigger a normal zone transition.

VI.3.2 Stability of Bi-2223 tapes in helium gas cooling condition

In the case of Bi-2223 tapes, despite the precautions taken during the clamping, few samples showed degradations of their superconducting properties before any experiments could be completed. Indeed, the sample showed a weak spot at the localization of the strain gages, which degraded with repeated heat pulses.

YBCO tapes being more fragile, this technology was abandoned and was replaced by a similar technology based on a NiCr wire.

VI.4 Nitrogen gas cooling experiment

In this section, experiments carried out with Bi-2223 and YBCO tapes are presented. These experiments were performed in nitrogen gas cooling conditions using a NiCr wire as heater. This heater appeared suitable since no degradations of the samples were observed after repeated stability tests.

After describing the experimental setup, the results obtained on Bi-2223 and YBCO tapes will be discussed and compared to some extent.

Table VI.4: Distances between voltage taps for Bi-2223 and YBCO tapes.

Bi-2223 tape		YBCO tape	
Pairs of voltage taps	Distance (mm)	Pairs of voltage taps	Distance (mm)
V_1	8	V_1	15
V_2	9	V_2	11
V_3	10	V_3	12
V_4	9	V_4	12
V_{tot}	155	V_{tot}	155

VI.4.1 Experimental setup and G-10 Sample holder

Experiments were carried out in a LN_2 jacketed cryostat from which cold exhaust gas was led into the sample chamber. The samples were then cooled down by a slight flow of nitrogen gas to a bottom temperature of ~ 80 K. Samples of ~ 25 cm long were mounted on a cylindrical G-10 sample holder and soldered to two copper rods connected to the current leads (see Figure VI.6, page 204). Bi-2223 tapes were soldered with regular tin solder. However, YBCO tapes were soldered with indium to avoid removing the thin silver layer thereby degrading the sample. A layer of thick tissue was placed between the YBCO sample and the G-10 holder to smoothen the differential thermal contraction and to insulate the sample from the sample holder. This protection was not used while testing the Bi-2223 tape.

Three evenly spaced voltage taps V_2 , V_3 , and V_4 were soldered with PbSn solder on the tapes to measure the Normal Zone Propagation Velocity (NZPV). A pair of voltage taps, V_1 , was soldered across the heater to record the early stage of the normal zone transition and the influence of the heater presence. An additional pair of voltage taps, V_{tot} , was located across the entire sample for end-to-end critical current measurements.

In the first series of measurements, three similarly spaced CernoxTM thermal sensors (C_1 , C_2 , and C_3) were glued with GE-varnish to one side of the heater¹. These thermal sensors were subsequently removed during the series of tests carried out on the YBCO tape. Indeed, their time response was not fast enough to yield accurate measurements of the temperature of the samples during a normal zone transition [1]. Figure VI.7 (page 206) and Figure VI.8 (page 206) show respectively a Bi-2223 and YBCO tape with the localization of their voltage taps and thermal sensors. Table VI.4 (page 205) summarizes the distance between the voltage taps for both the Bi-2223 tape and the YBCO tape.

VI.4.2 Acquisition system, electrical equipments

A sketch of the instrumentation and data acquisition system for the nitrogen gas cooling experiment is shown in Figure VI.9 (page 207). The current, which flowed through the sample, was measured across a precision shunt of 100 mV/500 A.

¹This assembly was designed assuming that the superconducting properties of the sample were homogeneous over the entire length of the sample. This assumption can be reasonably made for short sample lengths ; but, it is not likely to be verified for long length.

VI.4. NITROGEN GAS COOLING EXPERIMENT

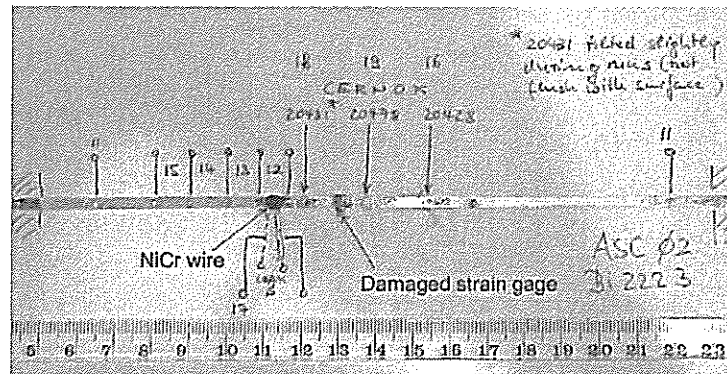


Figure VI.7: Localization of the pairs of voltage taps along the YBCO sample.

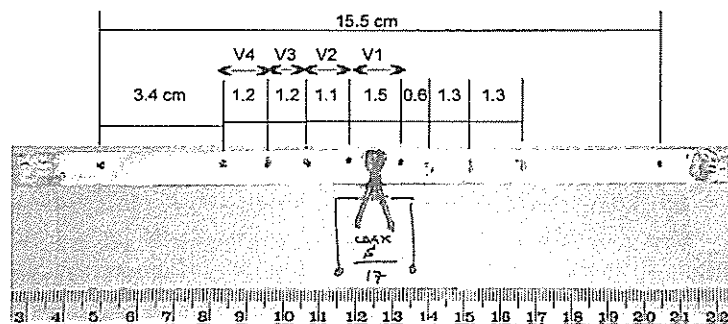


Figure VI.8: Localization of the pairs of voltage taps along the YBCO sample.

VI.4. NITROGEN GAS COOLING EXPERIMENT

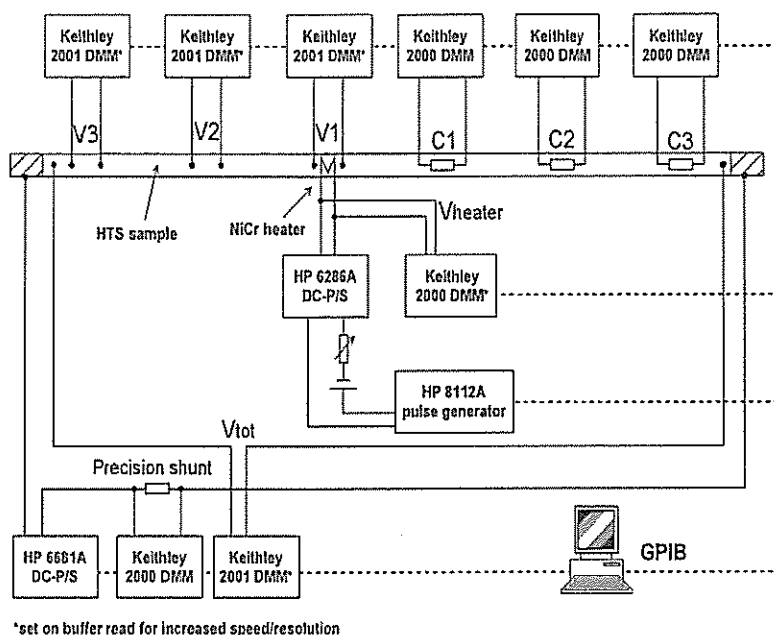


Figure VI.9: Electrical sketch of the quasi-adiabatic experiment conducted on HTS tapes.

The voltage taps were connected to KeithleyTM 2001 DMM voltmeters and the CernoxTM sensors to KeithleyTM 2000 DMM voltmeters. The voltage drop across the heater was recorded by a digital oscilloscope (5104 Tektronix[®]) in parallel with an additional Keithley[®] 2000 DMM voltmeter. The voltmeters and the oscilloscope were connected to a computer via a GPIB bus for simultaneous readout. To increase the data acquisition speed, some voltmeters were set to burst mode, writing first to the internal buffer before communicating with the computer. The entire experiment was controlled via Labview 6[®].

VI.4.3 Results on Bi-2223 tapes

VI.4.3.1 Preliminary studies

To characterize the experimental setup, we carried out a first series of measurements on Bi-2223 tapes. The different parameters as noise level, and repeatability of the pulse currents were estimated [1]. The parasitic thermocouple voltages (at most a few 100 μV) resulting from the thermal gradient developed between the voltage taps appeared negligible compared to the voltage magnitudes recorded during the normal zone transition of the sample (in the milli-volt range). The relative error of the estimation of the energy pulse after repeated pulses was estimated inferior to <15% (see Figure VI.10, page 208).

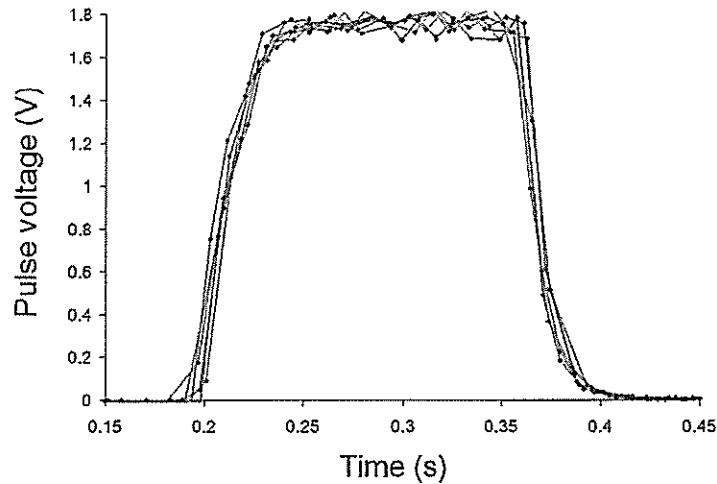


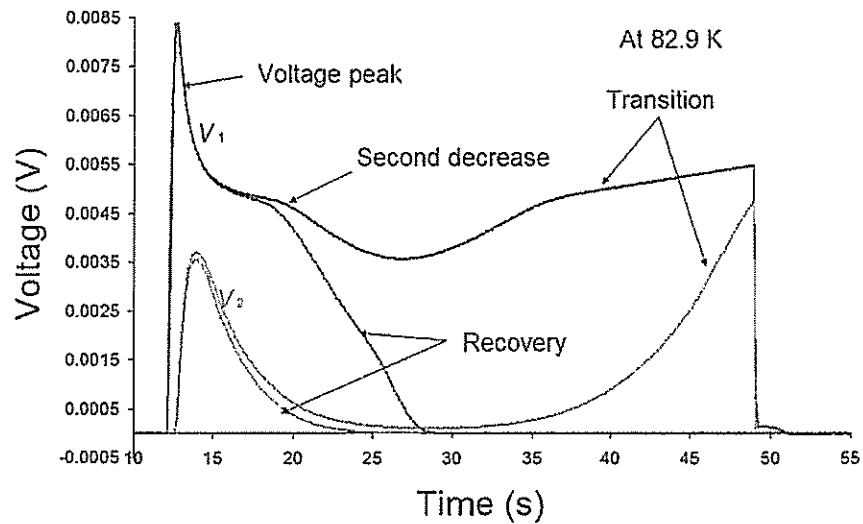
Figure VI.10: Typical pulse traces.

VI.4.3.2 Voltage-time and temperature-time plots of normal zone transitions and recoveries

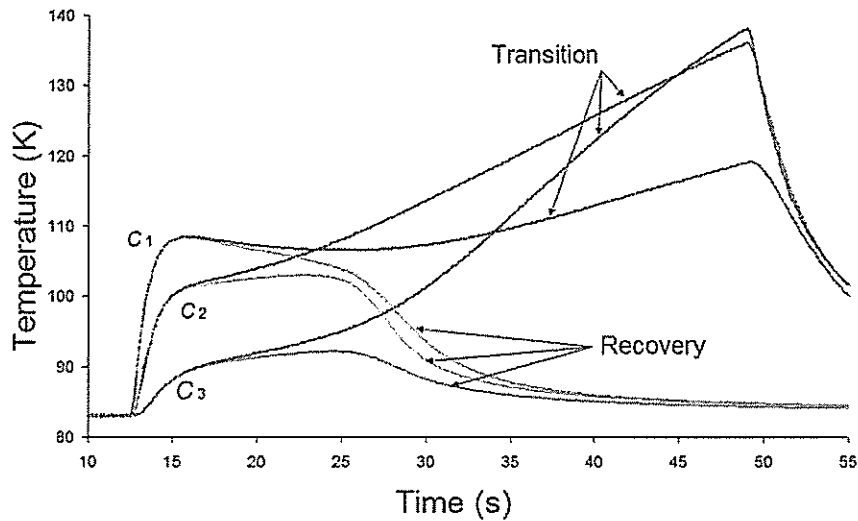
Temperatures and voltages versus time were simultaneously acquired along the Bi-2223 sample during normal zone transition. The initial sample temperature was 82.9 K, which gave a self-field I_c of ~ 37.7 A. The normal zone was initiated by increasing the transport current for a fixed energy pulse.

A normal zone transition was first observed at a transport current of ~ 32.4 A, corresponding to $\sim 87\%I_c$. An additional measurement was carried out at a energy pulse of ~ 59 mJ, which yields a normal zone transition at $\sim 84\%I_c$. Figure VI.11(a) (page 209) shows the voltage-time for two cases: one for which the sample recovers its superconducting state, and another for which normal zone transition is observed (at $\sim 0.87I_c$). After the heat pulse vanished, the heat diffused through the tape before the onset of the full normal-state transition characterized by a voltage and temperature run away. In the case of a recovery, the voltage initially increases following the same trend and slowly disappears while the superconductor recovers its superconducting state.

A voltage peak characterized the early growth of the normal zone transition. Subsequently, the voltage decreases rapidly toward the recovery of the superconducting state or the onset of the normal zone transition. According to S.B. Kim *et al.* [11], the peak of voltage is due to the presence of the heater. We suspect that it may result from the large heat capacity of the materials increasing with increasing temperature till a thermal equilibrium is reached as it can be seen in Figure VI.11(b) (page 209). From our point of view, the presence of the heater does not seem to play a major role in the normal zone transition. Indeed, the thermal diffusion time of the Stycast[®] 2850FT embedding the heater is relatively short compared to the evolution of the normal zone inside the superconductor (see Table VI.2, page 200). Assuming a thickness of ~ 1 mm, it is of the order of a few tenths of milliseconds, which must be compared to seconds. The results on YBCO tapes supports this assumption since such a behavior did not occur (see next section VI.4.4, page 210). However,



(a)



(b)

Figure VI.11: (a), Voltage traces V_1 across the heater and V_2 along the sample recorded during a normal zone propagation and a recovery of the superconducting state at 82.9 K and 0 T for $0.87I_c$. The large heat capacity of the materials at this range of temperatures can explain the large shrinkage of the normal zone before the onset of the normal zone propagation. (b), variations of the temperature recorded during the recoveries and transitions corresponding to the voltage recordings (a).

the shape of the voltage V_1 presents some particular characteristics which do not appear on the remaining voltage traces. In addition, the temperature recorded by the thermal sensors does not reproduce the same exact trend (see Figure VI.11(b), page 209). The temperature of C_1 shows a smoother transition and recovery than the voltage taps of V_1 even if the localization of the thermal sensor corresponds to the one of the voltage taps of V_1 on the other side of the heater. Nevertheless, it shows a decrease of the temperature before the onset of normal zone transition characterized by a thermal run away. The voltage characteristic depends on the current flowing through the silver matrix. This current redistributes from the superconductor to the matrix and reversely while the normal zone growth and shrinks. The thermal cooling process responding slower than the magnetic diffusion, the temperature profile appears smoothened. It must be pointed out that the thermal sensor was cooled down by nitrogen gas, which may slow down the thermal response of the thermal sensors.

Over such a long diffusion process characterized by a quench decision time superior to ~ 15 s, it is likely that the thermal interactions between the sample and the G-10 holder influenced the normal zone development and ultimately the propagation or collapse of the normal zone. These parameters may have acted in conjunction with a large current sharing zone of ~ 10 K which is illustrated in Figure VI.12 (page 211) [12]. The temperature profile spreads out across a large portion of the sample lowering the flux of conducted heat. It would explain the slow normal zone transition phenomenon without a clear propagation. This assumption is supported by the larger recovery of voltage V_2 compared to V_1 in Figure VI.11(a) (page 209) and explains the discrepancy observed on voltages V_3 and V_4 in Figure VI.13 (page 211). In a real propagating phenomenon, it would be expected that the voltage traces would increase continuously due to the increasing of the silver resistivity with temperature and the shape of voltage V_3 and V_4 would repeat itself. These two voltages have been recorded at different energy pulses for a different set of measurements explaining thereby the difference of time scale.

VI.4.4 YBCO tape

After the successful trial of this heater technology on Bi-2223 tape, it was subsequently applied on an YBCO tape. The fraction of silver thickness over the entire cross-section is relatively small $\sim 6/10000$ and it is comparable to YBCO $\sim 3/10000$. The ratio between the YBCO thickness and the silver one is one of the main parameter influencing the normal zone propagation. The influence of the nickel substrate is not clearly understood on the stability issue of YBCO tapes [13]. X. Wang *et al.* [14] showed that a small fraction of current is redistributed into the nickel layer. However, it remains negligible compared to the current flowing through the stabilizer. In addition, the nickel layer does not seem participate in the propagating phenomenon since no normal zone propagation can be distinguished. Nevertheless, it may indirectly participate by acting as a thermal buffer.

VI.4.4.1 Voltage-time plots of normal zone propagations and recoveries

The stable equilibrium temperature was 80.6 K, corresponding to a self-field I_c of ~ 22 A. Figure VI.14 (page 212) shows voltage versus time at a transport current, I_t , of ~ 15 A ($0.68I_c$) for 3 heat pulses with equal amplitudes but varying durations.

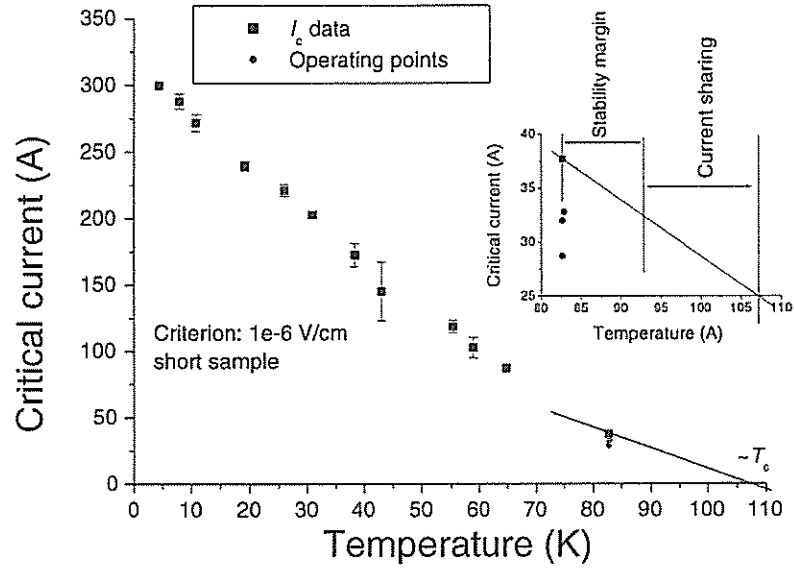


Figure VI.12: Short sample critical current of Bi-2223 tapes versus temperature.

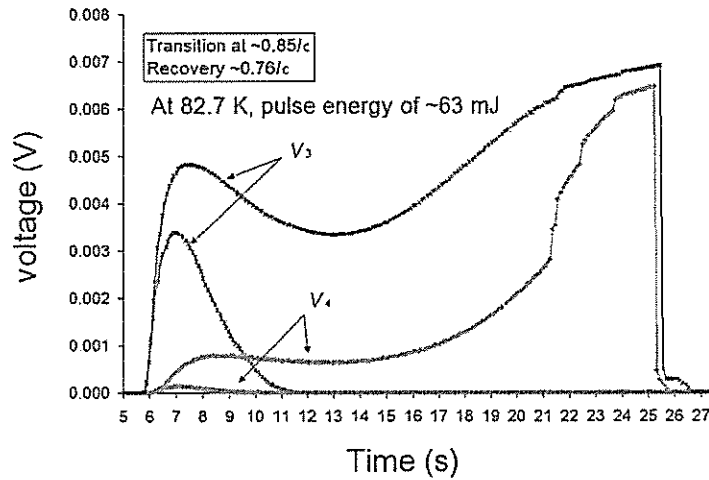


Figure VI.13: Voltage traces V_3 and V_4 along the sample recorded during a normal zone propagation (at $0.85 I_c$) and a recovery of the superconducting state (at $0.76 I_c$) during a previous campaign of measurements at 82.7 K and 0 T for an energy pulse of 63 mJ. The typical relaxation of the normal zone generated in the the conductor appears also away from the heater (~ 13 mm).

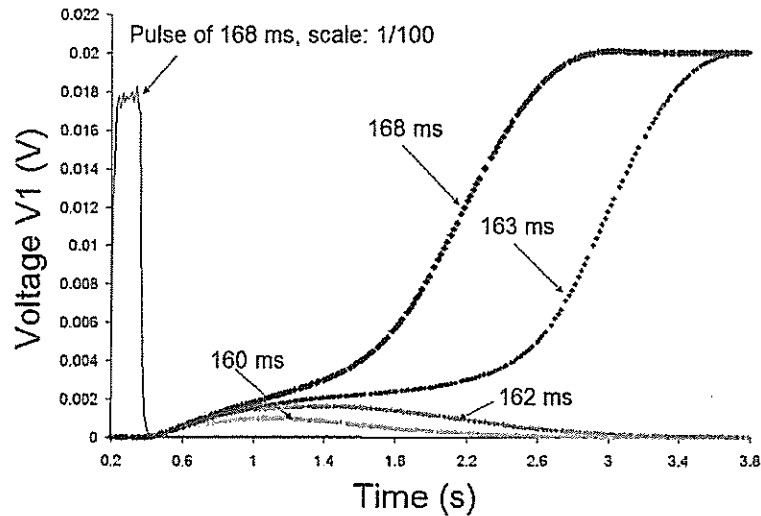


Figure VI.14: Voltage trace V_1 across the heater recorded at increasing energy pulse. The measurements were carried out at $0.68I_c$, 80.6 K and 0 T.

The minimum energy to initiate normal zone propagation was equal to ~ 272 mJ (corresponding to a pulse duration of ~ 163 ms). Below this value, the sample fully recovered its superconducting state. Above this value, the conductor undergoes a normal zone propagation. The voltage V_1 rises slowly after the end of the pulse, following the recovery plot as for Bi-2223 voltage plots. It rises until reaching a maximum value for which the portion of sample located between its voltage taps has reached a thermal equilibrium.

Compared to the voltage traces obtained with the Bi-2223 tape, no voltage peak appears at the beginning of the transition. In addition, the quench decision time occurs earlier at ~ 0.6 s which is one order of magnitude faster than for Bi-2223 tape. Indeed, the behavior of the YBCO tape tends to the behavior of LTS conductor for which the heat generation increases rapidly. It is further confirmed by Figure VI.16 (page 214), which shows voltage V_1 , V_2 , V_3 and V_4 at various percentages of critical current. The early growth of the normal zone is similar to the one of the voltage plots that we obtained for NbTi wires at low background magnetic field. The normal zone propagates also as "a normal zone propagating front" even if the characteristic times of the propagation are few orders of magnitude larger than for LTS conductors. Despite the large heat capacity of the materials at ~ 80 K, there is a distinctive propagation owing to the small current sharing zone spreading only over ~ 1 K (see Figure VI.15, page 213) and the large current density. The current sharing zone is comparable to the magnitude of the temperature range of the one of LTS conductors. The slowness of normal zone propagation is explained by the large operating temperature for which the heat capacities of the materials are larger.

The magnitude of the transport current mainly influences the normal zone transition. At large transport current, the voltage rises quickly and reaches a larger value. If we still refer to Figure VI.15 (page 213), the stability margin decreases with increasing transport current. The difference between the operating temperature and the current sharing temperature is reduced. In addition, at the full transition, a larger

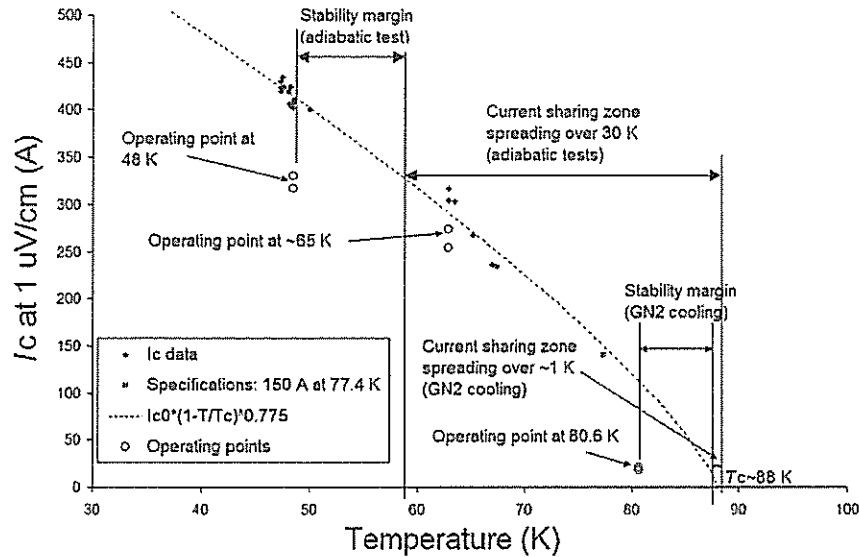


Figure VI.15: Critical current measurements of an YBCO short sample at various temperatures. For these temperatures of measurements ("operating points"), the stability margin is given.

fraction of current is redistributed to the stabilizer. A larger heat is dissipated. Consequently, the temperature of the conductor increases faster. the resistivity of silver increases with increasing temperature and the voltage reaches its maximum value faster. Besides, the resistivity being larger, a larger maximum voltage is reached. However, it would be expected to see a continuous increase of the voltage since the resistivity of silver increases quasi-linearly above ~ 25 K. A thermal equilibrium may have been reached, which is directly related to the cooling capacity of the thermal bath (hardware plus cold N_2 gas) and heat generation. The nickel substrate may help reaching this equilibrium by lowering the current flowing through the silver matrix, lowering thereby the heat generation. To some extent, this behavior looks similar to the one encountered with the titanium mandrel used to perform stability tests on NbTi wires (see chapter III, page 77). At that time, a possible redistribution of current may have occurred between the wire and its titanium mandrel support.

VI.4.4.2 Minimum Pulse Energy versus the fraction of critical current

Figure VI.17 (page 214) shows the Minimum Pulse Energy dissipated by the heater to initiate normal zone propagation as a function of the fraction of critical current. The presence of the embedding glue and the nature of the interface between the NiCr wire and the sample do not allow to estimate accurately the Minimum Quench Energy. The heater not being calibrated, the energy pulse over-estimates the real energy necessary to trigger normal zone propagations in the conductors. Indeed, it is expected that the Minimum Quench Energy would vanish at the critical current, which is not the case here.

For comparison, data obtained on Bi-2223 tape are given. The stability margins of the Bi-2223 tape being smaller than the one of the YBCO tapes, the energy

VI.4. NITROGEN GAS COOLING EXPERIMENT

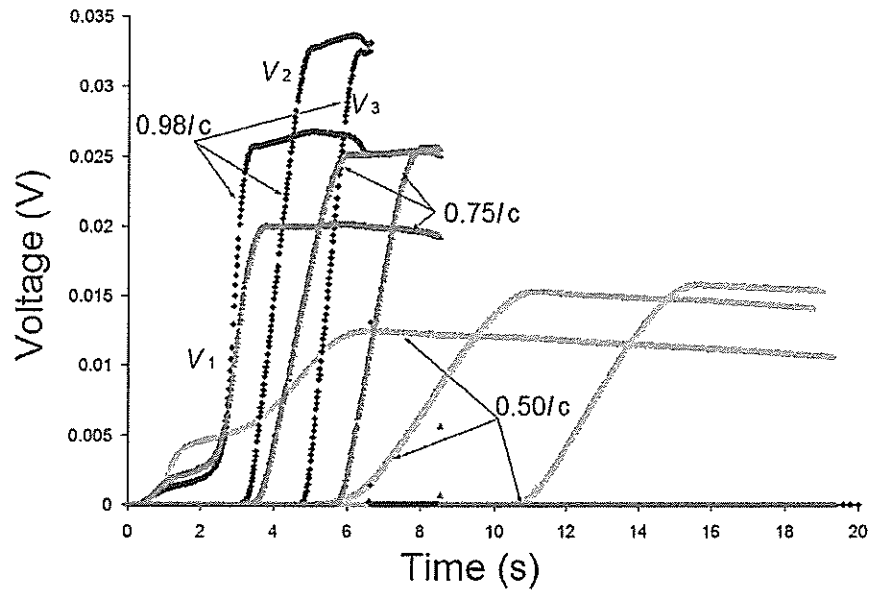


Figure VI.16: Voltage traces V_1 , V_2 and V_3 versus time for different fractions of critical current at 80.6 K in self-field.

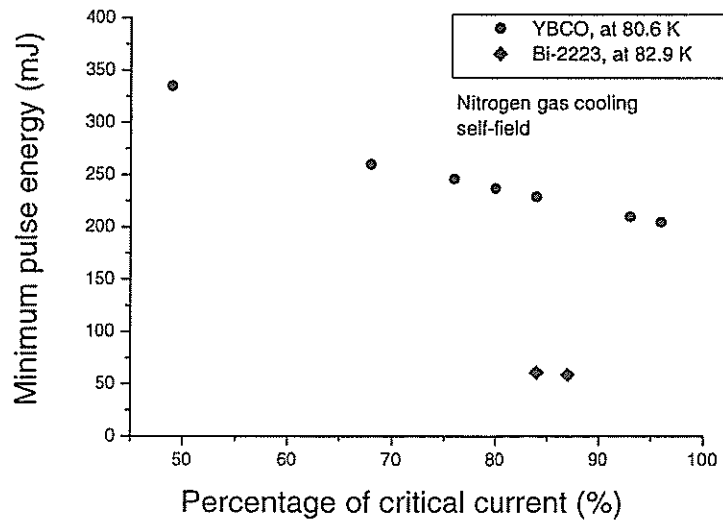


Figure VI.17: Minimum Pulse Energy versus the fraction of critical current at 80.6 K in self-field.

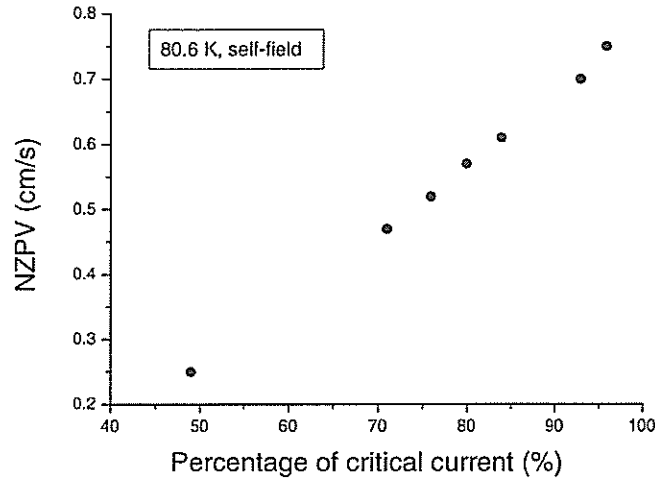


Figure VI.18: Normal Zone Propagation Velocity versus the fraction of critical current at 80.6 K in self-field.

necessary to trigger the normal zone propagation is reduced. Indeed, less energy is necessary to raise the temperature of the conductor from the operating temperature to the current sharing temperature².

VI.4.4.3 Normal Zone Propagation velocity

In this case, we have chosen to estimate the Normal Zone Propagation Velocity (NZPV) as follow:

$$\nu = \frac{L_{2-3}}{\Delta t} \quad [m] \quad (\text{VI.1})$$

where L_{2-3} is the distance between the first voltage tap of V_2 and the first voltage tap of V_3 . $\Delta t = t_f - t_i$ is the time lag between the voltage slopes V_2 and V_3 measured at 0.01 V (see Figure VI.18, page 215). The propagation velocity increases with the fraction I_t/I_c . The propagation velocity is related to the ratio between the energy generated in the sample and the cooling. When the fraction I_t/I_c increases, the amount of current transferred to the metallic layers increases during the transition. Hence, the normal zone propagation velocity increases by the increase of the Joule heating. The nitrogen gas cooling environment does not change much. The NZPV appears then proportional to the fraction of critical current.

The NZPV ranges from 0 to 1 cm/s.

Table VI.5: Distances between voltage taps for the YBCO tapes (quasi-adiabatic measurements).

Pairs of voltage taps	Distance (mm)
V_{10}	10.6
V_{11}	10.7
V_{12}	12
V_{13}	13

VI.5 Conduction cooling Experiment

VI.5.0.4 Description of the experimental setup

A double stage Gifford-McMahon cryocooler was used to cool down the samples. The cold head was inserted into the cryostat, which was evacuated down to 5×10^{-6} mbar. This configuration provided a quasi-adiabatic environment by eliminating convection cooling. The first stage and the second stage of the cold head had a cooling capacity of ~ 18 W and ~ 10 W, respectively. Several sheets of super-insulation were wrapped around the whole assembly to reduce heat losses. The sample holder, covered of Kapton[®] tape for electrical insulation, was machined into an OFHC copper thin wall cylinder that was screwed at the bottom of the second stage. The sample was mounted onto the outer surface of the copper cylinder (see Figure VI.19, page 217). As previously, a pad of tissue was placed underneath the sample to reduce the thermal coupling between the sample and the sample holder. It prevented also any degradations due to the differential thermal contraction during cool down. The sample, measuring ~ 20 cm long, was soldered to two copper current leads that were attached to the sample holder for a good thermal connectivity. Electrical insulation was accomplished using sapphire disks. The current leads were attached to both stages of the cryocooler in the same manner as on the sample holder. With this setup, equilibrium temperatures between 45 K and 70 K could be achieved, depending on the transport current of the sample.

Five pairs of voltage taps, named V_{10} , V_{11} , V_{12} , V_{13} , and V_{14} , were soldered with regular PbSn solder as shown in Figure VI.20 (page 217). The pair of voltage taps, V_{10} , was located across the heater while V_{11} , V_{12} , V_{13} , and V_{14} were distributed on each sides of the heater. This configuration allowed to check the homogeneity of the critical current along the tape. Table VI.5 (page 216) summarizes the distance between the voltage taps.

VI.5.0.5 Electrical equipments, acquisition system

The acquisition system remained the same as the one used in the nitrogen gas cooling experiment. However, the heater power supply was replaced by a Bipolar Digital power supply (50 V-4 A) controlled by a pulse Generator.

²We assumed a similar heat capacity between Bi-2223 and YBCO material, which is likely to be inaccurate. The knowledge of the physical properties of these materials lacks to understand clearly the different stability behavior of Bi-2223 and YBCO tapes.



Figure VI.19: OFHC copper sample holder for quasi-adiabatic measurements, on which is mounted a Bi-2223 tape.

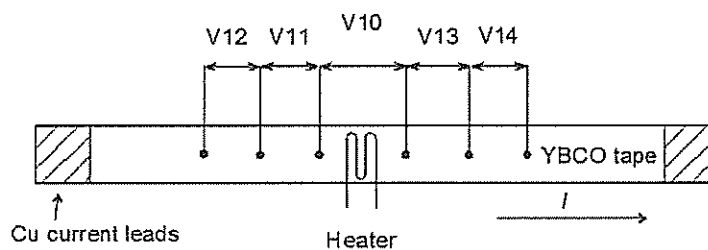


Figure VI.20: Localization of the pairs of voltage taps along the YBCO sample for conduction cooling measurements. The thermal sensors previously used in the nitrogen gas cooling experiment were replaced by additional voltage taps.

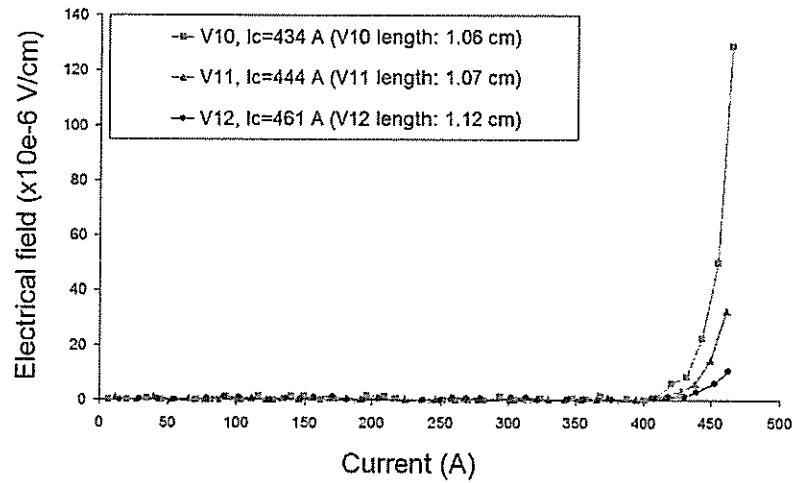


Figure VI.21: Verification of the hypothesis of critical current homogeneity along the sample.

Table VI.6: Average critical current.

Temperature (K)	Critical current (A)	STDV (A)
47	447.8	11.5
65	272	7

VI.5.0.6 Homogeneity of the critical current

Figure VI.21 (page 218) compares the electric field versus the transport current curves of a mounted sample for the sections covered by V_{10} , V_{11} and V_{12} at 47.4 K in self-field. The critical current is relatively homogeneous over the three pairs of voltage taps covering 3.25 cm of the sample. The following Table VI.6 (page 218) summarizes the different values of critical current. The N-value was ranging between 30 and 40.

VI.5.0.7 Normal zone propagation measurements

The measurements were carried out for a constant pulse width of 300 ms. Figure VI.22 (page 219) shows voltage-time plots of V_{10} for various heater energies at 48.5 K and $0.8I_c$ in self-field. Table VI.7 (page 219) summarizes the critical current measured in situ before the stability tests. It appears that the slope in the $V(t)$ curves is steeper for measurements taken closer to the Minimum Pulse Energy. The heater element dissipates heat into the Ag-matrix of the sample and raises its temperature. The time delay between the heat pulse and the first voltage rise is determined by the thermal diffusion process, which depends on the amount of energy generated by the heater and the contact resistance between the layers. Subsequently, the heat is transferred into the YBCO layer causing current sharing with the Ag layer. At low heat energy pulses, this is a relatively slow process ; heat generation

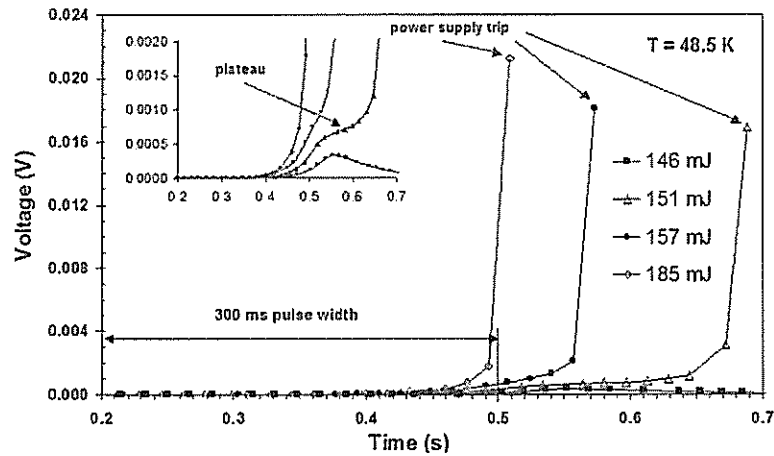


Figure VI.22: Voltage V_{10} recorded at increasing energy pulse. The measurements were carried out at 48.5 K and 80% of the critical current. The heating power before the trip of the power supply reaches about 7 W.

Table VI.7: Critical current measured in situ before the stability tests.

Temperature (K)	Critical current (A)
48.5	330
79	33

and conduction cooling of the sample compete, causing only a slight voltage rise. If the normal zone grows sufficiently, the normal-zone propagates. The steepness of the slope is related to the speed of the propagation of the normal zone.

With increasing heater energy around the Minimum Pulse Energy, a plateau appears for the V_{10} signal, suggesting a competing process between heat dissipation and normal zone generation. At even higher heater energy, the plateau disappears and the sample quenches after the heat pulse vanished. In the previous experiments using N_2 gas cooling, the voltages reached a maximum value after the normal zone established in the sample due to convection cooling of the sample surface. This was not the case during these experiments at low operating temperature. For the investigation of the voltage evolution on successive voltage taps away from the heater, this is a complicated feature at large transport currents or/and low operating temperatures. Under vacuum conditions the voltage drop over the section closest to the heater rises till the destruction of the sample while the normal zone has not reached other sections of the sample. Figure VI.23 (page 220) is a plot of the delay between the onset of the heat pulse and the onset of the normal zone propagation versus heater energy. It is clearly visible that the delay decreases with increasing heater energy and that the normal zone appears faster at higher energy. This indicates that the voltage variations over the successive voltage taps represent a normal zone propagation, as opposed to thermal conduction of the heat pulse.

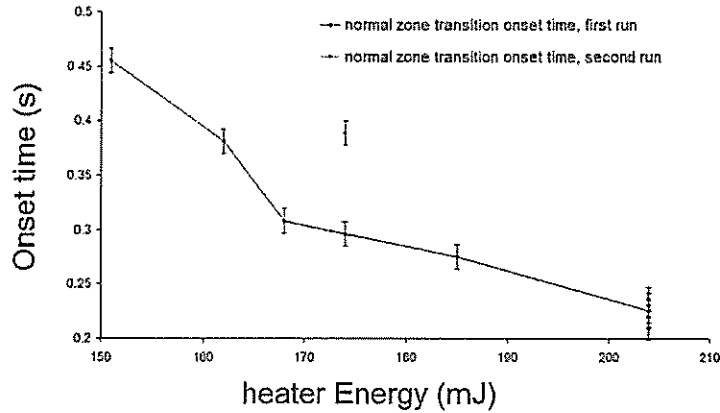


Figure VI.23: Quench Decision Time versus energy of the heat pulse at 65 K. The error bars are a measure of the accuracy with which the onset times can be determined from the $V(t)$ curves.

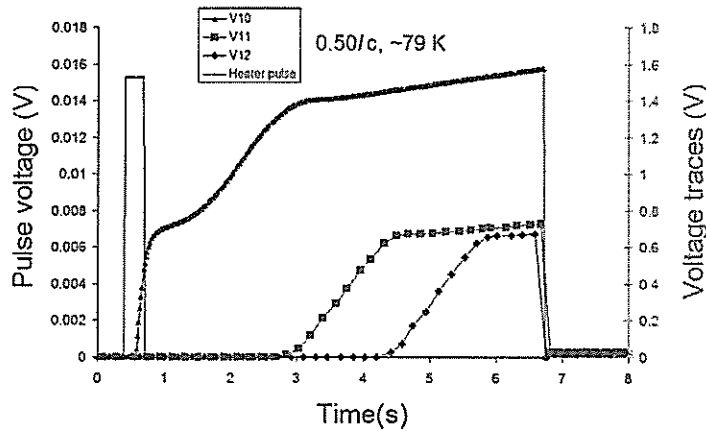


Figure VI.24: Voltages V_{10} , V_{12} , and V_{13} recorded at ~ 79 K for 50% of critical current. The Minimum Pulse Energy triggering a normal zone transition was equal to 227 mJ. The shape of the plots (in a vacuum or nitrogen gas cooling) are very similar to the ones of NbTi wires tested in liquid helium.

Figure VI.24 (page 220) shows the $V(t)$ curves of voltage taps V_{10} , V_{12} and V_{13} at 79 K and $0.5I_c$. In this test, the operating temperature is larger than the previous one. The critical current is lowered, which decreases heat generation. However, the shape of the voltage plots is very similar to the one of LTS conductors. In contrary to Bi-2223, the normal zone transition propagates even if the Normal Zone Propagation velocity remains slow compared to LTS conductor. As we noted in the N_2 convection cooling experiment, this result holds on the small current sharing zone, which appears at temperatures close to the critical temperature.

VI.5.0.8 Normal Zone Propagation Velocity versus the fraction of critical current

Due to a relatively slow Normal Zone Propagation Velocity, the temperature of the sample increases rapidly at high transport currents and the voltage rises sharply. To protect the sample from permanent degradation, the tap around the heater (V_{10}), was used to trip the power supply. Figure VI.24 (page 220) shows the $V(t)$ curves of voltage taps V_{10} , V_{12} and V_{13} at 79 K. For voltages V_{12} and V_{13} (see Figure VI.24, page 220), it was assumed that most of the transport current was flowing in the silver matrix. The voltage rising linearly along the sample, it is then possible to use the following expression to estimate the Normal Zone Propagation Velocity:

$$V = \rho_m \frac{L_{2-3}}{A_m} I_t \quad [\text{V}] \quad (\text{VI.2})$$

$$\nu = \frac{dL}{dt} = \frac{A_m}{\rho_m I_t} \frac{dV}{dt} \quad [\text{m/s}] \quad (\text{VI.3})$$

where V corresponds to the voltage traces V_{12} and V_{13} ; ρ_m is the resistivity of the matrix at a given temperature (here 88 K at the critical temperature taken from Figure VI.15, page 213), A_m is the cross-section of the silver matrix³, I_t is the transport current, $\frac{dV}{dt}$ is the slope of the $V(t)$ curve, and L_{2-3} the distance between the voltage taps of V_{12} and V_{13} .

Figure VI.25 (page 222) shows results on nitrogen gas cooling and conduction cooling. It appears that the Normal Zone Propagation Velocity increases linearly with increasing transport current. The fraction of critical current does not appear to vanish at zero velocity. It exists a minimum current, I_{mpc} , for which there is no propagating phenomenon. In some respect, it is similar to the cold-end recovery model, which states the existence of a minimum propagating current [15]. Below this current, no quench occurs and the sample recovers. The propagation velocity is necessarily zero. Above this minimum current, a normal zone propagates and the Normal Zone Propagation Velocity increases with increasing transport current as long as the input energy is larger than the Minimum Pulse Energy. On the same basis, J.W. Lue *et al.* [16], implicitly assumed the existence of this minimum propagating current and used the following equation:

$$\nu = \frac{(I_t - I_{\text{mpc}})}{A_w C_s} \sqrt{\frac{\lambda_m \rho_m}{(T_c - T_0)}} \quad [\text{m/s}] \quad (\text{VI.4})$$

where A_w is the cross-section of the conductor. $C_s = 1 \times 10^6$ J/m-K is the heat capacity of YBCO, and $\lambda_m = 370$ W/m-K and $\rho_m = 3.5 \times 10^{-9}$ Ωm are respectively the thermal conductivity and the resistivity of the matrix (values taken from J.W. Lue *et al.* [16]). We apply this equation to fit the data of NZPV in adiabatic conditions. We took as parameter the critical temperature, which has not been measured and has been obtained using a fit of the critical current versus temperature plot (see Figure VI.15, page 213). The minimum propagating current being equal to 6.8 A ($0.20I_c$), we found a critical temperature of ~ 94 K, which is of the order of generic YBCO superconductor.

³In first approximation, we did not consider the presence of the subtract which resistivity is larger than the one of the silver matrix.

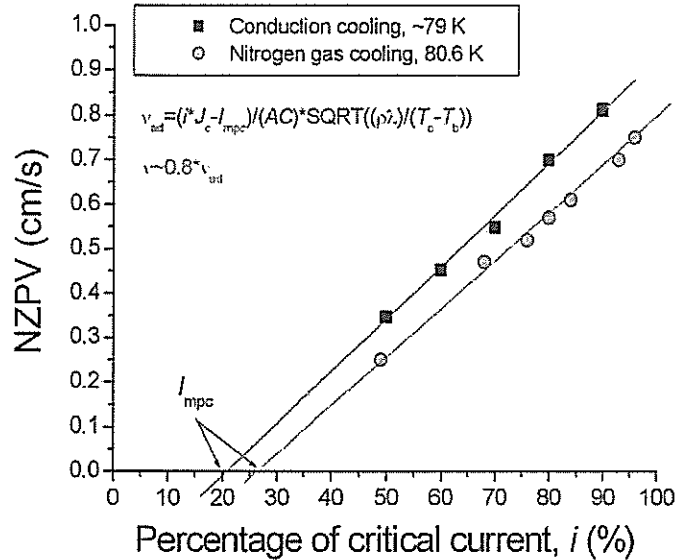


Figure VI.25: Comparison of the normal zone propagation velocity versus the percentage of critical current of nitrogen gas cooling and conduction cooling. The discrepancy is due to the influence of the coolant which lowers the normal zone propagation velocity.

We subsequently applied this formula to fit the data of nitrogen gas cooling experiment with a correcting factor, χ , to take into account of the presence of the coolant:

$$\nu = \chi \nu_{ad} \quad [\text{m/s}] \quad (\text{VI.5})$$

χ is found equal to ~ 0.8 and the minimum propagating current to 5.5 A ($0.25I_c$). A model of the exchanged power between the sample and the nitrogen gas coolant has not been attempted in the present work. However, with a simple correction, the above equation gives a good agreement with the experimental results.

The stability is enhanced with the presence of the coolant, which helps cooling down the sample. The NZPV is lowered but remains in the range of 0.1-1 cm/s.

VI.5.0.9 Minimum Pulse Energy versus the fraction of critical current

Figure VI.26 (page 223) is a plot of the Minimum Pulse Energy dissipated by the heater inducing a quench versus temperature. As expected, the Minimum Pulse Energy increases with increasing temperature following the increase in the heat capacity of the materials.

Figure VI.27 (page 224) shows a comparison between YBCO measurements in a vacuum and in nitrogen gas cooling conditions. Data from Bi-2223 measurements are also given. YBCO tape appears more stable than Bi-2223 tapes. One of the possible explanation is related to the quality of the bonding between the silver matrix and the YBCO layer. In the case of Bi-2223, this bonding is relatively good since the filaments of superconductors are fully embedded into a silver matrix. In the case of YBCO tape, the silver matrix is laminated on top of the YBCO layer. The bonding

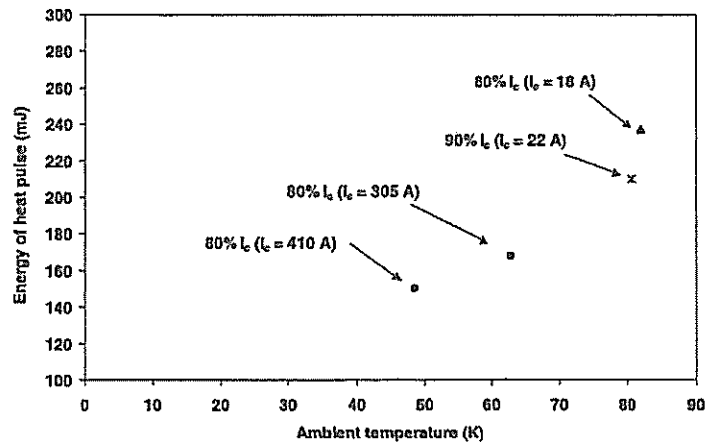


Figure VI.26: Minimum Pulse Energy versus the operating temperature. As expected the energy necessary to trigger a quench increases with the temperature since the enthalpy of the materials increases.

is not intimate and more heat source are necessary to increase the temperature of the YBCO layer through the Ag/YBCO contacts. The proportion of silver does not seem an influencing factor explaining the discrepancy between both tapes. Less energy would be expected to trigger a normal zone transition in the YBCO tape since the thickness of the silver layer is relatively small. The nickel substrate may explain this discrepancy by adding a thermal enthalpy to the system. However, the lack of information concerning the actual thermal properties of the samples cannot allow to clarify this assumption.

The discrepancy between the measurements of the YBCO tape in adiabatic conditions and nitrogen gas cooling conditions is not very large. The influence of the nitrogen gas is relatively weak especially at large transport currents for which the stability margin is reduced.

VI.5.1 Conclusion

We have developed an experimental methodology to initiate normal zone propagations and to measure the corresponding Normal Zone Propagation Velocities in HTS conductors subjected to pulsed thermal disturbances. For the deposition of heat, it was found that a NiCr wire is more efficient than the traditional approach using strain gauges.

The results obtained with the YBCO sample are very different from the preliminary Bi-2223 results. The voltage traces of the YBCO tape indicates a true normal zone propagation whereas the normal zone induced in the Bi-2223 tape relies more on diffusion process. In the case of YBCO, the voltage-rise amplitudes are an order of magnitude greater, which corresponds to a larger heat dissipation into the conductor boosting the normal zone growth. There are two explanations which are not mutually exclusive. Firstly, the possible significant differences in material properties may affect the normal zone behavior. Secondly, the presence of the padded tissue may also affect it. This tissue separated the YBCO coated conductor from the G-10

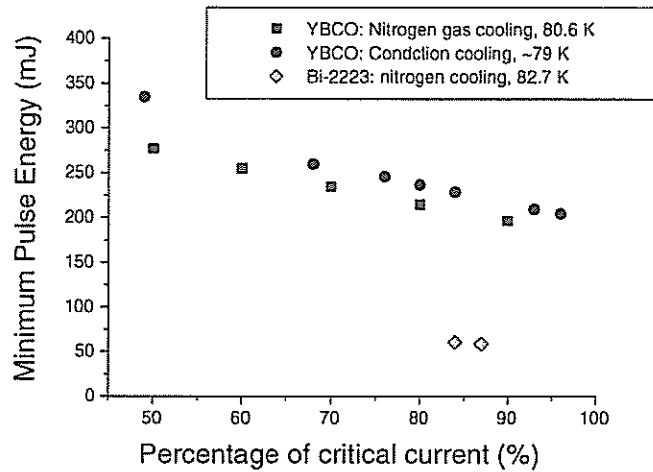
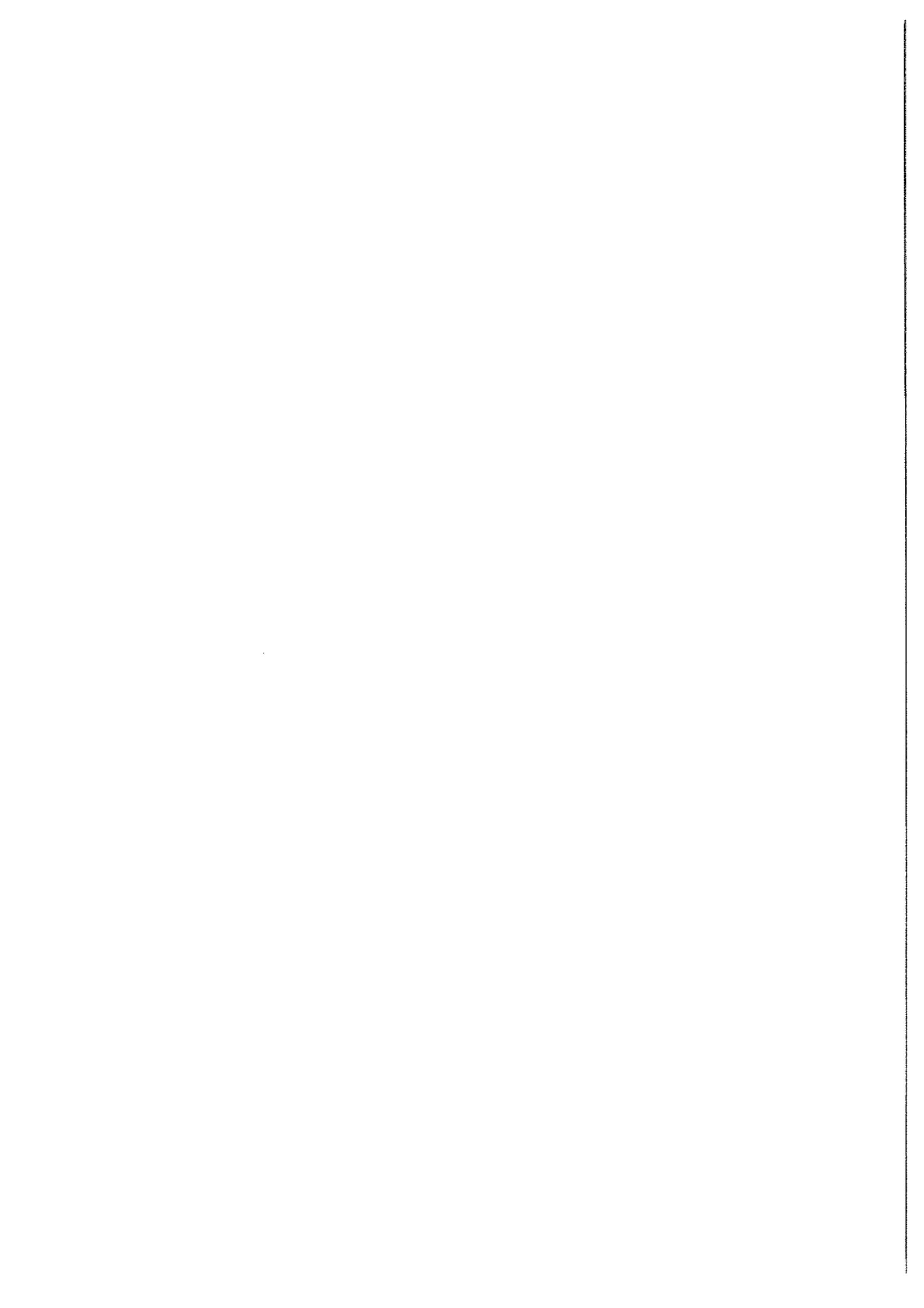


Figure VI.27: Comparison of Minimum Pulse Energy triggering a quench. The discrepancy is due to the influence of the coolant.

holder thereby preventing heat transfer from one to the other. It was not present during the Bi-2223 experiments.

The minimum energy required from the heater to initiate normal zone propagation in the YBCO coated conductor was significantly greater than that of the Bi-2223 sample. The geometrical characteristics of the tapes, the ratio between the cross-section of silver and superconductor [17], the relatively low electric and thermal conductivities of Nickel, and the critical current density are factors influencing the required energy. Additional measurements, microstructural studies of both samples, and more complete knowledge of their material properties would give more information about the observed differences. In any case, it is necessary to calibrate the heater to give a clear conclusion on the results and future simulations (estimation of the real amount of energy yielded by the heater absorbed by the HTS conductor). The Normal Zone Propagation velocity of the YBCO tape remains in the range of 0.1 to 1 cm/s, which is not large enough to ensure self-protection. A self-protection is usually assumed when the propagating velocity is superior to 1 m/s. This condition is fulfilled for LTS conductors, but, it is not fulfilled by HTS conductors. Even if these last conductors are more stable, they are likely to be damaged if a perturbation appears.



Bibliography

- [1] F. Trillaud, H. Palanki, U.P. Trociewitz, S.H. Thompson, H. W. Weijers, and J. Schwartz. Normal zone propagation experiments on HTS composite conductors. *Cryogenics*, 23(3-5):271–279, 2003.
- [2] F. Trillaud, A. Caruso, J. Barrow, B. Trociewitz, U.P. Trociewitz, H. W. Weijers and J. Schwartz. Normal Zone Generation and Propagation in $\text{YBa}_2\text{Cu}_3\text{O}_{7-\delta}$ Coated Conductors Initialized by Localized, Pulsed Disturbances. *Transaction on ICMC*, 20:852–859, 2004.
- [3] J.L. Duchateau, CEA/Cadarache. private communications, 2005.
- [4] M.W. Rupich, U. Schoop, D.T. Verebelyi, C. Thieme, W. Zhang, X. Li, T. Kodenkandath, N. Nguyen, E. Siegal, D. Buczek, J. Lynch, M. Jowett, E. Thompson, J-S. Wang, J. Scudiere, A.P. Malozemoff, Q. Li, S. Annavarapu, S. Cui, L. Fritzemeier, B. Aldrich, C. Craven, F. Niu, R. Schwall. YBCO Coated Conductors by an MOD/RABiTSTM Process. *IEEE Transactions on Applied Superconductivity*, 13(2):2458–2461, 2003.
- [5] Goodfellow. www.goodfellow.com.
- [6] J.F. Shackelford and W. Alexander. *Handbook of Materials Science & Engineering*. CRC Press Boca Raton, 2001.
- [7] J.G. Weisend II, editor. *Handbook of cryogenic engineering*. Taylor and Francis, 1998.
- [8] Emerson & Cuming. www.emersoncuming.com.
- [9] C.A. Swenson. Linear thermal expansivity (1.5-300 K) and heat capacity (1.2-90 K) of Stycast 2850FT. *Review on Science Instrument*, 68(2):1312–1315, February 1997.
- [10] F. Rondeaux, CEA/Saclay. private communications, 2005.
- [11] S.B. Kim, Y. Ueno, A. Ishiyama. Experiment and Numerical Analysis of Normal Zone Propagation Properties in Ag Sheathed Bi-2223 Superconducting Tapes. *IEEE Transactions on Magnetism*, 32(4):2822, July 1996.
- [12] S.B. Kim, A. Ishiyama, H. Okada, S. Nomura. Normal-zone propagation properties Bi-2223/Ag superconducting multifilament tapes. *Cryogenics*, 38(8):823–831, 1998.

BIBLIOGRAPHY

- [13] R.C. Duckworth, J.M. Pfothenauer, J.W. Lue, M.J. Gouge, D.F. Lee, and D.M. Kroeger. Quench Dynamics In Silver Coated YBCO Tapes. *Advances in Cryogenics Engineering: Proceedings of the International Cryogenic Materials Conference - ICMC*, 48:313–320, 2003.
- [14] X. Wang, R.C. Caruso, M. Breschi, G. Zhang, U.P. Trociewitz, H.W. Weijers, and J. Schwartz. Normal Zone Initiation and Propagation in Y-Ba-Cu-O Coated Conductors with Cu Stabilizer. *IEEE Applied Superconductivity*, 15(2):2586–2589, 2005.
- [15] B.J. Maddock, G. James, and W.T. Norris. Superconductive composites: heat transfer and steady state stabilization. *Cryogenics*, pages 261–273, August 1969.
- [16] J.W. Lee, M.J. Gouge, R.C. Duckworth, D.F. Lee, D.M. Kroeger, and J.M. Pfothenauer. Quench Tests of a 20-cm-Long RABiTS YBCO Tape. *Advances in Cryogenics Engineering: Proceedings of the International Cryogenic Materials Conference - ICMC*, 48:321–328, 2003.
- [17] A. Ishijama, M. Yanai, T. Morisaki, H. Ueda, Y. Shiohara, T. Izumi, Y. Lijima, T. Saitoh. Normal transition and Propagation Characteristics of YBCO Tape. *IEEE Transactions on Applied Superconductivity*, 15(2):1659–1662, 2004.

Chapter VII

General Conclusions

VII.1 Superconducting magnet stability

A superconducting magnet is a complicated device, made-up of various components which interact and are fitted together to yield the nominal magnetic field. We can distinguish two types of magnets: those which are a part of a scientific or/and a R&D project and those which target an established commercial market (such as MRI and RNM applications). In the first case, the technology is pushed to its limit. The magnet designer try to achieve the high performances which may lead to possible "quenches". In the second case, reliability is the main concern. So, larger stability margins are applied to guaranty stability over hours and years of operation. The technology is now mastered and reliability and safety magnets are produced for commercial applications (see chapter II, section II.2, page 52). In the present work, our background subject deals with the first type of devices for which instabilities can arise.

Discussing the stability of a single cell such as a conductor is not representative of what happens in a large entity as a magnet. However, it is an important task for wire manufacturers which would like to improve the current technology of conductors in order to supply more performing products to magnet designers. In addition, it is a preliminary step toward more complicated stability experiments to study cables and small windings whose behavior are more representative of a full magnet.

The difficulty to relate the knowledge accumulated on the thermo-electric behavior of a single conductor to the unexpected quenches of magnets lies in the difficulty to simulate the actual conditions prevailing in large coils. The influence of the helium coolant is a key-parameter in the study of superconductor stability. A vast amount of data has been gathered on the heat-exchange coefficient between helium coolant and metallic surfaces. However, they depend a lot on experimental setups resulting in a broad range of data. For a preliminary conservative study, one can neglect the influence of the helium coolant and only study the adiabatic case. It is the simplest case, but, it is often far too conservative compared to the conditions of an actual magnet. It may be more applicable to potted coils for which the helium coolant does not wet directly the surface of the conductors. Most of the past stability studies were based on steady-state helium heat transfer models. These models are relevant for continuous released of heat, but, they are too conservative for transient heat disturbances, which are thought to be the dominant origins of quenches.

The work presented in this thesis does not answer all the questions relative to the

influence of cooling on stability. We do present a large body of data as well as a numerical model simulating the thermo-electric behavior of a Cu/NbTi type LHC-02 composite wire. However, no model has been attempted to simulate HTS tapes for which the availability of material properties and their laminar structure adds complexity to the model.

In spite of leak issues that were not resolved in the time frame of this work, the newly designed experimental setup for LTS stability studies proved to be suitable and enabled detailed measurements. Indeed, using a new heater to simulate quench precursors, a fibered diode laser, we achieved a very good repeatability and we demonstrated the possibility to calibrate the absolute amount of energy actually absorbed by the wire sample, which had never been done so far.

In the time frame of this thesis and after the numerous efforts to seal the leaks, we did not have time to pursue additional measurements on different oxidized samples. We expect that a calibration in situ will allow to quantify the level of reproducibility of the measurements. However, without calibration, the coefficient of absorption and the behavior of the heat-exchange coefficient, depending on the surface characteristics of the sample, may vary considerably between samples.

VII.1.1 Right choice of heaters to simulate quench precursors

Most of this work dealt with the development of a new heater technology to simulate quench precursors. A lot of trials have been attempted. At first, we tried a charged point heater, a mixed technology between tip-heater and charged epoxy. The idea was to control the value of the contact resistance at the interface between the wire sample and the charged resin. However, in spite of various improvements, we could not achieve reproducible results. This technology was then abandoned and two alternative ones were subsequently tried: induction coils and diode laser. For these heaters, we needed a new experimental setup which could house both of them. Our first idea was to compare results of the two heaters.

The small induction coils, which were not discussed here, could not give exploitable results. Indeed, the large inductance of the coils led to a large error in the determination of the energy dissipated in the sample. In addition, the voltage data could not be exploited because of a large inductive noise. In the other hand, the fibered diode laser showed a large improvement both in terms of repeatability of the measurements and of the ease of use. It requires some precautions (temperature control and current polarity), but, it is adaptable to most experimental setups. If necessary, additional optics can be used to focus, collimate or guide the laser beam from the diode to the target. Several commercial products of different dimensions and usefulnesses can fulfill the needs of the experimentalists. The main advantage of this technology is the possibility of performing an "in situ" calibration. In the present work, we carried out a proof of principle and we demonstrated how the calibration could be made. We have chosen a bolometric technology which appeared to us as the simplest and the cheapest way to carry out calibration. Experimental setups can be imagined to perform stability tests and calibration at once based on this calorimetric method.

VII.1.2 Comparison of charged point heater and diode laser results

Two main experimental setups with two different heaters have been used to study the stability of Cu/NbTi composite wires. We have characterized two batches of samples with slightly different characteristics. The order of magnitude of the results obtained with the charged point heater and the diode laser is consistent. We cannot strictly compare the results obtained with both technologies since the measurements were not performed in the same experimental conditions. However, despite the issues encountered with the VAMAS-type experiment, either for the quench energy or the Normal Zone Propagation Velocity, the orders of magnitude are consistent from one experiment to the other.

VII.1.3 Comparison between HTS and LTS conductors

Our work covered both LTS and HTS conductors. A large experience has been accumulated on various heater technologies and related issues. A large body of data has been gathered on Quench Energies and Normal Zone Propagation Velocities.

Quench Energy: LTS conductors appear largely more sensitive to heat disturbances than HTS conductors. While Quench energies of LTS conductors range from micro-Joules to hundreds of micro-Joules, HTS conductors can handle to a few hundreds of milli-Joules.

Normal Zone Propagation Velocity: This parameter enables one to define the criterion for which a magnet can be considered as self-protected. It is commonly assumed that, below 1 m/s, active protection is necessary to ensure safe quenches. This is the case for HTS conductors whose Normal Zone Propagation Velocity is of the order of centimeters per seconds, at most. However, the NZPV's of LTS conductors are above a few meters per seconds. While HTS conductors can suffer from local hot spots which diffuse slowly resulting in damaging overheating, LTS conductors spread the normal zone quickly enough owing to their good thermal conductivity to minimize local overheating. In addition, this gives enough time to dump the energy of the magnet.

VII.2 Further improvements of the actual experimental setup and numerical simulation

This work clears a new path to carry out accurate and reproducible experiment on superconductors. It demonstrated the powerfulness of diode laser technology for stability studies. However, additional works must be carried out. In the following section, we introduce a few additional improvements and possible routes of research.

VII.2.1 Experimental setup

A lot of efforts has been carried out to design a new experimental setup which houses the diode laser. We tried to carry out experiments in liquid helium and in a vacuum at 4.2 K. Unfortunately, leak issues did not allow us to fulfill our goal and, despite our efforts, we did not succeed in sealing the experimental setup. Vacuum experiments appear necessary since the issue related to the simulation of helium

heat transfer disappears and the problem is far more simple. Consequently, it would have given an experimental validation of the numerical simulation and it would have led to a better understanding of the influence of helium cooling.

Improvements in the laser light guidance can be also carried out. Small optics are available commercially and lenses of small dimensions can be purchased to collimate or focus a laser beam.

Coatings or a thicker oxide layer can improve the coefficient of absorption of the samples. By reducing the illuminated surface of the sample, the surface of the oxidized sample can be also diminished to minimize local interface effects in the heat transfer with helium. Nevertheless, a study of the influence of the oxide layer thickness and extension on the local heat transfer is required. In particular, it would lead to an estimation of the order of magnitude of the thermal gradient appearing across the oxide layer which may have to be taken into account in the numerical model. It is expected that tinned wire do not require any surface treatments. Indeed, due to its silver-like color, a better coefficient of optical absorption may result. Otherwise, with the rapid improvements in diode laser technology, diode laser of wavelengths in the green-blue region will be hopefully commercialized which will enable measurements on bare copper utilizing all the power capability of the diodes¹.

In addition to these improvements, some studies must be carried out to take into account the formation of helium bubbles and of vapor film. It is a relevant parameter for short pulse durations for which the power absorbed by the sample is large, driving rapidly the formation of bubbles at the surface of the sample. Due to the small difference in the indices of refraction of liquid helium and gaseous helium, it may become an important issue in term of light scattering. In adiabatic conditions, no such issues exist and the laser technology is a powerful tool. Indeed, the temperature variations of the samples due to the heat disturbance do not extend above twenty Kelvins. Then, the resistance of the metallic matrix remains equal to the residual resistance and the coefficient of optical absorption is quasi independent of the temperature of the sample. For temperatures outside the plateau of residual resistivity (≥ 30 K), this assumption is not verified any more and the coefficient of optical absorption is likely to change with temperature. From our calibration "proof-test", we did not see any influence of the temperature on the coefficient of optical absorption of the oxidized layer, and the samples behaved as expected.

VII.2.2 Numerical model

A first version of helium transient heat transfer has been implemented into a numerical program which solves a non-linear heat balance equation. Some simplifications have been made to give an insight view of the quench phenomenon undergone by a Cu/NbTi LHC-02-type composite wire. Among the improvements, which should be done, a model taking into account the diffusion process through liquid helium must be carried out. We did not consider the helium bubbling phase since its simulation is, until now, very difficult to do. So far, this improvement does not appear essential. However, a better model of the time evolution of the voltage across the heated zone is necessary. In the current version, we neglect the resistance of the superconducting filaments and state a linear evolution of the electric field with the current density as in the flux flow regime. By comparing the model to experimental

¹At these wavelengths, the optical absorption of copper tends toward the one of a black-body.

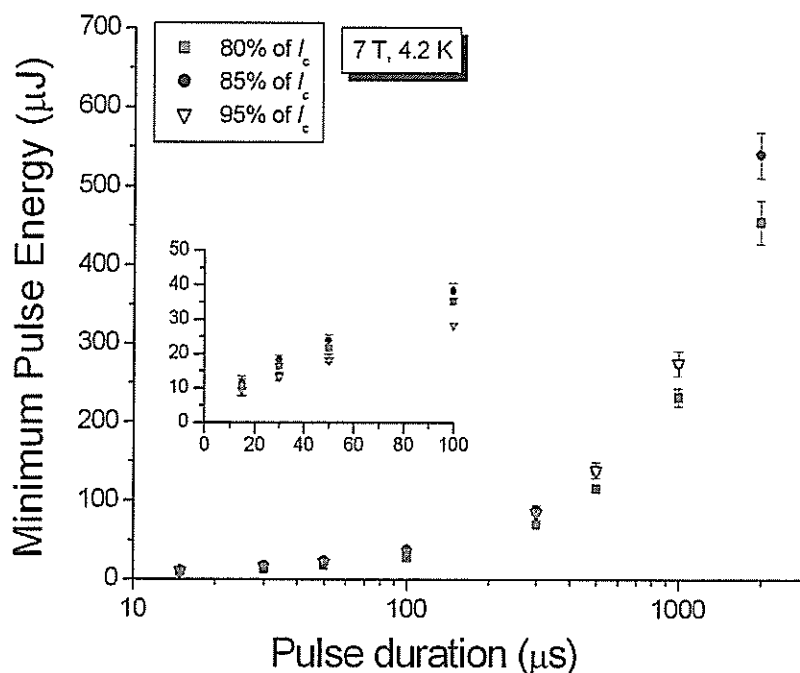


Figure VII.1: Minimum Pulse Energy as a function of the pulse duration at 7 T and 4.2 K for various percentages of critical current.

data, it does not appear accurate enough to simulate the early time evolution of the voltage between the current sharing temperature and the critical temperature. However, it gave some important information about the helium coolant influence on the stability and it enabled us to draw some preliminary conclusions. From the results of the numerical model, the film of gaseous helium blanketing the surface of the sample grows very rapidly and is triggered before the end of the heat disturbance has vanished. Then, the regime turns to film boiling for which the helium heat transfer is drastically reduced. The decision occurs in this regime where the heat conduction becomes the main factor determining whether the evolution will be toward a quench or a recovery.

VII.3 Perspectives: Nb₃Sn

To fulfill the contract with our industrial partner Alstom/MSA (France), we have also tested a new experimental setup on Nb₃Sn wires. These wires are currently used to wind a Nb₃Sn quadrupole model for the next generation of particle accelerators. Despite a larger transport current and the ensuing reduction of the active zone of measurements to carry out stability experiments, a few tests at 7 T, 4.2 K have been carried for various pulse durations and percentages of critical current. Figure VII.1 (page 231) gives the compilation of the first results. Nb₃Sn behaves as NbTi wires. We could draw at short pulse durations below $\sim 100 \mu\text{s}$ the pseudo-plateau of the Minimum Quench Energy.

On the contrary to NbTi, a better repeatability has been achieved for the whole

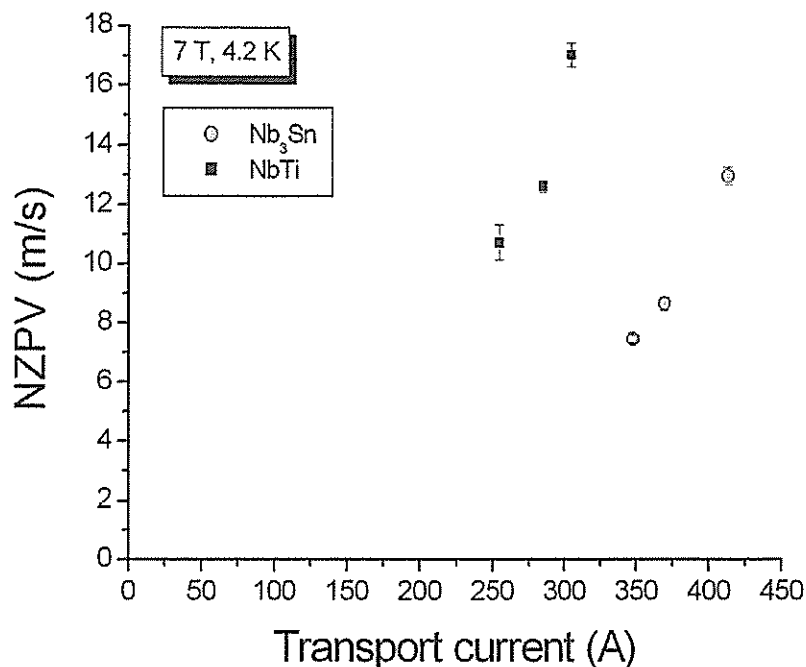


Figure VII.2: Normal Zone Propagation Velocity as a function of the transport current at 7 T and 4.2 K.

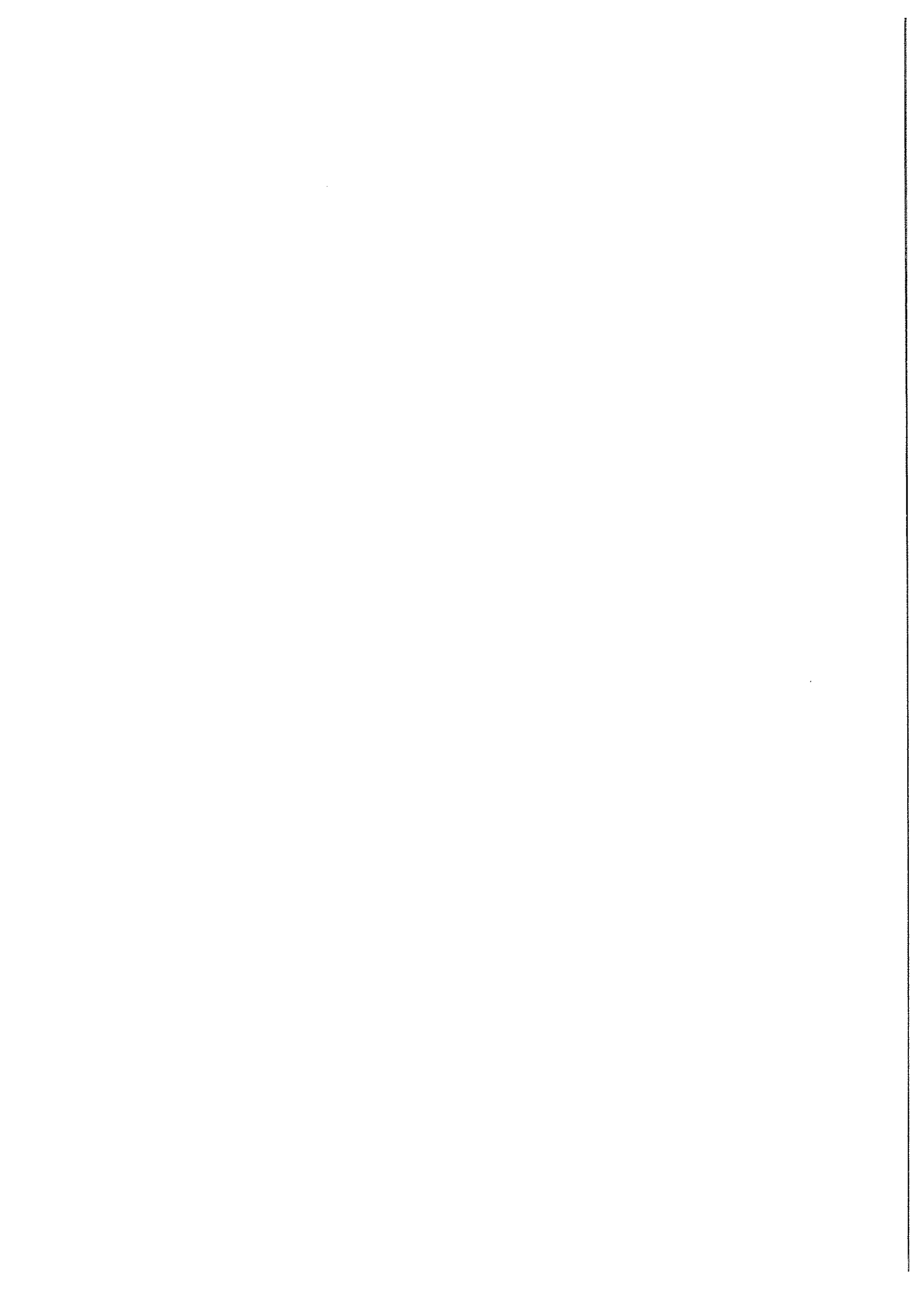
range of pulse durations. The Minimum Pulse Energy is of the order of $10 \mu\text{J}$, which is twice smaller than NbTi in the same experimental conditions. Different reasons lead to such a discrepancy. We give here a few hints on the normal zone propagation of Nb₃Sn. For about the same diameter ($\sim 0.82 \text{ mm}$), the copper-to-non-copper ratio of Nb₃Sn is 1.37 with a Residual Resistivity Ratio measured at ~ 67 (0 T) after the stability experiment ² while the one of NbTi is more stabilized with a ratio of 1.96 with a Residual Resistivity ratio of ~ 150 . Besides, the structure of the wires are different. Indeed, the filaments of Nb₃Sn are bundled in substructures. These substructures are embedded in a high thermal conductive copper sheath. In each substructure, the filaments are surrounded by bronze having a poor thermal conductivity and a larger resistivity than copper. Conversely, in a NbTi wire, the superconducting filaments are in direct contact with high thermal conductive copper. In addition to these structural differences, the critical current of Nb₃Sn is larger than the one of the NbTi for the same operating conditions. It is equal to 430 A ($\pm 5 \text{ A}$) for Nb₃Sn compared to 320 A for NbTi. The creation of the normal zone and its growth is at first a very local process. In the case of Nb₃Sn, Joule dissipation takes over rapidly at a very early stage of the normal zone growth. Furthermore, due to the degradation of the outer copper stabilizer, the cooling capacity is then globally reduced. The temperature profile flattens slowly

²Even if the sample was reacted on a metallic cast of the same U-shaped characteristics than the sample holder, the bending and the manipulations of the wire may have damaged anti-diffusion barriers enabling tin to diffuse through the outer copper stabilizer. According to Alstom/MSA, Residual Resistivity Ratio of ~ 260 was estimated on samples from the same batch.

due to the poor thermal conductivity of bronze and the Minimum Propagating Zone is expected to be smaller. In the case of $NbTi$, the presence of the copper matrix in an intimate contact with the superconducting filaments helps conducting away the excess heat.

In term of NZPV, we find the same order of magnitude (Figure VII.2, page 232). We did not perform a separate calibration in the Nb_3Sn case.

For further studies on Nb_3Sn wires, VAMAS-like sample holders are required to prevent the sample from damaging during curing or manipulations.



Appendix A

Residual resistivity of metals

The following Figure A.1 (page 234) shows a schematic view of the temperature evolution of the resistivity of silver and copper. Below ~ 30 K, the resistivity appears independent of the temperature. It is defined as the residual resistivity which is dependent on the purity of the metal.

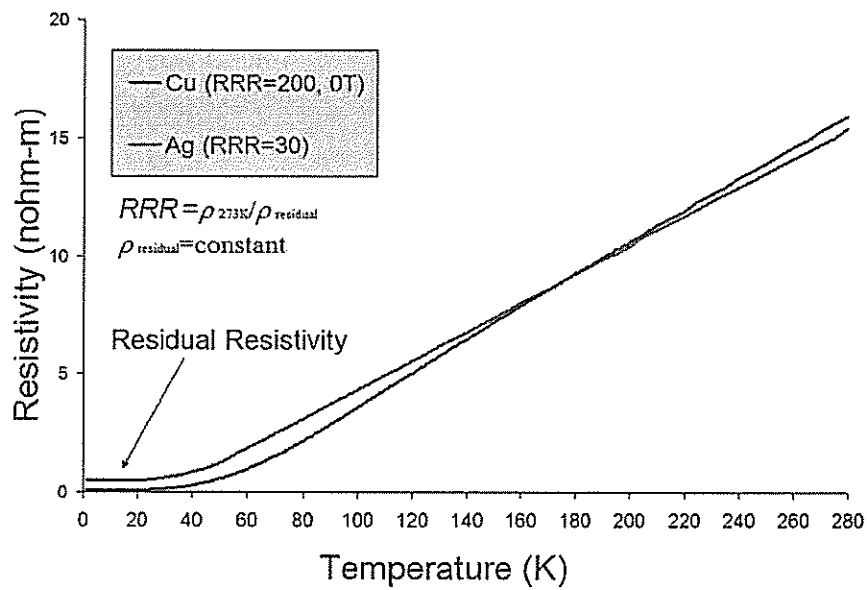
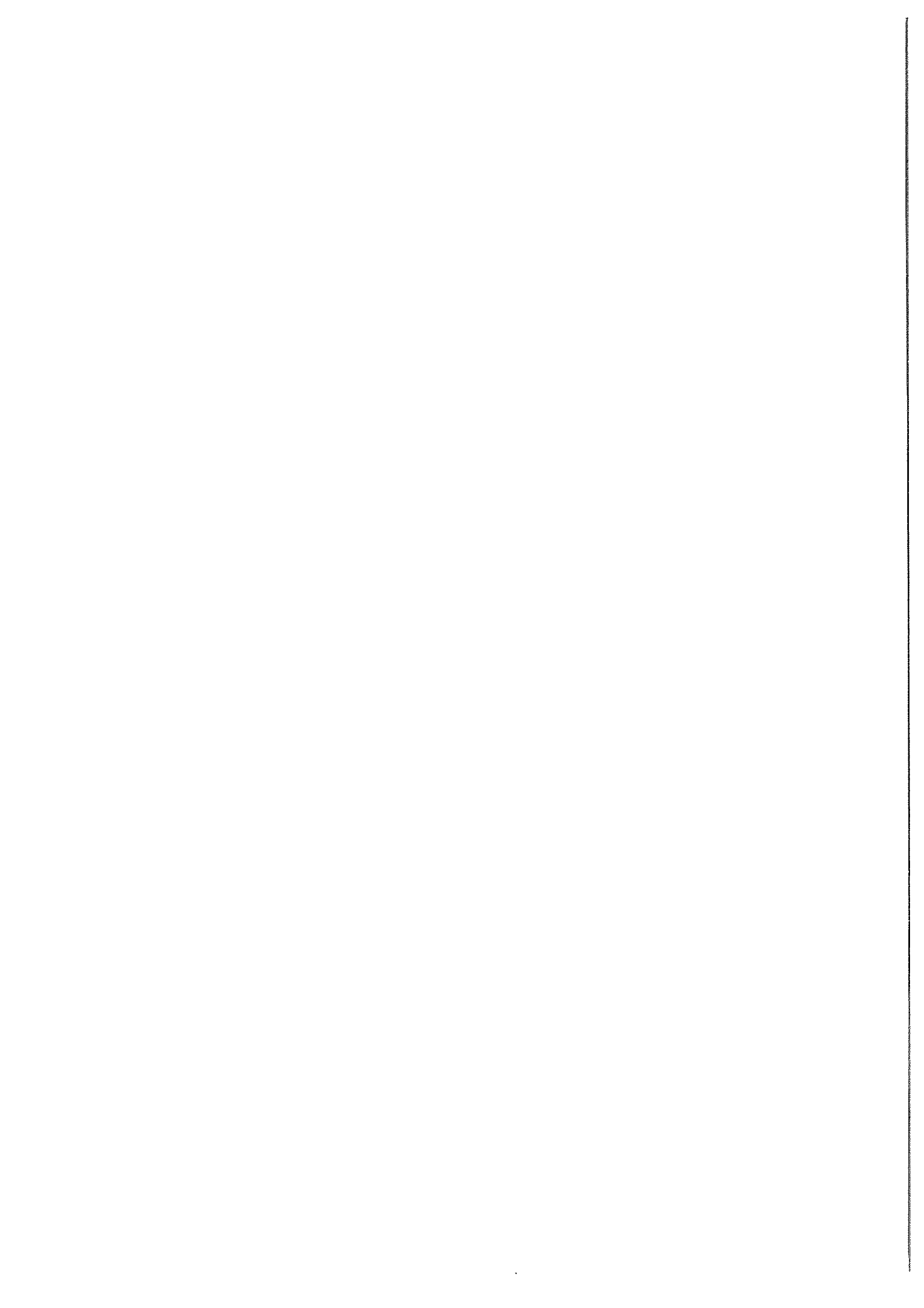


Figure A.1: Schematic view of the temperature evolution of silver and copper.



Appendix B

Critical current parametrization

NbTi alloy material is a type-II superconductor which is characterized by three parameters. These parameters are:

- The critical temperature, T_c
- The upper critical magnetic field, B_{c2}
- The critical current density, J_c

It exhibits superconducting behavior as long as the temperature, T , background magnetic field, B , and current density, J , remain within the critical surface defined by these parameters (T_c, B_{c2}, J_c). Figure B.1 (page 236) is a three dimensional view of the critical surface of a commercial NbTi alloy [1]. This critical surface was parametrized by Luca Bottura [2] based on the Lubell's formula, which give the temperature dependence of the upper critical magnetic field, B_{c2} and the field dependence of the critical temperature, T_c :

$$B_{c2}(T) = B_{c20} \left[1 - \left(\frac{T}{T_{c0}} \right)^{1.7} \right] \quad [\text{T}] \quad (\text{B.1})$$

$$T_c(B) = T_{c0} \left[1 - \left(\frac{B}{B_{c20}} \right)^{\frac{1}{1.7}} \right] \quad [\text{K}] \quad (\text{B.2})$$

The intrinsic parameters of NbTi alloy as the upper critical magnetic flux density at zero temperature, B_{c20} and the critical temperature at zero magnetic flux density, T_{c0} , are summarized in the following table B.1 (page 236). One of the critical surface is then given by the following relation:

$$J_c(B, T) = J_{c, \text{ref}} \frac{C_0}{B} \left[\frac{B}{B_{c2}(T)} \right]^a \left[1 - \left(\frac{B}{B_{c2}(T)} \right) \right]^\beta \left[1 - \left(\frac{T}{T_{c0}} \right)^{1.7} \right]^\gamma \quad [\text{A}/\text{mm}^2] \quad (\text{B.3})$$

So, the critical current versus magnetic field curve can be simply derived from this parametrization in the plane (J, B) at a given temperature of 4.2 K as follow:

$$I_c(B) = A_{\text{NbTi}} \times J_c(B) \quad [\text{A}] \quad (\text{B.4})$$

With A_{NbTi} , the cross-section of NbTi within the wire. To scale our results, we adjusted the parameters: C_0 , α , β and γ of this above equation. All these parameters, used in the fits of the two NbTi batches, are given in Table B.2 (page 236). These fits, which are given with the results in Figure III.2 (page 80), were subsequently used in the numerical simulation of the superconducting wires to fix the value of the transport current as a fraction of the critical current and to determine their sharing temperature.

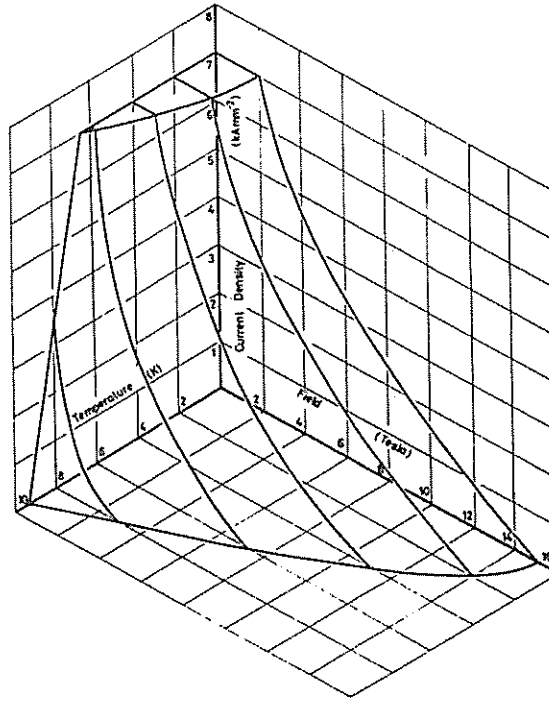


Figure B.1: Critical-current surface for commercial NbTi alloy (not corresponding to Equation B.3, see reference [1]).

Table B.1: Intrinsic parameters of NbTi alloy.

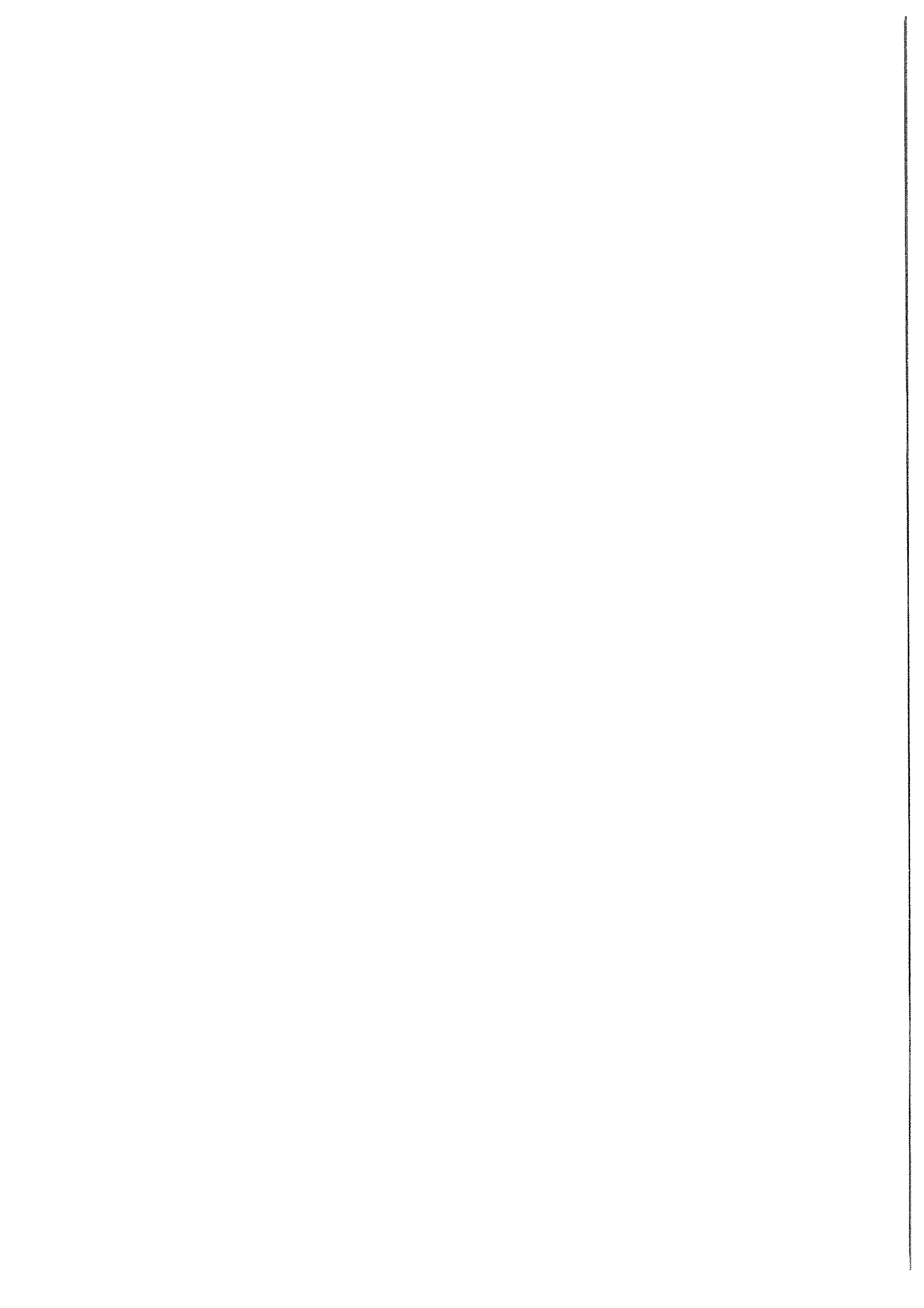
T_{c0}	9.2 K
B_{c20}	14.5 T
B_{c2} at 4.2 K	~ 10.7 T

Table B.2: Parameters of Luca Bottura's fit for NbTi-1 and NbTi-2 wires.

Parameters	NbTi-1	NbTi-2
A_{NbTi} ($\times 10^{-7} \text{m}^2$)	1.843	1.811
$J_{C,ref}$ (A/mm^2)	3000	3000
C_0	30.7	30.7
α	0.559	0.581
β	1.129	1.016
γ	2.3	2.3

References

- [1] R. Hampshire, J. Sutton, and M.T. Taylor. Proceeding of the conference on low temperatures and electric power. In *International Institute of Refrigeration, London*, 1969.
- [2] L. Bottura. A practical Fit for the Critical Surface on NbTi. *IEEE Transactions on Apply Superconductivity*, 10(1):1054–1057, 2000.



Appendix C

Interpolation of the optical power delivered by the diode laser

To estimate the optical power flowing out of the tip of the optical fiber following the variation of forward currents, we did not use a linear interpolation as it could be suggested by Figure IV.16(a) (page 123).

This linear interpolation could not approximate with accuracy the behavior of the diode laser at low forward current. Indeed, below ~ 700 mA, the optical power versus forward current characteristic presents a non-linear behavior. To have a better approximation, we tried polynomial fits at different orders or a cubic spline. As an example, Figure C.1 (page 239) extracted from a Matlab[®] output screen shows a comparison of a linear and cubic spline interpolation. The best fit, over the all range of forward current, is achieved by the cubic spline interpolation which has been subsequently retained. For forward currents close to the threshold current, the linear interpolation underestimates the pulse optical energy by more than 50%. However, it yields accurate values for large forward currents. For information, a linear fit which can be used to derive a quick estimation of the pulse energy at large forward current is:

$$P_{\text{opw}} = \epsilon_{\text{opw}}(I_{\text{F}} - I_{\text{Th}}) \quad [\text{W}] \quad (\text{C.1})$$

where $\epsilon_{\text{opw}} \simeq 0.670$ W/A, is the slope efficiency, I_{F} , the forward current and, $I_{\text{Th}} \simeq 270$ mA, the threshold current (values at 77 K, see Table IV.6 page 126). We do not detail the cubic spline interpolation which is a part of the standard functions of Matlab[®]. The following reference can be consulted for detailed explanations of cubic spline interpolations [1][2].

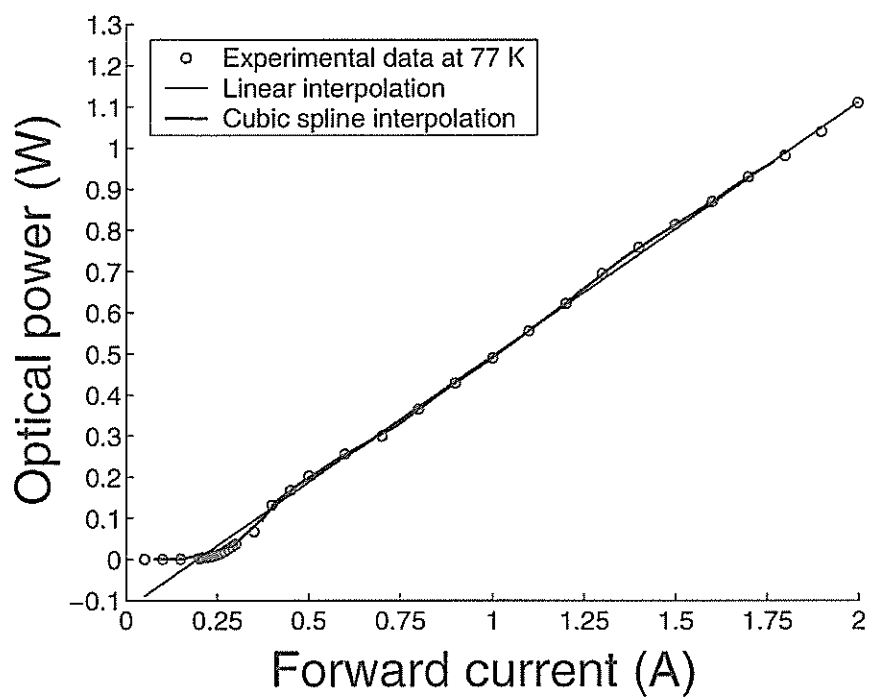
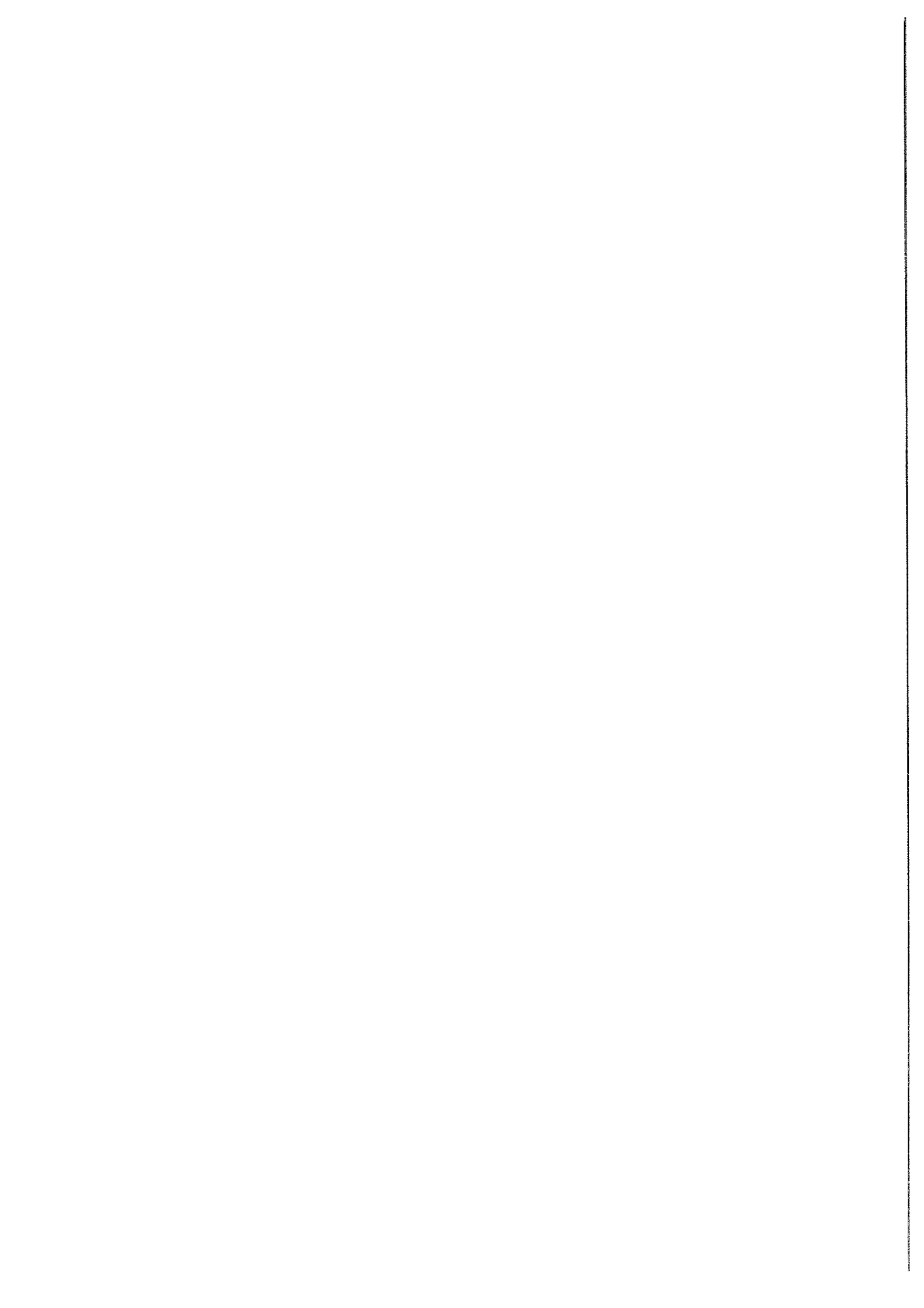


Figure C.1: Comparison of two different fits to determine the optical power delivered by the diode laser. In our analysis, we retained the cubic spline fit.

References

- [1] P. Chenin, M. Cosnard, Y. Gardan, F. Robert, Y. Robert, and P. Witomski. *Mathématiques et CAO: méthodes de base*. Hermes Publishing, 1985.
- [2] C. de Boor. *A Practical Guide to Splines*. Springer Edition, 2001.



Appendix D

Description of the new probe for stability studies

This appendix completes the brief description of the experimental setup given in chapter IV, subsection IV.2.4 (page 114).

The new probe and a detailed view of the vacuum chamber are illustrated in Figure D.1 (page 242) and Figure D.2 (page 243). The entire probe is not fully described. Only the parts, which were especially designed to improve the reproducibility of the stability measurements will be detailed in the next subsections.

Following the nomenclature¹ introduced in Figure D.1 (page 242) and Figure D.2 (page 243), these parts are:

- The G-10 tube and the supports of the probe (07)(04)(09).
- The helium vapor cooled current leads (05).
- The main tube (02).
- The diode laser support and its fiber tube (01)(20).
- The vacuum chamber support (12), the bus bars (10), and feedthrough connectors (11).
- The G-10 sample holder (21), (Figure D.2, page 243).

D.1 G-10 tube and supports of the probe

The G-10 tube (07) (680 mm in length, 141 mm in outer diameter, and 2.5 ± 0.5 mm thick) is squeezed between a top flange and a G-10 block. It prevents the copper thermal shields of the probe from touching those of the cryostat. With the help of 4 metallic rods (09), it allows also to rigidify the whole probe.

D.2 Helium vapor cooled current leads

Two helium vapor cooled current leads (05), supplied by American Magnetics Inc., are fixed onto the top flange and go through the G-10 block. Exhaust helium gas from the helium vessel flows through the current leads, which can feed the sample up to 1000 A. These current leads are extended with tinned braided copper wires

¹This nomenclature will be used throughout the text and figures in the subsequent sections.

D.2. HELIUM VAPOR COOLED CURRENT LEADS

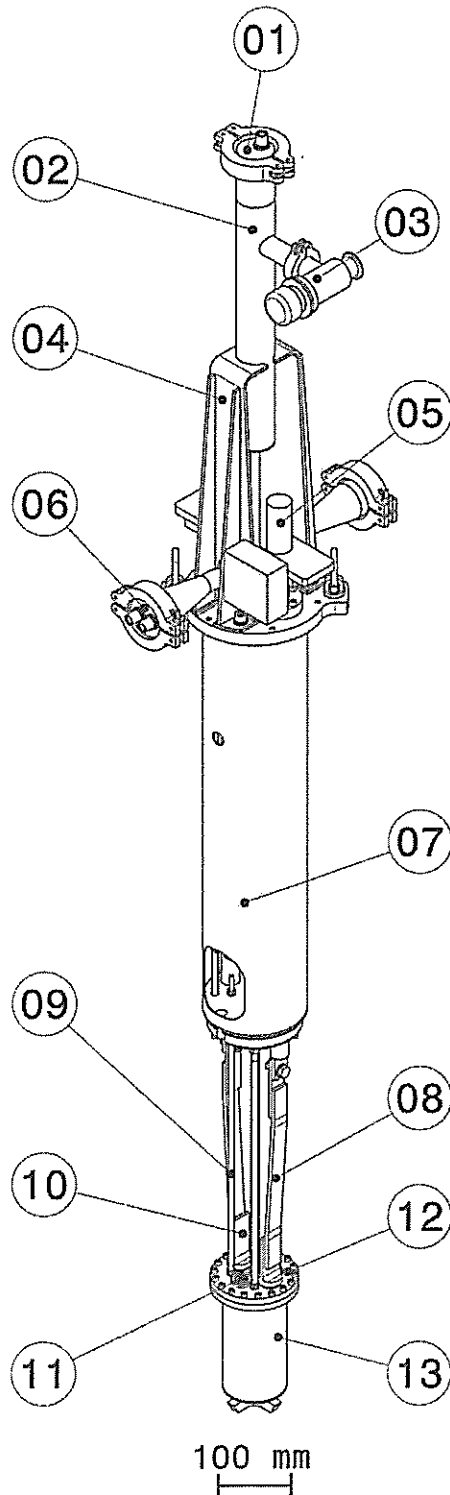


Figure D.1: New probe for stability tests:

- 01- Sealing tap belonging to the diode laser support.
- 02- Main tube serving as pumping pipe.
- 03- Manual valve to seal the main tube (02) for measurements in a vacuum.
- 04- Massive metallic reinforcement to support the main tube (02).
- 05- One of the two helium vapor cooled current lead screwed to the top flange.
- 06- One of the two trumps soldered to the top flange in which goes electrical connectors.
- 07- G-10 cylinder to facilitate the dipping of the probe into the cryostat squeezed between the top flange and a G-10 block.
- 08- One of the two tinned braided copper wire bonding the helium vapor cooled current leads to the bus bars (10).
- 09- One of the four metallic rods to support mechanically the main tube (02) and the vacuum chamber (12)(13).
- 10- One of the two OFHC copper bus bars on which is soldered the sample.
- 11- One of the two electrical feedthrough connectors.
- 12- Vacuum chamber support.
- 13- Vacuum box sealing the vacuum chamber owing to an Indium join.

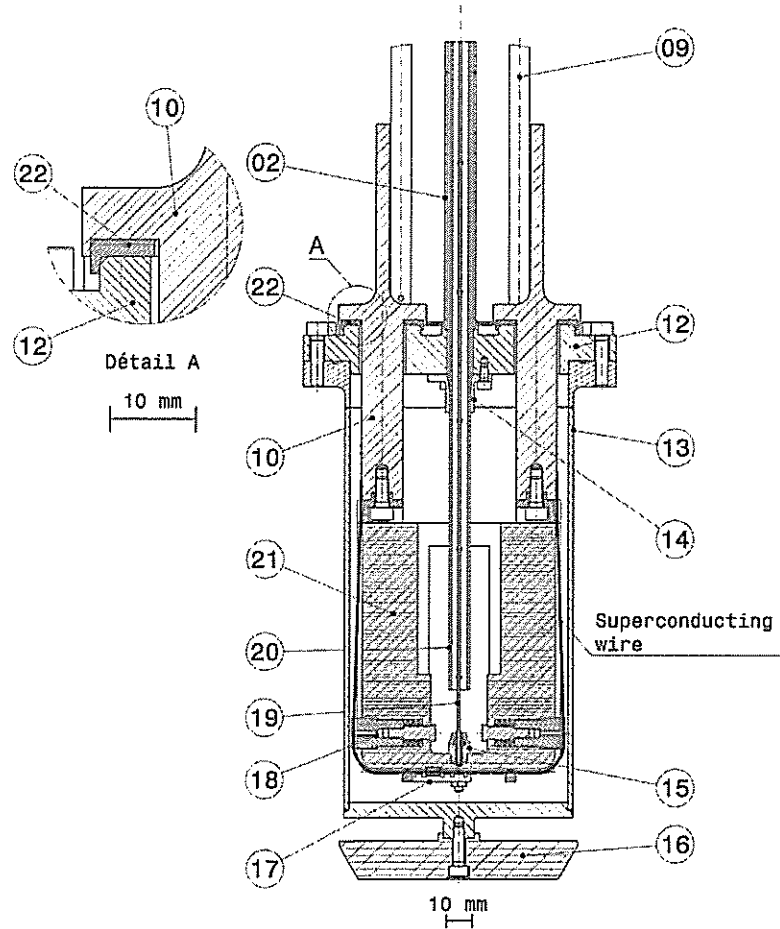


Figure D.2: Cross-section of the vacuum chamber and the sample holder:

- 02- Main tube.
- 09- Metallic rod supporting the vacuum chamber.
- 10- OFHC copper bus bar.
- 12- Vacuum chamber support.
- 13- Vacuum box, which can be replaced by an opened box for measurements in liquid helium.
- 14- Metallic piece to guide the optical fiber tube (20).
- 15- Metallic assembly to position and maintain the tip of the optical fiber (19).
- 16- G-10 guiding part to center the probe into the magnet of the cryostat.
- 17- G-10 piece with a lug to maintain the sample in its lodging.
- 18- Customized springs to tension the sample.
- 19- Extension optical fiber (additional fiber).
- 20- Fiber tube protecting the extension optical fiber.
- 21- G-10 sample holder.
- 22- One of the two electrical insulating G-10 disks.

(08). These copper wires are soldered to 2 bus bars (10) onto which the sample is also soldered.

D.3 Main tube

Figure D.1 (page 242) shows a better view of the main tube (02) while Figure D.2 (page 243) shows one of its extremities soldered to the vacuum chamber support (12). This tube, straightened over the whole height of the probe, is made-up of two stainless steel tubes of different diameters soldered one to another. The tube of larger diameter (484 mm height and 54 mm of outer diameter) is located at the top of the probe at room temperature. It welcomes the diode laser and its support. The second tube of smaller diameter (1314 mm height and 12 mm in outer diameter) extends the previous tube down to the bottom of the probe where it is soldered to the vacuum chamber support.

When mounted on the probe, the larger tube, the smaller one and the vacuum chamber support form one unit, which is sealed by the vacuum box (13) and the diode laser support through its sealing tape (01) for measurements in a vacuum.

A manual valve (03) and a pressure sensor to measure the magnitude of vacuum are connected to an outlet of the larger tube.

D.4 Support of the vacuum chamber

Figure D.2 (page 243) details the vacuum chamber support (12). Two bus bars (10), made-up of Oxygen-Free High Conductivity (OFHC) copper, were designed to supply up to 1000 A to the sample with minimum heat dissipation. G-10 disks (22) were placed between the bus bars and the vacuum chamber support to provide electrical insulation (see detail A, Figure D.2, page 243). They were glued with DP490 epoxy structural adhesive (supplied by 3M Scotch-WeldTM) to sustain the heat generated by the soldering of the samples. To guaranty a better sealing under thermal shrinkage, the whole assembly was concentrically arranged. Copper material having a larger thermal shrinkage than fibered epoxies and stainless steel squeezed the G-10 disks onto the vacuum chamber support when it was cooled down at low temperature.

Additional electrical feedthrough connectors (11) (see Figure D.1, page 242), in which were glued with black Stycast[®] 2850FT AWG copper wires, provided 36 electrical wires for acquisition and voltage detection. Two series of connectors, supplied by Plug in (France), have been designed and showed poor reliability for measurements in a vacuum surrounded by liquid helium. For measurements in a vacuum, these feedthrough connectors (11) (see Figure D.1, page 242) were replaced by sealing taps and acquisition wires were passed through the optical fiber tube (20). They were subsequently soldered to a sealing connector (19 pins, Fischer) located at room temperature on the same outlet than the manual valve (03) (see Figure D.1, page 242).

Unfortunately, the different manipulations on the probe degraded the sealing of the bus bars and measurements in a vacuum could not be achieved in the time frame of this study.

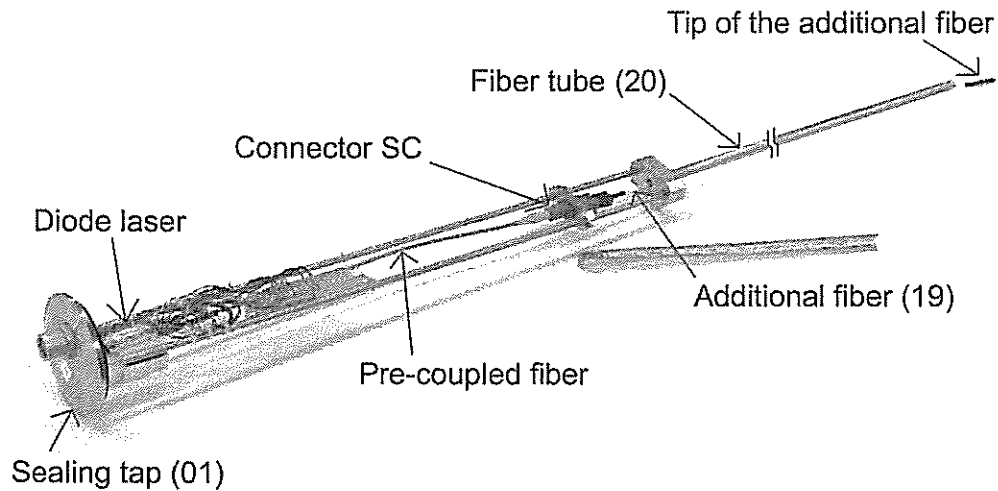
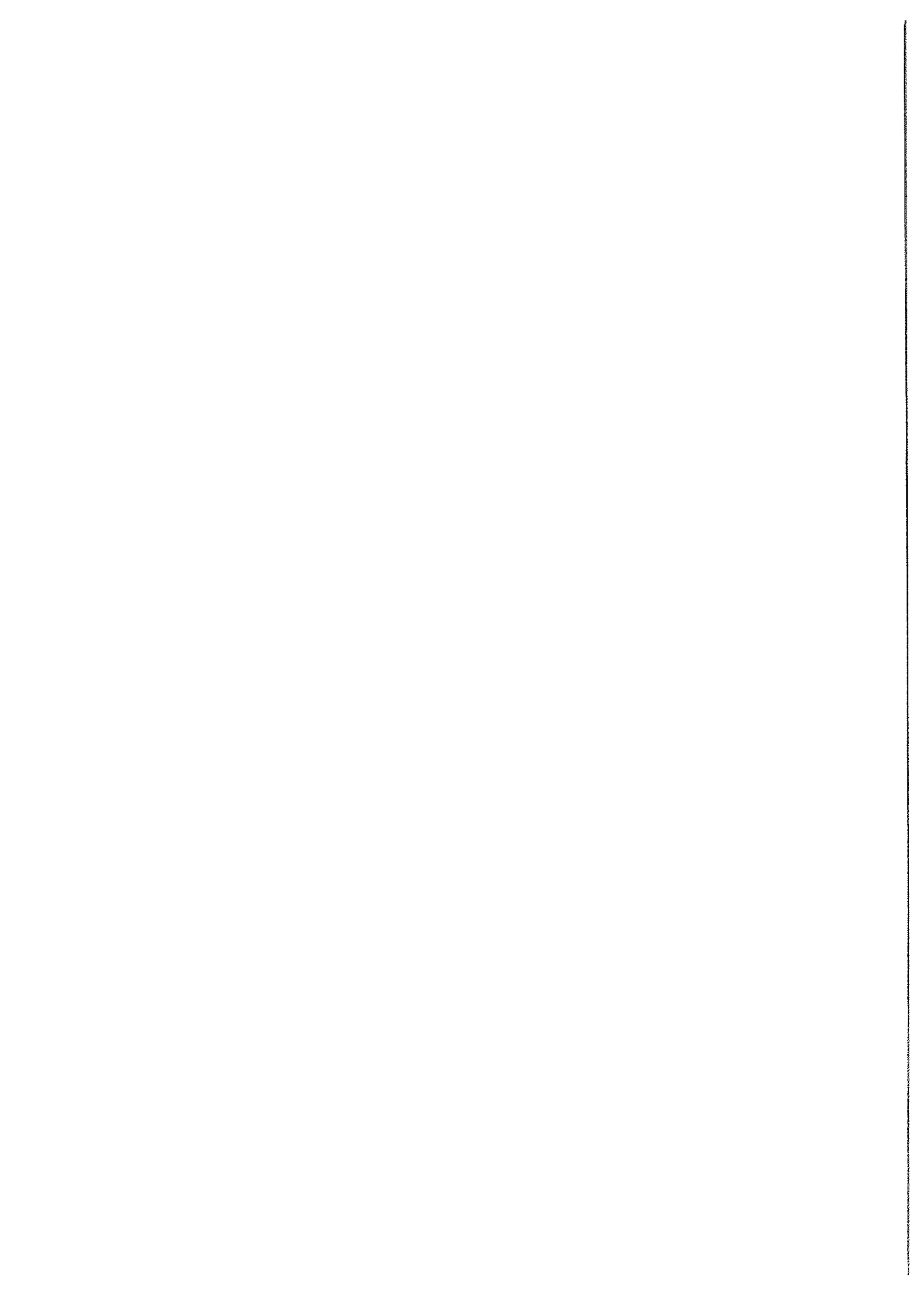


Figure D.3: Support of the diode laser and its drilled fiber tube used to protect the optical fiber extension during mounting and dismounting from the probe.

D.5 Diode laser support and its fiber tube

Figure D.3 (page 245) depicts the entire sub-assembly making the support of the diode laser. At the top of it, there is a sealing tap (01) prolonged by two metallic rods going to a massive block in which was inserted and glued a stainless steel tube (20). The sealing tap was designed to receive a sealed connector, the diode laser, and its cooling element (see section IV.2.3 page 113). Along the two metallic rods extending the sealing tap, a mechanical support was designed to facilitate the holding of the connector (standard SC) hooking up the pre-coupled optical fiber and the optical fiber extension. This latter fiber was protected by a stainless steel tube (20) of 8 mm in diameter. This tube, called fiber tube, was drilled with tiny holes every 50 mm along its 1575 mm height to avoid thermo-acoustic effects during tests in liquid helium. It also helps pumping the vacuum chamber for measurements in a vacuum.

Finally, this whole sub-assembly was also designed as a single unit which could seal the main tube (02) and be easily mounted and dismantled from this same tube.



Appendix E

Thermal and magnetic flux diffusion in a composite wire

A few hypothesis have been made to simulate the thermoelectric behavior of a Cu/NbTi multifilament composite wire undergoing a quench (see chapter IV, page 103). We assumed that the temperature was homogeneous over the cross-section of the wire and the time constant of the current redistribution in the matrix was negligible compared to the time characteristic of the the creation of the MPZ. In first approximation, these assumptions can be verified by comparing the diffusion time of the heat through the cross-section of the wire and the magnetic diffusion time during the redistribution of current from the superconductor to the copper matrix¹ to the Quench decision time.

Thermal and magnetic diffusion equations: The equations of current and thermal diffusion are as follow (adapted from reference [1]):

$$D_{\text{th}} \frac{\partial^2 T}{\partial u_r^2} = \frac{\partial T}{\partial t} \quad (\text{E.1})$$

$$D_{\text{mag}} \frac{\partial^2 J_r}{\partial u_r^2} = \frac{\partial J_r}{\partial t} \quad (\text{E.2})$$

where $\mathbf{u}(u_r, u_\theta, u_z)$ is a cylindrical vector coordinate, $J_r(r, z)$ is the radial coordinate of the current density and $T(r, z)$ is the temperature of the wire. The thermal and magnetic diffusivities appeared respectively as D_{th} and D_{m} . The physical properties of the wire have been assumed homogeneous across the cross-section, the diffusivities are:

$$D_{\text{th}} = \frac{\lambda_{\text{mr}}}{C_w} \quad [\text{m}^2/\text{s}] \quad (\text{E.3})$$

$$D_{\text{mag}} = \frac{\rho_{\text{mr}}}{\mu_0} \quad [\text{m}^2/\text{s}] \quad (\text{E.4})$$

¹In first approximation, we consider that all the current flows in the copper matrix while the current sharing temperature is exceeded.

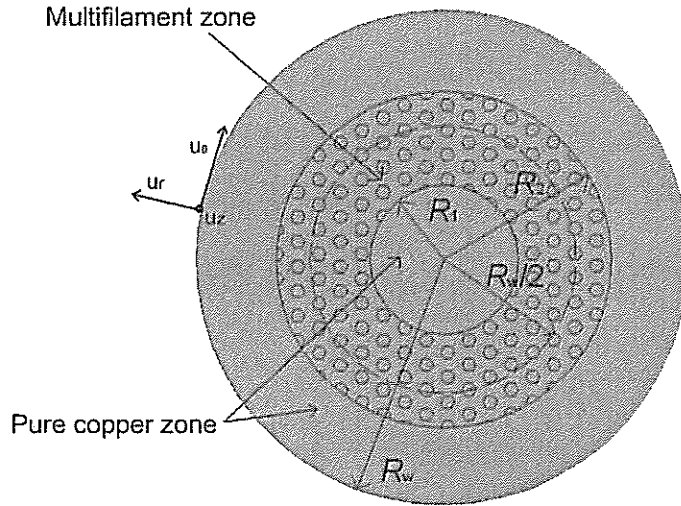


Figure E.1: Sketch of the cross-section of a multifilament Cu/NbTi composite wire.

Table E.1: Homogeneous physical properties following the wire radius and estimation of the diffusion parameters at 4.2 K.

	5 T	6 T	7 T
ρ_{mr} ($\times 10^{-9} \Omega m$)	0.5	0.6	0.7
λ_{mr} (W/m/K)	916	824	748
C_w (J/m ³ K)	2800	2800	2800
D_{th} (m ² /s)	0.33	0.3	0.27
D_{mag} ($\times 10^{-6} m^2/s$)	400	480	530
τ_{th} (μs)	0.21	0.23	0.25
τ_{mag} (μs)	43	35	32
QDT (μs)	60	110	200

Let us name:

$$l_1 = \frac{R_1 + R_w - R_2}{R_w} \quad (\text{E.5})$$

$$l_2 = \frac{R_2 - R_1}{R_w} \quad (\text{E.6})$$

the fraction of radius of pure and degraded copper (see Figure E.1, page 247). Then, the average thermal conductivity λ_{mr} and the average resistivity of the copper matrix ρ_{mr} are defined as:

$$\lambda_{\text{mr}} = \frac{1}{\frac{l_1}{\lambda_{\text{Cu1}}} + \frac{l_2}{\lambda_{\text{Cu2}}}} \quad (\text{E.7})$$

$$\rho_{\text{mr}} = l_1 \rho_{\text{Cu1}} + l_2 \rho_{\text{Cu2}} \quad (\text{E.8})$$

Table E.1 (page 247) summaries values of the different physical parameters at various background magnetic flux densities.

Solution of the diffusion equations and definition of the diffusion time: In a slab of width $2w$, the solutions of Equations E.2 (page 246) take the following form [2]:

$$T/J = \sum_1^{\infty} A_n \sin\left(\frac{n\pi r}{2w}\right) e^{-\frac{D_{\text{th/mag}} n^2 \pi^2}{4w^2} t} \quad [\text{K}] \quad (\text{E.9})$$

where A_n are Fourier's coefficients. In first approximation, we apply the above result to the case of the wire sample². We can then deduce from the above solution the thermal and magnetic diffusion time:

$$\tau_{\text{th}} = \frac{4R_w^2}{\pi^2 D_{\text{th}}} \quad [\text{s}] \quad (\text{E.10})$$

$$\tau_{\text{m}} = \frac{R_w^2}{\pi^2 D_{\text{mag}}} \quad [\text{s}] \quad (\text{E.11})$$

In the case of the magnetic diffusion, we only considered half of the wire radius.

Discussion: In Table E.1 (page 247), it appears that the thermal diffusion time is negligible compared to the characteristic time of the MPZ creation. However, this assumption is not fully satisfied in the case of the magnetic diffusion. Especially at 5 T, the magnetic diffusion time and the QDT are of the same order of magnitude. Then, in this case, a fine analysis would require to model thermo-electrically the cross-section of the wire which has not been done here.

²This is a crude assumption since the round geometry of the wire does not match the hypothesis of the solution presented hereby. However, it is a convenient approximation to estimate orders of magnitude.

References

- [1] M.N. Wilson. *Superconducting Magnets*, page 143. Oxford University press, 1983.
- [2] H.S. Carslaw and J.C. Jaeger. *Conduction of heat in solids*. Oxford university press, 1959.

Appendix F

Material properties

F.1 Heat capacity of the conductor

F.1.1 Heat capacity of NbTi superconductor

To find the heat capacity of NbTi, it is necessary to distinguish the normal-state and the superconducting state of the material.

Normal state: In the normal-state, NbTi acts as a normal metal for which the heat capacity results from the contribution of phonons (lattice vibration) and electrons [1]:

$$C_s(T > T_c) = \gamma_{\text{sum}}T + \beta_{\text{Debye}}T^3 \quad [\text{J/Km}^3] \quad (\text{F.1})$$

where $\gamma_{\text{sum}}T$ is the contribution of electrons and $\beta_{\text{Debye}}T^3$ is the contribution of phonons.

Superconducting state: Between the normal state and the superconducting state, the contribution of phonons to the total heat capacity remains unchanged since the structure of the lattice is not modified. However, the electrons of the conduction band condensate into a highly ordered state and the contribution of the electrons to the total heat capacity changes abruptly. In the superconducting state, the heat capacity of electrons becomes:

$$C_{\text{NbTi}}(T > T_c) = \frac{\gamma_{\text{sum}}}{H_{c20}}BT + \frac{3\gamma_{\text{sum}}}{T_c^2}T^3 \quad [\text{J/Km}^3] \quad (\text{F.2})$$

with H_{c20} , the upper critical field at 0 K, and T_c the critical temperature. The resulting heat capacity of NbTi is then:

$$C_{\text{NbTi}}(T > T_c) = \frac{\gamma_{\text{sum}}}{H_{c20}}BT + (\beta_{\text{Debye}} + \frac{3\gamma_{\text{sum}}}{T_c^2})T^3 \quad [\text{J/Km}^3] \quad (\text{F.3})$$

Table F.1 (page 251) summaries the values of the different parameters used in our computation.

F.1.2 Heat capacity of copper

The heat capacity of copper, C_{Cu} , has been extracted from the CRYOCOMP® software [2]. A table of values as a function of temperature has been implemented into the stability program.

Table F.1: Numerical values to evaluate the heat capacity of NbTi.

Parameters	Values
Summerfeld's parameter: γ_{sum}	1011.8 J/m ³ K ²
Debye's parameter: β_{Debye}	16.07 J/m ³ K ²
Upper critical field: H_{c20}	11 T
The critical temperature: T_c	9.5 K

F.1.3 Average heat capacity of the Cu/NbTi composite wire

The average heat capacity of the wire, C_w , is estimated as:

$$C_w = x_s C_{\text{NbTi}} + (1 - x_s) C_{\text{Cu}} \quad [\text{J/Km}^3] \quad (\text{F.4})$$

Figure F.1 (page 252) shows a comparison of the heat capacities of copper, NbTi and of the wire at 7 T.

F.2 Resistivity of the wire

F.2.1 Resistivity of NbTi

In the flux flow regime, the resistance of the superconductor is a lot larger than the one of the copper. It is about $6.5 \times 10^{-7} \Omega \text{ m}$ at 6 T for the NbTi and $0.34 \times 10^{-9} \Omega \text{ m}$ for copper ($RRR=150$) at 6 T. So, it can be neglected in the case of the normal-state transition of the superconductor compared to the resistivity of copper.

F.2.2 Resistivity of copper

It is necessary to distinguish the high purity copper surrounding the multifilament zone and at the wire core from the copper which is intimately bonded to the NbTi filaments in the multifilament zone. Indeed, the presence of the filaments reduces the mean free path of the electrons thereby increasing the apparent resistivity of copper [3] [4] [5].

High purity copper, Cu1: A subroutine implemented into the procedures of the stability program calculates a table of copper resistivity versus temperature using input parameters as temperature range and increment, background magnetic field, and Residual Resistivity Ratio (RRR) of the material. The subroutine was adapted from the routines of the CRYOCOMP[®] software [2].

Degraded copper of the multifilament zone, Cu2: At low temperature, the mean free path of the electrons increases and it becomes larger than the interfilament spacing. It appears then a size effect which must be taken into account to model the thermal and electrical properties of the copper [6].

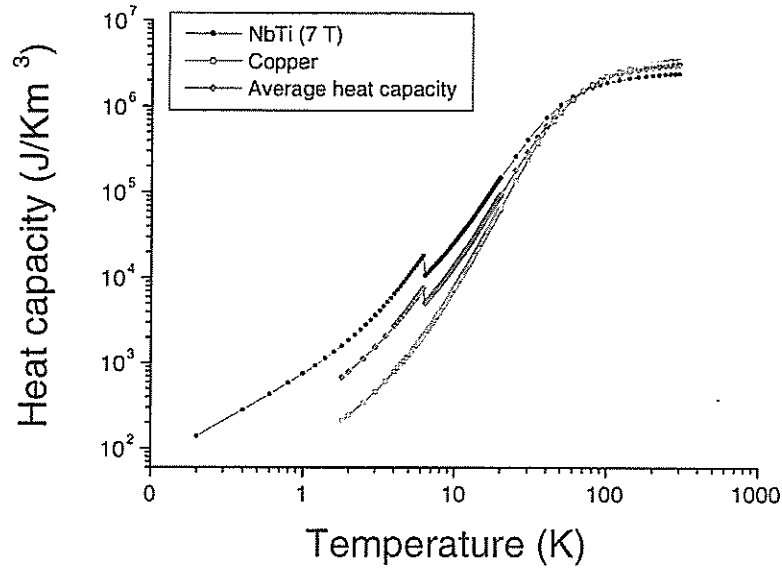


Figure F.1: Heat capacity of the Copper and NbTi, and resulting average heat capacity of the wire as a function of temperature at 7 T.

Considering the size effect, the total resistivity of the copper in the multifilament zone is given by Nordheim's formula [7]:

$$\rho_{Cu2} \simeq \rho_{Cu1} + \rho_{deg} = \left(1 + \frac{l_f}{d}\right) \rho_{Cu1} \quad [\Omega m] \quad (F.5)$$

$$l_f = \frac{m\nu_F}{ne^2\rho} \simeq \frac{4.7 \times 10^{-16}}{\rho_{Cu1}} \quad [m] \quad (F.6)$$

with [8]:

- $d \simeq 1 \mu m$ is the interfilament spacing.
- l_f is the mean free path of the electron.
- $\nu_F \simeq 1.57 \times 10^6$ m/s is the velocity at the Fermi surface.
- $n \simeq 8.45 \times 10^{28}$ m⁻³ is the electron concentration.
- $m \simeq 9.10956 \times 10^{-31}$ kg is the electron rest mass.
- $e = 1.9 \times 10^{-19}$ C is the elementary charge of the electron.

These equations prevail at low temperatures for which $l_f \gg d$. In particular, it remains true at temperatures below ~ 30 K corresponding to the plateau of Residual Resistivity Ratio (Appendix A).

As an example, let us compare the mean free path of copper between 4.2 K and 293 K at 7 T. At 4.2 K, the mean free path of copper ($RRR = 150$), is equal to $\sim 1.2 \mu m$ which is of the order of the distance between the filaments and the size effect must be considered. It does not meet the hypothesis of Nordheim's formula. nevertheless, it is a sufficient approximation for a conservative calculation¹. At 293 K, the mean free

¹For a thorough investigation, we refer to Brandli and Olsen's work [6].

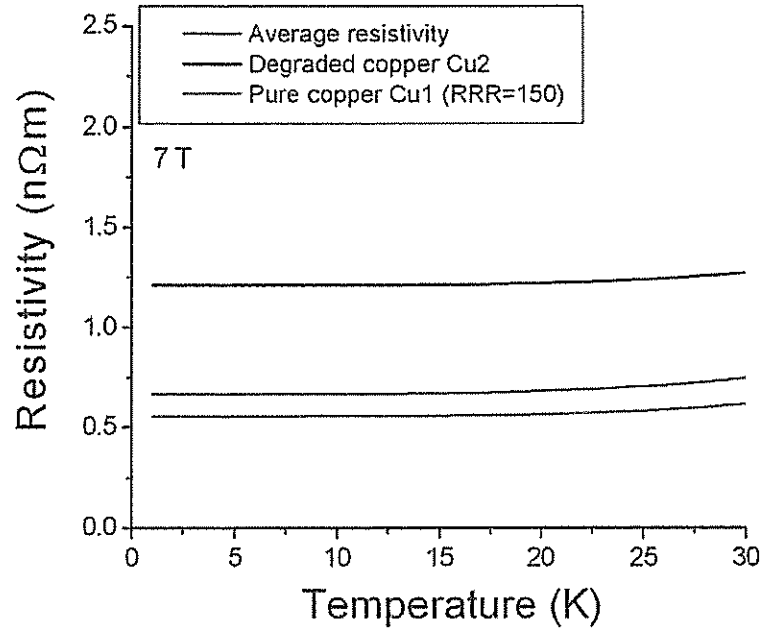


Figure F.2: Resistivity of the different coppers (pure copper Cu1 and degraded copper Cu2) and resulting average resistivity of the wire as a function of the temperature at 7 T.

path becomes equal to $\sim 0.3 \mu\text{m}$ which is inferior to the interfilament spacing and the size effect is negligible. In our simulation for which the temperature excursion of the wire sample does not extend beyond 30 K, the size effect has been taken into account. For large temperature excursions, the mean free path of copper decreases such that the resistivity of copper Cu2 can be assumed equal to ρ_{Cu1} .

F.2.3 Average resistivity of the wire

The average resistivity of the wire, ρ_w , is computed as the average resistivity of the pure copper Cu1 and of the degraded copper Cu2. We get:

$$\rho_w = \frac{\rho_{\text{Cu1}}\rho_{\text{Cu2}}}{x_{\text{Cu1}}\rho_{\text{Cu1}} + x_{\text{Cu2}}\rho_{\text{Cu2}}} \quad [\Omega\text{m}] \quad (\text{F.7})$$

Figure F.2 (page 253) shows the resistivity of the pure copper Cu1 for $RRR = 150$, the corresponding degraded copper Cu2, and the resulting average resistivity at 7 T.

F.3 Thermal conductivity

F.3.1 Thermal conductivity of high purity copper

The subroutine implemented into the procedures of the stability program to calculate the resistivity of copper (see paragraph F.2.2, page 251) also calculates the thermal conductivity of copper with the same parameters: background magnetic field and Residual Resistivity Ratio.

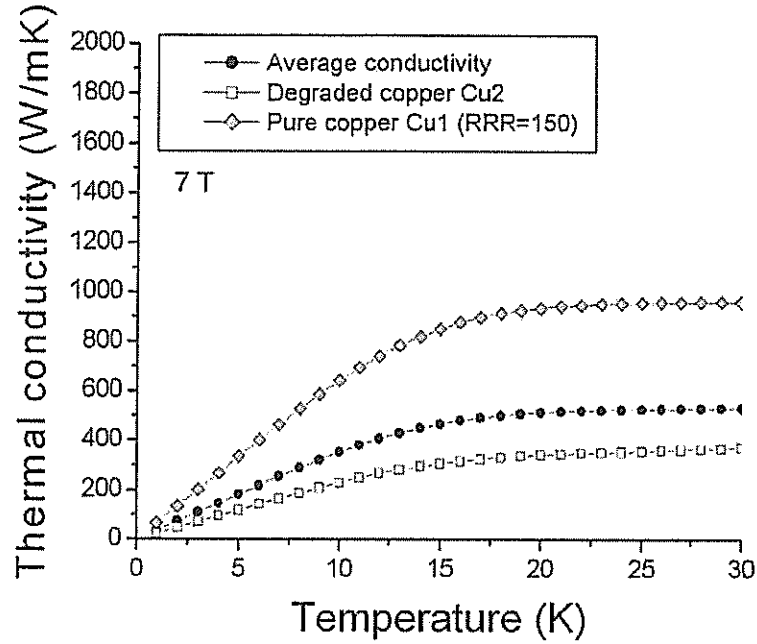


Figure F.3: Thermal conductivity of the different coppers (pure copper Cu1 and degraded copper Cu2) and the average thermal conductivity as a function of the temperature at 7 T.

F.3.2 Thermal conductivity of the degraded copper of the multifilament zone

To derive the thermal conductivity of the degraded copper, λ_{Cu2} , we rely on Wiedemann-Franz's law prevailing at low temperature [9]. This law yields the following relation between the thermal conductivity, λ , and the resistivity of the material, ρ , at low temperature:

$$\rho\lambda = L_0T \quad [\Omega\text{W/K}] \quad (\text{F.8})$$

where $L_0 = 2.45 \times 10^{-8} \text{ W}\Omega/\text{K}^2$ is the Lorentz's constant. By writing this equation for the two copper types, and by taking the ratio between them, the thermal conductivity of the degraded copper of the multifilament zone can be derived as:

$$\lambda_{\text{Cu2}} = \frac{\rho_{\text{Cu1}}}{\rho_{\text{Cu2}}} \lambda_{\text{Cu1}} \quad [\text{W/m/K}] \quad (\text{F.9})$$

This equation prevail at low temperature. We did not correct this result for temperature above 30 K since the numerical temperature rise does not rise beyond a few tenths of Kelvins (see remark in paragraph F.2.2, page 251).

F.3.3 Thermal conductivity of NbTi

The thermal conductivity of NbTi is about two orders of magnitude inferior to the one of copper. The proportion of copper in the multifilament zone being of the same order of magnitude as the one of NbTi, the thermal conductivity of NbTi has been

neglected.

For example, at 7 T and 4.2 K, the thermal conductivity of copper ($RRR=150$) is ~ 55 W/m-K (calculated from equation F.9, page 254) while the one of NbTi is only ~ 0.1 W/m-K.

F.3.4 Average longitudinal thermal conductivity of the conductor

As we neglect the longitudinal thermal conductivity of NbTi, the one of the wire is reduced to:

$$\lambda_w = x_{Cu1}\lambda_{Cu1} + x_{Cu2}\lambda_{Cu2} \quad [\text{W/m/K}] \quad (\text{F.10})$$

Figure F.3 (page 254) gives the thermal conductivity of the pure copper Cu1, the degraded copper Cu2, and the average thermal conductivity at 7 T.

References

- [1] C. Kittel. *Introduction to Solid State Physics-7th ed.* John Wiley & Sons, 1996.
- [2] CryoData. CRYOCOMP®.
- [3] W.B. Sampson, M. Garber, and A.K. Ghosh. Normal state resistance and low temperature magnetoresistance of superconducting cables for accelerator magnets. *IEEE Transactions on Magnetics*, 25:2097–2100, March 1989.
- [4] R. Monnier C. Cavalloni, K. Kwasnitza and I. Horvath. Size effect of the longitudinal resistivity of multifilamentary superconducting wires. *Applied Physics Letter*, 42:734–736, 1983.
- [5] F.R. Fickett. *Materials at low temperature*, chapter 5: Electronic properties. American Society for Metals, 1983.
- [6] G. Brandli and J.L. Olsen. Size effect in electron transport in metals. *Material of Science and Engineering*, 4:61–83, 1969.
- [7] L. Nordheim. The anomalous skin effect and the reflectivity of metals. I & II. *Acta Scientiae et Industriae*, 131, 1934.
- [8] C. Kittel. *Introduction to Solid State Physics-7th ed.*, page 159. John Wiley & Sons, 1996.
- [9] L. Dresner. *Stability of Superconductors*. Plenum Press, New York, 1995.

